Studies of the Drell-Yan process for luminosity monitoring and new physics searches with the ATLAS detector

Thesis submitted in accordance with the requirements of
the University of Liverpool for the degree of Doctor in Philosophy
by

Michael William O'Keefe

Under the supervision of
Prof. Uta Klein

Department of Physics
University of Liverpool
United Kingdom

December 2021

Abstract

This thesis focuses on investigations of the Drell-Yan production of gauge bosons in dilepton final states at the ATLAS detector, both in the context of the Standard Model (W and Z) and beyond (W'). The analyses presented utilise the full Run-2 ATLAS pp dataset recorded between 2015 – 2018 at $\sqrt{s} = 13$ TeV.

The luminosity recorded by the ATLAS detector can be monitored by measuring the production rate of the Z boson. Detector inefficiencies are modelled directly from the data itself over time periods of 60 seconds, which gives the method excellent stability with respect to the changing conditions inside the detector. The measurement is performed in the $Z \rightarrow e^+e^-$ and $Z \rightarrow \mu^+\mu^-$ channels which have completely independent chains of corrections and show excellent agreement to within 0.8% of one another for the full Run-2 dataset. In particular, the novel addition of the $Z \rightarrow e^+e^-$ channel greatly increases the power of the method by providing an internal cross-check as well as increased statistical precision by combining the two channels. These two measurements are used to monitor the stability of the baseline ATLAS luminosity measurement, which could improve the understanding of the associated systematic uncertainties.

A search for a new heavy charged gauge boson (W') in the lepton + missing energy final state is also presented. This channel is experimentally very clean, and offers an excellent lens with which to search for new physics at hadron colliders. No significant excess is observed with respect to the expected background predicted by the Standard Model, which is dominated by charged-current Drell-Yan production. An observed (expected) lower limit of $6\,\mathrm{TeV}$ $(5.8\,\mathrm{TeV})$ is set on the mass of the W' boson in the context of the Sequential Standard Model (SSM), the highest such limit set by any physics experiment to date. Model independent limits are also provided for a range of generic signal models, greatly increasing the range of possible theoretical interpretations of the presented results. In addition to this limits are set on the visible cross section, ranging from $4.6\,\mathrm{pb}$ at W' masses of $130\,\mathrm{GeV}$ to $22\,\mathrm{ab}$ above $3.4\,\mathrm{TeV}$.

Acknowledgements

With immense gratitude I would like express my thanks to: my supervisor Uta Klein for the constant guidance and encouragement, without which this thesis would certainly not have been possible; my family for their love and support; my better half Lucy for being a constant source of inspiration; and the many other people who have helped me along the way.

'One generation passeth away, and another generation cometh: but the earth abideth for ever. The sun also ariseth, and the sun goeth down, and hasteth to his place where he arose. The wind goeth toward the south, and turneth about unto the north; it whirleth about continually, and the wind returneth again according to his circuits. All the rivers run into the sea; yet the sea is not full; unto the place from whence the rivers come, thither they return again'. (Ecclesiastes 1:4-7)

Contents

List of Figures

List of Tables

Introduction

The analyses presented in this thesis focus on the Drell-Yan production of dileptons at the ATLAS detector. An overview of the Standard Model and its limitations is presented in Chapter 1, and a more thorough examination of the Drell-Yan process is given in Chapter 2. The experimental setup of the Large Hadron Collider and ATLAS detector is presented in Chapter 3.

Chapter 4 presents a novel method for monitoring the luminosity recorded by the ATLAS detector by measuring the production rate of the Z boson. The stability of the baseline ATLAS luminosity measurement has been monitored using $Z \rightarrow \mu^+\mu^-$ events since 2015, which was expanded during 2018 data-taking to include a completely new measurement using $Z \rightarrow e^+e^-$ events. This work was undertaken by the author as the basis for an ATLAS service task, and has been continually developed and expanded afterwards to improve the stability of the method. The framework runs during early data-processing, and can provide fast feedback to the ATLAS luminosity group about the operational conditions during data-taking. This measurement could also contribute to an improved characterisation of the systematic uncertainties affecting the baseline ATLAS luminosity. The results of this analysis were published in an ATLAS public note [1], where the author was a lead editor, and were also presented by the author at ICHEP 2020 [2]. Subsequently, the author co-founded a new ATLAS analysis group based on this analysis, aiming to reinterpret the data in the context of probing potential Lorentz-invariance violating coefficients in Standard Model extension models. An initial analysis is presented in Appendix C.

Chapter 5 presents the results of a search for new a heavy charged gauge boson (W') at ATLAS using the full Run-2 dataset. Various theoretical interpretations are presented in order to provide a vast landscape for comparison of the ATLAS data with W' signal models. Specific focus is placed on the electron channel analysis ($W' \rightarrow e\nu$), where the author was the lead analyser and analysis contact in this channel. These results were among the first produced by ATLAS using the full Run-2 dataset and were published in Phys. Rev. D [3]. The author then went on to present the results at the annual ATLAS UK conference in Cambridge (2019), as well as at Epiphany (Krakow, 2021) [4]. Chapter 6 provides a summary of the analyses presented within and their results.

Chapter 1

The Standard Model and its limitations

1.1 A brief overview

The Standard Model (SM) of particle physics is a relativistic quantum field theory that describes the properties of elementary particles and the interactions between them at energies below the Planck scale (1.22×10^{19}GeV). Elementary particles are the fundamental constituents of matter, and the interactions between them make up three of the four fundamental forces: electromagnetic, weak and strong. Gravity is the exception as it is not described by the Standard Model and is instead explained by General Relativity [5]. The three forces that are described in the Standard Model are mediated by the exchange of gauge bosons, particles with integer spins, each of which is associated with some symmetry group (gauge). The electromagnetic and weak sectors are described by a single unified description known as the electroweak interaction [6, 7, 8], which is governed by the exchange of photons, W and Z bosons ($SU(2) \times U(1)$), while the strong interaction is governed by the exchange of gluons ($SU(3)$) [9].

In addition to the force carrying gauge bosons, there is the Higgs boson [10, 11, 12] which is responsible for generating the masses of the weak bosons and massive fermions via spontaneous symmetry breaking. Gauge invariance means that the W and Z bosons should be massless, a fact which is contradicted by experimental evidence and the short range of the weak force. The introduction of a complex scalar Higgs field mediated by the Higgs boson leads to spontaneous symmetry breaking, giving the weak bosons their mass while still respecting global gauge invariance. The masses of the W and Z bosons are free parameters in the Standard Model and must be determined experimentally, as are the masses of the fermions which are generated as a result of a Yukawa coupling term between the fermion and Higgs fields.

Tables 1.1 and 1.2 show all the currently known particles of the Standard Model, arranged into their respective families and generations. The families into which particles can be organised are most broadly fermions and bosons, with fermions having half-integer spin and bosons integer spin. Within the fermion

Fermions: half-integer spin particles						
Generation	**Particle**	**Charge**	**Mass [MeV]**	**Interactions**		
				EM	Weak	Strong
1	u	+2/3	2.2	✓	✓	✓
	d	-1/3	4.7	✓	✓	✓
	e	1	0.511	✓	✓	✗
	ν_e	0	< 0.001	✗	✓	✗
2	c	+2/3	1280	✓	✓	✓
	s	-1/3	96	✓	✓	✓
	μ	1	105.66	✓	✓	✗
	ν_μ	0	< 0.17	✗	✓	✗
3	t	+2/3	173.1×10^3	✓	✓	✓
	b	-1/3	4180	✓	✓	✓
	τ	1	1777	✓	✓	✗
	ν_τ	0	< 18.2	✗	✓	✗

Table 1.1: All known Standard Model fermions arranged into their respective generation, with their charge, mass, and mode of interaction shown.

Bosons: integer spin particles					
Particle	**Charge**	**Spin**	**Mass [GeV]**	**Force**	**Gauge group**
γ	0	1	0	EM	$U(1)$
$W^\pm$	±1	1	80	Weak	$SU(2)_L$
Z	0	1	91	Weak	$SU(2)_L$
g	0	1	0	Strong	$SU(3)_c$
H	0	0	125	-	$SU(2)$

Table 1.2: All known bosons of the Standard Model, with their charge, spin, mass, corresponding force and gauge group given.

family there are two further divisions, the quarks and leptons. Quarks (u, d, c, s, t, b) interact via the weak, electromagnetic and strong forces. Within the lepton family there is a distinction between the charged leptons (e, μ, τ) which interact via the electromagnetic and weak forces, and the almost massless neutrinos (ν_e, ν_μ, ν_τ) [1] which interact only via the weak force. The term generation refers to the fact that in both the quark and lepton families, for a given charge there are three distinct particles, with the only difference being their masses.

There are further quantum numbers associated with SM particles, some examples of which are weak hypercharge, weak isospin, colour charge, lepton number and baryon number. The lepton and baryon numbers simply relate to the number and type of particles present in an interaction. Weak hypercharge and isospin [2] are the generators of $SU(2)$ and $U(1)$ in electroweak interactions, and can be understood as eigenstates of the flavour and charge operators. Colour charge is associated with the eigenstates of $SU(3)$ in the strong interaction, and can take values of red, green or blue (with anti versions of these colours for anti-particles). The strong interaction is described by quantum chromodynamics, a quantum field

---

[1] The current upper limit on the mass of the neutrino is 1.1 eV [13].

[2] Here weak isospin refers to the third component of weak isospin, the component which must be conserved in electroweak interactions.

theory that governs the interactions between quarks and gluons. Combining the constituent forces of the Standard Model, one can define the SM gauge group as $SU(3) \times SU(2) \times U(1)$, with the corresponding Lagrangian,

$$\begin{aligned}
\mathcal{L}_{\mathrm{SM}} = &-\frac{1}{4}F_{\mu\nu}F^{\mu\nu} && \text{(gauge sector)} \\
&+ i\bar{\psi}D\psi + h.c. && \text{(matter-gauge coupling)} \\
&+ \psi_i y_{ij} \psi_j \phi + h.c. && \text{(Yukawa sector)} \\
&+ |D_\mu \phi|^2 - V(\phi). && \text{(Higgs sector)}
\end{aligned} \tag{1.1}$$

The first line of Eq. 1.1 contains the kinetic terms of the three gauge sectors of the Standard Model; the second line describes the interactions between the fermionic matter fields and the bosonic gauge fields; the third line accounts for the Yukawa interaction between matter fields and the Higgs field, giving rise to the fermion masses as a result of electroweak symmetry breaking; and the fourth line contains the kinetic and potential terms of the Higgs sector.

Even though all the particles predicted by the Standard Model have already been discovered, many of their properties are still being probed by experiment. To take just one interesting example; analyses are performed to probe lepton universality, which refers to the fact that there is an equal probability for a W or Z boson to decay into a e, μ or τ lepton. The ratio of the decay rates of $W \to \tau\nu$ and $W \to \mu\nu$ ($R(\tau/\mu)$) is measured by ATLAS to be 0.992 ± 0.013, the most precise measurement to date [14]. This result indicates that there is no evidence yet for lepton universality violation in the Standard Model, however, many other important analyses are performed to study the properties of Standard Model particles; for example the polarisation of the top quark [15], Higgs decays to $b\bar{b}$ pairs [16], photon-induced W^+W^- production [17] and many other interesting analyses. As will be discussed in Chapter 4, measuring the well-understood production rate of the Z boson at hadron colliders can provide a powerful method of monitoring the luminosity that is delivered to the detector.

1.2 Searching for new physics

While the discovery of the Higgs boson in 2012 [18, 19] marked the completion of the Standard Model as such, there are still many phenomena as yet unexplained by the theory; for example the asymmetry between matter and anti-matter, the nature of Dark Energy and Dark Matter, the difference in the effective scale and measured scale of some physical parameters (the hierarchy problem) and why gravity is not governed by the exchange of a gauge boson - or is it governed by an as yet undiscovered gauge boson?

Answers to these questions can be provided by both searching for new, as yet undiscovered particles, or by measuring the properties of existing particles to greater precision (direct and indirect searches).

Collider experiments at the LHC offer means of directly searching for new elementary particles by colliding beams of high-energy protons and measuring the resulting final state particles. The Higgs boson was the latest particle to be discovered in 2012 by the ATLAS and CMS experiments at CERN by analysing $4.8\,\text{fb}^{-1}$ $(5.8\,\text{fb}^{-1})$ [3] of pp collision data recorded at a centre-of-mass energy of $\sqrt{s} = 7\,\text{TeV}(8\,\text{TeV})$. By comparing the observed mass distribution to the background expectation and calculating the probability of a background fluctuation creating an excess greater than or equal to that observed in the data, the significance of the observation can be measured. This was found to be 5.9σ (local) for the ATLAS measurement and 5.1σ for CMS, consistent with a Standard Model Higgs boson of mass 126 GeV. Further analyses of the Higgs boson at ATLAS and CMS have measured its mass to be 125.25 ± 0.17 GeV [20].

The $g-2$ experiment is an example of an indirect search for new physics. By measuring the anomalous magnetic moment of the muon to extremely high precision (11 decimal places), evidence for new forces or particles could be indirectly detected. The anomalous magnetic moment arises due to radiative corrections resulting from virtual effects involving fermions, photons, electroweak bosons and the Higgs boson. In the presence of new undiscovered particles, there would be tension between the value predicted by the Standard Model and the experimentally observed value. The world average for this value has a significance of 4.2σ when compared with the value predicted by the Standard Model [21], suggesting that there could be strong evidence for interactions between the muon and an additional non Standard Model particle.

The discovery of the Higgs boson and the interesting results of the $g-2$ experiment only scratch the surface of the work done to search for physics beyond the Standard Model. There are many other theories which predict particles beyond the Standard Model, and searches are undertaken at the ATLAS detector to look for evidence of their existence. One broad class of theories is known as supersymmetry, which predicts bosonic partners to the SM fermions and fermionic partners to the SM bosons [22, 23]. Another set of models predict the existence of bosons with both lepton and baryon number, known as leptoquarks [24, 25]. Searches are also performed for evidence of dark matter [26, 27], as well as for extended Higgs [28, 29] and electroweak sectors [30].

Effective field theories (EFTs) are another class of models which only focus on one particular scale or degree of freedom, ignoring effects coming from different scales or higher degrees of freedom, although physics at different scales can be introduced using perturbation theory. Many popular models treat the Standard Model as an effective field theory, in which additional couplings are suppressed at low-energy scales. [4] One such model is the Standard Model Effective Field Theory (SMEFT) [31, 32], which

---

[3] These numbers correspond to the ATLAS detector. The corresponding CMS luminosities are 5.1 and $5.3\,\text{fb}^{-1}$.

[4] For instance, below the Planck scale in the Standard Model Extension or below $\mathcal{O}(10$ TeV$)$ in the SMEFT.

introduces 2499 dimension-6 operators ($\mathcal{O}_i$) to the SM Lagrangian,

$$\mathcal{L}_{\mathrm{SMEFT}} = \mathcal{L}_{\mathrm{SM}} + \sum_{i=1}^{2499} \frac{C_i}{\Lambda} \mathcal{O}_i. \tag{1.2}$$

The interaction scale of the SMEFT (Λ) is much larger than the scale of SM particles, and so the low-energy behaviour of the SMEFT mimics that of the SM. Fits are performed to experimental data to probe for evidence of higher-dimensional operators, and as it is impractical to include 2499 operators, certain fermionic flavour assumptions are made to simplify the model. So far no evidence of further interactions has been found, and limits have been set on the dimension-6 SMEFT Wilson coefficients (C_i) in the Warsaw basis [33] by measuring $H \to \ell\ell\ell\ell$ decays at ATLAS [34].

Searches are a fundamental component of the LHC physics programme, and the second part of this thesis is devoted to the quest to find evidence of new heavy charged gauge bosons using the full Run-2 dataset (Chapter 5). The discovery of additional heavy electroweak gauge bosons would have a dramatic impact on the landscape of particle physics and could offer an explanation of the difference in hierarchy between some of the fundamental physical parameters of the Standard Model. An additional proof-of-principle analysis is presented in Appendix C, using Z boson production rate data to probe for Lorentz-invariance violation in the quark sector. Such effects are predicted by the Standard Model Extension (SME) [35], an effective field theory which introduces Lorentz-invariance violating coefficients.

Chapter 2

The Drell-Yan process

The analyses presented in this thesis focus on neutral- and charged-current Drell-Yan production of gauge bosons; measuring the production rate of the SM Z boson to monitor the luminosity delivered to the detector as well as searching for new heavy gauge bosons produced via the Drell-Yan mechanism (W') where the dominant Standard Model background contribution comes from the charged-current Drell-Yan interaction. This chapter presents a theoretical overview of the Drell-Yan process, as well as the phenomenological framework which is used to make predictions at high-energy hadron-hadron colliders.

2.1 Introduction

Predicted in 1970 by Sidney Drell and Tung-Mow Yan [36], the Drell-Yan mechanism is a process that occurs in hadron-hadron collisions whereby a quark and antiquark annihilate one another to produce a virtual boson. Neutral-current scattering refers to the production of a virtual photon or Z boson, while charged-current scattering refers to the production of a charged W boson. In the case of neutral-current scattering, the produced boson subsequently decays into a pair of oppositely charged leptons, while the final state of charged-current scattering consists of a charged lepton and a neutrino, as demonstrated in Figure 2.1. The branching fraction of $W \to e\nu$ ($W \to \mu\nu$) is 10.7 ± 0.16 % (10.63 ± 0.15 %) and the branching fraction of $Z \to e^+e^-$ ($Z \to \mu^+\mu^-$) is 3.3632 ± 0.0042 % (3.3662 ± 0.0066 %) [20]. It is important to note that in this thesis decays to τ leptons will be considered as a source of background, accounting for approximately 11.4% of the branching fraction of the W and 3.7% of the Z.

The QCD-improved parton model describes the proton as being composed of quarks bound together by the exchange of gluons. At low-resolution the proton is composed of uud quarks, bound together by the exchange of gluons. These are known as *valence quarks*. However, since the gluon also carries colour charge it can split to produce two so-called *sea quarks*, which can in turn annihilate one another to produce

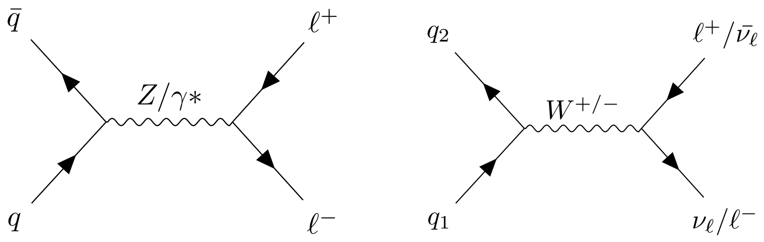

Figure 2.1: Feynman diagrams for charged (left) and neutral (right) current Drell-Yan scattering at leading order.

another gluon. The total proton momentum is split between the valence quarks, sea quarks and gluons, therefore, the internal dynamics of the proton are complex, and there is no reliable way in QCD to predict this internal structure.

Much experimental effort is devoted to understanding these complex interactions by measuring *parton distribution functions* (PDFs, Section 2.3), primarily by exploiting deep inelastic scattering (DIS) scattering data. Since the Drell-Yan process is sensitive to the internal structure of the proton, precise predictions require accurate knowledge of the parton distribution functions. On the other hand, measuring the kinematic properties of particles produced by the Drell-Yan process can also provide constraints to the internal structure of the proton by probing the quark/anti-quark composition. Measurements of inclusive W and Z cross sections using ATLAS data, combined with charged- and neutral-current deep inelastic scattering data collected by the H1 and ZEUS collaborations [37] found evidence that the amount of strange quarks in the proton sea is roughly equivalent to the number of up/down quarks [38], providing evidence of light-flavour symmetry at Bjorken $x < 0.01$ (the fraction of the protons momentum carried by each parton).

2.2 Phenomenological overview

In general, calculating the cross section of any process relies on first calculating the matrix element. Ignoring the integration over the phase space (spin, flavour, polarisation), the general form of an s-channel matrix element in $2 \rightarrow 2$ scattering is,

$$\mathcal{M} = \langle p_1|V|p_2\rangle \, P \, \langle k_1|V|k_2\rangle \tag{2.1}$$

where p and k are the propagators of the incoming and outgoing particles, V is the scattering potential and P is the propagator of the virtual boson. Matrix elements can be derived by following the Feynman rules [39], which consists of: external fermion propagators, virtual boson propagators and vertex factors. The product of the incoming fermion, vertex factor and outgoing fermion is calculated for each vertex in the interaction. The matrix element is equal to the product of each of these terms and the propagator of the virtual exchange boson, the square of which is proportional to the cross section of the process.

To leading order (LO), the differential Drell-Yan cross section can be expressed in terms of the invariant mass of the dilepton system (M) and the rapidity of the produced boson (y) V [40]

$$\frac{d^2\sigma_V}{dM \cdot dy} = \frac{4\pi\alpha^2(M_V)}{9} \cdot 2M_V \cdot P_V(M_V) \cdot \Phi_V(x_1, x_2, M_V), \tag{2.2}$$

where $\alpha(M_V)$ represents the fine structure constant, $P_V(M_V)$ is the propagator, Φ_V is the parton distribution term and $x_{1,2}$ are the Bjorken x values of each parton participating in the collision. Rapidity is a measure of the angle between the $x-y$ plane and z axis, where the z axis is along the beamline and the $x-y$ plane is perpendicular. A particle with infinitesimally small momentum along the z axis (p_z) will have a rapidity of 0, while a particle with extremely large p_z will tend towards $y \rightarrow \inf$. There are distinct propagator and parton distribution terms for W and $Z/\gamma*$ production as a result of the different properties of the exchange bosons involved.

Charged-current scattering The propagator term for W production is given by

$$P_W = \frac{1}{(4\sin^2\theta_W)^2 \cdot [(M^2 - M_W^2)^2 + (\Gamma_W M_W)^2]}, \tag{2.3}$$

where θ_W is the weak mixing angle, Γ_W is the width of the W and M_W its pole mass. The parton distribution term is sensitive to the charge of the W boson, and there are therefore distinct terms taking into account the flavour composition of the incoming partons

$$\Phi_{W^+} = x_1x_2[U_{ud}^2(u_1\bar{d}_2 + u_2\bar{d}_1) + U_{cs}^2(c_1\bar{s}_2 + c_2\bar{s}_1) + U_{us}^2(u_1\bar{s}_2 + u_2\bar{s}_1) + U_{cd}^2(c_1\bar{d}_2 + c_2\bar{d}_1)], \tag{2.4}$$

$$\Phi_{W^-} = x_1x_2[U_{ud}^2(\bar{u}_1d_2 + \bar{u}_2d_1) + U_{cs}^2(\bar{c}_1s_2 + \bar{c}_2s_1) + U_{us}^2(\bar{u}_1s_2 + \bar{u}_2s_1) + U_{cd}^2(\bar{c}_1d_2 + \bar{c}_2d_1)], \tag{2.5}$$

where U_{ij} are the CKM matrix elements [41] - values which govern the strength of the flavour-changing weak interaction - and u, d, c and s are the parton distribution functions for each quark flavour, where the dependence on Bjorken x and the scale M^2 has been dropped to improve readability. This formalism uses the 4-flavour scheme (u, d, c, s), which can be extended to five (u, d, c, s, b) or even six flavours (u, d, c, s, b, t); however, the bottom and top contributions are much smaller than the light quark contributions as they have small off-diagonal CKM matrix elements.

Neutral-current scattering Since the neutral-current process (Z/γ^*) has contributions from pure Z and γ^* exchange, as well as their interference, the cross section is calculated by taking the sum over all propagators,

$$P_Z = \frac{(v_e^2 + a_e^2)}{(4\sin^2\theta_W \cdot \cos^2\theta_W)^2 \cdot [(M^2 - M_Z^2)^2 + (\Gamma_Z M_Z)^2]}, \tag{2.6}$$

$$P_\gamma = \frac{1}{M^4}, \tag{2.7}$$

$$P_{Z\gamma} = \frac{v_e(M^2 - M_Z^2)}{4\sin^2\theta_W \cdot \cos^2\theta_W \cdot M^2\,[(M^2 - M_Z^2)^2 + (\Gamma_Z M_Z)^2]}, \tag{2.8}$$

where v_e (a_e) is the vector (axial) coupling of the electron. The vector and axial couplings are defined as $v_f = T_f^3 - 2e_f \sin\theta_W$ and $a_f = T_f^3$, where T_f^3 is the third component of weak isospin of the fermion of type f [1] and e_f is its electric charge. Each propagator also has its own unique parton distribution term, which is sensitive to the universal PDF for a quark of that flavour ($q(x, M^2)$)

$$\Phi_Z = \sum_q (v_q^2 + a_q^2) F_{q\bar{q}}, \tag{2.9}$$

$$\Phi_\gamma = \sum_q e_q^2 F_{q\bar{q}}, \tag{2.10}$$

$$\Phi_{Z\gamma} = \sum_q 2e_q v_q F_{q\bar{q}}. \tag{2.11}$$

$$F_{q\bar{q}} = x_1 x_2 [q(x_1, M^2)\bar{q}(x_2, M^2) + \bar{q}(x_1, M^2) q(x_2, M^2)] \tag{2.12}$$

As a result of the form of the propagator terms in Eq. 2.3 and Eq. 2.6-2.8, the Drell-Yan cross section decreases rapidly as a function of M^2 (Q^2), except near the W and Z mass where there is a resonance. This is one of the defining features of the Drell-Yan process. It is also evident from Eq. 2.4-2.5 and Eq. 2.9-2.11 that there is a significant component of the cross section which is sensitive to the internal structure of the proton. Therefore, it is of the utmost importance that a state-of-the-art description of these internal dynamics is obtained using the best possible theoretical predictions, both for testing the accuracy of the Standard Model and for searching for evidence of physics beyond.

The description given so far is only the leading order picture, and a vital component of the Drell-Yan process are higher order corrections. As will be discussed in Section 2.4, there are large radiative corrections to the Drell-Yan process due to additional QCD and electroweak (EW) radiation. These

---

[1] This is $+1/2$ for neutrinos and *up-type* quarks (u, c, t) and $-1/2$ for charged leptons and *down-type* quarks (d, s, b).

higher order corrections modify the total cross section of the process, as well as the kinematic behaviour of the decaying bosons and become especially large at high masses. This is of particular importance when searching for new heavy resonant gauge bosons (Chapter 5), where state-of-the-art background descriptions are crucial to detect unexpected excesses of data with respect to Standard Model predictions.

2.3 Parton distribution functions

Parton distribution functions describe the probability of finding a parton of a certain flavour and momentum fraction inside the proton. There is no practical way in QCD to predict the shapes of these functions, and much of this information comes from electron-proton deep inelastic scattering data [37]. However, proton-proton data is starting to play an increasingly important role in testing PDFs with the inclusion of Drell-Yan, gauge boson production and jet production data providing valuable insight [42]. There are many groups dedicated to the QCD fits of parton distribution functions, with varying model assumptions and large uncertainties at very high ($x > 0.5$) and small ($x < 0.0001$) Bjorken x values [37, 42, 43, 44].

In high-energy deep inelastic scattering, the time taken by an electron or photon to traverse the proton is extremely small, and can therefore be considered as an interaction with a stationary distribution of partons inside the proton. Since the time-scale is so short, the partons have no time to interact with one another, and therefore the electron (or photon) probes the probability distribution of finding a parton of flavour i and momentum fraction x inside the proton. In practice, this is done by measuring a variety of differential cross sections as a function of Bjorken x at various values of Q^2 and performing a global QCD fit [45].

The Bjorken x value is related to the scale, momentum transfer and proton momentum ($\mathbf{p}$) of the interaction

$$x = \frac{Q^2}{2\mathbf{p} \cdot \mathbf{q}}. \tag{2.13}$$

In the case of the Drell-Yan process, the scale is equal to the square of the mass of the exchanged vector boson ($Q^2 = M^2$), and the Bjorken x value is related to the rapidity (y) of the produced boson at leading-order

$$x_{1,2} = \frac{M}{\sqrt{s}} \cdot e^{\pm y}. \tag{2.14}$$

The rapidity can be expressed in terms of experimental observables by measuring the energy (E) and longitudinal momentum (p_z) of the boson,

$$y = \frac{1}{2} \ln \frac{E + p_z}{E - p_z}. \tag{2.15}$$

The functional form of the fit is generally a polynomial of fixed order in Bjorken x, taking for example the assumed parameterisation of parton distribution functions $f(x)$ at some starting scale used by the ZEUS collaboration,

$$xf(x) = p_0 x^{p_1} (1 - x)^{p_2} (1 + x p_4). \tag{2.16}$$

The scale of the interaction can be measured very precisely in deep inelastic scattering by measuring the difference between the incoming (k) and outgoing (k') lepton four-momentum,

$$Q^2 = -q^2 = -\left(k - k'\right)^2. \tag{2.17}$$

Similarly, the Bjorken x of the probed parton can be accurately measured by measuring the inelasticity (y) of the scattered electron in the lab-frame

$$y = 1 - \frac{E'_e}{2E_e} \left(1 - \cos\theta_e\right), \tag{2.18}$$

where E_e (E'_e) is the incoming (outgoing) electron energy and θ_e is the angle between the scattered electron and the proton beamline (following the same convention as the HERA experiment). The Bjorken x of the scattered parton is given by

$$x = \frac{Q^2}{s \cdot y}, \tag{2.19}$$

where s is the centre-of-mass energy of the electron-proton system,

$$s = 4 E_e E_p. \tag{2.20}$$

Bjorken scaling states that the parton distribution functions are independent of the scale at which they are measured (Q^2_{exp}) [46]. This foundational observation was pivotal in the discovery of the point-like constituents of the proton, but is only approximately true, as scaling breaks down due to quark-gluon interactions. PDFs can be extrapolated to scales far outside the range at which they are measured using the DGLAP equations [47, 48, 49, 50]. This is essential since the mass range covered by the experiments dedicated to determining PDFs is different to that of the LHC.

Furthermore, each flavour of quark has its own distribution, as well as a corresponding distribution for its anti-particle and the gluon. These are determined by measuring specific processes; for example, photon exchange is identical for u and $\bar{u}$, whereas W exchange is sensitive to the charge of the parton involved. This also helps to define what is meant by the valence quarks, since we know that there are many more quarks inside the proton than the simple constituents. The valence quark distribution of the proton can be calculated using the isospin sum rule constraints by taking the difference between the number of up and down type quarks and anti-quarks,

$$\int u_v(x)dx = \int \left(u(x) - \bar{u}(x)\right) dx = 2, \tag{2.21}$$

$$\int d_v(x)dx = \int \left(d(x) - \bar{d}(x)\right) dx = 1. \tag{2.22}$$

Integrated over all Bjorken x values there should be two more up type quarks than anti-up quarks, and one more down type quark than anti-down quark in order to ensure that the proton is colourless and restore the simple constituents. This parameterisation relies on the assumption that the number of sea quarks of each flavour is equal to the number of anti-quarks of that flavour, $q_{\text{sea}} = \bar{q}$. Another important assumption is that the sum momentum of all partons in the proton must equal the momentum of the proton itself, or in other terms, that the sum probability of all quarks across all Bjorken x values must be 1,

$$\int \left(xu_v + xu_d + xS + xg\right) dx = 1. \tag{2.23}$$

The parton distribution functions can be further parameterised in terms of the sea quark (xS) and gluon (xg) densities, where

$$xS = 2x(\bar{u} + \bar{d} + \bar{s} + \bar{c}). \tag{2.24}$$

Figure 2.2 shows the HERAPDF2.0 parton distribution functions, obtained by performing a QCD analysis at NNLO using a combination of H1 and ZEUS data [37]. At $x < 0.1$ the gluon term is the dominant contribution to the total parton momentum, followed by the sea and valence quark terms. This gluon dominance is even greater at higher values of Q^2, as Bjorken scaling begins to break down further. At approximately $x = 1/3$ the valence terms are dominant and account for almost all of the protons momentum ($xu_v \approx 2/3$ and $xu_d \approx 1/3$).

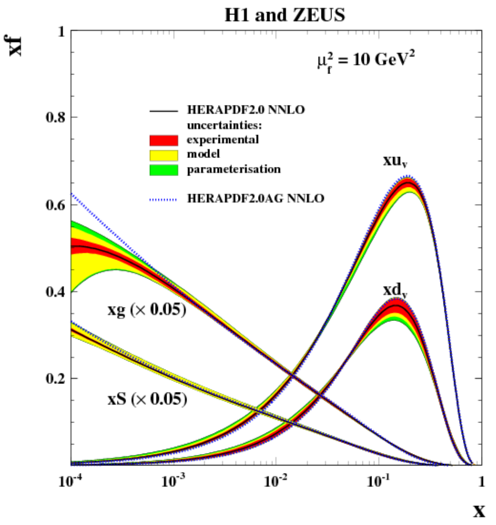

Figure 2.2: HERAPDF2.0 parton distribution functions at NNLO at $Q^2 = 10$ GeV^2. The sea and gluon contributions have been scaled down by a factor of 20. The red, yellow and green bands represent the experimental, model and parameterisation uncertainties respectively. Figure source: [37].

Parton distribution functions also have associated experimental, model and parameterisation systematic uncertainties. Experimental uncertainties arise due to the fact that experiments do not have perfect precision or accuracy, and this must be taken into account when evaluating the results. Model and parameterisation uncertainties arise due to the assumptions that must be made when performing QCD fits to the data, for instance certain physical parameter values or the functional form of the fit itself. The total uncertainty is obtained by adding these three components in quadrature.

2.4 Higher order corrections

2.4.1 Overview

The diagrams in Figure 2.1 show the Drell-Yan process at LO, not taking into account higher order electroweak and QCD emissions. However, the Drell-Yan process is much more complicated, and there can be additional gluon radiation by the initial state quarks (next-to-leading-order) and even radiation of additional quarks (next-to-next-to-leading-order), as well as final state photon radiation and virtual loop corrections. It is vitally important that these higher order corrections are calculated accurately, so that the predicted cross section best describes the experimental observables.

Calculating higher order corrections to the Drell-Yan cross section relies on the factorisation theorem, which allows one to express the total cross section in terms of universal, non-perturbative infrared long range PDF components and a short range ultraviolet hard scattering component [51],

$$\frac{d\sigma}{dQ^2} = \sum_{i,j} \int dx_1 dx_2 \left(q_i(x_1, Q^2) \cdot q_j(x_2, Q^2) \cdot \sigma_{i,j}(Q^2, \mu_r, \mu_f) \right). \tag{2.25}$$

The term $\sigma_{i,j}(Q^2, \mu_r, \mu_f)$ is the partonic hard scattering cross section and is the short range component of the factorised cross section, which must be calculated using pertubation theory. The long range components are the parton distribution functions ($q_{i,j}$), and as discussed are measured experimentally. The hard scattering cross section has contributions from the leading order prediction, electroweak radiative corrections and perturbative QCD corrections,

$$\sigma_{i,j} = \sigma_{i,j}^{\mathrm{LO}}(1 + \delta_{\mathrm{virtual}}^{\mathrm{QCD}} + \delta_{\mathrm{virtual}}^{\mathrm{photon}} + \delta_{\mathrm{virtual}}^{\mathrm{weak}}) + \sigma_{i,j}^{\mathrm{real,photon}} + \sigma_{i,j}^{\mathrm{real,QCD}}. \tag{2.26}$$

The factors $\delta_{\mathrm{virtual}}$ describe the virtual corrections to the leading order matrix element, which, as will be discussed in the next section, has contributions from QCD and electroweak processes while the real contributions are a result of initial or final state QCD or QED radiation. The renormalisation (μ_r) and factorisation scales (μ_f) are introduced to eliminate UV and IR divergences respectively. Many calculations use the minimal subtraction ($\overline{\mathrm{MS}}$) renormalisation scheme [52, 53] with both scales are set to $M^2 = Q^2$.

2.4.2 NLO electroweak corrections

At next-to-leading-order (NLO) there are virtual corrections to the Drell-Yan cross section due to diagrams with a single loop containing a W, Z or a photon, and real corrections due to the emission of a single photon. Examples of some of the one-loop diagrams which contribute to virtual EW corrections can be found in Figure 2.3. The following discussion uses the theoretical framework outlined in Refs. [54, 55].

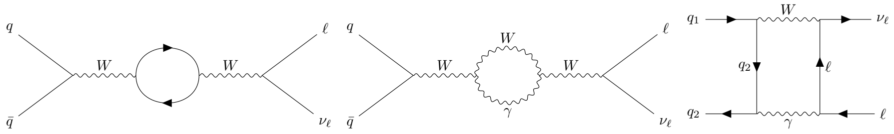

Figure 2.3: Examples of NLO one-loop electroweak virtual corrections.

Virtual corrections

Higher order virtual corrections affect both the propagator and coupling constant of the process [54], both of which impact the calculation of the matrix element (cross section). Different schemes are available which parameterise the matrix element as a function of different electroweak quantities which are free parameters. One of the most popular EW schemes for hadron-hadron colliders is the G_μ scheme, which uses the relationship between the weak coupling (g) to the Fermi constant (G_μ) and the W (Z) mass, m_W (m_Z),

$$\frac{G_\mu}{\sqrt{2}} = \frac{g^2}{8m_W^2}(1+\Delta r), \tag{2.27}$$

where Δr represents the radiative corrections to muon decay [56]. The effective weak coupling at tree-level is then given by

$$g^2 = 4\sqrt{2}G_\mu m_W^2(1-\Delta r) \tag{2.28}$$

with an effective electromagnetic coupling of

$$\alpha_{G_\mu} = \frac{\sqrt{2}G_\mu \sin^2\theta_W m_W^2}{\pi}, \tag{2.29}$$

which differs from the fine structure constant (α) as a result of higher order effects. These effective couplings permit the calculation of higher-order cross sections by pertubatively expanding the matrix element to the desired order in the couplings. The one-loop virtual amplitude ($\mathcal{M}_\alpha^{virt}$) has contributions from counterterm, self-energy, vertex and box corrections. This amplitude is added to the Born level amplitude ($\mathcal{M}_0$), which is the parton level matrix element in the absence of higher order corrections,

$$\mathcal{M} = \mathcal{M}_0 + \mathcal{M}_\alpha^{virt} + \dots . \tag{2.30}$$

In the Feynman-'t Hooft gauge [39], the W, Z and $Z\gamma$ interference propagators at one-loop [54, 55] are given by,

$$P_W = (-ig^{\mu\nu})\frac{1}{s-m_W^2+i\Gamma_W m_W}\left(Re(\Pi_{WW}(s)) + \delta m_W^2 + (s-m_W^2)\delta\Phi_W\right)\frac{1}{s-m_W^2}, \tag{2.31}$$

$$P_Z = (-ig^{\mu\nu})\frac{1}{s-m_Z^2+i\Gamma_Z m_Z}\left(Re(\Pi_{ZZ}(s)) + \delta m_Z^2 + (s-m_Z^2)\delta\Phi_Z\right)\frac{1}{s-m_Z^2}, \tag{2.32}$$

$$P_{Z\gamma} = (-ig^{\mu\nu})\frac{1}{s-m_Z^2+i\Gamma_Z m_Z}\left(Re(\Pi_{\gamma Z}(s)) + \frac{(s-m_Z^2)}{2}\delta\Phi_{\gamma Z} + \frac{1}{2}\delta\Phi_{Z\gamma}\right)\frac{1}{s}, \tag{2.33}$$

where $\Pi_{W(Z)}$ is the transverse part of the $W(Z)$ self-energy corrections, $\delta m_{W(Z)}^2$ is the $W(Z)$ mass renormalisation constant and $\Phi_{W(Z)}$ is the wave function renormalisation constant. In practice, matrix elements are calculated numerically using specially designed software packages, an example of which is *MCSANC* [57].

Real corrections

In addition to the virtual corrections, there are real corrections to the cross section due to the emission of Bremsstrahlung photons, by far the biggest radiative correction to the Drell-Yan process. Photon emission can come from any of the charged particles involved in the process, and impacts both the cross section of the process and experimental observables. Inclusion of higher-order effects can significantly shift the value of the W mass by values which are comparable with the experimental precision of measurements at hadron-hadron colliders [58]. For example, a measurement of the W boson mass at ATLAS yielded an experimental value of $m_W = 80370 \pm 19\,\mathrm{MeV}$ [59]. QED final state radiation of $\gamma^* \rightarrow \ell\ell$ contributes a systematic uncertainty of 0.8 to $4.4\,\mathrm{MeV}$, a considerable fraction of the total uncertainty of the final measurement. [2]

The NLO Bremsstrahlung corrections can be split into two distinct hard and soft regions, where the sum of the two contribute to the NLO matrix element

$$\mathcal{M}_1 = \mathcal{M}_1^{soft} + \mathcal{M}_1^{hard}. \tag{2.34}$$

Below the photon energy threshold (ΔE) the photon is considered as soft and does not modify the kinematics of the leading order process. In this region the matrix element is proportional to the Born level matrix element, where the proportionality factor depends only on the charge (q_i) and momentum (p_i) of the external particles [60],

$$\mathcal{M}_1^{soft} = -e\mathcal{M}_0 \sum_i \pm q_i \frac{\epsilon p_i}{k p_i}, \tag{2.35}$$

where k is the momentum of the radiated photon and ϵ is the photon polarisation vector. The soft photon cross section can then be calculated by squaring the matrix element and integrating over the photon polarisations and phase space, requiring the photon energy to satisfy $\lambda < E < \Delta E$. The photon mass (λ) must be introduced to avoid infrared divergences [60], and the sum of the real and virtual corrections is independent of the choice of λ, provided λ is sufficiently small. Furthermore, the sum of the soft and hard photon contributions is independent of the photon energy threshold ΔE.

Above the photon energy threshold radiated photons are considered hard and change the kinematic properties of the radiating fermions. While the soft photon contribution can be calculated exactly analytically, the hard photon contribution must be calculated numerically using programmes such as *PHOTOS* [61], which computes radiative corrections as a result of single- or multiple-photon emission. The squared matrix element is integrated over the phase space defined by $\Delta E < E < E_{max}$ to obtain the

---

[2] The systematic uncertainty associated with physics-modelling is $\pm 14\,\mathrm{MeV}$, with statistical and experimental systematic uncertainties of $\pm 7\,\mathrm{MeV}$ and $\pm 11\,\mathrm{MeV}$ respectively.

hard photon contribution to the cross section.

Photon induced processes

At the high-energies achieved by hadron colliders such as the LHC, the quarks inside the proton can also radiate photons in addition to gluons, leading to the formation of a photon sea inside the proton [62]. As such, both neutral and charged-current Drell-Yan processes receive corrections as a result of so called photon-induced processes, where a quark interacts with a photon, for example processes such as $\gamma\gamma \rightarrow \ell\ell$ (LO) and $\gamma q \rightarrow q'\ell\nu$, $\gamma q \rightarrow \ell\ell q'$ (NLO). In charged-current Drell-Yan interactions these effects are quite small [63], however they can become large in the neutral-current, particularly at high (low) dilepton invariant masses [64]. This can become important when performing searches for new heavy gauge bosons with masses in the TeV range, and for neutral-current Drell-Yan precision measurements at low masses ($m_{\ell\ell} < 60\,\mathrm{GeV}$).

2.4.3 QCD corrections

Higher order QCD effects are calculated using perturbative QCD, which relies on the asymptotic freedom of the strong coupling constant which becomes small for extremely small distances (high energies). Perturbative QCD can be used to expand the cross section to the desired order in the strong coupling constant, with most modern predictions going to order α_S^2 (NNLO) [65, 66, 67]. Recent advancements have also been made in the calculation of next-to-next-to-next-to leading order (N3LO) corrections [68].

Experimental observables such as the transverse momentum of final state leptons are sensitive to further QCD radiation. At LO, the transverse momentum of the produced boson (p_T^V) is zero, and NLO is the first perturbative order with a non-zero boson transverse-momentum due to initial state parton emissions. Programmes such as FEWZ [69, 70] and DYNNLO [65, 71] are used to calculate differential cross sections at NNLO. Calculations of the W boson transverse-momentum differential cross section agree with the observed data in pp data produced at $\sqrt{s} = 7\,\mathrm{TeV}$ to within 20% [72], with the agreement improving towards high p_T^W.

Similar to the case of EW higher order corrections, in QCD there are both virtual and real corrections, resulting from initial state gluon radiation and loop corrections respectively. At NLO, real corrections are the result of the emission of a single hard gluon, which is reconstructed as an additional jet; virtual corrections arise due to diagrams with a single loop. These contributions are individually infrared divergent but are convergent when the sum of both effects are taken into account [65]. At NNLO there are three processes which contribute: the emission of two initial state gluons (real-real), diagrams with an ISR gluon at one-loop level (real-virtual) and diagrams at two-loop level (virtual-virtual). Again these three contributions are separately divergent and must be summed together to cancel out the divergences.

The NNLO cross section is given by,

$$\sigma^V_{NNLO} = \mathcal{H}^V_{NNLO} \times \sigma^V_{LO} + \left(\sigma^{V+\text{jets}}_{NLO} - \sigma^{CT}_{NLO}\right), \tag{2.36}$$

where $\mathcal{H}^V_{NNLO}$ is the perturbative expansion of the of the hard scattering up to order α_S^2,

$$\mathcal{H}^V_{NNLO} = 1 + \frac{\alpha_S}{\pi}\mathcal{H}^V_1 + \left(\frac{\alpha_S}{\pi}\right)^2 \mathcal{H}^V_2 . \tag{2.37}$$

The theoretical form of $\mathcal{H}^V_1$ is known through perturbative expansion, and $\mathcal{H}^V_2$ can be calculated analytically [65]. The counter term (σ^{CT}_{NLO}) accounts for the divergent behaviour of $\sigma^{V+\text{jets}}_{NLO}$ in the limit of zero transverse momentum [73] and $\sigma^{V+\text{jets}}_{NLO}$ is the cross section for V production in association with an additional hard jet. Both σ^{CT}_{NLO} and $\sigma^{V+\text{jets}}_{NLO}$ can be calculated accurately using the so-called subtraction procedure [74].

2.4.4 Combining higher order electroweak and QCD corrections

Once NNLO QCD and NLO EW (excluding FSR[3]) cross sections are obtained they must be combined in order to calculate state-of-the-art theoretical predictions. A practical approach to this problem is to use mass-dependent k-factors [75], defined as follows,

$$k_{\text{QCD}} = \frac{\sigma_{\text{NNLO}_{\text{QCD}}}}{\sigma_{\text{LO}_{\text{QCD}}}}, \tag{2.38}$$

$$k^{fact}_{\text{EW}} = \frac{\sigma_{\text{LO}_{\text{QCD}},\text{NLO}_{\text{EW}}}}{\sigma_{\text{LO}_{\text{QCD}}}}, \tag{2.39}$$

$$k^{add}_{\text{EW}} = 1 + \frac{\sigma_{\text{LO}_{\text{QCD}},\text{NLO}_{\text{EW}}} - \sigma_{\text{LO}_{\text{QCD}}}}{\sigma_{\text{NNLO}_{\text{QCD}}}}, \tag{2.40}$$

where the ratio of the higher order QCD and EW cross sections relative to the LO QCD cross section provides a measure of the shift due to the higher order effects. This formalism requires that whatever PDF is used to calculate the highest order QCD term is also used to calculate the LO QCD (EW) term. Each of these k-factors is calculated as a function of the Born level invariant mass of the boson in order to encapsulate the main kinematic dependence, which is then applied as an additional weight to simulated Drell-Yan Monte Carlo events(Section 3.6)

The superscripts "fact" and "add" refer to the two main methods of using these k-factors to obtain a state-of-the-art NNLO QCD + NLO EW (except QED FSR) cross section prediction: the factorised and additive methods. The factorised method assumes that the fractional higher order EW corrections are the

---

[3] QED final-state-radiation is modelled in Monte Carlo simulations using programmes such as *PHOTOS* [61]. In the context of this discussion (Eq. 2.41-2.44), EW refers specifically to higher-order electroweak except QED final state radiation.

same for all orders of QCD, and can therefore be determined relative to the leading order calculation and applied to any higher order,

$$\begin{aligned}\sigma_{\mathrm{NNLO_{QCD}+NLO_{EW}}} &= k_{\mathrm{QCD}} \times k_{\mathrm{EW}}^{fact} \times \sigma_{\mathrm{LO_{QCD}}} && (2.41)\\ &= \frac{\sigma_{\mathrm{NNLO_{QCD}}}}{\sigma_{\mathrm{LO_{QCD}}}} \times \frac{\sigma_{\mathrm{LO_{QCD},NLO_{EW}}}}{\sigma_{\mathrm{LO_{QCD}}}} \times \sigma_{\mathrm{LO_{QCD}}}. && (2.42)\end{aligned}$$

The additive method assumes that the NLO EW (except QED FSR) cross section contribution is the same for all orders of QCD and can be added to the predicted cross section. Since the EW contribution is the same for each order in QCD, the fractional EW correction varies depending on the order in QCD,

$$\begin{aligned}\sigma_{\mathrm{NNLO_{QCD}+NLO_{EW}}} &= \sigma_{\mathrm{NNLO_{QCD}}} \times k_{\mathrm{EW}}^{add}, && (2.43)\\ &= \sigma_{\mathrm{NNLO_{QCD}}} \times \left(1 + \frac{\sigma_{\mathrm{LO_{QCD},NLO_{EW}}} - \sigma_{\mathrm{LO_{QCD}}}}{\sigma_{\mathrm{NNLO_{QCD}}}}\right). && (2.44)\end{aligned}$$

Predictions for combined NNLO QCD + NLO EW are obtained using the additive method. A systematic uncertainty is estimated by calculating the difference with respect to the results obtained using the factorised method which is then symmetrised. These techniques are utilised to estimate the Drell-Yan related background in exotic searches such as that presented in Chapter 5, and for high-precision measurements of Drell-Yan production cross sections in *pp* collisions at ATLAS [38].

Chapter 3

Experimental setup

This chapter presents an outline of the accelerator complex at the Large Hardon Collider and introduces the ATLAS detectors subsystems and how they are used to reconstruct particles from pp collisions. Particular focus is placed on the reconstruction of leptons and missing energy, as these are the primary objects dealt with in the analyses presented within (Chapters 4-5).

3.1 The Large Hadron Collider

The Large Hadron Collider (LHC) [76], measuring $27\,\mathrm{km}$ in circumference and operating at a centre-of-mass energy of $13\,\mathrm{TeV}$ throughout Run 2, is the largest and most powerful particle collider in the world. Based at CERN, the LHC occupies the former Large Electron Positron (LEP) collider tunnel, with installations beginning in 1998 and finishing in 2008. While LEP collided beams of electrons and positrons, the LHC primarily collides beams of protons, although heavy ion collisions also take place. Herein all discussions will pertain to proton-proton (pp) collisions as the dataset which is the focus of this thesis is a pp dataset recorded by the ATLAS detector [77]: one of the four main detector experiments based at CERN, the other three being ALICE [78], CMS [79] and LHCb [80]. Each of these experiments is positioned at one of the four LHC interaction points (IPs - the point at which the primary beam collisions take place), and record the resulting particles produced by the colliding beams in order to measure properties and interactions of the fundamental particles of the Standard Model.

The protons which are accelerated around the LHC beamline are produced using a simple bottle of hydrogen gas. These hydrogen atoms are then passed through an electric field, in order to strip them of their electrons, and are then accelerated incrementally through a chain of accelerators in order to achieve an energy of $6.5\,\mathrm{TeV}$. The layout of these accelerators is presented in Figure 3.1.

The first accelerator is Linac 2, which, as the name suggests, is a linear collider that accelerates the

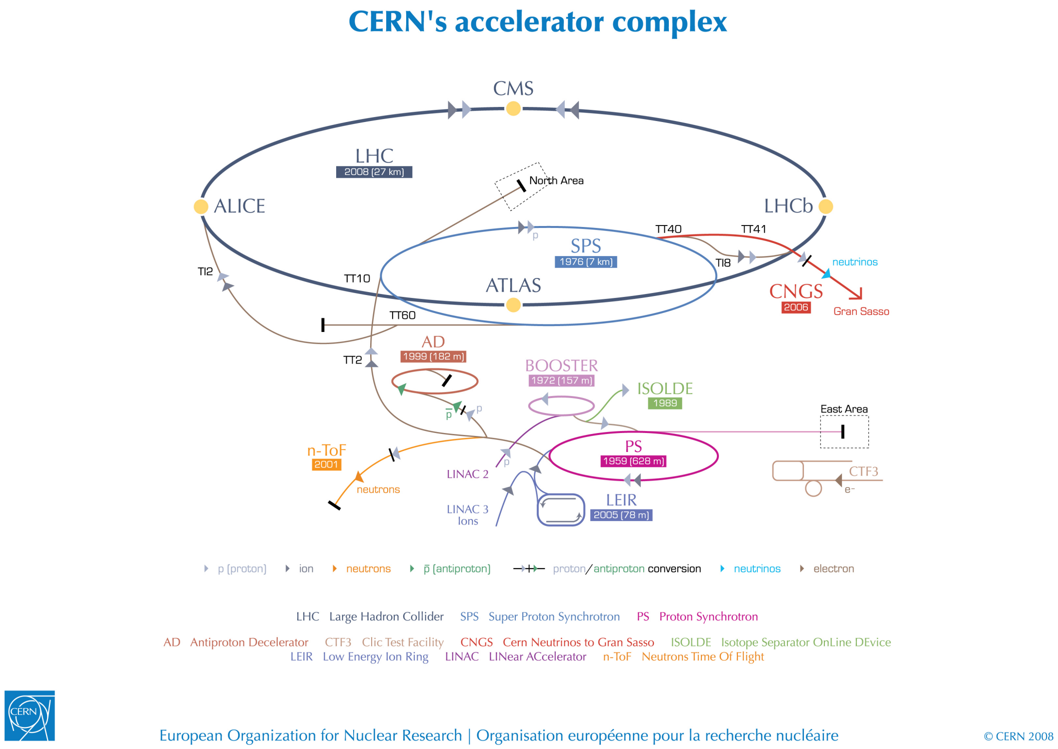

Figure 3.1: Schematic layout of the CERN accelerator complex. Figure source: [81].

protons to an energy of $50\,\mathrm{MeV}$. Acceleration is achieved by means of radiofrequency (RF) cavities, which are metal chambers constructed in such a way as to contain a resonant electromagnetic field. When charged particles pass through this cavity at the same frequency as the resonant field, a force is applied along their direction of motion, thereby accelerating them to higher energies. The protons then pass into the Proton Synchrotron Booster (PSB), a circular accelerator where they are accelerated to an energy of $1.4\,\mathrm{GeV}$. Consisting of four superimposed rings of $50\,\mathrm{m}$ diameter, the PSB is a synchrotron accelerator and works by accelerating particles whilst simultaneously keeping them on an orbit of constant radius. Acceleration is again achieved by using RF cavities, while a varied magnetic field is used to ensure the particles remain on a constant trajectory, as the bending achieved by a magnetic field is proportional to both the field strength and the velocity of the particle in question. Therefore, as the particles accelerate the magnetic field strength is also increased such that their radius of orbit remains constant.

The next stage in the acceleration is also provided by a synchrotron accelerator, the Proton Synchrotron (PS), which operates according to the same principles and accelerates the protons to $25\,\mathrm{GeV}$. In addition to accelerating the beam, the PS also splits the beam into bunches by separating the beam longitudinally and merging/splitting bunches until the desired bunch structure is achieved. In the most common configuration, successive bunches are separated by $25\,\mathrm{ns}$, which corresponds to a distance of $7.5\,\mathrm{m}$ between each bunch at $6.5\,\mathrm{TeV}$. Each bunch contains approximately $1.15 \times 10^{11}\mathrm{protons}$ and has a width of around $3.5\,\mu\mathrm{m}$.

These bunches are then injected into the Super Proton Synchrotron (SPS), where they are accelerated to $450\,\mathrm{GeV}$, before finally being injected into the main LHC beamline. Further acceleration is obtained by 16 RF cavities placed around the main LHC beamline, increasing the energy of the beams from $450\,\mathrm{GeV}$ to $6.5\,\mathrm{TeV}$. To keep the bunches on their circular orbit, magnetic fields are used to provide force perpendicular to both the direction of the field and the velocity of the bunches. Dipole magnets are responsible for keeping the particles on their trajectory, while quadrupole, sextupole and octupole magnets are used to keep the beam focused [82]. Once the proton bunches have achieved an energy of $6.5\,\mathrm{TeV}$ collisions begin at each of the LHC interaction points, starting what is known as an LHC fill. Collisions continue to occur until the beam is dumped, at which point data-taking stops.

3.2 The ATLAS detector

ATLAS (A Toroidal LHC ApparatuS) is a general purpose detector experiment positioned at IP4 on the LHC beamline [83] and was installed between 2003 and 2008 with data first recorded later that same year; the first good-for-physics data was recorded in 2010. ATLAS is designed to perform a range of different measurements of physics phenomena, ranging from precision tests of the Standard Model to searches for new physics beyond. ATLAS is a collection of subdetectors, all working in unison to provide optimal reconstruction of various final state objects. A schematic view of the ATLAS detector can be seen in Figure 3.2 illustrating the positions of the various subdetectors, a description of which will be given in the subsequent sections.

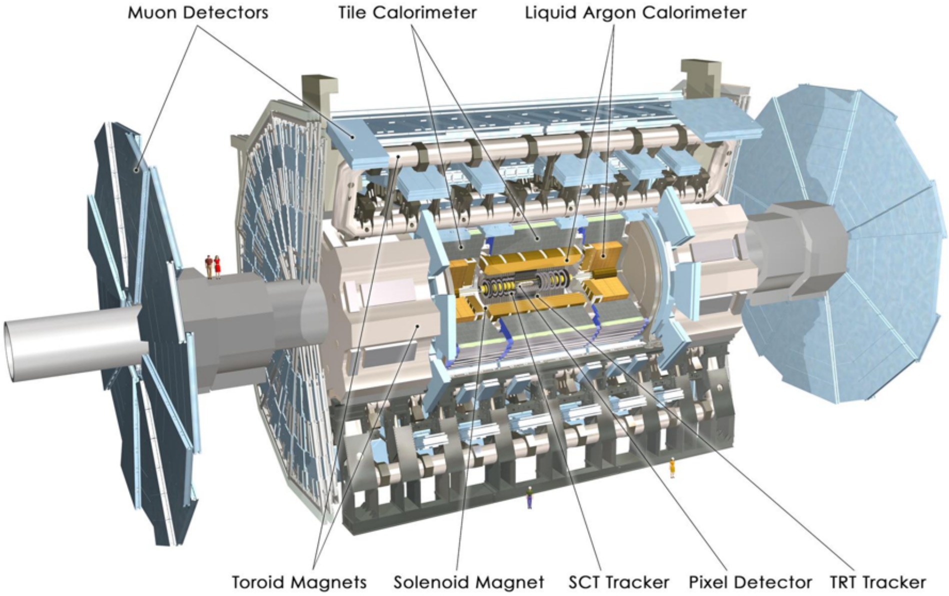

Figure 3.2: Schematic view of the ATLAS detector indicating the various subsystems. Figure source: [84].

ATLAS uses a right-handed coordinate system with its origin at the nominal interaction point in the centre of the detector and the z-axis along the direction of the LHC beam 2. The x-axis points from the IP to the centre of the LHC ring, and the y-axis points upwards. Cylindrical coordinates $(r,\ \phi)$ are used in the transverse plane, ϕ being the azimuthal angle around the z-axis. The pseudorapidity is defined in terms of the polar angle θ as

$$\eta = -\ln\left(\tan\frac{\theta}{2}\right). \tag{3.1}$$

Eq. 3.1 shows that the pseudorapidity is zero when $\theta = \pi/2$, and is infinite when $\theta = 0$. These two scenarios correspond to being perpendicular and collinear with the beam line respectively. Psuedorapidity is related to rapidity y, in the relativistic limit where a particles energy far exceeds its rest mass,

$$\begin{aligned} y &= \frac{1}{2}\ln\left(\frac{E-p_z}{E+p_z}\right) \qquad (3.2) \\ &= \frac{1}{2}\ln\left(\frac{\sqrt{p^2+m^2}-p_z}{\sqrt{p^2+m^2}+p_z}\right) \qquad (3.3) \end{aligned}$$

In the limit where $p >> m$, both the numerator and denominator can be binomially expanded, the numerator being equal to $\cos^2\frac{\theta}{2}$ and the denominator $\sin^2\frac{\theta}{2}$; Substituting the identity $\tan\frac{\theta}{2} = \frac{\cos\frac{\theta}{2}}{\sin\frac{\theta}{2}}$ yields Eq. 3.1. This is a useful quantity as it is far easier and faster to calculate in complex proton-proton collisions at the LHC. Angular distance is measured in units of the Lorentz invariant quantity $\Delta R = \sqrt{(\Delta\eta)^2 + (\Delta\phi)^2}$.

3.2.1 Inner detector

The first component of the ATLAS detector which particles interact with is the tracking system known as the Inner Detector (ID). The ID consists of four separate systems which together can measure the direction, momentum and charge of the particles it interacts with. These are, in order of radial distance from the beampipe, the Insertable B-Layer (IBL), the Pixel Detector, the Semiconductor Tracker (SCT) and the Transition Radiation Tracker (TRT). A schematic diagram of the Inner Detector can be seen in Figure 3.3.

The entire system is immersed in a 2 T magnetic field parallel to the beamline. This magnetic field is provided by the central solenoid and is necessary in order to extract information on a particles charge and momentum.

The IBL is the closest component to the beamline and was installed during Long Shutdown 1 in order to mitigate the effects of accumulated radiation damage and bandwidth limitations, and maintain full ID tracking performance throughout Run 2 [85]. The IBL consists of 14 staves of width 2 cm and length

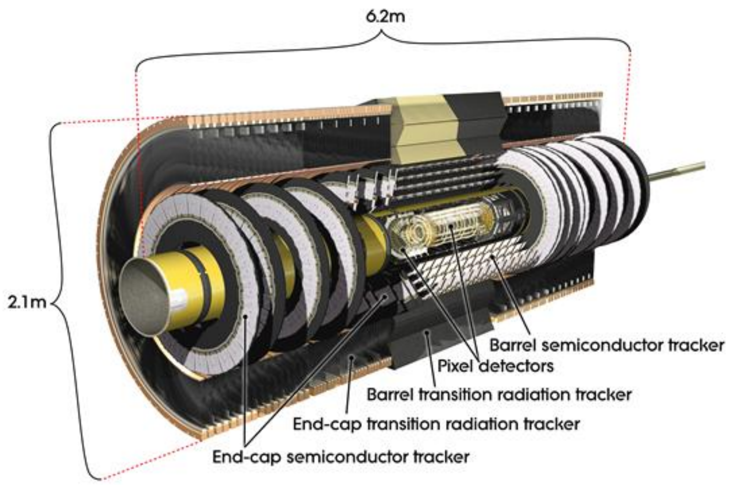

Figure 3.3: Cross section of the ATLAS Inner Detector without the Insertable B-Layer. Figure source: [77].

$64\,\mathrm{cm}$, each of which supports 20 pixel sensor modules made up of $250 \times 50\,\mathrm{\mu m}^2$ pixels[1]. Two types of sensors are used, planar and 3D, with approximately 12 million total pixels throughout the IBL. The addition of the IBL improves the tracking resolution of low-p_T tracks: the z_0 and d_0 resolution of $1\,\mathrm{GeV}$ tracks increased by a factor of approximately 2 with the addition of the IBL [86].

The Pixel Detector is the second closest component to the beamline and uses $50 \times 400\,\mathrm{\mu m}^2$ silicon pixels with resolution of $14\,\mathrm{\mu m}^2 \times 115\,\mathrm{\mu m}^2$ as the active material. These pixels consist of n-doped silicon on the readout side and a p-n junction on on the back side. This p-n junction has a depletion zone, where there are essentially no free holes or electrons. When a charged particle passes through electron hole pairs are created. A bias voltage is applied which causes the electrons and holes to drift across the pixel, and the electrical signal is read out if it exceeds a certain threshold. This constitutes a hit in the sensor. In total there are 80 million such pixels that make up the Pixel Detector, arranged in three concentric barrels around the beamline, as well as three disks in each end cap. The barrel layer is the curved surface of the cylindrical detector, and the end caps are the flat edges.

After particles interact with the Pixel Detector, they then move into the SCT which uses strips of silicon as the active material. Pairs of strip sensors are glued back-to-back at an angle of $2.3°$ to provide tracking information in 2-dimensions. The entire SCT system consists of a barrel of 2112 modules, where a module is defined as a pair of strip sensors, as well as 1976 more modules in the end caps (988 in each). Both the Pixel Detector and the SCT have pseudorapidity coverage up to $|\eta| < 2.5$.

The final Inner Detector component is the TRT. Operating within pseudorapidities of $|\eta| < 2.0$, the TRT consists of 300,000 straw tubes of $4\,\mathrm{mm}$ diameter. There are 50,000 such tubes in the barrel layer ($|\eta| < 1.0$), each of which is $144\,\mathrm{cm}$ long, while in the endcaps ($1.0 < |\eta| < 2.0$) there are 250,000 tubes

---

[1] In (ϕ, z) space.

of 39 cm length. In the barrel layer the tubes are aligned with the beamline and each end of the tube is read out separately, while in the endcaps the tubes are arranged perpendicularly to the beamline and there is a single readout channel per tube; meaning that there are 350,000 distinct readout channels.

Each of these tubes is made up of a central anode (30 $\mathrm{\mu m}$ gold-plated tungsten wire), surrounded by a gas-mixture of 70 % Xenon, 27% $\mathrm{CO_2}$ and 3% Oxygen encased in a 60 $\mathrm{\mu m}$ thick multi-layer film of carbon-polyimide-aluminum-Kapton-polyurethane acting as a cathode. Particles passing through can ionise this gaseous mixture, and the subsequent electrons can be read out as an electrical signal. Transition radiation is also produced when a highly relativistic particle crosses the boundary between two materials of different dielectric constants. The amount of radiation produced is proportional to the relativistic γ factor ($\gamma = E/m$), which is much larger for electrons than pions, for instance. This provides a rudimentary identification of the type of particle passing through the TRT.

3.2.2 Calorimetry

The ATLAS electromagnetic calorimeter (ECAL) consists of a cylindrical barrel around the beamline and two endcaps. Liquid argon is used as the active material, in an accordion design with lead absorbers layered throughout. Ionisation caused by the showering particles is measured directly from the liquid argon with readout electrodes. The ECAL has pseudorapidity coverage up to $|\eta| < 4.9$, however the granularity becomes coarser outside of the region $|\eta| < 2.5$. The barrel ($|\eta| < 2.5$) region has granularity $\Delta\eta\times\Delta\phi = 0.025\times0.025$, while the endcaps ($2.5 < |\eta| < 4.9$) have granularity $\Delta\eta\times\Delta\phi = 0.125\times0.125$. The electron energy scale can be measured with uncertainties of around one per-mille in the barrel region and two to five per-mille in the endcaps, while the energy resolution is less than 1% in the barrel region and around 1-2% in the endcaps [87]. The high precision of the barrel region provides precise measurements of electrons and photons in this region (muons do not interact much with the ECAL), while the endcaps provide important information in the determination of the missing energy component (Section 3.4.4). The region between $1.37 < |\eta| < 1.52$ contains non-active materials necessary to cool the detector, and as such is usually excluded from the fiducial region of most precision analyses.

The hadronic calorimeter (HCAL) also uses liquid argon calorimeters for the end cap and forward calorimeters and tile calorimeters for the barrel region. The barrel component covers the pseudorapidity range up to $|\eta| < 1.7$, and consists of scintillating tiles as the active material with steel providing absorption. Photons are produced in the scintillating material by the particles of the hadronic shower, which can then be read out by photomultiplier tubes. The endcap component ($1.5 < |\eta| < 3.2$) operates in the same way, using copper as the absorbers and liquid argon as the active material. The forward calorimeter ($3.1 < |\eta| < 4.9$) consists of three modules of increasing radial distance from the interaction point. The module closest to the interaction point uses copper as the absorbing material and is an electromagnetic calorimeter; the remaining two modules are made mostly of tungsten and are used to detect hadronic activity.

3.2.3 Muon spectrometer

Muons produce significantly less Bremsstrahlung than electrons due to their large mass, approximately 200 times larger than the electron. Therefore, muons are not stopped by the ECAL system, and since they do not interact strongly they also pass through the hadronic calorimter. As a result, the Muon Spectrometer (MS) is the outermost piece of the ATLAS detector and along with the ID provides tracking information for muons. The entire system is immersed in a magnetic field, provided by three toroidal magnets - one for the barrel and one for each endcap.

The MS consists of 4 different types of chambers: monitored drift tubes (MDTs), cathode strip chambers (CSCs), resistive plate chambers (RPCs) and thin gap chambers (TGCs). Each of these chambers cover different pseudorapidity regions of the Muon Spectrometer, as detailed in Table 3.1.

Pesudorapidity range	Sensor
$\lvert\eta\rvert < 1.05$	Resistive plate chambers
$1.05 < \lvert\eta\rvert < 2.4$	Thin gap chambers
$\lvert\eta\rvert < 2$	Monitored drift tubes
$2 < \lvert\eta\rvert < 2.7$	Cathode strip chambers

Table 3.1: Types of sensor used in each region of the muon detector.

The barrel region is covered by three concentric layers of resistive plate chambers and monitored drift tubes, while the endcaps consist of 4 wheels composed of thin gap chambers and monitored drift tubes. Precision measurement of tracks is handled by MDTs over most of the pseudorapidity range, which work in a similar manner to the TRT of the Inner Detector. CSCs are high granularity multiwire proportional chambers and are used in the forward region to withstand the demanding rates (up to $100\,\mathrm{kHz}$) which would not be well suited to MDTs. The RPCs and TGCs are gaseous ionisation chambers and provide trigger information for the barrel and endcap regions respectively.

3.2.4 ATLAS trigger system

In the nominal configuration bunches in the LHC are separated by a $25\,\mathrm{ns}$ gap, leading to a bunch crossing rate of $40\,\mathrm{MHz}$. If all of the information from these collisions were to be stored to disk, the data-rate would be approximately $60\,\mathrm{TB/s}$, which is completely infeasible based on the bandwidth of the data-acquisition system and the available disk space. Hence, ATLAS uses the trigger system to select events which could contain interesting physics objects such as muon [88], electron [89], photon, tau lepton, jet, and b-jet candidates, as well as significant amounts of missing energy. Triggers are even defined to select events with different combinations of physics objects, for example ee, $\mu\mu$ or even $e\mu$

There are two levels to the ATLAS trigger system [90]: the hardware based level-1 trigger (L1), which reduces the output rate from $40\,\mathrm{MHz}$ to $100\,\mathrm{kHz}$ in $2.5\,\mu\mathrm{s}$; and the software based high-level trigger (HLT), which further reduces the output rate from $100\,\mathrm{kHz}$ to $1\,\mathrm{kHz}$ within a few seconds. The L1 trigger is comprised of multiple detector subsystems, primarily the L1Calo [91] and L1Muon [92] systems. The L1Calo system uses information from the electromagnetic and hadronic calorimeter systems by combining individual cells into *trigger towers* of size $\Delta\eta \times \Delta\phi = 0.1 \times 0.1$. The L1Muon system provides a rough measurement of muon candidates transverse momentum, pseudorapidity and azimuthal angle using the RPC system in the barrel and the TGC system in the endcaps. All of this information is fed to the Central Trigger Processor (CTP) [93], which then decides whether to accept or reject the event based on the tower energies and muon p_{T} with respect to predefined thresholds.

Once an event has been accepted by the L1 trigger, it is buffered in the Read-Out System (ROS) before being processed by the HLT. The HLT uses the full granularity of the calorimeter information, as well as incorporating information from the Inner Detector and Muon Spectrometer to allow for better identification of lepton and high-p_{T} jet signatures. If an event is selected by the HLT it is stored in local storage at the site of the ATLAS detector before being passed to the Tier-0 computing facility for offline reconstruction. There are many different trigger menus to cover the range of signal topologies measured at ATLAS, ranging from events with high-p_{T} electrons or muons, large missing energies, high-p_{T} jets and many more. These triggers are designed for precision measurements of Standard Model particles such as the Higgs, W and Z bosons, as well as searches for physics beyond the Standard Model such as heavy gauge bosons, supersymmetric particles and leptoquarks.

3.3 Luminosity determination at ATLAS

Instantaneous luminosity ($\mathcal{L}^{\text{inst.}}$) is a measure of how many collisions occur per unit time and per cm^{-2}, and is the proportionality factor between the production rate ($\frac{dN}{dt}$) of a particle and its cross section (σ),

$$\frac{dN}{dt} = \mathcal{L}^{\text{inst.}}(\mathrm{cm}^2) \cdot \sigma(\mathrm{cm}^{-2}). \tag{3.4}$$

The instantaneous luminosity for a single colliding bunch pair is given by

$$\mathcal{L}_b^{\text{inst.}} = \frac{f_r n_1 n_2}{2\pi \Sigma_x \Sigma_y} \quad [\mathrm{cm}^{-2}\ \mathrm{s}^{-1}], \tag{3.5}$$

where f_r is the revolution frequency of the colliding bunches, $n_{1,2}$ are the bunch populations of the colliding bunches and $\Sigma_{x,y}$ are the convolved beam sizes in the x and y planes. This can be integrated over a given time period to obtain the integrated luminosity delivered to the detector.

The primary luminometer (luminosity measuring device) in ATLAS is the Cherenkov radiation detector LUCID [94]. LUCID consists of 32 photomultiplier tubes (PMTs) placed either side of the interaction point at a distance of 17 meters (16 photomultipliers on each side). Cherenkov light is produced in the quartz windows of the photomultipliers as charged particle pass through, which can then be read out as an electronic signal. The measured number of hits (signal over threshold) in the PMTs is converted to a visible interaction rate per bunch crossing (μ_{vis}), which can in turn be divided by the visible cross section (σ_{vis}) to obtain a luminosity estimate,

$$\mathcal{L}_b = \frac{\mu_{\text{vis}} \cdot f_r}{\sigma_{\text{vis}}}. \tag{3.6}$$

Since LUCID is not 100% efficient, the visible interaction rate is the product of the detector/algorithm efficiency and the total interaction rate ($\mu_{\text{vis}} = \varepsilon \cdot \mu$). The total interaction rate, or the number of inelastic proton-proton collisions per bunch crossing, is known as the pileup parameter ($\mu = \frac{\mu_{\text{vis}}}{\varepsilon}$), and is a result of the fact that there are many protons in each colliding bunch. This type of pileup is also known as in-time pileup, but is commonly referred to simply as pileup. In contract, out-of-time pileup is a result of additional proton-proton collisions occuring in bunch crossings either just before or just after the current collision. The visible cross section is the fraction of the total inelastic cross section (σ_{inel}) which is measured by the detector ($\sigma_{\text{vis}} = \sigma_{inel} \cdot \varepsilon$).

The visible cross section is measured using the van der Meer (vdM) scan calibration procedure [95]. The vdM calibration method works by sweeping the colliding beams through different beam separations in the $x - y$ plane. By measuring any quantity (R) that is proportional to luminosity as a function of beam separation (Δx or Δy), the convolved beam size can be measured,

$$\Sigma_{x(y)} = \frac{1}{\sqrt{2\pi}} \frac{\int R(\Delta x(y)) d\Delta x(y)}{R(0)}. \tag{3.7}$$

$R(\Delta x(y))$ is the instantaneous luminosity as a function of beam seperation and $R(0)$ is the peak instantaneous luminosity. The total normalisation of these two values cancels, hence any quantity which is proportional to instantaneous luminosity can be used to perform the measurement. Figure 3.4 shows the visible interaction rate of the LUCID lucBiHitOR algorithm during the 2016 vdM scan [96]. A scan curve is fit to this data using a Gaussian function multiplied by a polynomial to extract the maximum interaction rate ($\mu_{\text{vis}}^{\text{max}}$) and the convolved beam size, which is taken as the standard deviation of the distribution.

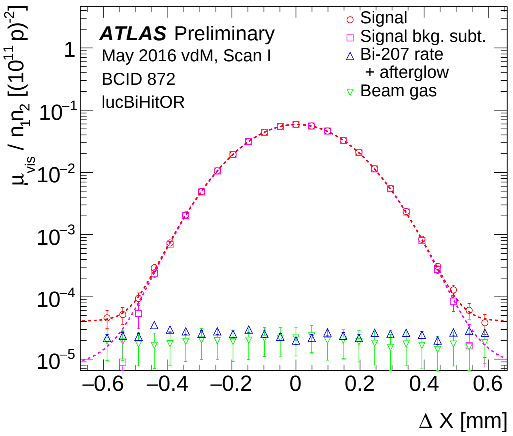

Figure 3.4: Visible interaction rate per bunch crossing and per unit bunch-population product for the LUCID algorithm (lucBiHitOR) versus nominal beam separation during horizontal scan 1 in the May 2016 luminosity-calibration session. The total rate is shown as red circles, and the background-subtracted rate as magenta squares. The background-subtracted rate is fitted by a Gaussian multiplied by a sixth-order polynomial (dashed curve). The error bars are statistical only. Figure source: [96].

Once the maximum interaction rate and the convolved beam sizes in the $x - y$ planes have been measured, the visible cross section can be measured by

$$\sigma_{\text{vis}} = \mu_{\text{vis}}^{\max} \frac{2\pi \Sigma_x \Sigma_y}{n_1 n_2}, \tag{3.8}$$

where n_1 and n_2 are the bunch populations. Throughout Run 2, vdM scans were performed once per-year at ATLAS and used to calibrate the luminosity delivered during that period.[2] Relative luminosity measurements from various detectors/algorithms are used to constrain the potential shift in calibration throughout the year; this is known as the scan-to-scan reproducibility uncertainty.

vdM scans are performed during special running periods with low-luminosity/pileup and isolated bunches. Since the van der Meer scan is performed under conditions vastly different to the standard ATLAS physics data-taking, the visible cross section calibration must be corrected to account for the difference in beam conditions. This is done via a procedure known as calibration transfer [96], which uses a track-based relative-luminosity measurement to correct for the significant non-linearities (with respect to pileup) in the μ_{vis} value measured by LUCID in the data-taking regime.

As luminosity is a key quantity for most physics analyses, it is important that the associated uncertainty is as well understood as possible. There are many components to this uncertainty [96], but the dominant contributions come from the absolute vdM scan calibration, calibration transfer and the long-term stability (scan-to-scan reproducibility). The long-term stability of the baseline ATLAS luminosity can be monitored by measuring the relative time-dependent stability of various luminosity measurements. Each of these

---

[2] With the exception of 2015 and 2016 which are combined into a single dataset.

luminosity measurements are normalised to the same integrated luminosity as the baseline ATLAS measurement in a reference LHC fill, so that the absolute scale of all measurements is the same. The normalised fill-by-fill integrated luminosity ratio therefore shows the relative stability of each of these measurements over the course of the data-taking period. The long-term stability can be evaluated by calculating a stability band which encloses the bulk of the points, providing an estimate of the systematic uncertainty associated with the baseline ATLAS luminosity. Chapter 4 will discuss a new method for monitoring the stability of the baseline ATLAS luminosity estimate by measuring the production rate of the Z boson.

3.4 Object reconstruction

ATLAS records data as electrical signals in different sub-components of the detector. This data is then subject to high-level reconstruction to extract information on the particles which produced these signals, such as their transverse momentum, pseudorapidity, charge etc. This section will detail the reconstruction of the main physics objects used in the analyses presented in this thesis; namely electrons, muons and jets. Other objects such as photons and taus can be reconstructed by the ATLAS detector [84], but will not be discussed herein as they are not pertinent to the analyses presented.

3.4.1 Electron reconstruction

Electron reconstruction at ATLAS starts with a seed cluster in the electromagnetic calorimeter matched to a track in the Inner Detector [97], while clusters which have no associated track are reconstructed as photons. Energy deposits in calorimeter cells are clustered using the *superclustering* method [98]. This innovative method uses variable sized clusters, which are determined dynamically according to the kinematics of the specific electron/photon, rather than the fixed size clusters used previously in the sliding-window algorithm technique at ATLAS [99]. The advantage of this method is that it provides greater energy recovery due to losses from bremsstrahlung, since the variable sized cluster can pick up on radiated photons that may be missed when using a sliding-window technique. Clusters are formed from proto-clusters formed by the topo-cluster reconstruction algorithm [100]. Proto-clusters are formed by measuring the significance (ψ) of all calorimeter cells by taking the ratio of the energy deposit (E) and expected cell noise (σ),

$$\psi = \frac{E}{\sigma}. \tag{3.9}$$

Cells with $|\psi| > 4$ are considered as seeds to the cluster, and neighbouring cells with $|\psi| > 2$

are added to the cluster and considered as seeds, iteratively repeating the process until no significant neighbouring cells are found. Once the clustering is complete, these preliminary clusters can then be processed with the *superclustering* algorithm. The procedure is similar to the one outlined above, matching satellite clusters to the main energy cluster [98]. Clusters which are within $|\Delta\eta| < 0.05$ and $-0.10 < q \cdot (\phi_{\text{track}} - \phi_{\text{clus}}) < 0.05$ [3] of an Inner Detector track are considered to be matched, and correspond to an electron; clusters which have no associated tracks correspond to photons.

Electron identification

Electrons are selected using a likelihood-based identification, using information from the tracking and calorimeter systems to determine whether an electron candidate is signal- or background-like. Here, signal-like electrons are prompt leptons coming from the primary vertex, while background-like electrons refer to non-prompt electrons or jets which have similar signatures as prompt electrons, as detailed in Ref. [97]. A brief outline of the methodology is presented.

The electron likelihood is calculated by considering the probability density functions for signal (background)-like electrons ($L_{S(B)}$),

$$L_{S(B)}(\vec{x}) = \prod_{i}^{n} P_{S(B),i}(x_i), \tag{3.10}$$

where $\vec{x}$ is a vector of all the discriminating variables used to calculate the likelihood and $P_{S(B),i}(x_i)$ is the value of the signal (background) pdf for quantity i at value x_i. From Eq. 3.10 a discriminant can be formed for each electron candidate,

$$d_L = \frac{L_S}{L_S + L_B}, \tag{3.11}$$

which has a sharp peak at unity for signal-like electrons, and a sharp peak at zero for background-like electrons. This is inconvenient, as it would require an extremely fine binning in order to be able to effectively select working points of varied efficiency. Instead, the inverse sigmoid function of this discriminant (d'_L) is used to determine the cut value for a given working point,

$$d'_L = -\tau^{-1} \ln\left(d_L^{-1} - 1\right), \tag{3.12}$$

where τ is a constant value set to 15 (explained in Ref. [101]). This inverse sigmoid function transforms the discriminating variable such that it varies smoothly between 0 and 1, allowing for effective separation between signal- and background-like electrons without the need for extremely fine binning. Working

---

[3] Where q is the reconstructed charge of the track.

points of varied efficiencies can be defined by a selection on this likelihood-discriminant with some additional requirements. Figure 3.5 shows the identification efficiency for the Loose, Medium and Tight likelihood working points. These working points have typical efficiencies of 93%, 88% and 80% respectively, decreasing as a function of pileup due to deterioration of the discriminating power of the likelihood-discriminant with increasing pileup.

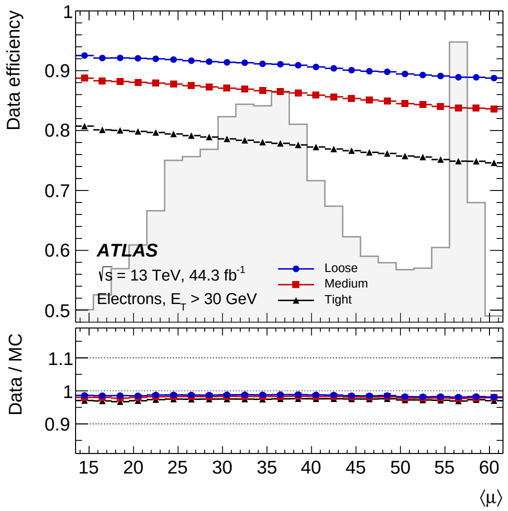

Figure 3.5: The electron identification efficiency in data for electrons with $E_{\mathrm{T}} > 30\,\mathrm{GeV}$ as a function of the average number of interactions per bunch crossing for the Loose, Medium and Tight likelihood operating points. The efficiencies are measured in $Z \rightarrow e^{+}e^{-}$ events in data recorded in the year 2017. The shape of the $\langle\mu\rangle$ distribution is shown as a shaded histogram. The bottom panel shows the data-to-simulation ratios. The total uncertainties are shown but are not visible. Source: [98].

The above description corresponds to what is known as likelihood-based identification, which can be contrasted with cut-based identification. Cut-based identification applies sequential requirements on selected variables, with an electron candidate passing identification if it passes all requirements. The benefits of likelihood-based compared to cut-based identification are that if an electron fails a single (or even multiple) selection criteria, it will not necessarily fail identification completely, since the likelihood combines the information of all discriminating quantities.

Electron isolation

The activity surrounding an electron can be quantified by both the number of tracks by which it is surrounded and by the nearby energy deposits in the calorimeter. Therefore, there are two types of isolation variables: track- and calorimeter-based. An isolated electron has little activity in a surrounding cone of $\Delta R = \sqrt{(\Delta\eta)^2 + (\Delta\phi)^2}$. This is used to further refine the selection and reconstruction of electron candidates to ensure that the probability that the selected object is a prompt electron is as high as possible.

Track based isolation uses information from the tracking system to build up a discriminating variable which is capable of determining (with some efficiency) whether or not an electron is prompt or not. An isolation variable can then be constructed by calculating the sum of the transverse momenta ($p_{\mathrm{T}}^{\mathrm{sum}}$) of all tracks within a cone of radius ΔR around the electron candidate, excluding the transverse momentum of the candidate itself. To minimise the pileup contribution, a cut is placed on the longitudinal impact parameter (z_0) of $|z_0 \sin\theta| < 3\,\mathrm{mm}$, helping to ensure that the tracks originate from the primary vertex, and not from pileup activity. A variable radius cone can then be defined as a function of the p_{T} of the electron candidate,

$$\Delta R = \min\left(\frac{10\text{ GeV}}{p_{\mathrm{T}}[\text{GeV}]}, R_{max}\right), \tag{3.13}$$

where the value 10 GeV is derived from $t\bar{t}$ MC and R_{max} is the maximum cone size [97]. This cone size decreases for high-momentum particles, where it is expected that other decay products can be very near to the electron candidate, hence a smaller cone is required to identify the isolated electron.

Calorimeter based isolation relies on summing the transverse energies of all topological clusters around an electron candidates position [100]. This is defined as the raw energy, $E_{T,raw}^{isolated}$, from which is subtracted: the contribution from the electron candidate itself, $E_{T,core}$, the contribution from leakage due to energy from the candidate being deposited in adjacent cells, $E_{T,leakage}$, and finally the pileup, $E_{T,pileup}$, and underlying-event contributions, $E_{T,UE}$. Underlying-event activity refers to additional quark or gluon scatters in the pp interaction in addition to the primary scattering vertex.

The resulting distribution ($E_{\mathrm{T}}^{\mathrm{cone}}$) can then be used to define working points of varied efficiency by applying different selections. Figure 3.6 shows the efficiency of the Gradient, HighPtCaloOnly, Loose and Tight working points, the selection requirements for which are summarised in Figure 3.7. Similar to the identification efficiency, the electron isolation efficiency decreases with increasing pileup. This is due to increased activity in both the inner tracker and calorimeter systems due to the increased number of pp interactions.

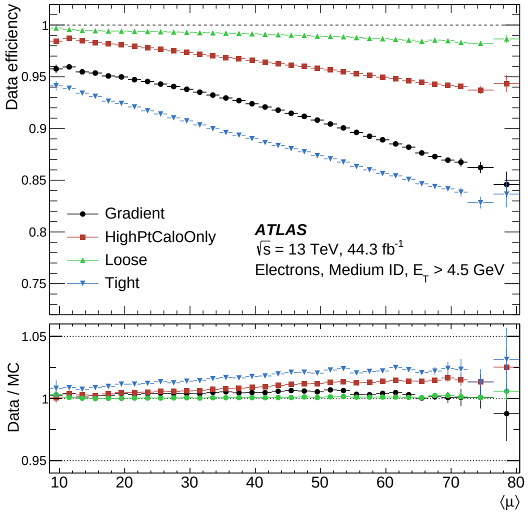

Figure 3.6: Efficiency of the different isolation working points for electrons from inclusive $Z \to e^+e^-$ events as a function of the number of interactions per bunch crossing $\langle\mu\rangle$. The electrons are required to fulfil the Medium selection from the likelihood-based electron identification. The lower panel shows the ratio of the efficiencies measured in data and in MC simulations. The total uncertainties are shown, including the statistical and systematic components. Source: [98].

Working point	Calorimeter isolation	Track isolation
Gradient	$\epsilon = 0.1143 \times p_{\mathrm{T}} + 92.14\%$ (with $E_{\mathrm{T}}^{\mathrm{cone20}}$)	$\epsilon = 0.1143 \times p_{\mathrm{T}} + 92.14\%$ (with $p_{\mathrm{T}}^{\mathrm{varcone20}}$)
HighPtCaloOnly	$E_{\mathrm{T}}^{\mathrm{cone20}} < \max(0.015 \times p_{\mathrm{T}}, 3.5\ \mathrm{GeV})$	-
Loose	$E_{\mathrm{T}}^{\mathrm{cone20}}/p_{\mathrm{T}} < 0.20$	$p_{\mathrm{T}}^{\mathrm{varcone20}}/p_{\mathrm{T}} < 0.15$
Tight	$E_{\mathrm{T}}^{\mathrm{cone20}}/p_{\mathrm{T}} < 0.06$	$p_{\mathrm{T}}^{\mathrm{varcone20}}/p_{\mathrm{T}} < 0.06$

Figure 3.7: Definition of the electron isolation working points and isolation efficiency. In the Gradient working point definition, the unit of p_{T} is GeV. All working points use a cone size of $\Delta R = 0.2$ for calorimeter isolation and $\Delta R_{max} = 0.2$ for track isolation. Source: [98].

3.4.2 Muon reconstruction

Three distinct methods are used when reconstructing muon tracks to ensure maximum efficiency across a broad momentum spectrum, ranging from as low as 3 GeV to as high as $3\,\mathrm{TeV}$. Muons can be reconstructed using only the Muon Spectrometer (stand-alone muon); using a combination of Inner Detector and Muon Spectrometer tracks (combined-muon); using an ID track and an MS segment, where a segment is a straight line track in an inner muon station (segment-muons).

Muon reconstruction starts by forming segments out of hit information in the MS. Segments are formed in individual muon stations by using a Hough transformation [102], and can then be combined into a preliminary muon track by performing a global χ^2 fit [103]. Standalone muons which do not have any associated Inner Detector track information are formed in this way, while combined muons can be formed by combining this preliminary MS track with a matched ID track and performing a track fit. Muon reconstruction efficiency is close to 99% in the fiducial region $|\eta| < 2.5$ and $p_{\mathrm{T}} > 5\,\mathrm{GeV}$, with a relatively flat momentum resolution of approximately 2%, rising to 3% at $p_{\mathrm{T}}^{\mu} = 2\,\mathrm{TeV}$ [104].

3.4.3 Jet reconstruction

The process of jet reconstruction is very similar to the procedure used to reconstruct electrons (Eq. 3.9). Calorimeter cells are clustered by considering the cell significance (ψ) of all calorimeter cells, which is defined as the ratio of the energy deposited in the cell (E) and the expected ambient noise (σ). From the raw calorimeter data topological clusters are formed by iteratively merging proto clusters with neighbouring cells above the noise threshold of $\psi > 2$ [100]. Jet clustering algorithms can then be applied to topological clusters to reconstruct jet objects, with the main algorithm used at ATLAS being the *anti-k_T* algorithm [105] with a distance parameter of $\Delta R = \sqrt{(\Delta\eta)^2 + (\Delta\phi)^2} < 0.4$. An additional threshold is applied requiring the energy of the jet candidates to be greater than 7 GeV. Once the jet candidates have been constructed, they must be calibrated to particle level using a jet energy scale (JES) correction factor [106, 107, 108]. These corrections are derived from Monte Carlo in order to account for differences in the truth-level and reconstruction-level detector response, and are then applied as scale factors as a function of the jet four-momentum [109]. Further considerations can be made for the jet energy resolution, but these are usually considered as systematic uncertainties rather than scale factors applied as a correction.

The above description applies to what is known as *EMTopo* jet reconstruction, which has been used by ATLAS throughout Run-1 and Run-2. Another method of jet reconstruction is known as *particle flow*, which utilises the trackers ability to accurately reconstruct charged particles and the calorimeters ability to reconstruct both charged and neutral particles [110, 111]. Making use of tracking information allows for better pileup rejection by identifying tracks which are not associated with the primary vertex and removing them and their associated calorimeter cluster from the reconstruction. In order to avoid double counting when using the tracking information, the track energy must be subtracted from the associated calorimeter cluster. This is achieved by matching each track in the ID to a single topological cluster based on their angular separation,

$$\Delta R = \sqrt{\left(\frac{\Delta\phi}{\sigma_\phi}\right)^2 + \left(\frac{\Delta\eta}{\sigma_\eta}\right)^2}, \tag{3.14}$$

where $\Delta\phi$ ($\Delta\eta$) is the distance between the track and topo-cluster barycentre in angular coordinates and σ_ϕ (σ_ϕ) is the width of the topo-cluster. Tracks and topo-clusters are matched by minimising ΔR, i.e. the track-cluster pair with the smallest value is paired. Similar to the EMTopo jet reconstruction method, particle flow jets are reconstructed using the *anti-k_T* algorithm, where the inputs are energy-corrected topological clusters and the selected tracks coming from the primary vertex.

3.4.4 Missing energy reconstruction

Missing energy ($E_\mathrm{T}^\mathrm{miss}$) refers to an imbalance of energy deposited inside the detector volume, a result of particles passing through the detector without interacting/depositing their energy. The only example of such a particle in the Standard Model is the neutrino, but many searches are performed at ATLAS for particles with similar signatures (the neutralino for example). Colliding beams at the LHC have no transverse component to their momentum, so the net p_T in the initial state is zero. As a result of the conservation of four-momentum, the final state must also have $p_\mathrm{T} = 0$. The presence of neutrinos can therefore be detected by reconstructing the momentum imbalance of all particles inside the detector volume. This is done by taking the vector sum of the transverse momenta of all reconstructed particles, which is equal and opposite to the missing energy,

$$\sum_{reco} \mathbf{p}_\mathrm{T} + \mathbf{E}_\mathrm{T}^\mathrm{miss} = 0. \tag{3.15}$$

Expanding Eq. 3.15 over all reconstructed particles and rearranging for the missing energy gives,

$$\mathbf{E}_\mathrm{T}^\mathrm{miss} = \underbrace{-\sum_{\substack{\text{selected}\\ \text{electrons}}} \mathbf{p}_\mathrm{T}^\mathrm{e} - \sum_{\substack{\text{selected}\\ \text{photons}}} \mathbf{p}_\mathrm{T}^{\gamma} - \sum_{\substack{\text{selected}\\ \tau\text{-leptons}}} \mathbf{p}_\mathrm{T}^{\tau_\mathrm{had}} - \sum_{\substack{\text{selected}\\ \text{muons}}} \mathbf{p}_\mathrm{T}^{\mu} - \sum_{\substack{\text{selected}\\ \text{jets}}} \mathbf{p}_\mathrm{T}^\mathrm{jet}}_{\text{hard term}} \underbrace{- \sum_{\substack{\text{unused}\\ \text{tracks}}} \mathbf{p}_\mathrm{T}^\mathrm{track}}_{\text{soft term}} . \tag{3.16}$$

The main distinction in Eq. 3.16 is between the hard and soft terms. The hard term takes into account all reconstructed objects associated with an event after final selection and calibration, usually corresponding to the high-p_T objects in the event. This means that the four-momentum of selected particles and jets is known as accurately as possible, leading to a better measurement of the missing transverse energy. Only particles and jets which pass the event selection criteria defined by the analysis are considered in the calculation of the hard term, otherwise their tracks are included in the soft-term. This ensures that there is a consistent definition between what is considered as a hard object in the analysis and what is considered in the hard term of the $E_{\mathrm{T}}^{\mathrm{miss}}$.

The soft term is constructed by taking the vector sum of the p_{T} of all tracks associated with the hard-scatter vertex that are not associated with any high-p_{T} (hard) object. Typically the soft term is calculated using tracking information exclusively from the Inner Detector (track-based soft term), however, there is also a calorimeter-based soft term which uses calorimeter clusters to calculate the $E_{\mathrm{T}}^{\mathrm{miss}}$ soft term, albeit with worse resolution due to residual pileup effects in the calorimeter [112].

3.5 The ATLAS Run 2 dataset

This thesis will focus on the pp dataset recorded by ATLAS at $\sqrt{s} = 13$ TeV throughout Run 2 (2015 – 2018), an overview of which is given in Table 3.2. As discussed in Section 3.3, the luminosity delivered to ATLAS is recorded by the Cherenkov radiation detector LUCID. Approximately 5% of the delivered luminosity is not recorded by ATLAS due the data acquisition system (DAQ) not being 100% efficient. In addition to this, a small amount of data is not recorded due to the time it takes for the ATLAS tracking detectors to ramp up their high-voltage systems and the turning on of the pixel system's preamplifiers.

Data is recorded at ATLAS in 60 second intervals known as luminosity blocks (LBs), over which the experimental conditions are assumed to be constant. Not all of the data that is recorded by the detector is suitable for physics analysis, and further data-quality criteria are applied to remove any data which was recorded under conditions when the detector performance was not optimal. This is known as the Good Run List (GRL), which is a set of XML files that contain a list of luminosity blocks that are certified for use in physics analyses [113]. The final GRLs are listed in Table 3.3; these contain all the luminosity blocks recorded in pp collisions throughout Run-2 at $13\,\mathrm{TeV}$ that are used in physics analyses. The overall data-taking efficiency of ATLAS throughout Run-2 was 95.6%. Figure 3.8 shows the luminosity delivered to and recorded by ATLAS, as well as the fraction of recorded data which is good for physics, and Figure 3.9 shows the pileup profile of each of the data-taking periods of Run 2.

In Run 2 the luminosity delivered to ATLAS was $156\,\mathrm{fb}^{-1}$, with $139\,\mathrm{fb}^{-1}$ found to be good for physics. The amount of luminosity delivered increased throughout each year of Run 2, reaching a maximum of $63.4\,\mathrm{fb}^{-1}$ in 2018. The average pileup at which this data was recorded was 33.7, averaged over the entire dataset. These values are not the final Run 2 measurement, and a further luminosity calibration will be performed with the aim of reducing the associated uncertainties.

	2015	***2016***	***2017***	***2018***	***Run-2***
Date	03/06 - 15/11	22/04 - 26/10	23/05 - 26/11	17/04 - 26/10	03/06/15 - 26/10/18
Run range	266904 - 284484	296939 - 311481	324320 - 341649	348197 - 364485	266904 - 364485
LHC fill range	3817 - 4569	4724 - 5452	5697 - 6417	6570 - 7358	3817 - 7358
N_{runs}	132	187	226	243	788
$\mathcal{L}^{int.}_{delivered}$ (fb^{-1})	4.0	38.5	50.2	63.4	156.1
$\mathcal{L}^{int.}_{recorded}$ (fb^{-1})	3.9	35.6	46.9	60.6	147.0
$\mathcal{L}^{int.}_{good}$ (fb^{-1})	3.3	32.9	44.3	58.5	139.0
$\mathcal{L}^{inst.}_{peak}$ (10^{33} cm^{-2} s^{-1})	5.0	13.8	20.9	21.0	21.0
$\langle\mu\rangle$	13.4	25.1	37.8	36.1	33.7

Table 3.2: Overview of the ATLAS full Run 2 dataset. The baseline ATLAS luminosity values were calculated using the preliminary calibration presented in Ref. [96].

Data-taking Period	**Good Run List**
2015	`20190708/data15_13TeV.periodAllYear_DetStatus-v105-pro22-13` `_Unknown_PHYS_StandardGRL_All_Good_25ns.xml`
2016	`20190708/data16_13TeV.periodAllYear_DetStatus-v105-pro22-13` `_Unknown_PHYS_StandardGRL_All_Good_25ns_WITH_IGNORES.xml`
2017	`20190708/data17_13TeV.periodAllYear_DetStatus-v105-pro22-13` `_Unknown_PHYS_StandardGRL_All_Good_25ns_Triggerno17e33prim.xml`
2018	`20200426/data18_13TeV.periodAllYear_DetStatus-v102-pro22-04` `_PHYS_StandardGRL_All_Good_25ns_BjetHLT.xml`

Table 3.3: Good run lists used to select events for different datasets.

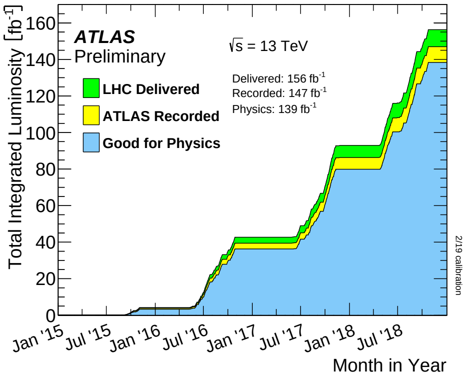

Figure 3.8: Cumulative luminosity versus time delivered to ATLAS (green), recorded by ATLAS (yellow), and certified to be good quality data (blue) during stable beams for pp collisions at $\sqrt{s} = 13$ TeV in 2015-2018. The delivered luminosity accounts for the luminosity delivered from the start of stable beams until the LHC requests ATLAS to put the detector in a safe standby mode to allow a beam dump or beam studies. The recorded luminosity reflects the DAQ inefficiency, as well as the inefficiency of the so-called "warm start": when the stable beam flag is raised, the tracking detectors undergo a ramp of the high-voltage and, for the pixel system, turning on the preamplifiers. Source: [114].

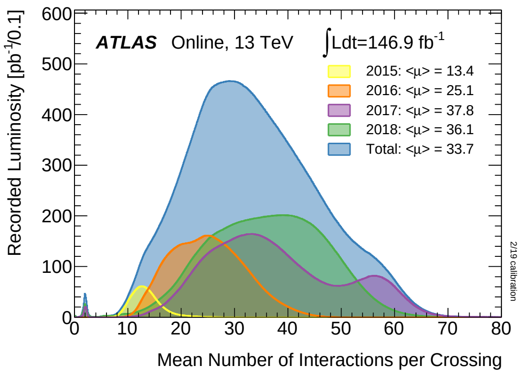

Figure 3.9: Luminosity-weighted distribution of the mean number of interactions per crossing for the 2015-2018 pp collision data at $\sqrt{s} = 13$ TeV. All data recorded by ATLAS during stable beams is shown, and the integrated luminosity and the mean pileup value are given in the figure. The luminosity shown represents the preliminary 13 TeV luminosity calibration for 2018, released in February 2019, that is based on van-der-Meer beam-separation scans. Source: [114].

3.6 Modelling physics processes

The use of simulated data to test model predictions is ubiquitous in particle physics. Therefore, it is of the utmost importance that the simulated data accurately models the underlying physics processes. When searching for evidence of new fundamental particles, incorrect modelling of the expected Standard Model background could lead to the observation of spurious signals. Likewise, precision measurements of the properties of Standard Model particles rely on extremely accurate modelling to compare with the observed data. Simulated data is produced using the Monte Carlo method [115], which relies on random sampling to model the properties of particle interactions. This process can be broadly split into three main stages; event generation, detector simulation and object reconstruction.

Event generation

The first stage of generating simulated data for high-energy physics experiments is to generate the hard scattering process. This involves using parton distribution functions to describe the momentum of the incoming partons, and then using perturbation theory to build and sample a probability distribution of outgoing particles. These events are generated in a format known as HepMC [116], and can be filtered to keep events with a specific type of particle; for example, events containing a W or a Z boson. The event-generator simulates the production of prompt particles, while also simulating and storing the subsequent decay products. For example, an event-generator can simulate the production of Z bosons, and the subsequent decay into a pair of charged leptons. One of the most popular event-generators in use at ATLAS is Powheg [117, 118].

Since the simulated partons and leptons are electrically (and in the case of partons colour) charged, they can emit secondary radiation in the form of photons and gluons. In the case of partons radiating gluons, this causes a cascade of secondary emissions known as a parton shower. As a result of colour confinement, the parton shower undergoes hadronisation to form colour neutral particles, corresponding to what is actually measured by the detector. This stage of simulation corresponds to what is known as *generator-level*, and describes the properties of the incoming and outgoing simulated particles before they interact with the detector. There are many programmes to simulate parton showering and hadronisation, with *Pythia* [119], *Sherpa* [120] and *Herwig* [121] being the most popular in use at ATLAS. The effects of final state photon radiation are simulated using *Photos* [122].

Detector simulation

Next, the simulated particles are passed through a detailed simulation of the detector response. At ATLAS this simulation is performed using GEANT4 [123], which simulates energy deposits (hits) in the sensitive regions of the detector, taking into account any misalignments and imperfections. After detector simulation the Monte Carlo data is stored at the so-called *truth-level*. Simulated Data Objects (SDOs) are then created through a process called digitisation by mapping the simulated detector hits (truth-level) back to the simulated particles (generator-level) that deposited the energy. Finally Raw Data Objects (RDOs) are produced by simulating digits, the electrical signals that are read out by the detector during data-taking. The ATLAS read-out driver system is then emulated to produce the simulated RDOs in exactly the same format as real data.

Object reconstruction

These RDOs are then passed through the same trigger, reconstruction, identification, isolation and tagging software as is used to process the real data. Therefore, the final output of the ATLAS simulation framework are *reconstruction-level* objects, which can then be compared with real ATLAS data.

Further experimental corrections can be applied to the simulated Monte Carlo data in the form of scale factors, which describe the relative efficiencies in data and Monte Carlo ($SF = \varepsilon_{data}/\varepsilon_{MC}$). Scale factors are applied either as event-level or object-level weights to the simulated data, and aim to improve the agreement with the data measured by the detector. Common scale factors include identification, isolation, trigger and reconstruction efficiency corrections. These are derived by the ATLAS combined performance (CP) group in dedicated analyses, and used by many analysis groups throughout the experiment. Another such scale factor is the pileup reweighting factor, which takes into account the difference between the simulated pileup profile and the actual pileup profile of the data. Since Monte Carlo is often generated before data-taking, the exact pileup distribution cannot be perfectly known/modelled in advance. Therefore, an additional event-level weight is applied to the reco-level Monte Carlo samples to shift the generated pileup distribution to more accurately reflect that of the real data. This is done separately for each data-taking campaign.

Chapter 4

Luminosity determination using $Z \to \ell^+\ell^-$ events

As discussed in Section 3.3, luminosity is a key quantity to describe how many collisions occur in the ATLAS interaction region. A precise measurement of the luminosity delivered to the detector is crucial, especially for cross section measurements where it is often one of the largest systematic uncertainties. Therefore, it is important to have various tools to monitor the baseline ATLAS luminosity measurement, not only to get a handle on the systematic uncertainty, but also to correct the central values as well. One such tool is the so called Z-counting method, which monitors the stability of the baseline ATLAS luminosity measurement by measuring the production rate of the Z boson. This method has been succesfully implemented at ATLAS since 2015 by measuring the rate of reconstructed $Z \to \mu^+\mu^-$ decays. The $Z \to e^+e^-$ channel was implemented in early 2018, and greatly increases the power of the method by allowing for internal cross checks between the channels, as well as the combination of their statistics.

All plots, with the exception of Figure 4.10, were produced by the author. Those marked as "ATLAS Preliminary" (with the exception of Figure 4.2, where the image source is given) were produced for the ATLAS Public Note ATL-DAPR-PUB-2021-001 [1], while those marked as "ATLAS Work in progress" are the unpublished work of the author.

4.1 Introduction

The cross section of any physics process, $\sigma_{X\to YZ}$, measured at ATLAS is given by

$$\sigma_{X\to YZ} = \frac{N_{X\to YZ}}{\mathcal{L}}, \tag{4.1}$$

where $N_{X\to YZ}$ is the decay rate of $X \to YZ$ and $\mathcal{L}$ the luminosity delivered to the detector. By rearranging Eq. 4.1 and substituting $\sigma_{X\to YZ}$ for a theoretical prediction, $\sigma^{theory}_{X\to YZ}$, a luminosity measurement can be obtained by

$$\mathcal{L} = \frac{N_{X\to YZ}}{\sigma^{theory}_{X\to YZ}}. \tag{4.2}$$

The decay of the Z-boson into a pair of electrons or muons is an excellent candidate process for such a measurement. It has a large cross section of 2 pb in pp collisions at $\sqrt{s} = 13$ TeV, for dilepton pairs with $m_{\ell^+\ell^-} > 60$ GeV, which can be precisely predicted from theoretical calculations. Figure 4.1 shows the Feynman diagram for this interaction, where off-shell photon production (γ^*) interferes with the Z boson. By requiring selected events to have dilepton invariant masses ($m_{\ell^+\ell^-}$) close to the Z resonance, the $\gamma^* \to \ell^+\ell^-$ is largely suppressed and the process can simply be considered a $Z \to \ell^+\ell^-$.

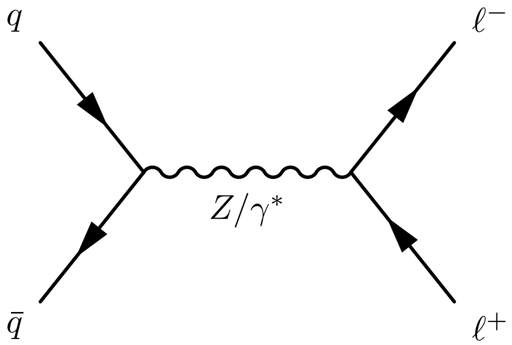

Figure 4.1: Neutral current Drell-Yan scattering at lowest order.

Measuring the decay rate of $Z \to \tau\tau$ or $Z \to q\bar{q}$ is not feasible at a hadron collider, since these processes are much more difficult to reconstruct in the detector and have much larger background contributions. Therefore, the following discussion will pertain specifically to $Z \to e^+e^-$ and $Z \to \mu^+\mu^-$ decays, which will be referred to collectively as $Z \to \ell^+\ell^-$.

The value of the $Z \to \ell^+\ell^-$ cross-section is predicted by calculations at next-to-next-to-leading order QCD with a total uncertainty of 3–4% at 90% CL, dominated by the current knowledge of the proton parton distribution functions (PDFs) [124]. Since the uncertainties associated with the baseline ATLAS luminosity measurement are approximately 2% [96], the Z-counting method is not yet competitive as an absolute measurement, but is nevertheless a powerful tool to monitor the stability of other luminometers. The method is robust against non-time-dependent systematic uncertainties, and a study by Harry Lyons showed that the simulated correction factor has systematic uncertainties in the per-mille range [125]. Currently a full evaluation of all time-dependent systematics has not been performed, however these are expected to be small.

In order to accurately measure the number of $Z \to \ell^+\ell^-$ decays that take place in the interaction region, it is important to ensure that detector inefficiencies are accurately modelled. As the detector is not perfectly efficient, not all $Z \to \ell^+\ell^-$ decays that take place at ATLAS are successfully reconstructed, and so it is crucial that the fraction of events not recorded be accounted for so that the production rate is not underestimated. Conditions in the detector can vary significantly over the course of a single LHC fill, as well as between successive fills, so it is important that this be modelled in a granular way by measuring the detector inefficiencies over relatively short time periods. To do this, data-driven techniques are used, measuring the inefficiency of the detector using the data itself over some time period, which is then applied to the data recorded in the same time period to obtain a corrected measurement of $N_{Z\to\ell^+\ell^-}$.

4.2 Methodology

The simple relationship in Eq. 4.2 assumes that the production rate has been corrected to account for detector inefficiencies and background, and that the cross section prediction corresponds to the fiducial volume used by the analysis. As discussed previously, data-driven techniques are used to derive the various efficiency components ($\varepsilon^{\mathrm{T\&P}}_{Z\to\ell^+\ell^-}$), which are themselves then subjected to a correction derived from Monte Carlo ($F^{\mathrm{MC}}_{Z\to\ell^+\ell^-}(\langle\mu\rangle)$). The fraction of generated events that are reconstructed inside the fiducial volume (acceptance, $A^{MC}_{Z\to\ell^+\ell^-}$) is also derived from Monte Carlo. Combining all of these factors with those given in Eq. 4.2, a Z-counting luminosity can then be obtained using Eq. 4.3, and an overview of all terms can be found in Table 4.1. The splitting of Eq. 4.3 into two terms is a cosmetic choice, in order to differentiate between the components which are time-dependent and those that are time-independent. This section will present a review of the Z-counting methodology, outlining the event-selection, data-driven efficiency corrections and Monte Carlo based correction factors.

$$\mathcal{L}_{Z\to\ell^+\ell^-}(LB) = \frac{N_{Z\to\ell^+\ell^-}(LB)}{\varepsilon^{\mathrm{T\&P}}_{Z\to\ell^+\ell^-}(LB)\cdot F^{\mathrm{MC}}_{Z\to\ell^+\ell^-}(\langle\mu\rangle)\cdot t(LB)} \times \frac{1-f_{\mathrm{bkg}}}{\sigma^{\mathrm{theory}}_{Z\to\ell^+\ell^-}\cdot A^{MC}_{Z\to\ell^+\ell^-}}. \tag{4.3}$$

Luminosity block live-time ($t(LB)$) The live time of a luminosity block at ATLAS is typically around 60 seconds, and takes into account the time lost due to trigger or data acquisition down times. For example, if a luminosity block was 62 seconds long, but the data acquisition system was down for 4 seconds, the live time of this LB would be 58 seconds.

Term	Meaning	Section
$\mathcal{L}_{Z\to\ell^+\ell^-}(LB)$	Z-counting luminosity	4.2
$N_{Z\to\ell^+\ell^-}(LB)$	measured number of $Z \to \ell^+\ell^-$ events	4.2.1
$\varepsilon^{\mathrm{T\&P}}_{Z\to\ell^+\ell^-}(LB)$	event-level tag-and-probe efficiency	4.2.2
$F^{\mathrm{MC}}_{Z\to\ell^+\ell^-}(\langle\mu\rangle)$	residual correction factor from simulation	4.2.3
$t(LB)$	live-time corrected luminosity block length	4.2
$1 - f_{\mathrm{bkg}}$	background correction factor to account for $t\bar{t}$ and diboson contamination	4.2
$\sigma^{\mathrm{theory}}_{Z\to\ell^+\ell^-}$	theoretical cross section prediction	4.2
$A^{MC}_{Z\to\ell^+\ell^-}$	fiducial acceptance factor	4.2.4

Table 4.1: Summary of all terms used in calculating a Z-counting luminosity, where LB indicates time-dependence and $\langle\mu\rangle$ the dependence on the pileup parameter.

Background subtraction ($1 - f_{\mathrm{bkg}}$) The factor f_{bkg} is the fraction of events in the signal region that originate from diboson or $t\bar{t}$ production and is determined from Monte Carlo studies. Since the signal region uses a tight mass window around the Z peak, this factor is extremely small, and is taken to be 0.005 in both $Z \to e^+e^-$ and $Z \to \mu^+\mu^-$ decays. In principle, there is also small contribution from multijet events, but this is even smaller at approximately 0.0005 and is therefore neglected.

Theoretical cross section ($\sigma^{\mathrm{theory}}_{Z\to\ell^+\ell^-}$) $\sigma^{\mathrm{theory}}_{Z\to\ell^+\ell^-}$ is the inclusive $Z \to \ell^+\ell^-$ cross section for dilepton pairs with invariant mass $m_{\ell^+\ell^-} > 60$ GeV, and has a value of $\sigma^{\mathrm{theory}}_{Z\to\ell^+\ell^-} = 1970 \pm 0.3$ (stat) $^{+69.6}_{-67.5}$ (pdf) pb. This is calculated at next-to-next-to leading order QCD using the FEWZ 3.1.b2 framework [126] and CT18ANNLO proton PDF [43]. As discussed in Section 4.1, the absolute scale of Z-counting luminosity is limited by this uncertainty, and so this thesis will focus on using Z-counting to monitor the stability of other luminometers. By normalising the integrated Z-counting luminosity over some time period to another luminosity measurement, the stability over time and pileup can be monitored by measuring the spread of the ratio around unity. Comparisons between the $Z \to e^+e^-$ and $Z \to \mu^+\mu^-$ luminosities are not sensitive to the choice of cross section or its uncertainty, and therefore provide a powerful internal cross check of the method.

4.2.1 Event selection

The first selection requirement is the application of the GRLs listed in Table 3.3. Events which pass the GRL requirements are then required to pass one of the unprescaled single-lepton triggers listed in Table A.1, as well as the selection criteria listed in Table 4.2.

Electron or muon candidates are required to have $p_{\mathrm{T}}^{\ell} > 27$ GeV and $|\eta^{\ell}| < 2.4$, with the additional requirement that electrons do not fall within the region $1.37 < |\eta^{e}| < 1.52$. They are also required to originate from the primary vertex of the event, defined as the vertex whose associated tracks have the highest sum of squared transverse momenta, with at least two reconstructed tracks with transverse momentum $p_{\mathrm{T}} > 0.4$ GeV. The transverse impact parameter (d_0) is the closest distance between a track and the primary vertex in the plane perpendicular to the beam direction, and the longitudinal impact parameter ($|z_0 sin\theta|$) is defined as the longitudinal distance between the track and the primary vertex along the beam line. The significance of the transverse impact parameter ($|d_0|/\sigma(d_0)$) is required to be less than 3 for muons and less than 5 for electrons, and the longitudinal impact parameter is required to satisfy $|z_0 sin\theta| < 0.5$ mm in both channels.

Electron candidates are required to pass a likelihood-based identification selection, using the LHMedium working point [97]. Muon candidates are required to be combined muons, as defined in Section 3.4.2, and to also satisfy the Medium muon selection criteria [104]. Both electrons and muons are required to satisfy the LooseTrackOnly isolation criteria [104]. If the invariant mass of two oppositely-charged, same-flavour leptons passing all of these criteria is within the range $66 < m_{\ell^+\ell^-} < 116$ GeV the event is selected. Figure 4.2 shows the dielectron (left) and dimuon (right) invariant mass distributions for events passing these selections in an example LHC fill. The raw number of $Z \rightarrow e^+e^-$ and $Z \rightarrow \mu^+\mu^-$ counts (before efficiency corrections) per luminosity block can be seen for each data-taking period in Figure 4.3. Due to the increasing instantaneous luminosity over the course of Run 2, the number of reconstructed $Z \rightarrow \ell^+\ell^-$ events per LB increases, improving the statistical precision of the Z-counting method. The shape of the distribution in 4.3 also reflects that of the pileup distribution in each of the data-taking periods of Run 2.

	Selection criteria	**Electron channel**	**Muon channel**
Single-lepton	Transverse momentum	$p_{\mathrm{T}}^{e} > 27\,\mathrm{GeV}$	$p_{\mathrm{T}}^{\mu} > 27\,\mathrm{GeV}$
	Pseudorapidity	$\lvert\eta^e\rvert < 1.37$ OR $1.52 < \lvert\eta^e\rvert < 2.4$	$\lvert\eta^\mu\rvert < 2.4$
	Track-vertex association	$\lvert z_0 \sin\theta\rvert < 0.5$ mm	$\lvert z_0 \sin\theta\rvert < 0.5$ mm
		$\lvert d_0\rvert/\sigma(d_0) < 5$	$\lvert d_0\rvert/\sigma(d_0) < 3$
	Identification	LHMedium	Medium, ID+MS combined muon
	Isolation	LooseTrackOnly	LooseTrackOnly
Event-level	Invariant mass	$66 < m_{e^+e^-} < 116\,\mathrm{GeV}$	$66 < m_{\mu^+\mu^-} < 116\,\mathrm{GeV}$

Table 4.2: Overview of event selection criteria, where two oppositely charged leptons (of the same flavour) passing the single-lepton selection criteria with invariant mass in the range $66 < m_{\ell^+\ell^-} < 116\,\mathrm{GeV}$ are required to form a Z-boson candidate. The fiducial volume is defined by the p_{T}^{ℓ}, η^{ℓ} and $m_{\ell^+\ell^-}$ selections, independently for each lepton flavour.

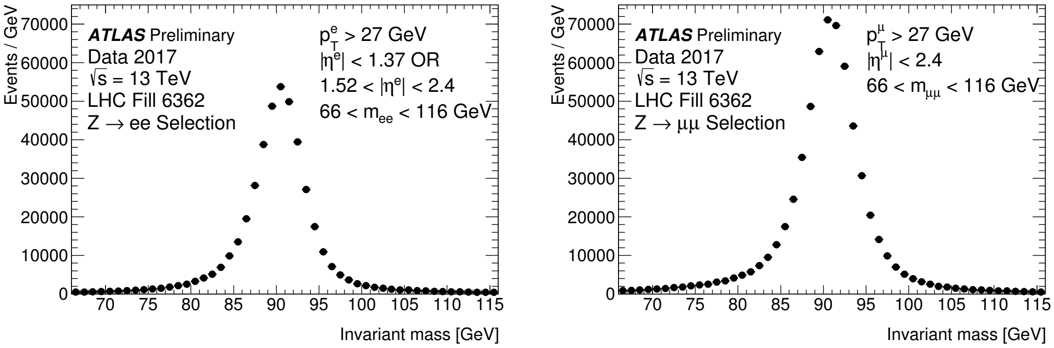

Figure 4.2: Dielectron (left) and dimuon (right) invariant mass distributions, where both leptons pass the selections listed in Table 4.2.

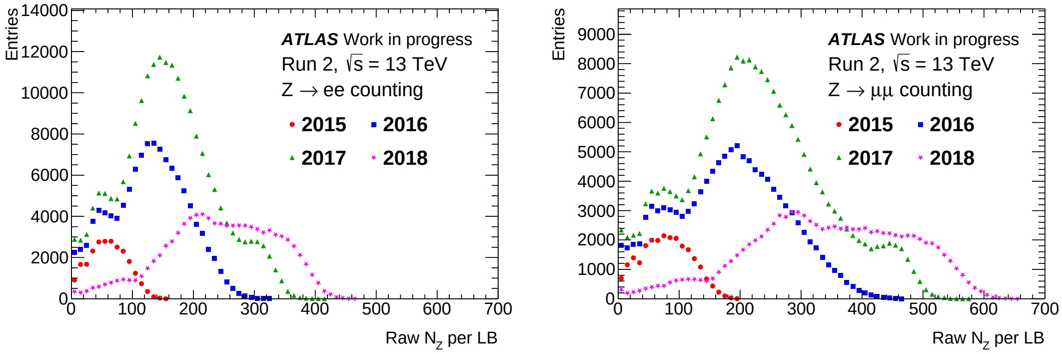

Figure 4.3: Distributions of the raw N_Z counts per luminosity block in the electron (left) and muon (right) channels for each data-taking period.

4.2.2 Data-driven efficiency estimation

Since the efficiency to trigger and reconstruct an electron or muon is not 100%, not all $Z \rightarrow \ell^+\ell^-$ decays produced in the detector are recorded. Therefore, it is important to accurately measure the trigger and reconstruction efficiencies so that the Z-production rate can be corrected accordingly. These efficiencies apply to a single lepton, and must be combined to an event-level efficiency, i.e. the efficiency of triggering and reconstructing two leptons of the same flavour. As mentioned in Section 4.2, these efficiencies are measured using a data-driven tag-and-probe method over the duration of a single luminosity block. Measuring the efficiencies with such fine time granularity ensures that changes in the beam and detector conditions are accurately modelled. The pileup at which the data is recorded greatly influences the efficiency of triggering and reconstructing an electron or muon, and the Z-counting benefits from being able to track this variation in real time.

Single-lepton trigger efficiency

By selecting all events with 2 electrons or muons passing the selection criteria listed in Table 4.2 (N), and counting the number of events where one (N_1) or two (N_2) leptons pass the trigger requirements, the single-lepton trigger efficiency ($\varepsilon_{\text{trig},1\ell}$) can be determined,

$$N_1 = 2 \times N \times \varepsilon_{\text{trig},1\ell} \times (1 - \varepsilon_{\text{trig},1\ell}), \tag{4.4}$$

$$N_2 = N \times \varepsilon^2_{\text{trig},1\ell}, \tag{4.5}$$

$$\varepsilon_{\text{trig},1\ell} = \frac{1}{\frac{N_1}{2N_2} + 1}. \tag{4.6}$$

This means that the trigger efficiency specifically refers to the probability that one of the selected leptons also passes the trigger, not the probability of *any* lepton passing the trigger requirements. In principle there is a small background component to N_1 and N_2, however due to the strict isolation and identification requirements, as well as the tight mass window around the Z peak ($66 < m_{\ell^+\ell^-} < 116$ GeV), this contribution is negligible and therefore neglected.

Figures 4.5 and 4.7 show the trigger efficiency (black circles) for an example LHC fill in the electron and muon channel respectively. The time-dependent efficiencies in Figures 4.5 and 4.7 have been averaged over groups of 20 LBs to improve the statistical precision, as discussed in Section 4.3, while the pileup-dependent efficiencies are averaged using the same procedure in each individual pileup bin. This is not how the efficiencies are applied when calculating the luminosity, and is only presented this way to monitor trends over the course of the fill. As expected, the trigger efficiency decreases with increasing pileup, and some other finer shapes can be resolved which could reflect the data-taking conditions of the detector itself. For example, the small dip in the muon trigger efficiency between LBs 920 and 1000 corresponds to a slight decrease in the coverage of the barrel muon trigger in this period.

Since the analysis uses single-lepton triggers, applied as an event-level selection and not per-lepton, the selected di-electron and di-muon events can contain either one or two leptons which passed the trigger. Therefore, the event-level trigger efficiency ($\varepsilon_{\text{trig, event}}$) is defined as

$$\varepsilon_{\text{trig, event}} = 1 - (1 - \varepsilon_{\text{trig},1\ell})^2, \tag{4.7}$$

taking into account the fact that either or both of the leptons can pass the trigger requirements. All statistical uncertainties are calculated by propagating the Poisson counting uncertainties on N_1 and N_2.

Single-lepton reconstruction efficiency

Both the single-electron and single-muon reconstruction efficiencies are determined using the tag-and-probe method. The tag-and-probe method works by selecting two leptons near a resonant peak, in this case the Z, to ensure that they have a high probability of being genuine prompt leptons and minimise the background contribution. One of the leptons (tag) is required to pass strict selection criteria to further increase the probability that the event is a genuine Z event, while the other lepton (probe) is subject to a looser selection. It is this loose probe object that is used to determine the reconstruction efficiency of the selected leptons in a $Z \to \ell^+\ell^-$ event. The tag and probe selection criteria can be found in Tables 4.3 and 4.4.

Tag selection criteria	**Electron channel**	**Muon channel**
Transverse momentum	$p_{\mathrm{T}}^{e} > 27\,\mathrm{GeV}$	$p_{\mathrm{T}}^{\mu} > 27\,\mathrm{GeV}$
Pseudorapidity	$0 < \|\eta^e\| < 1.37$ OR $1.52 < \|\eta^e\| < 2.4$	$0 < \|\eta^\mu\| < 2.4$
Track-vertex association	$\|z_0 \sin\theta\| < 0.5$ mm	$\|z_0 \sin\theta\| < 0.5$ mm
	$\|d_0\|/\sigma(d_0) < 5$	$\|d_0\|/\sigma(d_0) < 3$
Identification	*LHTight*	Medium, ID+MS combined muon
Isolation	LooseTrackOnly	LooseTrackOnly
Single lepton trigger object	*matched*	*matched*

Table 4.3: Selection criteria defining the tag lepton in the electron and muon channels. All selection criteria are identical to those in Table 4.2, other than the identification working point used in the electron channel, and the fact that both electrons and muons are required to pass the single-lepton trigger requirements.

	Electron channel	**Muon channel**
	Preselection criteria	
Object	Cluster loosely matched to ID track	ID track
Transverse momentum	$p_{\mathrm{T}}^{e} > 27\,\mathrm{GeV}$	$p_{\mathrm{T}}^{\mu} > 27\,\mathrm{GeV}$
Pseudorapidity	$\|\eta^e\| < 1.37$ or $1.52 < \|\eta^e\| < 2.4$	$\|\eta^\mu\| < 2.4$
Track-vertex association	—	$\|z_0 \sin\theta\| < 2$ mm
	Probe selection criteria	
Requirement	passes the single-electron selection criteria listed in Table 4.2	matched to combined muon which passes the single-muon selection criteria listed in Table 4.2 but with looser $p_{\mathrm{T}}^{\mu} > 21.6\,\mathrm{GeV}$

Table 4.4: Probe lepton preselection and selection criteria. All probe candidates are required to pass the preselection criteria, and the selection criteria determine whether a probe passes or fails.

All probe candidates are required to pass the preselection criteria in Table 4.4, and by measuring the fraction which also pass the selection criteria, an estimate of the efficiency to reconstruct a signal lepton can be obtained. The probe selection criteria are equal to the signal selection criteria given in Table 4.2, other than the p_{T} selection in the muon channel which is reduced to avoid a bias near the phase space boundary. [1] This is not the full efficiency to reconstruct a signal lepton, as it does not take into account

---

[1] If a track is reconstructed with $p_{\mathrm{T}} = 27.1$ GeV and a combined muon with $p_{\mathrm{T}} = 26.9$ GeV, but both have a cut of $p_{\mathrm{T}} > 27.0$ GeV there would be a bias, and so the muon p_{T} selection is relaxed.

the efficiency to reconstruct the loose probe leptons. Any missing efficiency components (loose lepton reconstruction, charge mis-identification) are estimated using Monte Carlo, as discussed in Section 4.2.3. In each $Z \to \ell^+\ell^-$ candidate event, each lepton is considered alternatively as a tag and then as a probe

Due to the loose preselection of the probe lepton, mis-identified leptons and combinatorial backgrounds can be significant, and must therefore be taken into account. The method used for the background estimation is the main way in which the electron and muon channel reconstruction efficiency determinations differ, and the tag-and-probe procedure will be outlined in detail for the electron and muon channels separately in the following sections. However, the general form of the tag-and-probe reconstruction efficiency is given by,

$$\varepsilon_{\text{reco},1\ell} = \frac{N^{\text{OS}}_{\text{pass}} - N^{\text{bkg}}_{\text{pass}}}{(N^{\text{OS}}_{\text{pass}} + N^{\text{OS}}_{\text{fail}}) - (N^{\text{bkg}}_{\text{pass}} + N^{\text{bkg}}_{\text{fail}})}, \tag{4.8}$$

where $N^{\text{OS}}_{\text{pass}}$ ($N^{\text{OS}}_{\text{fail}}$) is the number of opposite-charge tag-and-probe pairs where the probe satisfies (fails) the selection criteria in Table 4.4 and $N^{\text{bkg}}_{\text{pass}}$ ($N^{\text{bkg}}_{\text{fail}}$) is the corresponding background estimate. The event-level reconstruction efficiency to reconstruct two leptons is given by,

$$\varepsilon_{\text{reco,event}} = \varepsilon^2_{\text{reco},1\ell}. \tag{4.9}$$

Electron channel Electron candidates which pass the selection criteria given in Table 4.3 are considered as tags, and clusters of energy in the electromagnetic calorimeter which are loosely matched to an inner detector track are used as probe candidates. As mentioned previously, the tag-and-probe method does not measure the efficiency to reconstruct the loose probe object, which instead comes from Monte Carlo simulation. The efficiency of the probe preselection with respect to generated electrons is approximately 98% [97].

The reconstruction efficiency is estimated by counting the fraction of opposite-sign events which pass ($N^{\text{OS}}_{\text{pass,peak}}$) or fail ($N^{\text{OS}}_{\text{fail,peak}}$) the probe selection criteria in Table 4.4, where the subscript peak refers to the invariant mass range $75 < m_{ee} < 105\,\text{GeV}$. To estimate the background contribution, a background-enriched sample of events with minimal signal contribution is required. This is achieved by a so-called template method (N_{template}), which relies on inverting the isolation and identification requirements in Table 4.2, meaning that probe electrons are explicitly required to fail both isolation and identification but pass all other selections.

In order to obtain a smooth distribution over the entire invariant mass range, the statistics of an entire LHC fill are used to estimate the background template shape in each luminosity block. Therefore, the template shape must be normalised to the statistics of the individual luminosity block, as shown in Eq. 4.10.

$$\varepsilon_{\mathrm{reco},1e} = \frac{N^{\mathrm{OS}}_{\mathrm{pass,peak}} - N^{\mathrm{OS}}_{\mathrm{template,peak}} \cdot \frac{N^{\mathrm{SS}}_{\mathrm{pass,tail}}}{N^{\mathrm{SS}}_{\mathrm{template,tail}}}}{(N^{\mathrm{OS}}_{\mathrm{pass,peak}} + N^{\mathrm{OS}}_{\mathrm{fail,peak}}) - N^{\mathrm{OS}}_{\mathrm{template,peak}} \cdot \frac{N^{\mathrm{OS}}_{\mathrm{fail,tail}}}{N^{\mathrm{OS}}_{\mathrm{template,tail}}}}. \tag{4.10}$$

Opposite-sign template events ($N^{\mathrm{OS}}_{\mathrm{template,peak}}$) are used to estimate the background shape in the peak region, normalised independently for both numerator and denominator using a high-mass sideband in the invariant mass range $120 < m_{ee} < 250\,\mathrm{GeV}$ (tail). In the numerator, the template is normalised by taking the ratio of the number of same-sign events in the tail where the probe passes selection ($N^{\mathrm{SS}}_{\mathrm{pass,tail}}$), and the number of same-sign template events ($N^{\mathrm{SS}}_{\mathrm{template,tail}}$) in order to avoid signal contamination. The procedure is the same in the denominator, however the number of opposite-sign events where the probe fails selection ($N^{\mathrm{OS}}_{\mathrm{fail,tail}}$) and the opposite-sign template ($N^{\mathrm{OS}}_{\mathrm{template,tail}}$) are used. Figure 4.4 shows the invariant mass distributions of the numerator (left) and denominator (right) terms for an example LHC fill, where the normalised template distribution is indicated by $N^{\mathrm{pass}}_{\mathrm{bkg}}$ and $N^{\mathrm{total}}_{\mathrm{bkg}}$. The resulting efficiencies can be seen in Figure 4.5 (red squares), where it can be seen how the tag-and-probe procedure tracks the time/pileup dependence over the course of a single LHC fill.

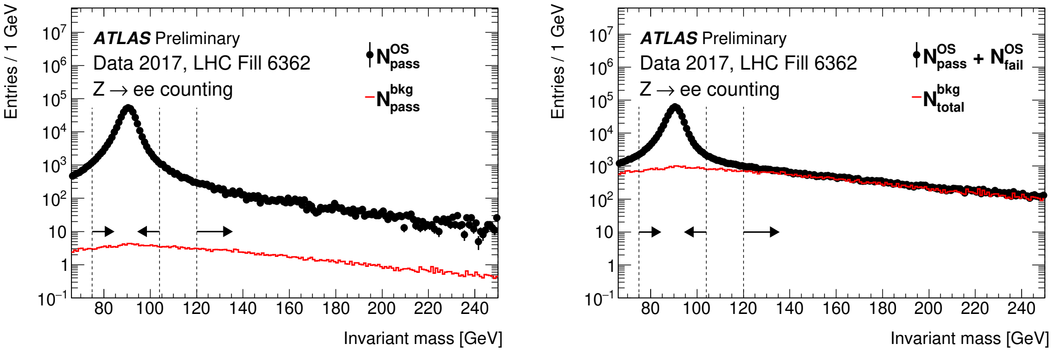

Figure 4.4: Invariant di-electron mass distributions used to calculate the reconstruction efficiency as given in Eq. 4.10, where the left (right) figure shows the contribution to the numerator (denominator). The vertical dashed lines illustrate the peak and tail ranges for the electron template method. The error bars show statistical uncertainties only.

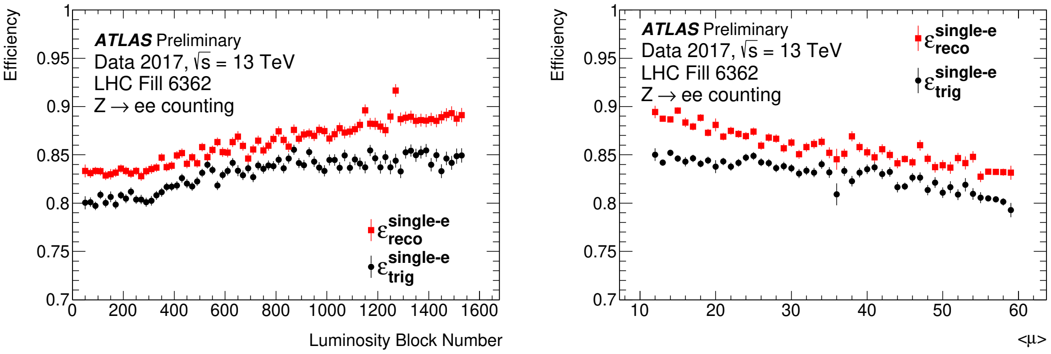

Figure 4.5: Data-driven single-electron trigger (black circles) and reconstruction (red squares) efficiencies determined using the tag-and-probe method. The x-axis represents the elapsed time in units of Luminosity Blocks (left) and average pileup (right). For display purposes only, each of the efficiencies has been averaged over 20 luminosity blocks (Section 4.3). The error bars show statistical uncertainties only.

Muon channel Muon candidates which pass the selection criteria in Table 4.3 are considered as tags and inner detector tracks are used as probes. These tracks must pass the preselection criteria given in Table 4.4, and a pass or fail of the probe is determined by the probe selection criteria. A probe is considered to pass selection if it is matched to a combined muon passing the selection criteria discussed previously. The probe preselection efficiency for generated muons is approximately 99% and well described by Monte Carlo simulation [104].

The background estimation in the muon channel is simply taken as the number of same-sign events which pass/fail selection, as the dominant background processes are roughly charge symmetric [104]. A tight mass window of $86 < m_{\mu\mu} < 96$ GeV is used to further reduce the background contamination. Following the general form of Eq. 4.8, the reconstruction efficiency in the muon channel is given by

$$\varepsilon_{\text{reco},1\mu} = \frac{N_{\text{pass}}^{\text{OS}} - N_{\text{pass}}^{\text{SS}}}{(N_{\text{pass}}^{\text{OS}} + N_{\text{fail}}^{\text{OS}}) - (N_{\text{pass}}^{\text{SS}} + N_{\text{fail}}^{\text{SS}})}. \tag{4.11}$$

The invariant mass distributions for the numerator and denominator terms can be seen in Figure 4.6, with the corresponding efficiencies in Figure 4.7 (red squares). Similar trends are observed as in the electron channel, with the muon reconstruction efficiency increasing over time (decreasing with pileup) as expected.

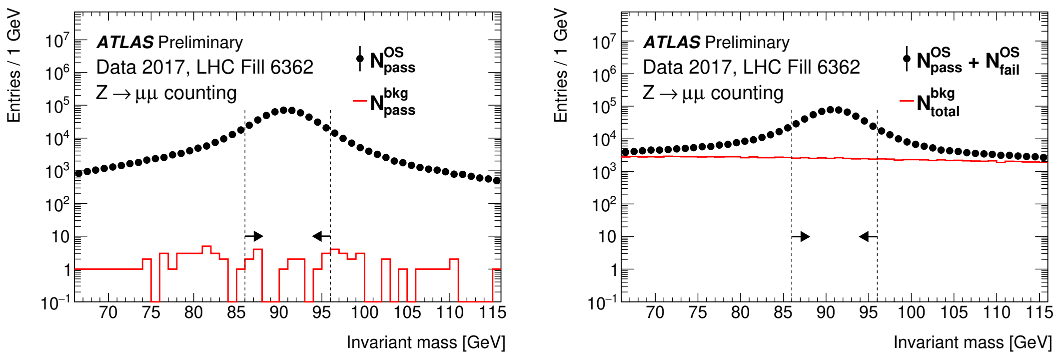

Figure 4.6: Invariant di-muon mass distributions used to calculate the reconstruction efficiency as given in Eq. 4.11, where the left (right) figure shows the contribution to the numerator (denominator). The vertical dashed lines illustrate the peak region ($86 < m_{\mu\mu} < 96\,\mathrm{GeV}$) used in the muon channel tag-and-probe procedure. The error bars show statistical uncertainties only.

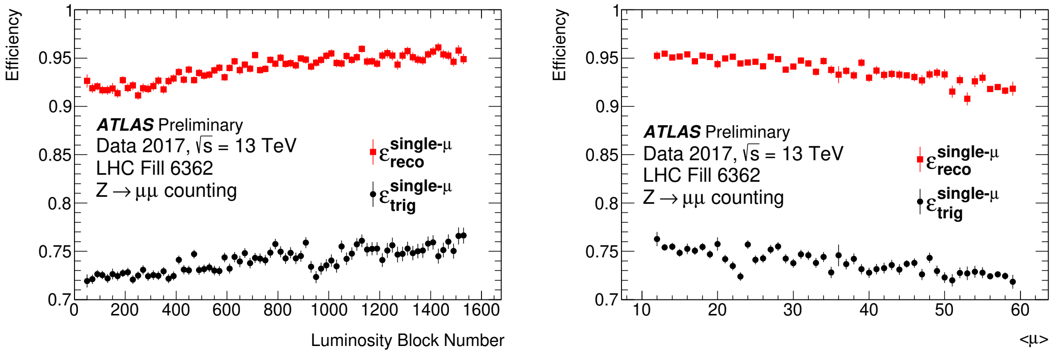

Figure 4.7: Data-driven single-muon trigger (black circles) and reconstruction (red squares) efficiencies determined using the tag-and-probe method. The x-axis represents the elapsed time in units of Luminosity Blocks (left) and average pileup (right). For display purposes only, each of the efficiencies has been averaged over 20 luminosity blocks (Section 4.3). The error bars show statistical uncertainties only.

Event-level efficiency

Once the single-lepton trigger and reconstruction efficiencies have been determined they must be combined to account for the fact that there are two leptons in a $Z \to \ell^+\ell^-$ event. This is done independently for di-electron and di-muon events, and as mentioned, only one lepton is required to pass the trigger selection, but both leptons must pass the signal selection criteria (reco). The event-level efficiency ($\varepsilon^{\mathrm{T\&P}}_{Z\to\ell^+\ell^-}(LB)$) is given by

$$\varepsilon^{\mathrm{T\&P}}_{Z\to\ell^+\ell^-}(LB) = \varepsilon_{\mathrm{trig,event}} \times \varepsilon_{\mathrm{reco,event}}, \tag{4.12}$$

$$\varepsilon^{\mathrm{T\&P}}_{Z\to\ell^+\ell^-}(LB) = (1 - (1 - \varepsilon_{\mathrm{trig},1\ell})^2) \times \varepsilon^2_{\mathrm{reco},1\ell}. \tag{4.13}$$

This is then used to correct the raw number of $Z \to \ell^+\ell^-$ events per luminosity block in each decay channel separately. Figure 4.8 shows the single-lepton and event-level efficiencies in the electron (left) and muon (right) channels as a function of luminosity block. Since the event-level efficiency depends on the square of both the trigger and reconstruction efficiencies, the trends seen in the single-lepton efficiencies are compounded. This is especially noticeable in the electron channel, where the pileup-dependence of the event-level efficiency is approximately 12% over the fill, while the single-lepton efficiencies have a pileup dependence of about 6%. The statistical uncertainty on $\varepsilon^{\mathrm{T\&P}}_{Z\to\ell^+\ell^-}(LB)$ is also larger than the individual components, as it is calculating by propagating the uncertainties on the square of each single-lepton efficiency. As the event-level tag-and-probe efficiency estimate does not take into account all efficiency effects, it is corrected with a pileup-dependent correction factor, determined from Monte Carlo (Section 4.2.3).

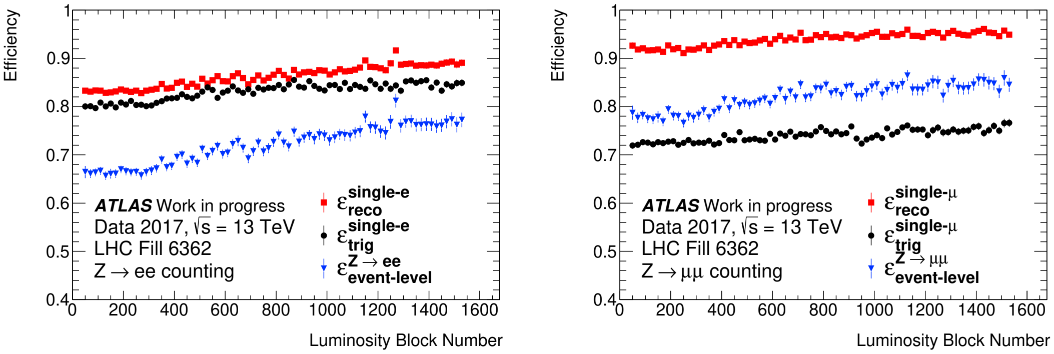

Figure 4.8: Data-driven single electron (left) and muon (right) trigger (black circles), reconstruction (red squares) and event-level (blue triangles) efficiencies. The x-axis represents the elapsed time in units of Luminosity Blocks with a typical length of one minute per LB. For display purposes only, each of the efficiencies has been averaged over 20 luminosity blocks (Section 4.3). The error bars show statistical uncertainties only.

Bunch position dependence of efficiencies

So far the only dependencies that have been tracked via data-driven efficiency estimation are time and pileup. Many luminosity monitoring algorithms monitor the bunch position dependence of the delivered luminosity, and for Z-counting to do the same bunch-dependent efficiencies would be required. Most proton bunches colliding at the ATLAS detector are not isolated bunches, but rather part of a larger bunch train. As such, there can be inter-bunch effects, due to the fact that the spacing between bunches is quite small (typically 25 ns for most of Run-2).

Figure 4.9 shows the dependence of the single-lepton trigger- and reconstruction-efficiencies on the position of the colliding bunches in the bunch train. These efficiencies are calculated using the entire 2018 dataset (58.5 fb^{-1}), in 48 bunch-position bins and four different pileup bins. Separating the data into pileup bins shows the correlation, if any, between the position of the bunch in the train and the number of interactions per bunch crossing. The 2018 dataset is a good illustrative example to test the bunch position dependence, as the high luminosity ensures good statistical precision, and the bunch filling pattern was consistent throughout the year (48 filled bunches in the train).

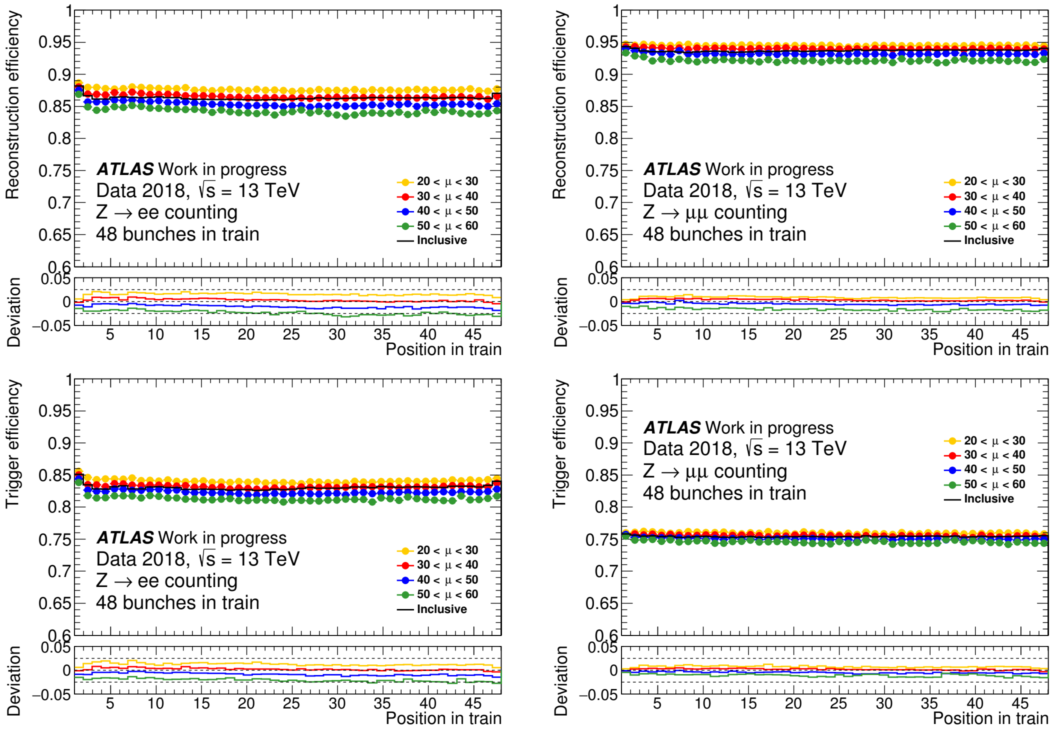

Figure 4.9: Data-driven single electron (left) and muon (right) reconstruction (top) and trigger (bottom) efficiencies as a function of the position of the colliding bunch in the train. The data have been split into various pileup bins, as well as an inclusive measurement over the entire pileup range. The deviation measures the difference of each pileup bin with respect to the inclusive measurement. The error bars show statistical uncertainties only.

In both channels, the dependence of the single-lepton efficiencies on the position of the bunch in the train is extremely small, while the pileup dependence is at the percent level, as seen earlier. In the electron channel, the first bunch in the train shows both a higher trigger and reconstruction efficiency, relative to the rest of the bunches in the train. This is an approximately 2% effect, which could be a result of the first bunch having less out-of-time pileup, and hence having slightly better energy resolution compared to the other bunches in the train as the energy correction is calculated as an average over all bunches in the train. As this affects only the first bunch in the train however, and the effect itself is so small, the impact of neglecting this dependence in the efficiency calculation is negligible (the effect would be approximately 0.07% if propagated to the event-level efficiency, taking into account both electrons and the fraction of data effected). The remarkable stability across all bunch positions (in all pileup bins) shows that measuring the Z-counting efficiencies as a function of time/pileup sufficiently models the efficiencies dependence on the changing run conditions in the ATLAS detector, and as such no further bunch-dependencies are propagated in the analysis.

4.2.3 Monte Carlo correction factor

The event-level efficiencies determined in the previous section do not necessarily account for all possible efficiency losses. For example, the muon reconstruction efficiency does not consider the inner-detector track reconstruction efficiency, and the electron reconstruction efficiency does not account for the track-to-cluster matching efficiency or the electron charge mis-identification probability. Furthermore, the assumption that the two efficiencies can be factorised into single-lepton components could lead to a small bias, if the efficiencies of the two leptons are correlated. All of these effects can be estimated by measuring the true $Z \to \ell^+\ell^-$ reconstruction efficiency in Monte Carlo and comparing to that measured by the tag-and-probe procedure, also in Monte Carlo. The closure of this ratio shows how well the tag-and-probe efficiencies are probing the true efficiency, indicating the magnitude of all untracked efficiencies and potential biases, and is then applied to the data-driven efficiency estimate as an additional correction factor ($F^{\mathrm{MC}}_{Z\to\ell^+\ell^-}(\langle\mu\rangle)$),

$$F^{\mathrm{MC}}_{Z\to\ell^+\ell^-}(\langle\mu\rangle) = \frac{N^{\mathrm{reco,fiducial,MC}}_{Z\to\ell^+\ell^-}(\langle\mu\rangle)}{N^{\mathrm{true,nocut,MC}}_{Z\to\ell^+\ell^-}(\langle\mu\rangle)} \times \frac{1}{A^{\mathrm{MC}}_{Z\to\ell^+\ell^-} \cdot \varepsilon^{\mathrm{T\&P,MC}}_{Z\to\ell^+\ell^-}(\langle\mu\rangle)}. \tag{4.14}$$

An overview of all terms can be found in Table 4.5. All quantities are evaluated with Monte Carlo simulated events and, with the exception of $A^{\mathrm{MC}}_{Z\to\ell^+\ell^-}$, as a function of the pileup parameter $\langle\mu\rangle$. The simulated $Z/\gamma^* \to \ell^+\ell^-$ signal events used for this analysis are generated using Powheg [117, 118] (hard scattering) and Pythia8 [127] with AZNLO tune [128] (fragmentation and hadronisation). Simulated minimum-bias events, generated with Pythia 8.186 using the NNPDF2.3LO set of PDFs [42] and A3 tune [129], are overlaid on the hard-scattering event in order to model the effect of pileup. The signal events are generated with dilepton invariant masses of $m_{\ell^+\ell^-} > 60\,\mathrm{GeV}$; therefore, a fiducial acceptance factor ($A^{\mathrm{MC}}_{Z\to\ell^+\ell^-}$) must be applied in order for the fiducial volume of the generated events to match that of the data.

The fraction on the left-hand-side of Eq. 4.14 is the true acceptance times efficiency, meaning the total fraction of generated events which are lost due to the phase space and selection requirements in Table 4.2. The inclusion of the factor $A^{\mathrm{MC}}_{Z\to\ell^+\ell^-}$ on the right-hand-side is therefore necessary, in order to compensate for the acceptance effects and to determine only the non-closure of the efficiency determination. Since this factor is in the denominator of Eq. 4.14, and is then applied again in Eq. 4.3, the final luminosity measurement is insensitive to the measured $A^{\mathrm{MC}}_{Z\to\ell^+\ell^-}$ value, and the purpose of this factor is to ensure

Term	Meaning
$N^{\text{reco,fiducial,MC}}_{Z\to\ell^+\ell^-}(\langle\mu\rangle)$	number of reconstructed MC events ('reco') which pass the fiducial phase space ('fiducial') and event selection requirements outlined in Table 4.2
$N^{\text{true,nocut,MC}}_{Z\to\ell^+\ell^-}(\langle\mu\rangle)$	number of generated Z boson MC events ('true') without any selection requirements ('nocut')
$A^{\text{MC}}_{Z\to\ell^+\ell^-}$	fiducial acceptance, calculated using leptons originating from a true Z boson as described in Section 4.2.4
$\varepsilon^{\text{T\&P,MC}}_{Z\to\ell^+\ell^-}(\langle\mu\rangle)$	event-level tag-and-probe ('T&P') efficiency estimate using reconstructed MC events following the same procedure as outlined in Section 4.2.2

Table 4.5: Summary of all terms used in calculating Monte Carlo based efficiency correction factors.

the closure of the measured correction factors.

The factor $\varepsilon^{\text{T\&P,MC}}_{Z\to\ell^+\ell^-}(\langle\mu\rangle)$ is the event-level efficiency determined using reconstructed Monte Carlo events following the same procedure as outlined in Section 4.2.2. However, since each event contains a genuine generated $Z \to \ell^+\ell^-$ event, there is no background contamination due to jets misidentified as leptons, which is the primary background contribution to the reconstruction efficiency estimate. A small amount of background could be present due to non-prompt lepton production and overlaid pileup events, and so every reconstructed lepton is required to originate from one of the generated leptons in the $Z \to \ell^+\ell^-$ decay (truth-matching). The single-lepton trigger efficiency is calculated using Eq. 4.6, with the condition that all reconstructed leptons be trigger-matched, while the single-lepton reconstruction efficiency is determined using

$$\varepsilon^{\text{MC}}_{\text{reco},1\ell} = \frac{N^{\text{OS}}_{\text{pass}}}{N^{\text{OS}}_{\text{pass}} + N^{\text{OS}}_{\text{fail}}}. \tag{4.15}$$

where again all reconstructed leptons are required to be trigger matched. These single-lepton efficiencies are then combined in the same way as those in data, using Eq. 4.13. A comparison between the tag-and-probe efficiencies obtained in Monte Carlo and data can be found in Appendix A.

The event-level efficiency (multiplied by $A^{\text{MC}}_{Z\to\ell^+\ell^-}$) is then compared with the true acceptance times efficiency, as shown in Eq. 4.14. To calculate the true acceptance times efficiency, the full signal selection (Table 4.2) is applied to the reconstruction level simulated events, and the number of selected events inside the mass window counted. This is then divided by the total number of generated events with no fiducial or object selections applied, in order to measure the fraction of events lost due to all detector efficiency and acceptance effects. The resulting ratios are fitted with a second order polynomial as a function of $\langle\mu\rangle$, and the results can be seen in Figure 4.10.

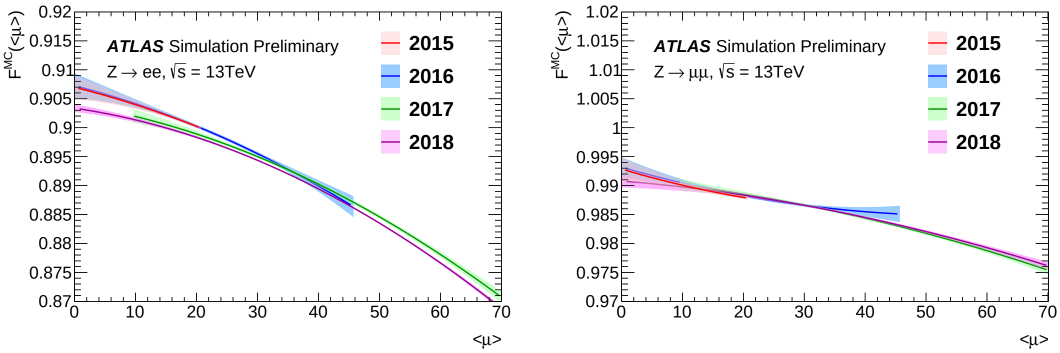

Figure 4.10: $Z \to e^+e^-$ (left) and $Z \to \mu^+\mu^-$ (right) correction factors used for each year of data (2015, 2016, 2017 and 2018) produced using the dedicated Monte Carlo campaigns.The lines show second-order polynomial fits to the correction factor for the corresponding $\langle\mu\rangle$ range per year, with bands indicating the statistical uncertainties. The behaviour of the fits for the 2016 samples, at the low and high ends of the pileup range, is due the limited MC statistics and affects only a very small fraction of the data. Source: [1], credit: **Harry Lyons**.

In order to effectively model the different conditions during each data-taking period, correction factors are derived for each period separately from Monte Carlo simulated events generated with similar pileup conditions to that of the data. The $Z \to \mu^+\mu^-$ correction factors are within 0.9% ($\langle\mu\rangle = 10$) to 2.5% ($\langle\mu\rangle = 70$) of unity over the pileup range at which the bulk of the data were recorded. As the ratio of the true and tag-and-probe efficiencies is close to one, the efficiency effects not tracked by the tag-and-probe method must be small. However, the difference between the true and tag-and-probe efficiencies increases with pileup, suggesting that with increasing pileup the tag-and-probe method is slightly over-estimating the efficiency.

The $Z \to e^+e^-$ correction factors are within 10% ($\langle\mu\rangle = 10$) to 13% ($\langle\mu\rangle = 70$) of unity. This suggests that the non-closure of the tag-and-probe efficiency estimate is approximately 10%, suggesting that there are more significant untracked efficiency components in the electron channel than in the muon channel. One contribution to this non-closure could be the track-cluster matching efficiency for electrons, as well as the charge misidentification probability, which is larger for electrons than muons. The pileup-dependence of the ratio is also slightly larger in the electron channel, around 3% across the entire range, although the effect in both channels is still relatively mild. The statistical uncertainty shown in Figure 4.10 is not propagated to the analysis. However, these uncertainties are extremely small, and are below 0.5% across the entire pileup range in both channels, with the bulk of the statistics falling into the pileup range with sub per-mille uncertainties.

4.2.4 Acceptance

The fraction of generated events inside the fiducial volume used in the analysis is known as the acceptance factor ($A^{\mathrm{MC}}_{Z\to\ell^+\ell^-}$), and is derived from $Z \to \ell^+\ell^-$ Monte Carlo. The only kinematic requirement of the generated events is that the invariant mass of the dilepton system be greater than 60 GeV, while the fiducial volume of the analysis requires two leptons with $p_{\mathrm{T}}^{\ell} > 27$ GeV, $|\eta| < 2.4$ (with the additional removal of the range $1.37 < |\eta^{\ell}| < 1.52$ for electrons) and $66 < m_{\ell^+\ell^-} < 116\,\mathrm{GeV}$. Therefore, the fraction of generated events outside this range must be calculated and accounted for, by dividing the number of events inside the fiducial volume ($N^{\mathrm{true,fiducial,MC}}_{Z\to\ell^+\ell-}$) by the total number of generated events ($N^{\mathrm{true,nocut,MC}}_{Z\to\ell^+\ell-}$),

$$A^{\mathrm{MC}}_{Z\to\ell^+\ell^-} = \frac{N^{\mathrm{true,fiducial,MC}}_{Z\to\ell^+\ell-}}{N^{\mathrm{true,nocut,MC}}_{Z\to\ell^+\ell-}}. \tag{4.16}$$

In the numerator, muons are selected *after* they have undergone QED final state radiation (FSR), since this is how they are reconstructed in the detector. Likewise, electrons are selected *after* QED FSR, but the energy of the radiated photons is added to that of the electron. All photons within a cone of $\Delta R = 0.1$ around the electron are added to the energy of the electron, since electron energy deposits are measured in the calorimeter, where the granularity is smaller than $\Delta R = 0.1$ and so the energy deposits of the electron and photons overlap. Table 4.6 gives the acceptance factors in the $Z \to e^+e^-$ and $Z \to \mu^+\mu^-$ channels.

$A^{\mathrm{MC}}_{Z\to e^+e^-}$	$A^{\mathrm{MC}}_{Z\to \mu^+\mu^-}$
0.2996 ± 0.0002	0.3326 ± 0.0002

Table 4.6: Fiducial acceptance values, $A^{\mathrm{MC}}_{Z\to\ell^+\ell^-}$, calculated for $Z \to e^+e^-$ and $Z \to \mu^+\mu^-$ decays using the corresponding MC signal samples. The uncertainties reflect the statistical uncertainty of the simulated data. Source: [1].

This factor is found in both Eq. 4.3 and Eq. 4.14, and therefore the final luminosity measurement is insensitive to the measured $A^{\mathrm{MC}}_{Z\to\ell^+\ell^-}$ value. However, it is an important factor in Eq. 4.14, as an incorrect value of $A^{\mathrm{MC}}_{Z\to\ell^+\ell^-}$ would have a large impact on the closure of the correction factors in Figure 4.10.

4.3 Results

Results will be presented for individual LHC fills (Section 4.3.1), as well as for the entire Run-2 dataset (Sections 4.3.2 to 4.3.6). To improve the statistical precision of the measurement over the course of a single LHC fill, the individual luminosity block values can be averaged over longer time periods. All time-dependent results shown in Section 4.3.2 are averaged over bunches of 20 successive luminosity blocks, weighting by the live-time of each individual luminosity block,

$$X(20LB) = \frac{\sum_{LB}^{LB+20} X(LB) \cdot t(LB)}{\sum_{LB}^{LB+20} t(LB)}, \tag{4.17}$$

where X is the Z-counting luminosity or single-lepton data-driven efficiency estimate. When calculating pileup-dependent averages, the same methodology is used to calculate the average efficiency/luminosity in each individual pileup bin,

$$X(\langle\mu\rangle) = \frac{\sum_{LB}^{N} X(\langle\mu\rangle, LB) \cdot t(LB)}{\sum_{LB}^{N} t(LB)}. \tag{4.18}$$

Luminosity blocks which do not pass the GRL requirements are not included in the averaging. Therefore, in the time-dependent averages, each bunch of LBs does not necessarily contain 20 entries, as some may have been rejected by the GRL.

Table 4.7 shows the average fractional uncertainty on the luminosity obtained in the electron and muon channels for each data-taking period of Run-2. The uncertainty is calculated by propagating the statistical uncertainties of the data-driven efficiency components, as well as the Poisson error on the number of reconstructed Z events. At present, no systematic uncertainties are considered. Values are presented for individual luminosity block measurements, as well as averaged over bunches of 20 LBs. As expected, the statistical precision improves by a factor of approximately $\sqrt{20}$ by averaging over successive bunches of 20 LBs. The statistical precision also improves over the course of Run 2, due to the increased instantaneous luminosity between 2015 and 2018.

	$\Delta\mathcal{L}_{Z\rightarrow\ell^+\ell^-}(LB)/\mathcal{L}_{Z\rightarrow\ell^+\ell^-}(LB)$ [%]		$\Delta\mathcal{L}_{Z\rightarrow\ell^+\ell^-}(20LB)/\mathcal{L}_{Z\rightarrow\ell^+\ell^-}(20LB)$ [%]	
Data-taking period	**Electron channel**	**Muon channel**	**Electron channel**	**Muon channel**
2015	17.7	14.6	4.6	3.5
2016	12.2	9.7	2.8	2.0
2017	10.9	8.8	2.5	1.9
2018	8.4	7.0	2.3	1.8

Table 4.7: Fractional uncertainty on the instantaneous luminosity determined in the electron and muon channels. This is calculated by taking an average of the fractional uncertainty in each individual luminosity block, as well as the combination of 20 successive luminosity blocks (Eq. 4.17), for each data-taking period in Run 2.

When comparing the Z-counting luminosity to the ATLAS baseline measurement [96], the absolute scale depends on the theoretically predicted cross-section, which is itself sensitive to the details of the proton structure function. Since the associated PDF uncertainties are approximately 3–4%, Z-counting cannot yet provide a competitive measurement of the absolute luminosity, as the uncertainty of the baseline ATLAS measurement is 1.7% [96]. However, the relative stability can be monitored by normalising the integrated Z-counting and baseline ATLAS luminosities to the same value over some time period. This can be done over the course of a single LHC fill (Section 4.3.1), or over the course of the entire data-taking period (Sections 4.3.2 to 4.3.5). Normalising the luminosity in this way ensures that the absolute scale of the measurements is the same, removing the dependence on the theoretical cross-section, and the relative stability can be monitored by measuring the spread of the ratio around unity. The spread is estimated by the 68^{th} percentile of all points (neglecting their statistical uncertainties) closest to unity (or the mean in the case of $\mathcal{L}_{Z\to e^+e^-}/\mathcal{L}_{Z\to\mu^+\mu^-}$).

In contrast, the $Z \to e^+e^-$ to $Z \to \mu^+\mu^-$ luminosity ratio is insensitive to the cross-section prediction, and by measuring the absolute value of this ratio, the efficacy of the of the data-driven efficiency determination and residual Monte Carlo correction factors can be quantified. A ratio near unity suggests that the corrections are working well, which is a non-trivial statement since both the methodology and magnitude of the corrections in the two channels are vastly different. The ratio of the $Z \to e^+e^-$ and $Z \to \mu^+\mu^-$ luminosities can also provide insight on trends observed in the comparison to the baseline ATLAS measurement. If the ratio of $\mathcal{L}_{Z\to e^+e^-}/\mathcal{L}_{Z\to\mu^+\mu^-}$ is flat, but $\mathcal{L}_Z/\mathcal{L}_{ATLAS}$ is not, this suggests that there are some time (pileup) dependent effects in the baseline ATLAS luminosity determination.

4.3.1 Z-counting results in typical LHC fills

Z-counting luminosity results are presented for an illustrative fill from each data-taking period. As discussed in the previous section, the obtained values are averaged of groups of 20 luminosity blocks or per pileup bin. An overview of the runs in question can be found in Table 4.8.

Data-taking period	**LHC fill**	**Date**	**Luminosity** $[\text{pb}^{-1}]$	**Average pileup** $\langle\mu\rangle$
2015	4485	11/10/15	163.5	15.1
2016	4985	03/06/16	313.0	21.8
2017	6362	04/11/17	725.3	39.9
2018	7144	09/09/18	416.8	37.5

Table 4.8: Information for the selected LHC fills used to illustrate the Z-counting methodology for each of the Run-2 data-taking periods [96].

Figure 4.11 shows the ratio of the luminosities determined in the electron and muon channels, with the corresponding mean and spread values given in Table 4.9. Since the sensitivity to the theoretical cross section cancels in this ratio, the absolute value can be monitored and the agreement with unity is physically meaningful. The mean is stable across all the fills, at approximately 0.990, and within each fill the spread ranges from approximately 4% (2015) to 2% (2018), indicating that the method is extremely stable over the course of a single LHC fill as well as between LHC fills. Such good agreement between the two channels suggests that the remaining non-closure of the efficiency corrections must be small (within around 1%), which, as mentioned, is a non-trivial result given the distinct methodology used in the two channels.

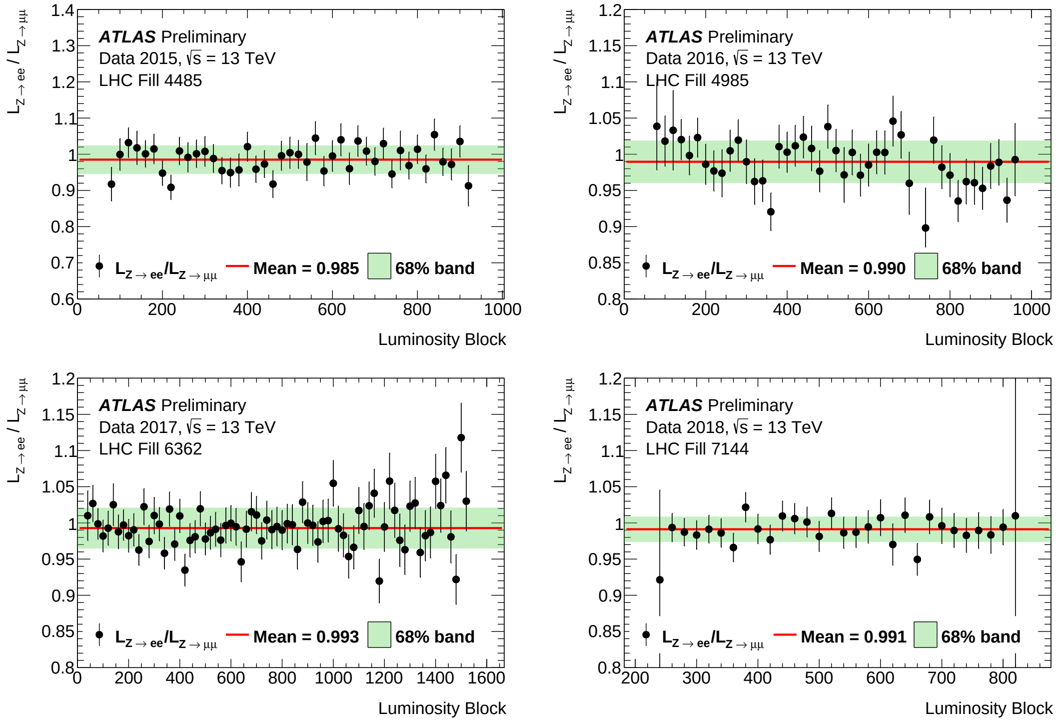

Figure 4.11: Time-dependent ratio of the instantaneous luminosities determined from $Z \to e^+e^-$ and $Z \to \mu^+\mu^-$ counting for an example LHC fill in each data-taking year. No normalisation factor is applied in the ratio, and hence the agreement with unity is a reflection of the absolute agreement between the channels.

		$\mathcal{L}_{Z\to e^+e^-}/\mathcal{L}_{Z\to\mu^+\mu^-}$	
Data-taking period	**LHC fill**	**Mean**	**Spread**
2015	4485	0.985	0.039
2016	4985	0.990	0.029
2017	6362	0.993	0.027
2018	7144	0.991	0.018

Table 4.9: Summary of the mean and spread (68% of all points centred around the mean) of the time-dependent $\mathcal{L}_{Z\to e^+e^-}/\mathcal{L}_{Z\to\mu^+\mu^-}$ ratio for each of the LHC fills listed in Table 4.8.

Figures 4.12 and 4.13 show a comparison between the normalised Z-counting and ATLAS baseline luminosities as a function of time and pileup respectively, with the corresponding spread values given in Table 4.10. Over the course of a single LHC fill, the stability of the baseline measurement can be monitored by normalising the integrated Z-counting luminosity to the baseline ATLAS luminosity and monitoring the spread around unity. In addition to this, time dependent trends can also be observed over the course of a single fill. For each lepton flavour, both as a function of time and pileup, the Z-counting luminosity shows good a stability with respect to the baseline ATLAS measurement. The time-dependent (pileup-dependent) ratios have spreads ranging from 1.5% to 2.9% (0.9% to 1.8%) for these example LHC fills.

		Time-dependence		***Pileup-dependence***	
Data-taking period	**LHC fill**	$\mathcal{L}_{Z\to e^+e^-}/\mathcal{L}_{ATLAS}$	$\mathcal{L}_{Z\to \mu^+\mu^-}/\mathcal{L}_{ATLAS}$	$\mathcal{L}_{Z\to e^+e^-}/\mathcal{L}_{ATLAS}$	$\mathcal{L}_{Z\to \mu^+\mu^-}/\mathcal{L}_{ATLAS}$
2015	4485	0.025	0.029	0.012	0.015
2016	4985	0.028	0.018	0.015	0.009
2017	6362	0.021	0.017	0.017	0.014
2018	7144	0.015	0.017	0.015	0.018

Table 4.10: Summary of the spread (68% of all points centred around unity) of the $\mathcal{L}_{Z\to e^+e^-}/\mathcal{L}_{ATLAS}$ and $\mathcal{L}_{Z\to \mu^+\mu^-}/\mathcal{L}_{ATLAS}$ ratio, as a function of time and pileup, for each of the LHC fills listed in Table 4.8.

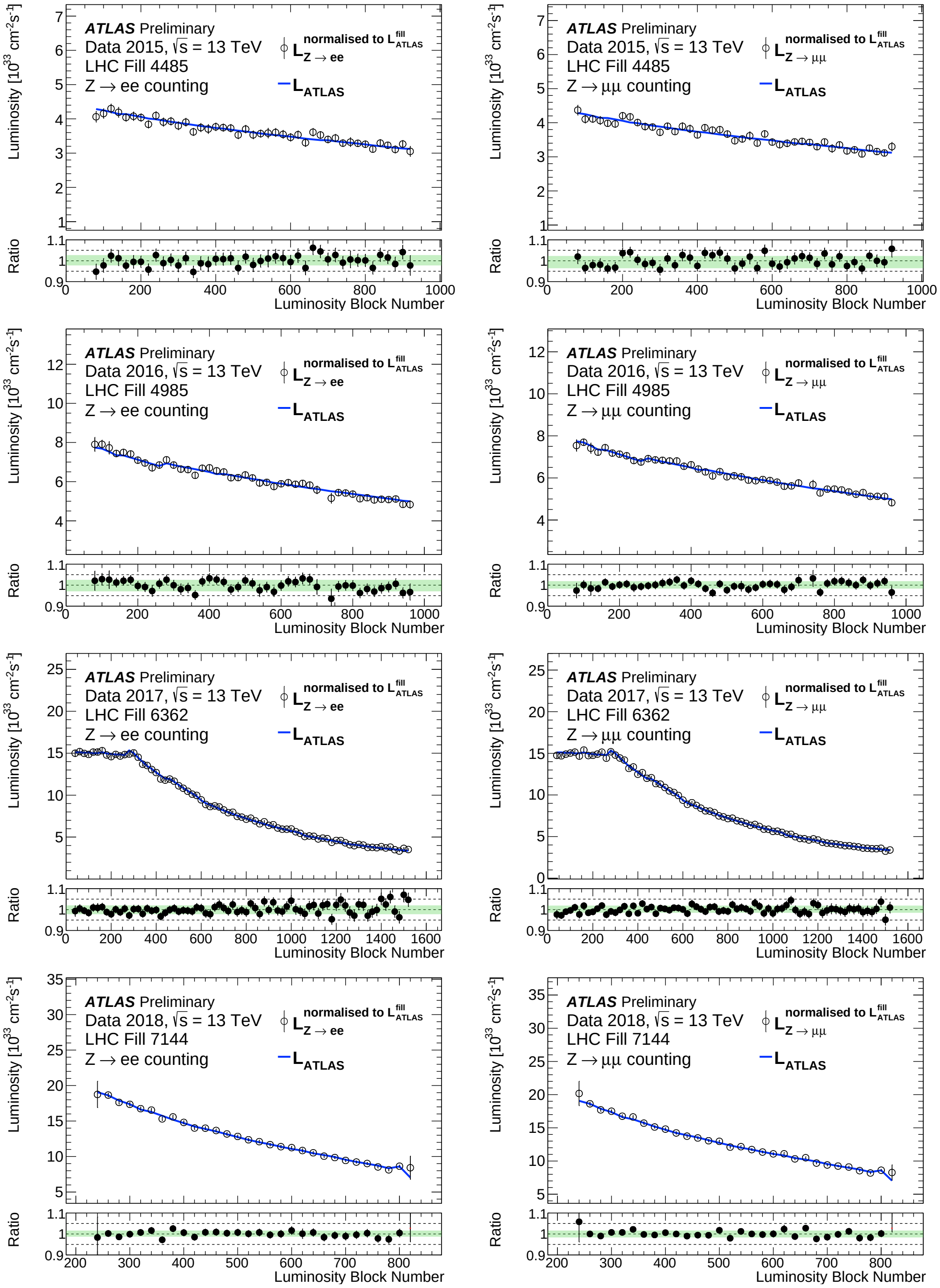

Figure 4.12: Time-dependence of the instantaneous luminosity determined from Z-counting (open circles) and the ATLAS-preferred luminosity measurement (blue line), as well as their ratio (full circles) for an example LHC fill in each data-taking year. The fill-integrated Z-counting luminosity is normalised to the corresponding baseline ATLAS luminosity for the electron (left) and muon channel (right) separately.

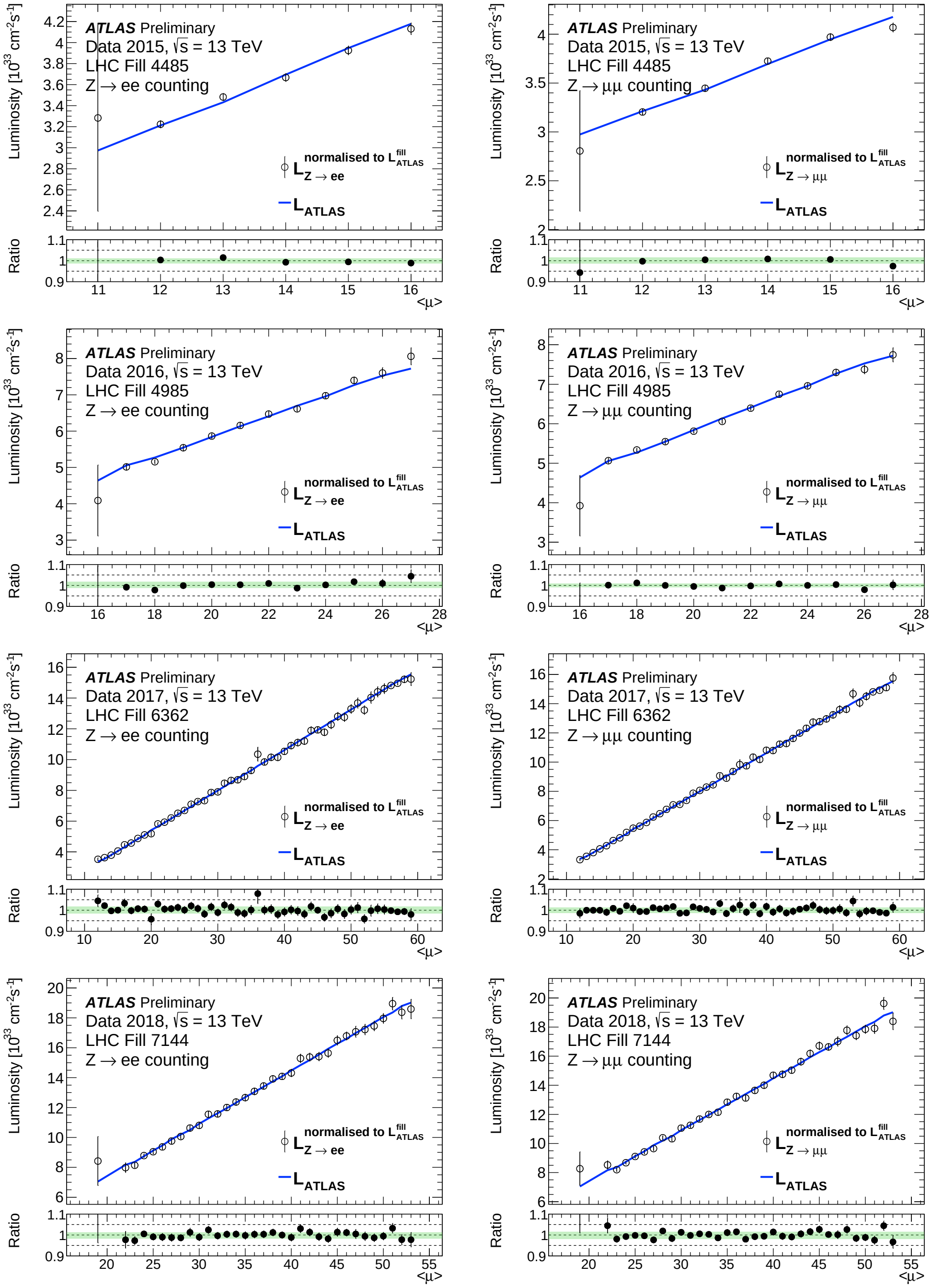

Figure 4.13: Pileup-dependence of the instantaneous luminosity determined from Z-counting (open circles) and the ATLAS-preferred luminosity measurement (blue line), as well as their ratio (full circles). The x-axis represents the bunch-averaged pileup parameter $\langle \mu \rangle$, defined as the mean number of inelastic pp interactions per crossing and is inferred from the baseline ATLAS luminosity The fill-integrated Z-counting luminosity is normalised to the corresponding baseline ATLAS luminosity for the electron (left) and muon channel (right) separately.

4.3.2 Time-dependence of $\mathcal{L}_{Z\rightarrow e^+e^-}/\mathcal{L}_{Z\rightarrow \mu^+\mu^-}$

Figure 4.14 shows the ratio of the integrated $\mathcal{L}_{Z\rightarrow e^+e^-}$ and $\mathcal{L}_{Z\rightarrow \mu^+\mu^-}$ luminosities for each LHC fill of Run 2. The data is separated into the constituent data-taking periods (2015 – 2018), and plotted as a function of the time at which the data were recorded (the start of the fill). Runs less than 40 minutes in length are excluded, as there are not enough reconstructed Z events to provide a statistically precise measurement. Monitoring the stability of this ratio over the whole Run-2 period provides a powerful cross check of the data-driven efficiency determination and the internal consistency of the Z-counting method. The two channels agree to within approximately 0.8% of unity (the mean ratio is around 0.992), similar to the values seen in the individual LHC fills in Figure 4.11, which, as discussed in Section 4.3.1, suggests that the time-dependent efficiency corrections are accurately modelling the detector conditions. This ratio is extremely stable throughout Run-2, and has a spread ranging from 1% (2015) to 0.6% (2018), suggesting there are no discernible time-dependent effects in either channel.

Figure 4.15 shows the same ratio, however, for the entire Run-2 dataset rather than each data-taking period separately. A consistent mean ratio of 0.992 is obtained over the full Run-2 period, with a spread of 0.6%. The extremely stable ratio clearly demonstrates that there are no time-dependent effects, both within each data-taking period as well as between successive periods. This value is similar to the long-term-stability error associated with the ATLAS baseline luminosity (0.6%), calculated by comparing 5 reference luminosity measurements in reference fills in each data-taking period. Table 4.11 summarises the results (mean and spread) for each of these comparisons, both as a function of time and pileup (Section 4.3.3).

	$\mathcal{L}_{Z\rightarrow e^+e^-}/\mathcal{L}_{Z\rightarrow \mu^+\mu^-}$			
	Time dependence		**Pileup dependence**	
Data-taking period	Mean	Spread	Mean	Spread
2015	0.993	0.011	0.9934	0.0066
2016	0.992	0.007	0.9924	0.0017
2017	0.993	0.005	0.9926	0.0027
2018	0.992	0.004	0.9918	0.0018
Run 2	0.992	0.006	0.9923	0.0015

Table 4.11: Summary of the mean and spread (68% of all points centred around the mean) of the $\mathcal{L}_{Z\rightarrow e^+e^-}/\mathcal{L}_{Z\rightarrow \mu^+\mu^-}$ ratio for each of the Run-2 data-taking periods, and for the full dataset as a function of time and pileup.

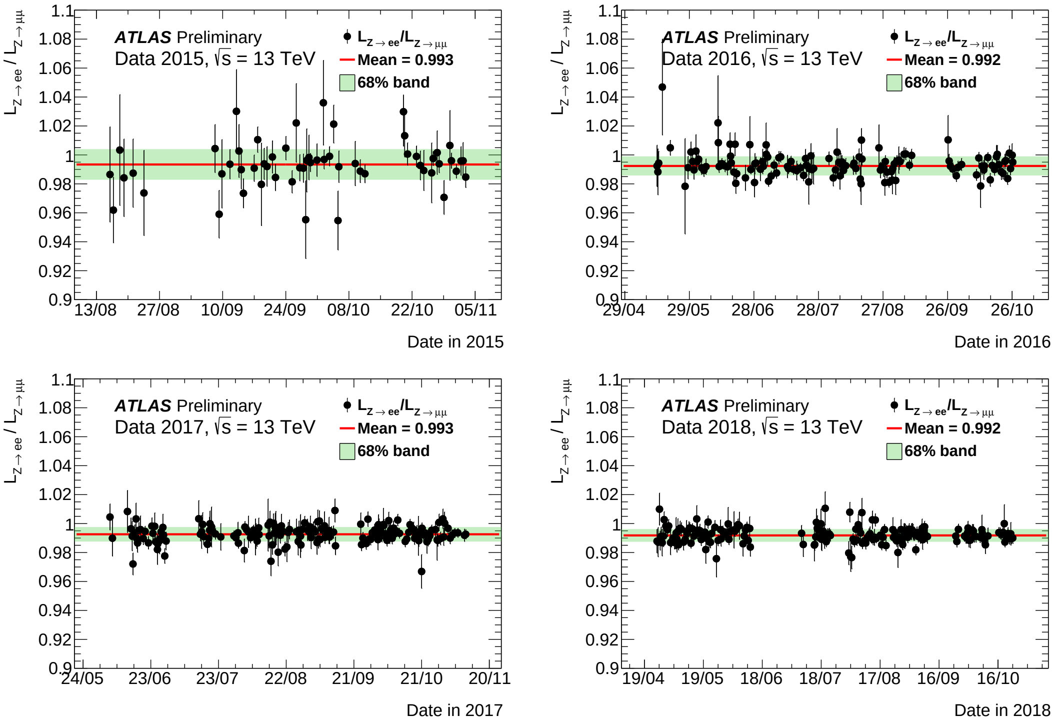

Figure 4.14: Ratio of the integrated luminosities obtained from the $Z \to e^+e^-$ and $Z \to \mu^+\mu^-$ channels per LHC fill ($\mathcal{L}_{Z\to e^+e^-}/\mathcal{L}_{Z\to\mu^+\mu^-}$) in each data-taking period. Only ATLAS runs with a minimum length of 40 minutes are included and error bars show the statistical uncertainties only. The red lines indicate the mean, and the green bands contain 68% of all points centred around the mean (Table 4.11).

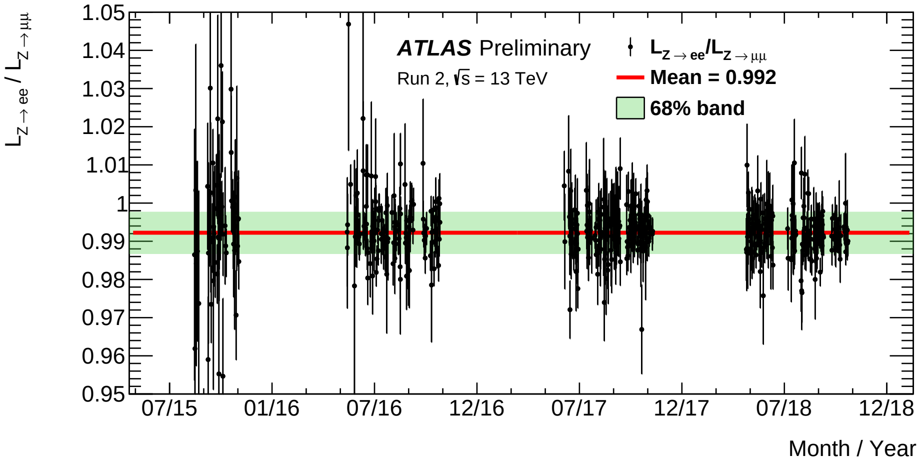

Figure 4.15: Ratio of the integrated luminosities obtained from the $Z \to e^+e^-$ and $Z \to \mu^+\mu^-$ channels per LHC fill ($\mathcal{L}_{Z\to e^+e^-}/\mathcal{L}_{Z\to\mu^+\mu^-}$) for the whole Run-2 data-taking period. Only ATLAS runs with a minimum length of 40 minutes are included and error bars show the statistical uncertainties only. The red line indicates the mean, and the green band contain 68% of all points centred around the mean (Table 4.11).

4.3.3 Pileup-dependence of $\mathcal{L}_{Z\rightarrow e^+e^-}/\mathcal{L}_{Z\rightarrow\mu^+\mu^-}$

Similar to the fill-integrated luminosities shown in Section 4.3.2, the integrated $Z \rightarrow e^+e^-$ and $Z \rightarrow \mu^+\mu^-$ luminosities can be calculated in bins of $\langle\mu\rangle$ and compared. The relative $\langle\mu\rangle$-dependence of the electron and muon channel luminosities is presented in Figure 4.16 for each data-taking period of Run 2. The mean ratios are identical (to 3 s.f.) to those in Figure 4.14, while the spread per data-taking period is significantly smaller; the $\langle\mu\rangle$-dependent spread of the $\mathcal{L}_{Z\rightarrow e^+e^-}/\mathcal{L}_{Z\rightarrow\mu^+\mu^-}$ ratio ranges from 0.66% (2015) to 0.18% (2018). Figure 4.17 shows the ratio of the electron and muon channel luminosities for the whole of Run 2, which also has a mean value of 0.992, and a spread of 0.15%. For each year separately, as well as for the full Run-2 combination, the $\mathcal{L}_{Z\rightarrow e^+e^-}/\mathcal{L}_{Z\rightarrow\mu^+\mu^-}$ ratio exhibits no significant pileup dependence, further demonstrating the robustness of the method against the changing LHC beam conditions.

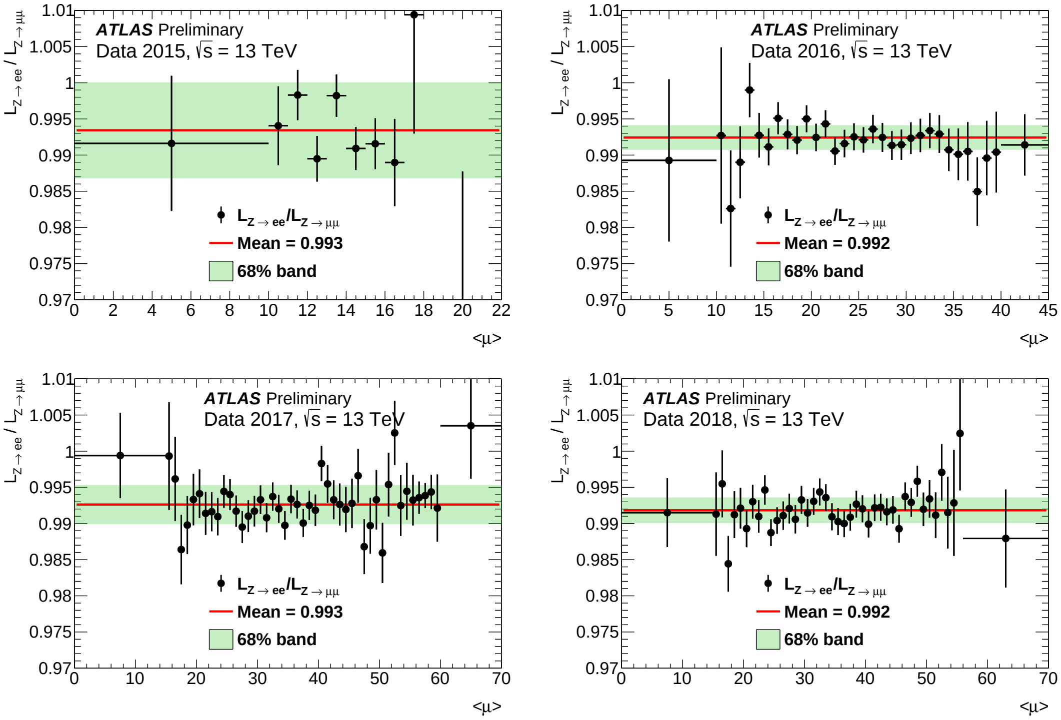

Figure 4.16: Ratio of the integrated luminosities obtained from the $Z \rightarrow e^+e^-$ and $Z \rightarrow \mu^+\mu^-$ channels ($\mathcal{L}_{Z\rightarrow e^+e^-}/\mathcal{L}_{Z\rightarrow\mu^+\mu^-}$) in each data-taking period. The x-axis represents the bunch-averaged pileup parameter $\langle\mu\rangle$, defined as the mean number of inelastic pp interactions per crossing and is inferred from the baseline ATLAS luminosity on an LB-by-LB basis [96]. The red lines indicate the mean, and the green bands contain 68% of all points centred around the mean (Table 4.11).

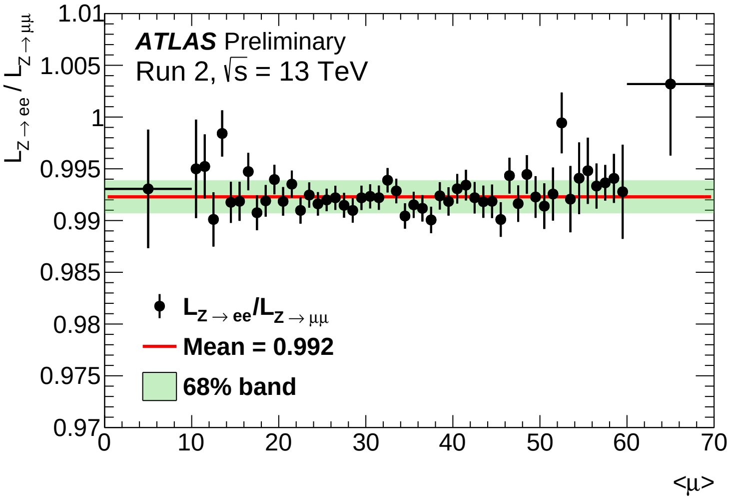

Figure 4.17: Ratio of the integrated luminosities obtained from the $Z \rightarrow e^+e^-$ and $Z \rightarrow \mu^+\mu^-$ channels ($\mathcal{L}_{Z\rightarrow e^+e^-}/\mathcal{L}_{Z\rightarrow\mu^+\mu^-}$) for the full Run-2 data-taking period. The x-axis represents the bunch-averaged pileup parameter $\langle\mu\rangle$, defined as the mean number of inelastic pp interactions per crossing and is inferred from the baseline ATLAS luminosity on an LB-by-LB basis [96]. The red lines indicate the mean, and the green bands contain 68% of all points centred around the mean (Table 4.11).

4.3.4 Time-dependence of $\mathcal{L}_Z/\mathcal{L}_{ATLAS}$

The ratio of the normalised Z-counting and baseline ATLAS luminosities can be used to study their relative stability over time and with respect to pileup (Section 4.3.5). To monitor the stability, and not the agreement between the absolute scale of the two measurements, the Z-counting luminosity is normalised to the baseline ATLAS measurement. This is done per data-taking period and lepton flavour separately, by normalising the integrated Z-counting luminosity to the baseline ATLAS luminosity of that period, with the resulting comparison presented in Figure 4.18. The relative stability of the two measurements is quantified by calculating the spread of their ratio around unity, ranging from approximately 0.8% (2015) to 0.4% in (2018), as shown in Table 4.12. The statistical precision of the method also improves over the course of Run 2, due to increasing instantaneous luminosity delivered to the detector.

The year-to-year stability of the ATLAS luminosity scale can be monitored by comparing the normalised Z-counting and baseline ATLAS luminosities over the full Run-2 period (Figure 4.19). Rather than normalising each data-taking period separately, the full Run-2 integrated Z-counting luminosity is normalised to the full Run-2 baseline ATLAS luminosity, and deviations from unity show the difference in scale between the years. Since the $\mathcal{L}_{Z\rightarrow e^+e^-}/\mathcal{L}_{Z\rightarrow\mu^+\mu^-}$ ratio is stable over the full Run-2 period (Figure 4.15), these deviations can be attributed to the absolute scale of the baseline ATLAS luminosity, determined via van der Meer scan and calibration-transfer procedures [96].

Both the $Z \rightarrow e^+e^-$ and $Z \rightarrow \mu^+\mu^-$ channels show the same trends, with deviations from unity of

-0.4% in 2015, $+0.6\%$ in 2016, $+0.2\%$ in 2017, and -0.5% in 2018 (calculated by taking the difference between the mean and unity in each data-taking period separately). The size of these deviations is within the uncorrelated year-by-year uncertainties that affect the absolute scale of the baseline ATLAS luminosity (1.3% for 2015/2016, 1.3% for 2017, and 1.0% for 2018 [96]). The overall spread of this ratio is 0.8% in both channels (Table 4.12). A prominent trend is seen in the 2016 dataset, showing a slope in both the $Z \to e^+e^-$ and $Z \to \mu^+\mu^-$ channels. Preliminary studies using an updated vdM scan calibration suggest that this slope is due to residual pileup dependencies in the baseline ATLAS luminosity.

The statistical power of the Z-counting method can be improved by combining the statistics of both channels, by calculating the arithmetic mean of the $Z \to e^+e^-$ and $Z \to \mu^+\mu^-$ luminosity values for each individual luminosity block. Figure 4.20 shows the ratio of the normalised, combined $\mathcal{L}_{Z\to\ell^+\ell^-}$ and baseline ATLAS luminosity values over the full Run-2 period. The same time dependencies as seen in Figure 4.19 are observed, with improved resolution as a result of the better statistical precision (although the spread around unity is the same at 0.8%). These results suggest that monitoring the year-to-year variations of the relative Z-counting and baseline ATLAS luminosities could contribute to an improved characterisation of the systematic uncertainties affecting the baseline ATLAS luminosity.

	Time dependence vs. $\mathcal{L}_{ATLAS}$			**Pileup dependence vs. $\mathcal{L}_{ATLAS}$**		
Data-taking period	$\mathcal{L}_{Z\to e^+e^-}$	$\mathcal{L}_{Z\to\mu^+\mu^-}$	$\mathcal{L}_{Z\to\ell^+\ell^-}$	$\mathcal{L}_{Z\to e^+e^-}$	$\mathcal{L}_{Z\to\mu^+\mu^-}$	$\mathcal{L}_{Z\to\ell^+\ell^-}$
2015	0.008	0.008	0.007	0.0040	0.0035	0.0040
2016	0.006	0.006	0.005	0.0028	0.0022	0.0024
2017	0.005	0.005	0.004	0.0021	0.0022	0.0017
2018	0.005	0.004	0.004	0.0014	0.0011	0.0011
Run 2	0.008	0.008	0.008	–	–	–

Table 4.12: Summary of the spread (68% of all points centred around unity) of the $\mathcal{L}_{Z\to e^+e^-}/\mathcal{L}_{ATLAS}$, $\mathcal{L}_{Z\to\mu^+\mu^-}/\mathcal{L}_{ATLAS}$ and $\mathcal{L}_{Z\to\ell^+\ell^-}/\mathcal{L}_{ATLAS}$ ratio for each of the Run-2 data-taking periods as a function of time and pileup, and as a function of time for the full Run-2 dataset.

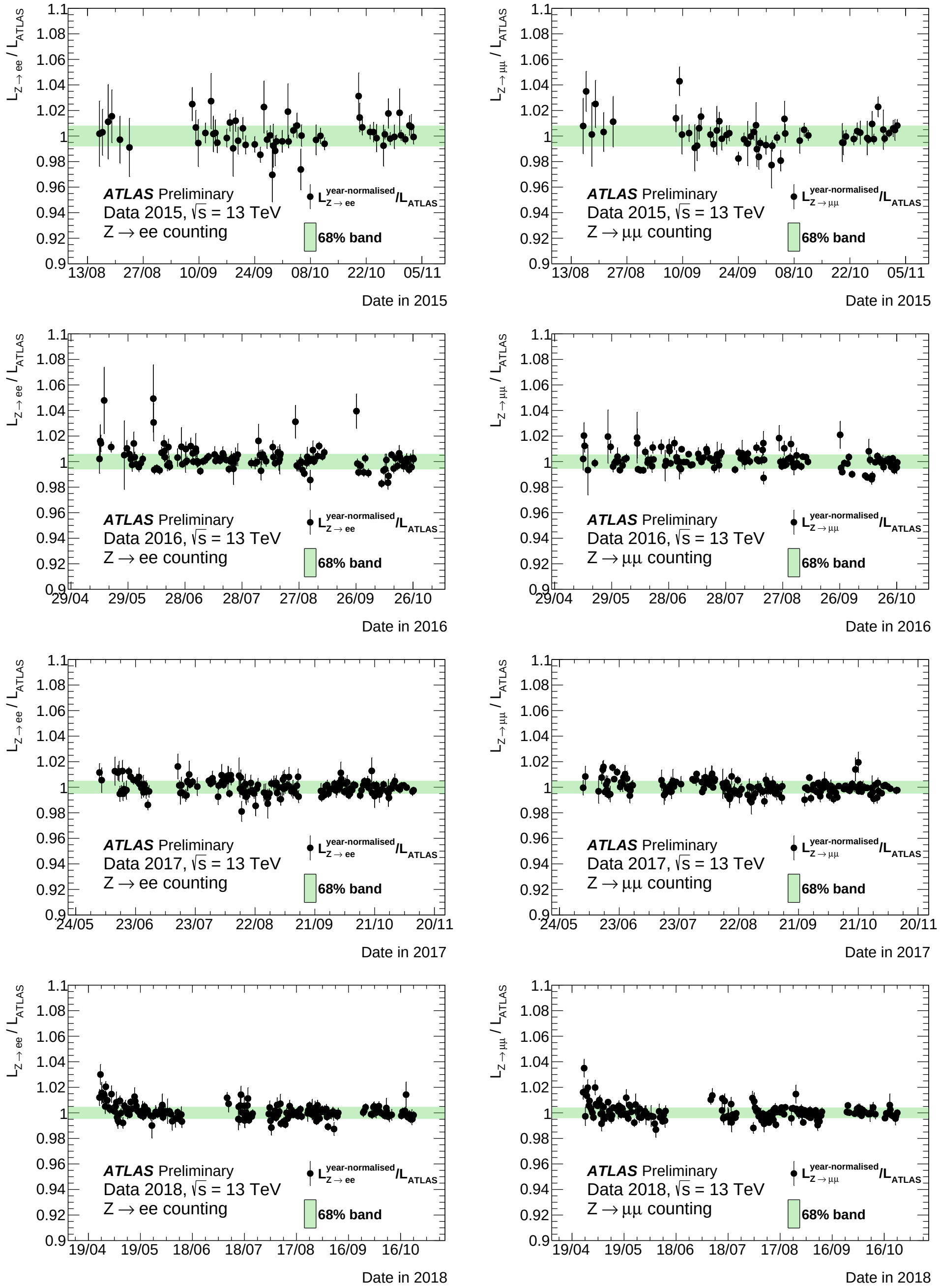

Figure 4.18: Ratio of the integrated Z-counting and baseline ATLAS luminosities per LHC fill taken from pp collisions at $\sqrt{s} = 13$ TeV in 2015 (1$^{\text{st}}$ row), 2016 (2$^{\text{nd}}$ row), 2017 (3$^{\text{rd}}$ row) and 2018 (4$^{\text{th}}$ row) for the $Z \to e^+e^-$ (left) and the $Z \to \mu^+\mu^-$ (right) channels. The Z-counting luminosity is normalised to the integrated baseline ATLAS luminosity per data-taking period [96]. The x-axis represents the date when the fill started, and only ATLAS runs with a minimum length of 40 minutes are included. The error bars show statistical uncertainties only, and the green bands contain 68% of all points centred around the mean.

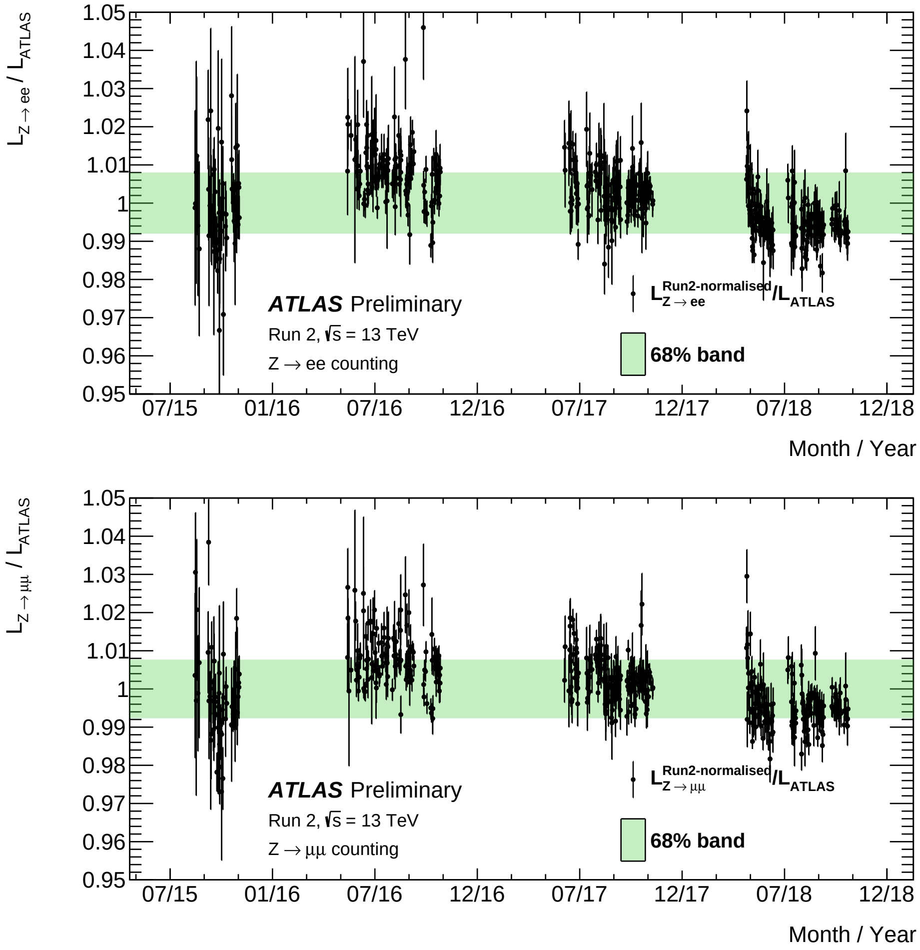

Figure 4.19: Ratio of the integrated Z-counting and baseline ATLAS luminosities per LHC fill taken from pp collisions at $\sqrt{s} = 13$ TeV for the full Run-2 data taking period for the $Z \to e^+e^-$ (upper plot) and the $Z \to \mu^+\mu^-$ (lower plot) channels. The Z-counting luminosity is normalised to the baseline ATLAS luminosity integrated over the Run-2 data-taking period [96]. The x-axis represents the date when the fill started, and only ATLAS runs with a minimum length of 40 minutes are included. The error bars show statistical uncertainties only, and the green bands contain 68% of all points centred around the mean.

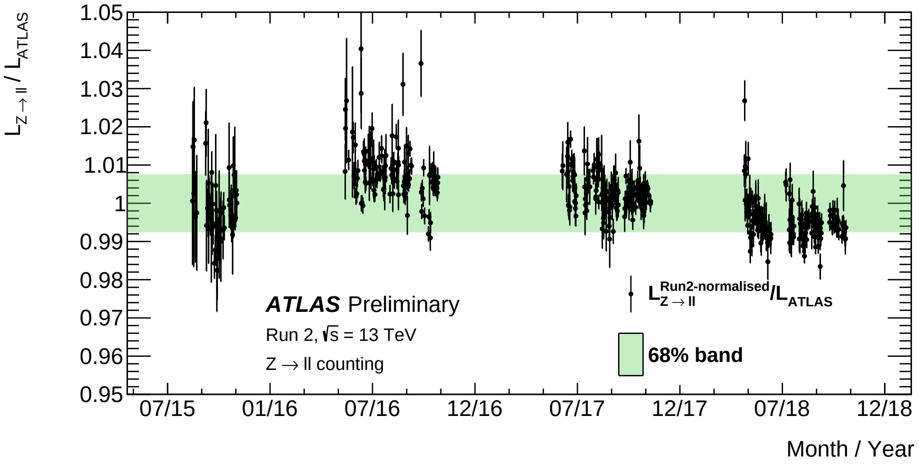

Figure 4.20: Ratio of the integrated, combined Z-counting and baseline ATLAS luminosities per LHC fill taken from pp collisions at $\sqrt{s} = 13$ TeV for the full Run-2 data-taking period. The combined Z-counting luminosity is normalised to the baseline ATLAS luminosity integrated over the Run-2 data-taking period [96]. The x-axis represents the date when the fill started, and only ATLAS runs with a minimum length of 40 minutes are included. The error bars show statistical uncertainties only, and the green bands contain 68% of all points centred around the mean.

4.3.5 Pileup-dependence of $\mathcal{L}_Z/\mathcal{L}_{ATLAS}$

The baseline ATLAS luminosity detector (LUCID) suffers from significant non-linearity with respect to $\langle\mu\rangle$, requiring a correction derived from other luminosity monitoring algorithms [96]. This correction can be as large as 10% at an $\langle\mu\rangle$ of 50. In contrast, the Z-counting data-driven efficiencies and Monte Carlo non-closure corrections are determined as a function of pileup (or time), which gives the method extremely good stability with respect to the changing LHC beam conditions. Figure 4.21 shows the normalised ratio of the Z-counting and baseline ATLAS luminosities for each lepton flavour and data-taking period as a function of pileup, with the combination ($\mathcal{L}_{Z\rightarrow\ell^+\ell^-}$) shown in Figure 4.22. The spread around unity ranges from approximately 0.4% (2015) to 0.1% (2018) (Table 4.12) which is approximately a factor of two to three times smaller than the corresponding time-dependent values.

Some small trends are observed in both channels, as well as their combination; for example in the low-pileup regime in 2016 and the high-pileup regime in 2016. Such trends were not observed in the comparison between the electron and muon channel Z-counting luminosities (Figure 4.17), which is independent of the baseline ATLAS luminosity measurement. This suggests that there could be some $\langle\mu\rangle$-dependent effects in the baseline ATLAS luminosity determination, however, these trends could be a result of residual time-dependencies. Since the $\langle\mu\rangle$ distribution is not uniform within each data-taking period, trends Figures 4.21 and 4.22 could in principle reflect those of Figures 4.18 and 4.20.

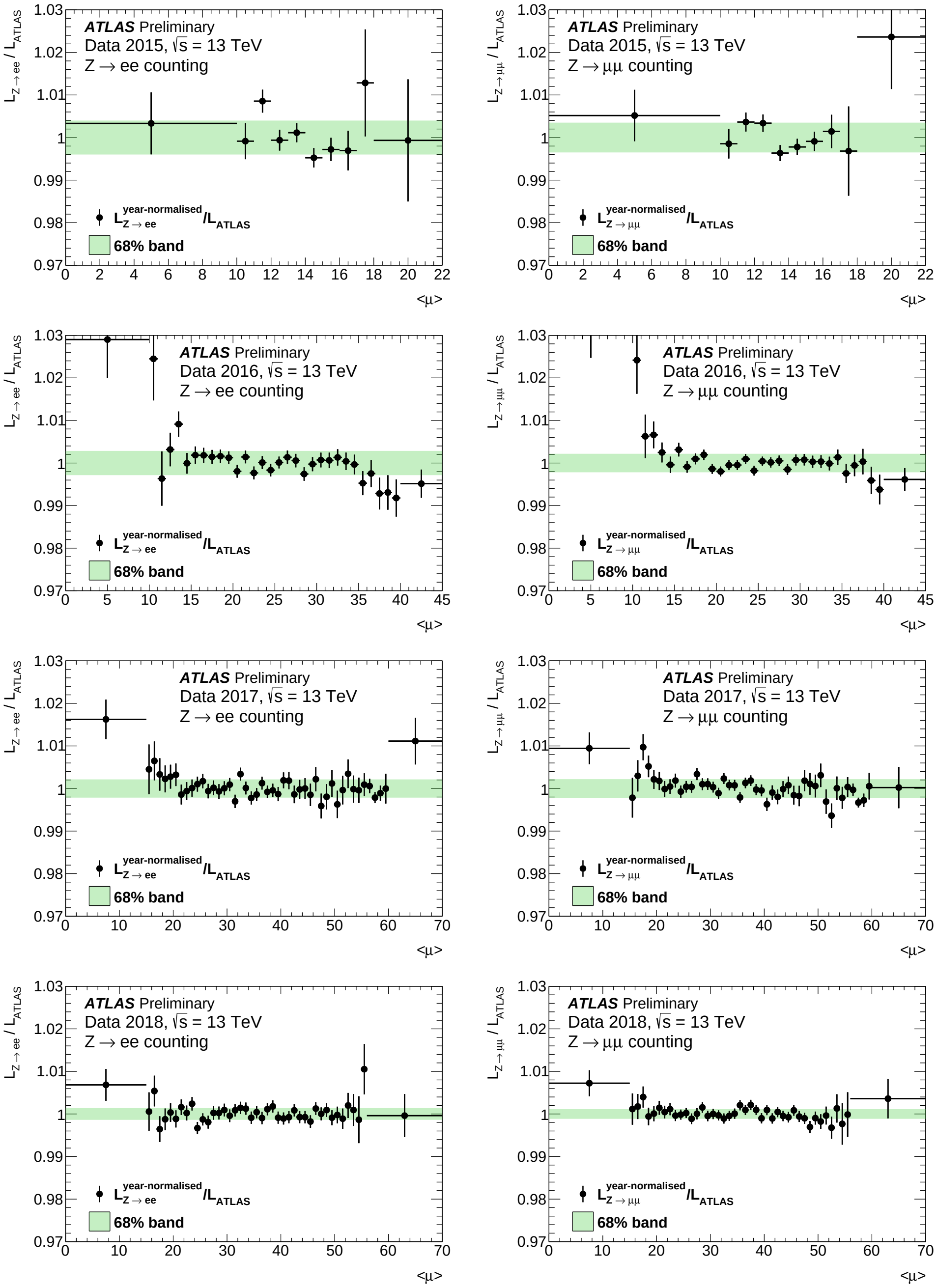

Figure 4.21: Ratio of the integrated Z-counting, $Z \to e^+e^-$ (left) and $Z \to \mu^+\mu^-$ (right), and baseline ATLAS luminosities for 2015 (1st row), 2016 (2nd row), 2017 (3rd row) and 2018 (4th row) ATLAS data from pp collisions at $\sqrt{s} = 13$ TeV. The x-axis represents the bunch-averaged pileup parameter $\langle\mu\rangle$, defined as the mean number of inelastic pp interactions per crossing and is inferred from the baseline ATLAS luminosity on an LB-by-LB basis. The Z-counting luminosity is normalised to the integrated baseline ATLAS luminosity per data-taking period. The error bars show statistical uncertainties only, and the green bands contain 68% of all points centred around the mean.

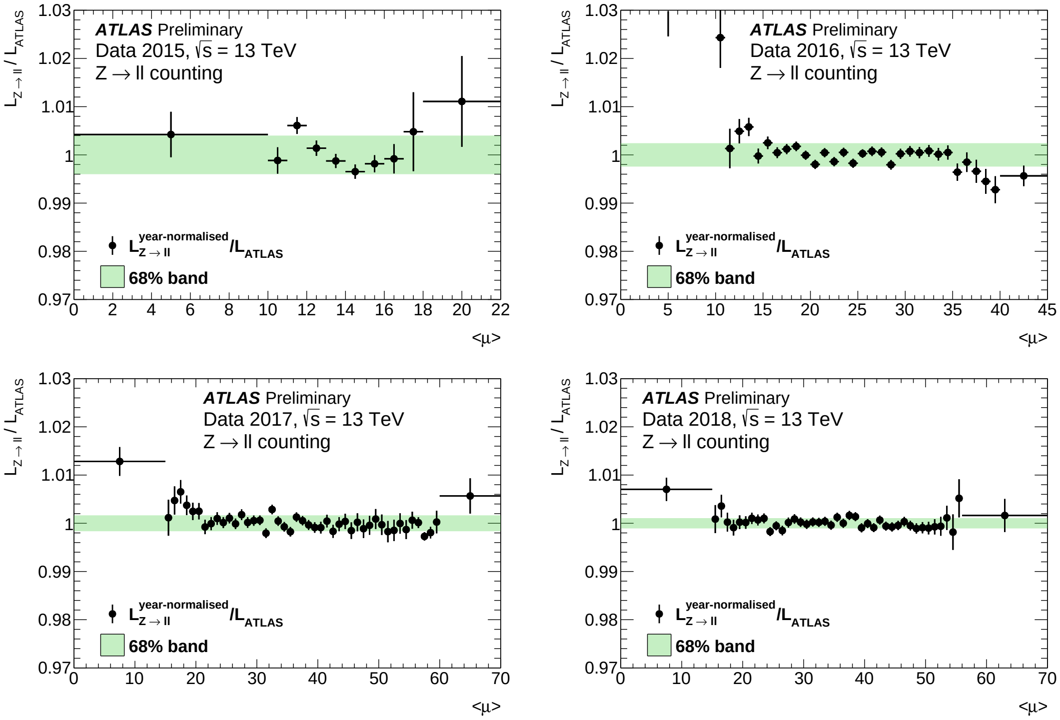

Figure 4.22: Ratio of the integrated $Z \to \ell^+\ell^-$ and baseline ATLAS luminosities in each data-taking period. The x-axis represents the bunch-averaged pileup parameter $\langle\mu\rangle$, defined as the mean number of inelastic pp interactions per crossing and is inferred from the baseline ATLAS luminosity on an LB-by-LB basis. The Z-counting luminosity is normalised to the integrated baseline ATLAS luminosity per data-taking period. The error bars show statistical uncertainties only, and the green bands contain 68% of all points centred around the mean.

4.3.6 Time-dependence of $\mathcal{L}_{Z\to\ell^+\ell^-}/\mathcal{L}_{\mathrm{track-counting}}$

An important alternative luminosity measurement can be obtained by counting the number of tracks reconstructed in the inner detector, known as the track-counting method. This method uses the fact that the number of charged particles produced in an inelastic collision (reconstructed as tracks in the ID), is proportional to the average number of inelastic interactions per bunch crossing. Tracks candidates are required to have $p_{\mathrm{T}} > 900$ MeV, $\eta < 1.0$ and at least nine hits in the ID. However, not all inelastic interactions are measured by the detector, only some fraction of them. This is known as the number of *visible* interactions. A measurement of the average number of visible inelastic interactions per bunch crossing ($\langle\mu\rangle_{\mathrm{vis}}^{\mathrm{track-counting}}$) can be obtained by measuring the mean number of reconstructed tracks per luminosity block.

The track-counting luminosity is obtained as follows. The number of visible inelastic interactions is multiplied by the revolution frequency of protons in the LHC (f_{rev}) and the number of filled proton bunches (n_B), and then divided by the visible cross section, σ_{vis}, as measured using the van der Meer scan procedure [130, 131],

$$\mathcal{L}_{\mathrm{track-counting}} = \frac{\langle\mu\rangle_{\mathrm{vis}}^{\mathrm{track-counting}} \cdot f_{\mathrm{rev}} \cdot n_B}{\sigma_{\mathrm{vis}}}. \tag{4.19}$$

Figure 4.23 shows the time-dependent ratio of the Z-counting and track-counting luminosities over the Run-2 period. To remove the dependence on the theoretical Z production cross section, $\mathcal{L}_{Z\to\ell^+\ell^-}$ is normalised to the same integrated luminosity as $\mathcal{L}_{\mathrm{track-counting}}$ following the same procedure as performed in Section 4.3.5. This ratio has a spread around unity of 0.3%, showing that the relative stability of $\mathcal{L}_{Z\to\ell^+\ell^-}/\mathcal{L}_{\mathrm{track-counting}}$ is significantly better than that of $\mathcal{L}_{Z\to\ell^+\ell^-}/\mathcal{L}_{ATLAS}$. Likewise, the year-to-year differences in scale are smaller than those given in Section 4.3.4, with deviations from unity of $+0.1\%$ in 2015, -0.04% in 2016, $+0.05\%$ in 2017, and -0.05% in 2018 as summarised in Table 4.13.

The results in Table 4.13 and Figure 4.23 suggest that the Z-counting and track-counting methods are in excellent agreement with one another over the Run-2 period. The spread of the results around unity is much tighter than the corresponding $\mathcal{L}_{Z\to\ell^+\ell^-}/\mathcal{L}_{ATLAS}$ values, further corroborating the conclusion that the Z-counting method can contribute to a better understanding of the systematic uncertainties affecting the baseline ATLAS luminosity measurement.

	Deviation from unity	
Data-taking period	$\mathcal{L}_{Z\to\ell^+\ell^-}/\mathcal{L}_{ATLAS}$	$\mathcal{L}_{Z\to\ell^+\ell^-}/\mathcal{L}_{\text{track-counting}}$
2015	-0.4%	+0.1%
2016	+0.6%	-0.04%
2017	+0.2%	+0.05%
2018	-0.5%	-0.05%

Table 4.13: Deviation from unity of the time-dependent, globally normalised $\mathcal{L}_{Z\to\ell^+\ell^-}/\mathcal{L}_{ATLAS}$ and $\mathcal{L}_{Z\to\ell^+\ell^-}/\mathcal{L}_{\text{track-counting}}$ ratios. The normalisation is calculated over the full 2016 – 2018 period, and the mean calculated in each individual data-taking period, with the deviation given by the difference between the mean and unity.

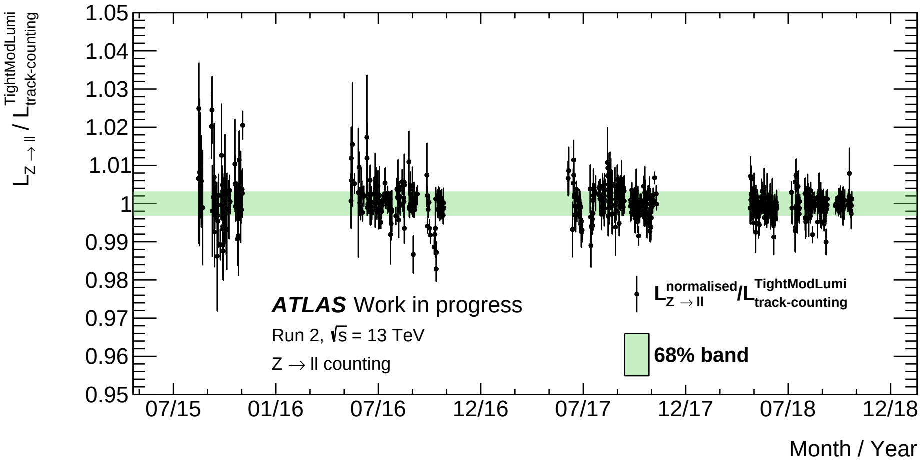

Figure 4.23: Ratio of the integrated, combined $Z \to \ell^+\ell^-$-counting and track-counting luminosities per LHC fill taken from pp collisions at $\sqrt{s} = 13$ TeV over the Run-2 period. The combined Z-counting luminosity is normalised to the track-counting luminosity integrated over the Run-2 period. The x-axis represents the date when the fill started, and only ATLAS runs with a minimum length of 40 minutes are included. The error bars show statistical uncertainties only, and the green bands contain 68% of all points centred around the mean.

4.3.7 Interactive dashboard

An interactive dashboard was also developed and deployed to allow members of the ATLAS luminosity group to lookup a whole suite of Z-counting information for a specific LHC fill or data-taking period. Information such as the trigger- and reconstruction-efficiency, Z-counting vs. baseline ATLAS luminosity comparison and $\mathcal{L}_{Z\to e^+e^-}$ vs. $\mathcal{L}_{Z\to\mu^+\mu^-}$ can be viewed for any given LHC fill. Drop-down menus allow the user to select the desired data-taking period and fill, as well an option to visualise time- or pileup-dependencies.

The input data is hosted on the CERN EOS server in the form of CSV files and is loaded to the web-page in real-time. This allows for rapid turnaround during data-taking, as the Tier-0 Z-counting outputs can output to the EOS server and loaded directly into the dashboard without any down-time. The application was developed in Python and deployed as an official CERN webpage using the CERN OpenShift platform.[2] Figure 4.24 shows some example screenshots from the dashboard using the 2017 LHC fill 6362. These plots contain the same information as those shown in Section 4.3.1, however they are available on-demand for all LHC fills. This represents a powerful tool for rapid visualisation of ATLAS data, which could be expanded to include other luminometers and significantly improve the efficiency of monitoring the luminosity delivered to ATLAS during the data-taking period.

---

[2] The webpage is deployed using a Docker image built based on the source-to-image (S2I) framework.

Run 2 Z-counting dashboard

This dashboard provides an overview of the Z-counting luminosity monitoring results for every run in Run 2; no good run list is applied. There are two options; time-dependent and pileup-dependent monitoring.

Figure 4.24: Screenshots from the interactive Z-counting dashboard illustrating the information which users can obtain for any given ATLAS data-taking run [132].

4.4 Conclusion

The Z-counting method is a powerful tool to monitor the luminosity recorded by the ATLAS detector. Detector inefficiencies are modelled in a granular, time-dependent way, giving the method excellent stability both with respect to time and pileup dependent effects. No bunch-position dependence is observed in the tag-and-probe efficiency measurements, indicating that the Z-counting method is stable with respect to the LHC bunch-structure. A luminosity measurement is obtained using both $Z \to e^+e^-$ and $Z \to \mu^+\mu^-$ events, with independent data-driven and simulated corrections for each. Electrons and muons also depend on different subdetectors and use different triggers, meaning the two channels are completely independent of one another, which allows for a powerful internal cross check of the results. Over the whole Run-2 period, the luminosity values determined in the electron and muon channels show excellent agreement, with a mean of 0.992 and a spread of 0.6% (0.15%) as a function of time (pileup).

Measurements are obtained for each individual luminosity block (60 seconds), which can then be averaged over periods of roughly 20 minutes to monitor the stability over the course of a single fill, or integrated over every LHC fill within a data-taking period to monitor trends over longer time periods. When averaged over periods of roughly 20 minutes, statistical uncertainties ranging from approximately 4% (2015) to 2% (2018) can be achieved, with the statistical precision improving at higher instantaneous luminosities. The $Z \to e^+e^-$ and $Z \to \mu^+\mu^-$ luminosities can be compared directly to the baseline ATLAS luminosity measurement, or they can be combined ($Z \to \ell^+\ell^-$), with similar trends found in each channel as well as their combination. Over the course of individual LHC fills, the comparison of the normalised Z-counting and baseline ATLAS luminosities has a spread around unity of approximately 2%.

In each data-taking period, the time-dependent ratio of the normalised Z-counting and baseline ATLAS luminosity values has a spread around unity of about 0.8% (2015) to 0.4% (2018), while the pileup-dependent ratio has a spread of approximately 0.4% (2015) to 0.1% (2018). Over the full Run-2 period, the time-dependent ratio has a spread of 0.8%, with deviations from unity of -0.4% in 2015, $+0.6$% in 2016, $+0.2$% in 2017, and -0.5% in 2018. The Z-counting luminosity is also compared to the track-counting luminosity, with deviations from unity of $+0.1$% in 2015, -0.04% in 2016, $+0.05$% in 2017, and -0.05% in 2018. The long term stability of the baseline ATLAS luminosity is also 0.6% over the Run-2 period, meaning that the Z-counting value is competitive with this measurement, which utilises 5 other luminometers to achieve this precision. Monitoring the year-to-year variations of the relative Z-counting and baseline ATLAS luminosities could contribute to an improved characterisation of the time-dependent systematic uncertainties affecting the baseline ATLAS luminosity.

Chapter 5

Search for new heavy charged gauge bosons

5.1 Introduction

There are many theoretical candidates for beyond the Standard Model (BSM) particles. One such candidate is the W' boson, which in the simplest model is a heavy charged Spin-1 gauge boson and has similar properties to the Standard Model W boson but a much larger mass. Many searches for these signatures have been performed at ATLAS, both in Run-1 and Run-2 [133, 134], and similar analyses have also been performed at CMS [135, 136]. This section presents a new search for this particle using the full Run-2 ATLAS dataset consisting of $139\,\mathrm{fb}^{-1}$ of pp data. The previous paper published by ATLAS analysed $36\,\mathrm{fb}^{-1}$ of pp data, meaning this analysis benefits from an approximately factor four increase in luminosity. Furthermore, this analysis extends the range of theoretical interpretations by including model independent results for the first time. The dominant source of background is Drell-Yan production of the Standard Model W boson, and the primary search variable is the transverse mass, which is calculated using the transverse momentum (p_{T}) of the selected electron and the missing energy ($E_{\mathrm{T}}^{\mathrm{miss}}$) in the event,

$$m_{\mathrm{T}} = \sqrt{2 p_{\mathrm{T}} E_{\mathrm{T}}^{\mathrm{miss}} (1 - \cos\phi_{e\nu})}, \tag{5.1}$$

where $\phi_{e\nu}$ is the azimuthal angle between the selected electron and missing energy. This section provides an overview of the theoretical motivation for such an exotic signal, outlines the techniques used in the analysis and presents the final results. All plots are the work of the author except Figures 5.16 and 5.17-5.19, which were produced by Magnar Bugge using input data provided by the author for the ATLAS publication [3]. The author was the lead analyser in the electron channel, as such, the following section will focus on the analysis details of the $W' \rightarrow e\nu$ channel.

5.2 Theoretical motivation

Many models predict the existence of heavy charged spin-1 gauge bosons (W'), the signal for which is a resonant peak over a flat background. Some example models include: *Left-Right symmetry models* [137, 138], *Little Higgs models* [139], *models with extra dimensions* [140, 141], *the Sequential Standard Model (SSM)* [142] and the *Heavy Vector Triplet (HVT) model* [143, 144]. These models aim to solve the hierarchy problem, which refers to the difference in scale between the mass of the Higgs boson ($m_h = 125$ GeV) and the Planck mass ($m_P = 10^{19}$ GeV). This difference in scale is a problem, as the Higgs mass term has contributions from all scales at which it interacts, meaning that the quantum field theory prediction for the Higgs mass is actually much larger than the effective value which is measured in experiment. Currently this is explained by the process of renormalisation [145, 146, 147] however, the introduction of new physics at the TeV scale offers a physical explanation for the cancellation of large quadratic terms in the Higgs mass.

Various theoretical interpretations are presented in this analysis, all of which focus on the Drell-Yan production of W' bosons decaying leptonically to an electron or muon ($pp \rightarrow W' \rightarrow \ell\nu$). Due to the difficulty of reconstructing τ leptons, they are the subject of a separate dedicated analysis. The flagship result of this analysis is the interpretation in the context of the SSM, which has been used as the historical baseline. Preliminary results will also be presented in the framework of the HVT model as well as in more model independent contexts, allowing for a greater potential range of reinterpretation.

Sequential standard model In the SSM the W' boson has the same couplings to fermions as the SM W boson and there can be significant mixing between the SM W and W'. An extension to this model is to apply a mixing factor of $\mathcal{O}(M_W^2/M_{W'}^2)$ to the coupling, mimicking the effect of models with extended gauge symmetries and significantly suppressing the mixing [142]. To simplify the theoretical description in this analysis and reduce the model dependence of the obtained results, the interference between W' and W/Z is neglected altogether. This simplified model is a useful benchmark in order to provide results that can be conveniently converted to specific models and is thus the primary theoretical framework used in this analysis.

Heavy vector triplet model In the HVT model, a new electroweak triplet is introduced consisting of the charged $W'^{\pm}$ bosons and the neutral Z' boson by extending the electroweak gauge symmetry to

$$SU(2) \times U(1) \rightarrow SU(2) \times U(1) \times SU(2)'. \tag{5.2}$$

These 3 gauge bosons are almost degenerate in mass, and in the analysis presented within, the $W'^{\pm}$ and Z' states are assumed to be fully degenerate. The HVT Lagrangian is constructed using a phenomenological approach, only taking into consideration those free parameters of the model which effect the mass and width of the resonance. These are the only parameters which the resonant search is sensitive to, and to simplify the underlying model description the free parameters which do not affect the mass and width can be neglected. This approach greatly increases the model independence of the interpretation, as the experimental results can be presented in the parameter space of the phenomenological Lagrangian. The phenomenological interaction Lagrangian is

$$\mathcal{L}_{\mathcal{W}}^{\text{int}} = -g_q \mathcal{W}_{\mu}^{a} \bar{q}_k \gamma^{\mu} \frac{\sigma_a}{2} q_k - g_{\ell} \mathcal{W}_{\mu}^{a} \bar{\ell}_k \gamma^{\mu} \frac{\sigma_a}{2} \ell_k - g_H \left(\mathcal{W}_{\mu}^{a} H^{\dagger} \frac{\sigma_a}{2} i D^{\mu} H + \text{h.c.} \right), \tag{5.3}$$

where q_k and ℓ_k represent the left-handed quark and lepton doublets for fermion generation k ($k = 1, 2, 3$), H represents the Higgs doublet, σ_a ($a = 1, 2, 3$) are the Pauli matrices and g_q, g_{ℓ}, and g_H correspond to the coupling strengths between the triplet field $\mathcal{W}$ and the quark, lepton, and Higgs fields, respectively. The results can then be transferred to a specific model scenario where the phenomenological parameters can be calculated.

5.3 Event selection

In the electron channel, events are selected using the selection criteria outlined in Table 5.1. The pseudorapidity requirements are determined by the region over which ATLAS has good electron reconstruction efficiency, i.e. excluding the barrel endcap transition region between $1.37 < |\eta| < 1.52$ and only using the region fully covered by the Inner Detector up to $|\eta| < 2.47$. The transverse momentum of the triggered electron is required to be $p_{\mathrm{T}} \geq 65\,\mathrm{GeV}$, with an associated missing energy of $E_{\mathrm{T}}^{\mathrm{miss}} \geq 65\,\mathrm{GeV}$. This threshold is determined by the triggers used in the analysis, and the transverse mass is the sum of the $E_{\mathrm{T}}^{\mathrm{miss}}$ and p_{T} cuts, i.e. $m_{\mathrm{T}} \geq 130\,\mathrm{GeV}$. These selection criteria also reflect the topology of the signal, namely a final state consisting of a high-p_{T} electron and a large missing energy. The event-level trigger information can be seen in Table 5.2.

Following on from the description given in Section 3.4, the three ID working points used in this analysis are Loose, Medium and Tight, and a description of the requirements of each can be found in Ref. [97]. These are constructed such that electrons which pass Tight will also pass Medium, and those which pass Medium will also pass Loose. In addition to the likelihood identification criteria, there are also the isolation requirements. The Gradient working point is used in the electron channel in this analysis, also described in Ref. [97]. This working point has been tuned for both calorimeter and track based isolation, and is designed in a similar manner to the Loose working point, with a rising efficiency up to a plateau of

99% at approximately 60 GeV. Therefore, the isolation efficiency should be roughly flat at 99% across the entire phase space of interest in this analysis.

In order to suppress background due to dielectron final states, signal events are required to contain exactly one electron passing the selections outlined in Table 5.1. An additional loose lepton (electron or muon) veto is also applied, rejecting events which pass the selection criteria listed in Table 5.3. Events with an electron and a muon in the final state have a significant contribution from processes involving top quark final states, which can be significantly suppressed with this additional lepton veto. Furthermore, events are required to pass basic data quality criteria as defined in Table 3.3.

Electron channel event selection	
Feature	*Criteria*
Pseudorapidity	$(\lvert\eta\rvert < 1.37)$ OR $(1.52 < \lvert\eta\rvert < 2.47)$
Object quality	Not from a bad calorimeter cluster
Transverse momentum	$\mathrm{p_T} > 65$ GeV
Bad-jet veto	LooseBad
Track-vertex association	$\lvert d_0^{\mathrm{BL}}\rvert/\sigma(d_0^{\mathrm{BL}}) < 5$
Identification	Tight
Isolation	Gradient
Missing transverse energy	$\mathrm{E_T^{miss}} > 65$ GeV
Transverse mass	$\mathrm{m_T} > 130$ GeV

Table 5.1: Summary of the event selection criteria in the electron channel, see text for further explanations.

Electron channel trigger information		
Period Used	*Trigger*	*Properties*
2015	HLT_e24_lhmedium_L1EM20VH	$p_{\mathrm{T}} > 24$ GeV ID: LHMedium $E_{\mathrm{T}}^{\mathrm{miss}} > 20$ GeV* (variable, compensate for E loss in passive material) $E_{\mathrm{T}}^{\mathrm{miss}}$ dependent veto
2015 - 2018	HLT_e60_lhmedium	$p_{\mathrm{T}} > 60$ GeV ID: LHMedium
2015	HLT_e120_lhloose	$p_{\mathrm{T}} > 120$ GeV ID: LHLoose
2016 - 2018	HLT_e140_lhloose_nod0	$p_{\mathrm{T}} > 140$ GeV ID: LHLoose (no d_0 cut)

Table 5.2: Summary of the triggers used in the electron channel.

Electron veto	
Feature	*Criteria*
Transverse momentum	$p_T > 20$ GeV
Pseudorapidity	$(\|\eta\| < 1.37) \quad \text{OR} \quad (1.52 < \|\eta\| < 2.47)$
Object quality	Not from a bad calorimeter cluster
Track-vertex association	$\|d_0^{\mathrm{BL}}\|/\sigma(d_0^{\mathrm{BL}}) < 5$
Identification	LHMedium
Isolation	Gradient
Muon veto	
Feature	*Criteria*
Transverse momentum	$p_T > 20$ GeV
Pseudorapidity	$\eta < 2.4$
Selection working point	Medium or High-p_{T}
Isolation	FCTightTrackOnly

Table 5.3: Summary of the additional lepton vetoes used in the electron channel, see text for further explanations.

Figures 5.1-5.2 shows the event yields in the 2015-2016 and 2017-2018 data-taking periods respectively. The event yield is the number of events which pass the selection per ATLAS run normalised to the luminosity of that run. This can be seen to be relatively stable across data-taking periods, as one would expect as this quantity is related to the production cross section and should therefore be independent of the machine running conditions.

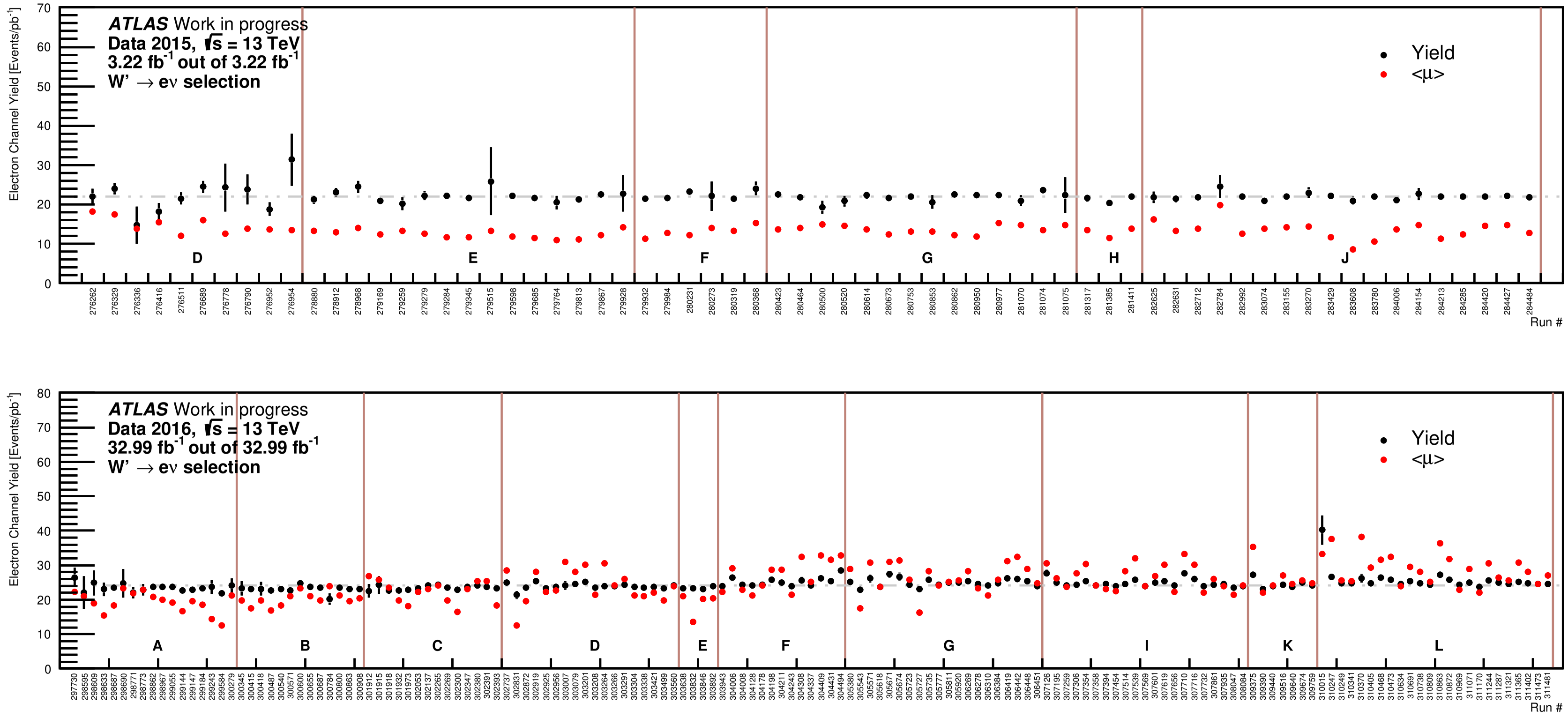

Figure 5.1: 2015 and 2016 electron channel event yields ($N_{\text{sel}}/L_{\text{int}}$, black dots) and $\langle\mu\rangle$ (red dots) for each run after requiring the final selection. The horizontal dashed line indicates the average yield across the entire data-taking period, and the vertical red lines indicate the sub-periods in each data-taking period (also indicated by the corresponding letter).

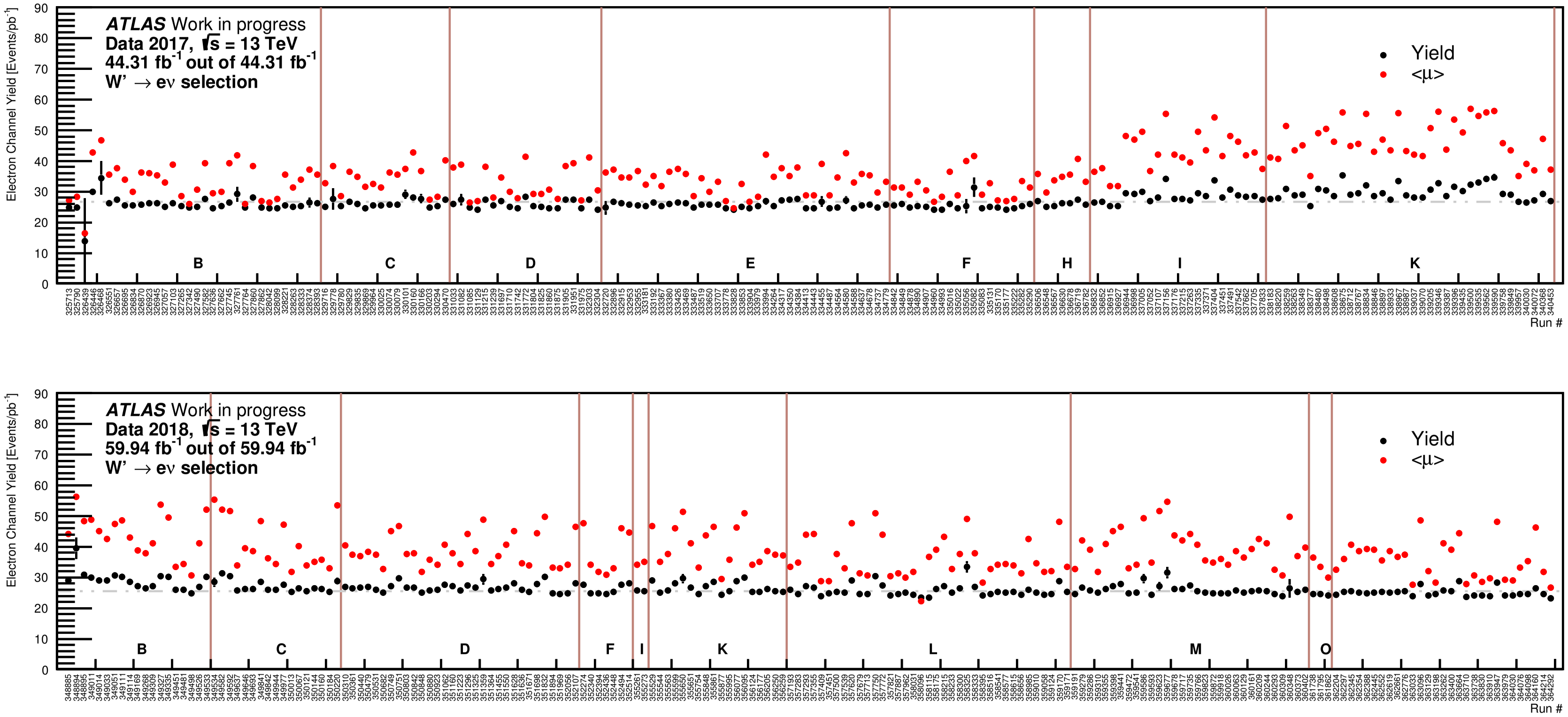

Figure 5.2: 2017 and 2018 electron channel event yields ($N_{\text{sel}}/L_{\text{int}}$, black dots) and $\langle\mu\rangle$ (red dots) for each run after requiring the final selection. The horizontal dashed line indicates the average yield across the entire data-taking period, and the vertical red lines indicate the sub-periods in each data-taking period (also indicated by the corresponding letter).

5.4 Monte Carlo simulation

5.4.1 Signal

Signal samples were generated in the context of the Sequential Standard Model with subsequent decay into an electron and a neutrino. These samples were produced at LO with the Pythia v8.183 [119] event generator with A14 tune [148] for parton shower and hadronisation. To remove the mass dependence of the generator level Monte Carlo, the square of the matrix element is divided by a function of lepton-neutrino invariant mass ($m_{\ell\nu}$) of the form

$$f(m_{l\nu}) = \left(\frac{m_{\ell\nu}}{\sqrt{s}}\right)^{p_2} \times \exp\left(\frac{-p_1 m_{\ell\nu}}{\sqrt{s}}\right), \tag{5.4}$$

where p_1 and p_2 are parameters that minimise the mass dependence of the cross section and $\sqrt{s}$ is the centre-of-mass energy. This mass-independent sample can then be reweighted to a range of different pole masses in order to scan the entire phase space of W' signals. Event-by-event weights are applied depending on the invariant mass of the lepton-neutrino system and the desired signal pole mass (M). Therefore, the exact shape of the resonance depends the event kinematics, the signal pole mass and the width assumptions. The event weights are calculated using Eq. 5.5.

$$w = \frac{10^{12}}{\left(m_{\ell\nu}^2 - M^2\right)^2 + \left(m_{\ell\nu}^2 \Gamma\right)^2}. \tag{5.5}$$

Γ is the relative width of the W' signal, which is calculated in the context of the SSM with W' couplings to fermions being set equal to the SM W and neglecting the interference between W' and W,

$$\Gamma = \frac{1 + \left(\left(1 + \frac{1}{3.5\log\left(M/0.151142\right)}\right) \times \left(3 - 1.5\left(\frac{M_t}{M}\right)^2 + 0.5\left(\frac{M_t}{M}\right)^6\right)\right)}{4sin^2\theta_W \left(\frac{1}{\alpha_{EM}} + 1.45\log\left(M_Z/M\right)\right)}. \tag{5.6}$$

θ_W is the weak mixing angle, M_t is the top quark mass, M_Z is the Z boson mass and α_{EM} is the fine structure constant at the Z mass scale. An additional $m_{\ell\nu}$ dependent factor is applied to the weight w to obtain the final event weight ($w_{W'}$). This factor has a distinct functional form, depending on the magnitude of $m_{\ell\nu}$ relative to the weak mixing angle.

$$w_{W'} = \begin{cases} \frac{w}{102.77\exp(11.5m_{\ell\nu})}, & \text{if } \frac{m_{\ell\nu}}{\sqrt{s}} < \frac{sin^2\theta_W}{10} \\ \frac{w}{\exp(16.1m_{\ell\nu} - 1.2\log(m_{\ell\nu}))}, & \text{if } \frac{sin^2\theta_W}{10} < \frac{m_{\ell\nu}}{\sqrt{s}} < sin^2\theta_W \\ \frac{w}{1.8675\times10^{-3}\times\exp(31.7m_{\ell\nu}) - 4.6\log(m_{\ell\nu})}. & \text{if } \frac{m_{\ell\nu}}{\sqrt{s}} > sin^2\theta_W \end{cases} \tag{5.7}$$

The branching ratio of the $W' \rightarrow e\nu$ is 10.8% at low mass (150 GeV) and is approximately constant at 8.2% above the tb production threshold, while the width ranges from 2.7% at low mass to 3.5% above the tb threshold. The generator level transverse mass distributions for various mass hypotheses and the acceptance times efficiency ($A \times \varepsilon$) for all signals at final selection can be seen in Figure 5.3. As expected, the signal line-shapes become significantly broader as the pole mass increases, due to more of the cross section being concentrated in the off-shell tail, and the number of events drops off rapidly due to the decreasing cross section (Figure 5.3 left). Likewise, the acceptance times efficiency of high mass signals begins to decrease as more of the signal is concentrated in the parton luminosity tail ($m_{\ell\nu} << m_{W'}$) and the kinematic cuts remove a larger fraction of events (Figure 5.3 right). However, the acceptance times efficiency is high over the entire the entire high-mass region, with $A \times \varepsilon \geq 62\%$ over the entire region above $m_{W'} \geq 1\,\mathrm{TeV}$. This can be contrasted with the muon channel where the acceptance is as low as 45% at $7\,\mathrm{TeV}$, thereby reducing the sensitivity in the muon channel at high-mass compared to the electron channel.

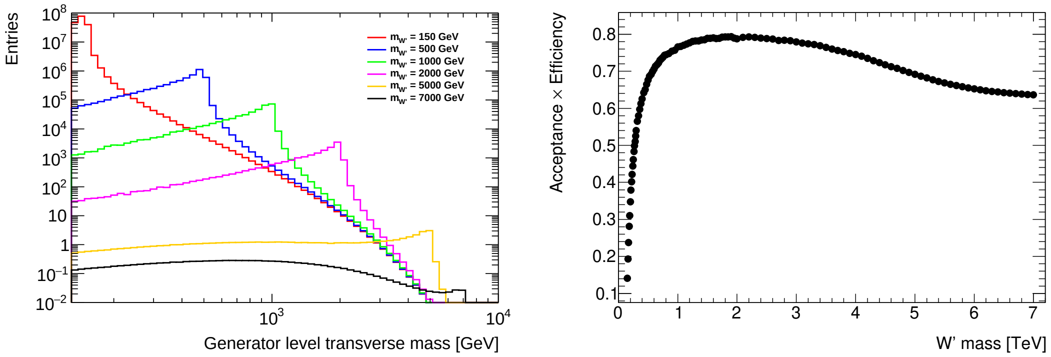

Figure 5.3: Left: Signal generator-level transverse mass distributions for various W' pole mass hypotheses. Right: Signal acceptance times efficiency versus W' pole mass after final selection in the electron channel.

5.4.2 Background

To reach sensitivities to very high masses where signals become increasingly broad, exotic searches such as this one rely on having an accurate description of the expected Standard Model background in order to measure a potential excess. As such, it is important to consider all SM processes with a final state with a similar topology to the proposed signal (high-p_{T} lepton and large missing energy). Monte Carlo simulation is used to evaluate all background contributions, other than the multijet contribution, where multijet refers to production of jets and non-prompt leptons which are misidentified as electrons and subsequently pass signal selection. The evaluation of the multijet contribution is the topic of Section 5.5.

The Standard Model backgrounds which are evaluated using Monte Carlo simulation are summarised in Table 5.4.2. Each of these samples is shown with its corresponding event generator, parton showering programme, PDF and approximate contribution to the total SM background.

Sample	Generator	Parton Shower	PDF	Contribution [%]
$W \rightarrow \ell_{e,\tau}\nu_{e,\tau}$	Powheg-Box v2 [117, 118, 149, 150]	Pythia v8.186 [119] (AZNLO tune [128])	CT10 [151]	70
$t/\bar{t}/t\bar{t}$	Powheg-Box [152, 153, 154]	Pythia v8.183 [119] (A14 tune [148])	NNPDF30 NNLO [155]	16
$Z \rightarrow \ell_{e,\tau}\ell_{e,\tau}$	Powheg-Box v2 [117, 118, 149, 150]	Pythia v8.186 [119] (AZNLO tune [128])	CT10 [151]	2.5
Diboson	Sherpa v2.2.1 [120]	–	NNPDF30 NNLO [155]	1.5

Table 5.4: Overview of Standard Model background processes modelled using Monte Carlo simulation. All samples are shown with their event generator, parton showering programme, PDF and their percentage contribution to the total background, including the data-driven multijet background component (Section 5.5).

To ensure sufficient statistics at high mass, both charged and neutral current DY backgrounds are generated in bins of invariant mass. Inclusively generated samples would require unrealistically large numbers of events to accurately estimate the W/Z boson background at high mass, where the contribution is a result of off-shell production. Summing the mass binned samples allows for an accurate description of the SM W/Z boson background across the whole mass spectrum. High statistics inclusive samples are also generated in the region before the mass binned sample starts ($m < 120\,\mathrm{GeV}$). These samples were generated at NLO QCD with the Powheg-Box v2 event generator [117, 118, 149, 150] using the CT10 NLO PDF set [151]. The higher order QCD corrections were computed with VRAP v0.9 [156] using the CT14 NNLO PDF set [157] and the NLO EW ISR and virtual corrections were calculated with MCSANC [57]. QED FSR effects are applied directly to the Monte Carlo during event generation using PHOTOS++ [61]. The central value of the NNLO QCD + NLO EW cross section for each mass bin is calculated using the additive method (see Section 2.4.4), and a symmetric systematic uncertainty is estimated by calculating the difference between the additive and factorised methods. Due to these higher order corrections, the NLO QCD cross section is reduced by approximately 10% at $m_{\ell\nu} = 1$ TeV and 20% at $m_{\ell\nu} = 6$ TeV.

While the DY samples are generated in slices of invariant mass, both the top and diboson backgrounds are generated inclusively across the whole mass spectrum. Therefore, these samples also suffer from limited statistics in the high-mass region, and so a transverse-mass-dependent functional form is fit to the background distribution to mitigate this effect. This is done by fitting the background distribution with a polynomial function in the high-statistics low-m_{T}region, and then using the results of this fit to estimate the background at high-$m_{\mathrm{T}}$where statistics are low. The multijet background is also subject to such an extrapolation, more details of which are discussed in Section 5.6.

5.5 Data-driven background estimation

Backgrounds arising from multijet production are poorly modelled using Monte Carlo due to the very large cross section of jet production in pp collisions, hence the data-driven matrix method is used instead. The matrix method exploits the different probabilities for real and fake leptons to pass certain selection criteria.

For example, a genuine prompt electron will have a high probability of passing tight identification criteria, compared to a non-prompt electron or a misidentified jet. By exploiting these different probabilities, the contribution of "fake" electrons to the measured data can be extracted.

The number of fake electrons in the data is not an observable quantity, and must be determined by measuring the relative proportion of "tight" and "loose" electrons. Tight selection is defined by strict selection cuts, designed to minimise the fake contribution, while the loose selection is designed to maximise the fake contribution. The number of real (N_R) and fake (N_F) electrons is statistically independent, and so must be the tight and loose selection requirements. Therefore, events which pass the loose selection are explicitly required to fail the tight selection. The observed number of tight (N_T) and loose (N_{LnT}) electrons is dependent on the number of real and fake electrons, with the proportionality factor being the real (ϵ_R) and fake (ϵ_F) efficiencies. These efficiency factors measure the probability that a real or fake electron which passes loose selection, also passes tight selection. Eq. 5.8 shows the relation between the "true" number of real and fake electrons and the number which pass the tight and loose selection criteria,

$$\begin{pmatrix} N_T \\ N_{LnT} \end{pmatrix} = \begin{pmatrix} \epsilon_R & \epsilon_F \\ 1-\epsilon_R & 1-\epsilon_F \end{pmatrix} \begin{pmatrix} N_R \\ N_F \end{pmatrix} \tag{5.8}$$

In this case, the tight selection is equivalent to the signal selection outlined in Section 5.3. The loose selection is similar to the signal selection, with looser identification requirements and no requirement on isolation. While not strictly necessary in the matrix method, in this analysis the loose region is defined in two separate regions of $p_{\mathrm{T}} < 145$ GeV and $p_{\mathrm{T}} > 145$ GeV. The reason for this is so that the selection criteria in each of these regions closely matches the trigger requirements. In the region of $p_{\mathrm{T}} < 145$ GeV the LHMedium ID working point is used, while in the $p_{\mathrm{T}} > 145$ GeV region the LHLoose ID working point is used (closely matching the selection outlined in Table 5.2).

The aim of the matrix method is to determine the number of fake electrons which pass selection ($\varepsilon_F N_F$). By inverting the matrix, an expression for N_F can be obtained in terms of measurable reconstruction level quantities (Eq. 5.9 and Eq. 5.10).

$$\begin{pmatrix} N_R \\ N_F \end{pmatrix} = \frac{1}{\epsilon_R(1-\epsilon_F)-\epsilon_F(1-\epsilon_R)} \begin{pmatrix} 1-\epsilon_F & -\epsilon_F \\ \epsilon_R - 1 & \epsilon_R \end{pmatrix} \begin{pmatrix} N_T \\ N_{LnT} \end{pmatrix} \tag{5.9}$$

$$N_F = \frac{1}{\epsilon_R - \epsilon_F}\left(\epsilon_R(N_{LnT}+N_T) - N_T\right) \tag{5.10}$$

In order to calculate the real efficiency component, the contribution from prompt leptons can be determined from MC. The real efficiency, ε_R, quantifies what fraction of real electrons which pass loose selection also pass tight selection. To ensure a high purity of prompt electrons, only $W \rightarrow e\nu$ MC is used, with an additional truth matching cut of $\Delta R(e^{truth}, e^{reco}) < 0.2$ applied. The efficiency is calculated by taking the ratio of the number of events which pass the tight and loose selections defined previously, without the $E_{\mathrm{T}}^{\mathrm{miss}}$ and m_{T} requirements applied in order to increase the statistics of the efficiency evaluation,

$$\epsilon_R = \frac{N_T^{real}}{N_{LnT}^{real} + N_T^{real}} = \frac{N_T^{real}}{N_L^{real}}, \tag{5.11}$$

where N_L is simply the number of events that pass loose selection, with no requirement that they also fail tight selection. The $E_{\mathrm{T}}^{\mathrm{miss}}$ and m_{T} cuts can be relaxed due to the high purity of the samples, since there is little-to-no contamination at low $E_{\mathrm{T}}^{\mathrm{miss}}/m_{\mathrm{T}}$ due to misidentified jets or non-prompt leptons. Figure 5.4 shows the real efficiency determined from $W \rightarrow e\nu$ Monte Carlo as a function of η and p_{T}. The real efficiency is greater than 94% over the entire phase space, and exhibits only a slight dependence on transverse mass and pseudorapidity.

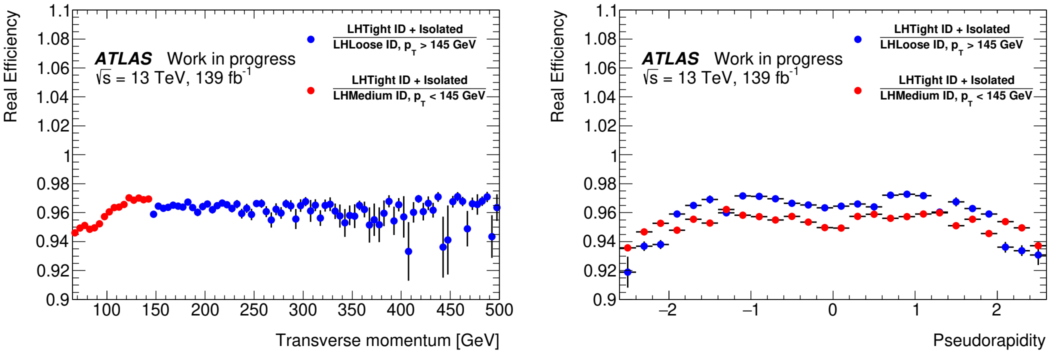

Figure 5.4: Real-electron efficiency as a function of η and p_{T} determined from W Monte Carlo samples.

While the real efficiency component can be determined from MC, the fake efficiency must be estimated using a data-driven approach, due to the fact that Monte Carlo should consist of almost entirely prompt electrons. To estimate the fake efficiency, the non-prompt contribution in real data must be calculated, with a background subtraction from MC in order to remove the contribution of prompt electrons which have been misidentified as fake. This subtraction is calculated by applying the same selection to MC as is applied in data[1]

$$\epsilon_F = \frac{N_T^{fake,data} - N_T^{fake,MC}}{N_L^{fake,data} - N_L^{fake,MC}}. \tag{5.12}$$

The tight and loose selection criteria follow those previously defined, with some additional cuts in order to minimise the prompt-lepton contribution from W and Z decays. These selection criteria are detailed in Table 5.5.

---

[1] The prompt dilution in the fake efficiency determination can be seen in Figures B.1 and B.2.

Targeted background	*Selection*
W	$E_{\mathrm{T}}^{\mathrm{miss}} < 60$ GeV
Z	$\lvert m_{ee} - m_Z \rvert > 20\,\mathrm{GeV}$ for events with 2 electrons passing LHLoose and $p_T > 20\,\mathrm{GeV}$

Table 5.5: Additional selection cuts applied to the fake efficiency region. Events with large missing energy are vetoed in order to reduce the W contribution, while events with 2 electrons which pass LHLoose ID and have $p_{\mathrm{T}} > 20\,\mathrm{GeV}$ and are within 20 GeV of the Z mass are vetoed to minimise the Z contribution.

Figure 5.5 shows the fake efficiency as a function of p_{T} and $\Delta\phi$. It can also be noted that this figure shows the effect of systematic variations on the selection used in defining the enriched fake region. This is simply due to the fact that the definition of the control region is rather arbitrary, so varying it slightly gives an estimate of the systematic uncertainty associated with the phase-space definition. The efficiency labelled as "Nominal" shows the efficiency obtained using the selection given previously, while the other efficiencies are obtained by adding the selections listed in Table 5.6. The fake efficiency exhibits a strong dependence both on the transverse momentum of the selected lepton and the $\Delta\phi$ between the selected lepton and the missing energy. The discontinuity at $p_{\mathrm{T}} = 145\,\mathrm{GeV}$ is a result of the LHLoose identification working point being used in the high-p_{T} region, while the LHMedium working point is used at low-p_{T}. Since the requirements of the LHMedium working point are stricter than those of LHLoose, the probability that an electron which passes LHMedium also passed LHTight is higher than for LHLoose electrons.

Selection
$E_{\mathrm{T}}^{\mathrm{miss}} < 20$ GeV
20 GeV $< E_{\mathrm{T}}^{\mathrm{miss}} < 60$ GeV
No Z veto applied

Table 5.6: Variations applied to the fake efficiency control region. Each of these selections can be propagated to an efficiency estimate, and in turn an estimate of the multijet background.

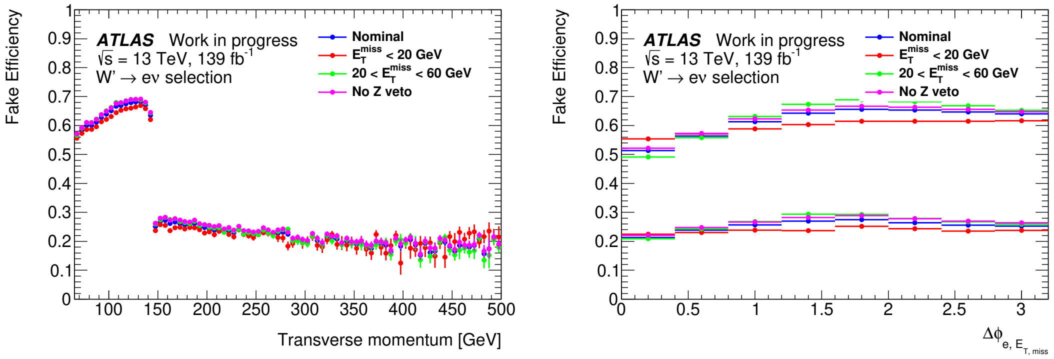

Figure 5.5: Fake efficiency variations as a function of p_{T} (left) and $\Delta\phi_{e,E_{\mathrm{T}}^{\mathrm{miss}}}$ (right) determined from fake enriched data sample.

In order to increase the granularity of the real and fake efficiency estimates, those which are applied to the data are binned in two dimensions (Figures 5.4 and 5.5 are for illustrative purposes). The real efficiency component is binned as a function of the p_{T} and η of the selected electron, and the fake efficiency component is binned as a function of the p_{T} of the electron and the $\Delta\phi_{eE_{\mathrm{T}}^{\mathrm{miss}}}$ between the electron and missing energy. The real/fake efficiency estimates can then be obtained on an event-by-event basis, based on the kinematics of the event. Figure 5.6 shows the 2-dimensional real (left) and fake (right) efficiencies. The real efficiency is high at $\varepsilon > 94\%$ across the entire phase space, while the fake efficiency is high in the $p_{\mathrm{T}} < 145\,\mathrm{GeV}$ region and low above $p_{\mathrm{T}} > 145\,\mathrm{GeV}$. High fake efficiencies lead to a larger multijet background estimate, and so the multijet background is larger in the low transverse mass/missing energy region due to the dependence on p_{T}^{e} and $\Delta\phi_{eE_{\mathrm{T}}^{\mathrm{miss}}}$.

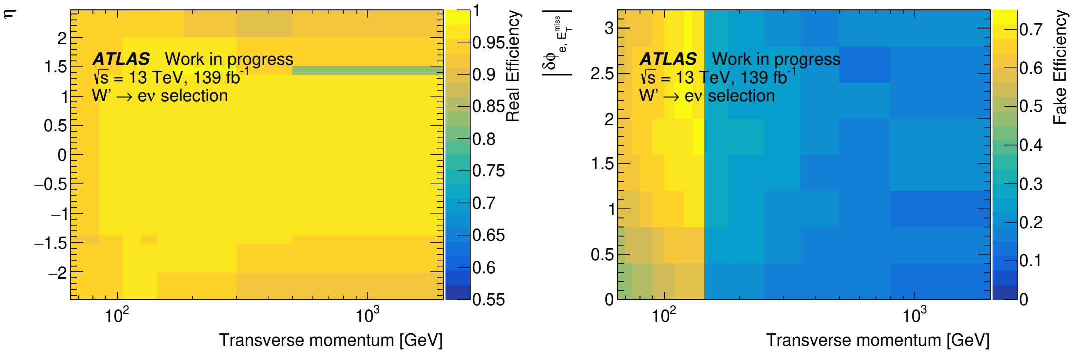

Figure 5.6: Real efficiency as a function of p_{T} and $|\eta|$ is shown on the left. Fake efficiency as a function of p_{T} and $|\Delta\phi_{e,E_{\mathrm{T}}^{\mathrm{miss}}}|$ is shown on the right.

In principle, the efficiencies could be binned in as many variables as necessary, however given statistical limitations previous iterations of the analysis chose to use 2-dimensions only. Given that this dataset is a factor 4 larger than the previously published version, a test was performed to see how extending the binning to 3-dimensions effected the multijet estimate in the signal region. Figure 5.7 shows the result of this comparison, where the fake efficiency is binned in 3-dimensions as a function of p_{T}, $\Delta\phi_{e,E_{\mathrm{T}}^{\mathrm{miss}}}$ and η. It should be noted that the uncertainties shown in this figure are not representative of the uncertainty on this ratio, and it is the central value which defines the uncertainty between the two methods, i.e. the relative agreement. No pseudorapidity dependence was included for the real efficiency, as the variations are negligible at below the 1% level. While there is an approximately 10% difference between the two estimates above $300\,\mathrm{GeV}$, this is within the systematic uncertainties shown in Figure 5.9, and so the final estimation of the multijet background was obtained using the two-dimensional fake efficiencies. It is important to note that the error bars shown in this figure should not be taken into consideration in this comparative analysis. The uncertainties shown are simply the combined Gaussian errors on the 3D/2D multijet estimates, without propagating the fake efficiency uncertainties or using Poisson statistics.

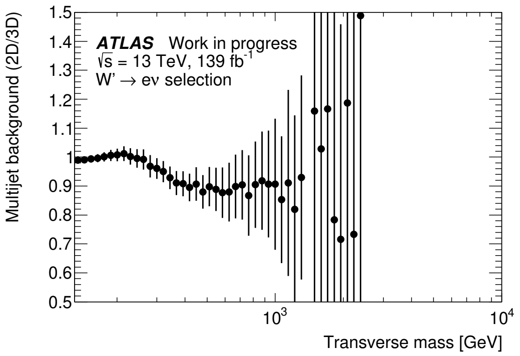

Figure 5.7: Comparison of the multijet background estimate obtained when using 2-dimensional vs. 3-dimensional binning for the fake efficiency estimate.

5.5.1 Multijet validation region

In order to test the predictive power of the matrix method, a validation region is defined which is designed to have an enriched multijet contribution. This validation region is defined similarly to the signal region, only releasing the requirement on $E_{\mathrm{T}}^{\mathrm{miss}}$ and m_{T}, as the multijet contribution is dominant in the low-$E_{\mathrm{T}}^{\mathrm{miss}}$ region. The η, ϕ, p_{T}, $E_{\mathrm{T}}^{\mathrm{miss}}$, $\Delta\phi_{e,E_{\mathrm{T}}^{\mathrm{miss}}}$, m_{T} distributions in the multi-jet validation region can be seen in Figure 5.8, where it can be seen that the multi-jet contribution can be as large as 40% of the total background contribution.

Overall agreement in this region is good, with some small disagreement seen at high-η and a roughly flat shift from unity in the $E_{\mathrm{T}}^{\mathrm{miss}}$ distribution above 50 GeV. This $E_{\mathrm{T}}^{\mathrm{miss}}$ mis-modelling is assumed to be attributable to mis-modelling of non-leptonic activity such as jet emissions, parton showering and underlying event activity, leading to a better $E_{\mathrm{T}}^{\mathrm{miss}}$ resolution in Monte Carlo than data (studies performed by M. K. Bugge in the muon channel and documented in Ref. [158]). An excess of data over background can also be seen in the m_{T} distribution in the $100-200$ GeV region, which is also attributed to the $E_{\mathrm{T}}^{\mathrm{miss}}$ resolution mis-modelling. This excess is well described when taking into account the pulls of nuisance paramaters associated with the jet energy resolution and $E_{\mathrm{T}}^{\mathrm{miss}}$ soft term.

5.5.2 Systematic uncertainty

As discussed in Section 5.5 (Figure 5.5), the selections used to calculate the fake efficiency can be varied to estimate the systematic uncertainty. No such variation is applied to the real efficiency, as it is stable with respect to the selection criteria as the selected events are genuine prompt electrons. The statistical uncertainty associated with both the real and fake efficiencies is negligible. Two-dimensional fake efficiencies are calculated using each of the selections in Table 5.6, and an estimate of the multijet contribution in the signal region calculated with each. Each of these variations is then compared with the

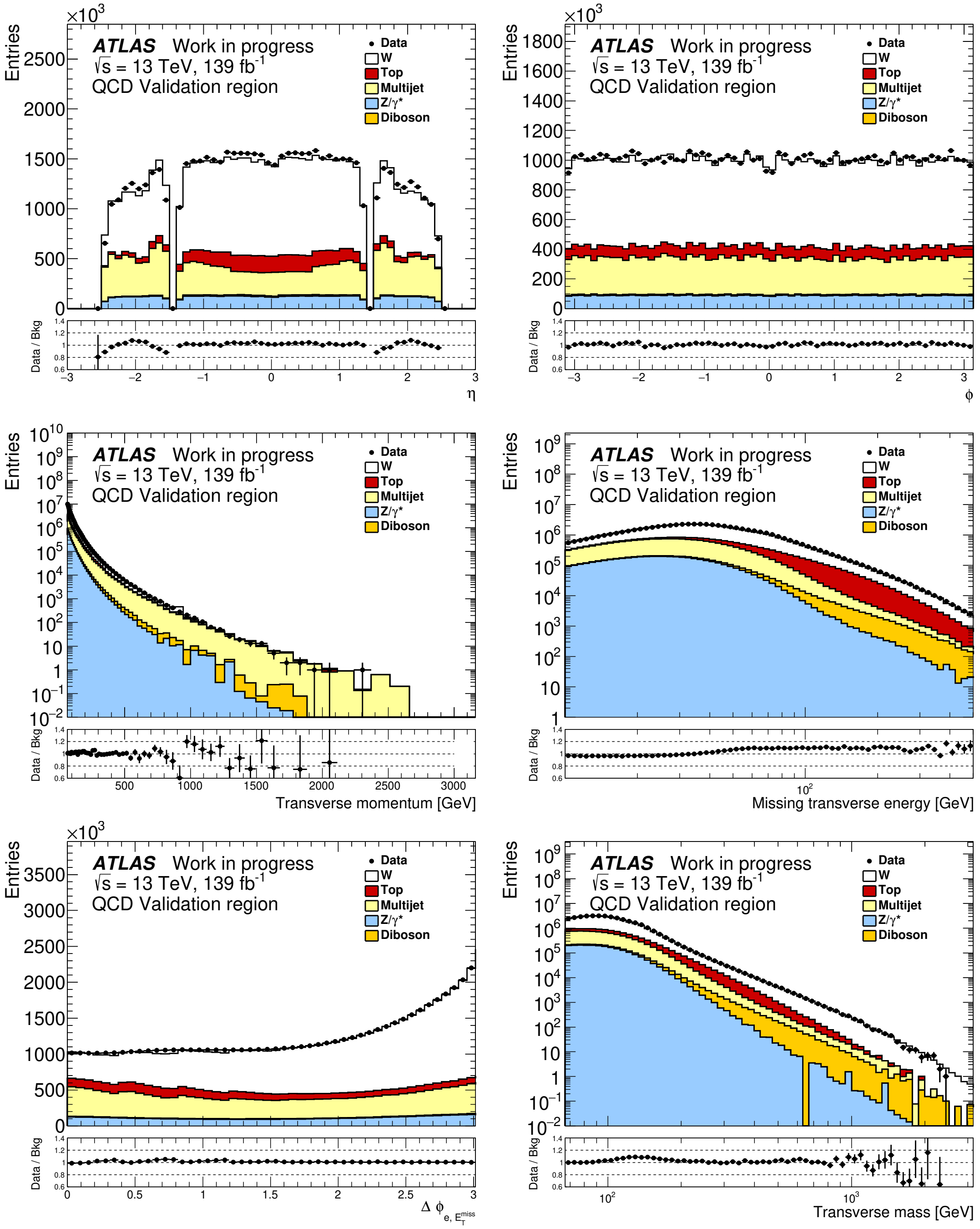

Figure 5.8: η, ϕ, p_{T}, $E_{\mathrm{T}}^{\mathrm{miss}}$, $\Delta\phi_{e,E_{\mathrm{T}}^{\mathrm{miss}}}$, m_{T} distributions in the multi-jet validation region, where there is no requirement on $E_{\mathrm{T}}^{\mathrm{miss}}$ and m_{T}. See text for further details.

nominal, and the envelope of all ratios used to set the systematic uncertainty on the multijet background normalisation. Figure 5.9 shows the ratio of each of multijet background variation with respect to the nominal as a function of m_{T} (left) and p_{T} (right). From this figure, a flat systematic uncertainty of 15% is set on the multijet background normalisation as a function of transverse mass. The systematic uncertainty as a function of p_{T} is slightly larger, however, the statistical analysis uses the transverse mass as the primary search variable so the p_{T} dependence is neglected.

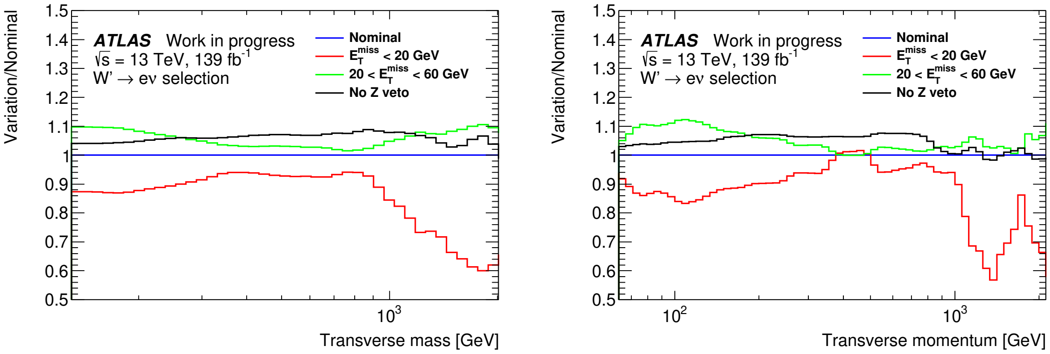

Figure 5.9: Ratio of multi-jet background variations for the different fake efficiency variations and the nominal, as a function of transverse mass and the transverse momentum.

5.6 Background extrapolation

As some samples (top, multijet and diboson) run out of statistics at high-$m_{\mathrm{T}}$and it becomes too computationally expensive to produce more, a fit is performed and the functional form used to estimate the background contribution in this region. Searches at CDF, ATLAS and CMS [159, 160, 161] have shown that the functional forms in Eq. 5.13 and 5.14 provide a good description of top, diboson and multijet backgrounds at high-m_{T}.

$$f(m_{\mathrm{T}}) = e^{-a} m_{\mathrm{T}}^{b} m_{\mathrm{T}}^{c\log(m_{\mathrm{T}})}, \tag{5.13}$$

$$f(m_{\mathrm{T}}) = \frac{a}{(m_{\mathrm{T}} + b)^{c}}. \tag{5.14}$$

Various fits are performed using both fit functions, varying both the upper and lower bound of the fitting range. For the top and diboson backgrounds, the fit with the best χ^2/N_{dof} is taken as the central value and used to estimate the background in the high-mass region. The raw Monte Carlo estimate is used in the low-mass region, and the two distributions are stitched together to obtain a background estimate across the entire phase space. The ratio of each fit with respect to the central value is then calculated, and the ratio furthest from unity is used to estimate a symmetric systematic uncertainty. This is done for each m_{T} bin individually so that the uncertainty is constructed from the most discrepant fit in each bin, thereby covering all possible fits across the entire m_{T} spectrum. All fits are consistent with the data in the high-statistics region of the phase space. While the fitting procedure is the same for the multijet contribution, the choice of central value is determined differently. Instead of using χ^2 minimisation, the quantity Q is defined as

$$Q = \frac{1}{N_B} \sum_{b>b_s}^{n_b^{est}>0} \frac{\left(n_b^{est} - n_b^{fit}\right)^2}{\sigma_b^2}, \tag{5.15}$$

where N_B is the number of bins, b_s the stitching bin, n_b^{est} and n_b^{fit} the number of entries according to the matrix method and the fit and σ_b is the uncertainty in bin b. This quantity is defined such that $Q \approx 1$ for fits which describe the high-m_{T} tail well. The fit with the smallest Q value is taken as the central value, and only fits with $Q < 1.5$ are considered when calculating the uncertainty.

Table 5.7 shows the range over which the fits are performed, as well as the step size (Lower/Upper

Increment) and stitch point. The step size is the size by which the lower and upper point of the fits are varied, and the stitch point the point beyond which the resulting functional form is used as the background extrapolation. The fit range of the central value is also presented, as well as which functional form was used to obtain said central value. Figure 5.10 shows the obtained fits for each channel, where the central value is shown by a dashed red line.

Sample	m_{T} [GeV]						Fit Function
	Lower Fit Range	Lower Increment	Upper Fit Range	Upper Increment	Stitch Point	Central Value Fit Range	
Top	300 - 450	10	1000 - 1400	20	800	400 - 1000	Eq. 5.13
Multi-jet	350 - 500	25	800 - 1000	10	1000	350 - 1000	Eq. 5.14
Diboson	350 - 500	15	1000 - 2000	40	700	425 - 1000	Eq. 5.13

Table 5.7: Fit parameters for top, multijet and diboson backgrounds, showing the m_{T}range (in GeV) over which the start of the fit is varied, the step size with which it is varied, and the corresponding range/step size for the end point of the fit. The stitch point is the point above which the extrapolation is used to estimate the background, and the central value fit range shows the start and end point of the fit with the best χ^2/N_{dof}.

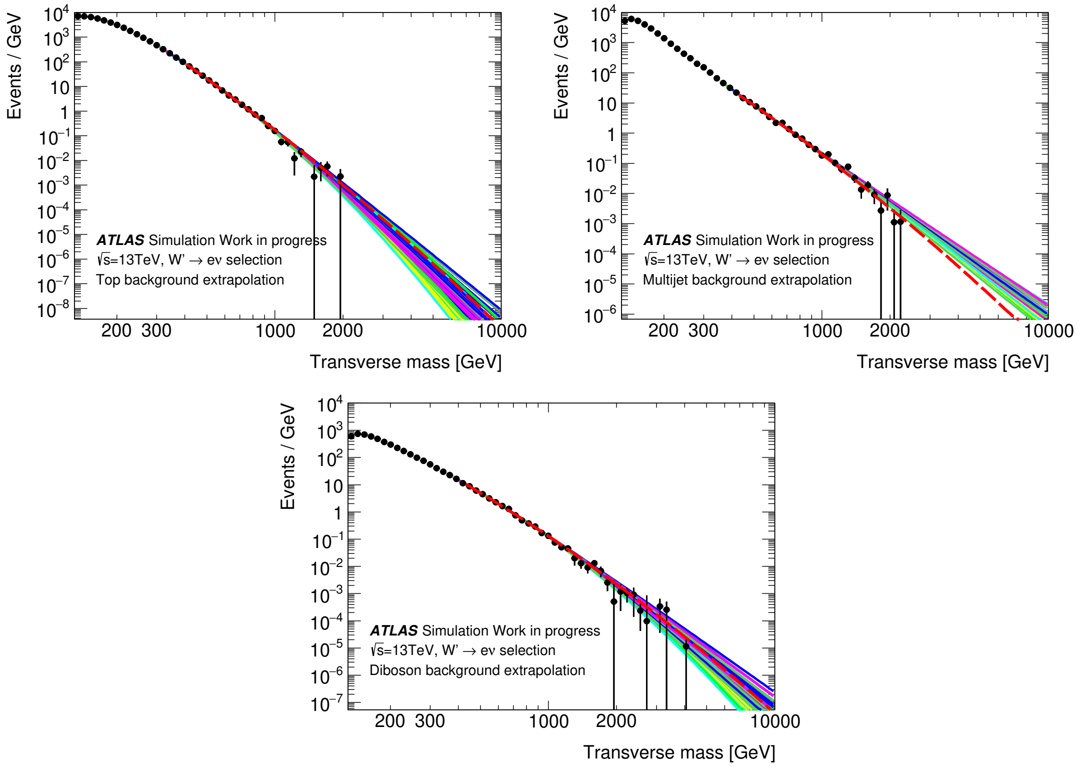

Figure 5.10: Results of fitting and extrapolation for the top, multijet and diboson backgrounds. The full set of individual fits can be seen, with the central value given by the dashed red line. The envelope of all these fits gives the associated uncertainty due to this extrapolation.

5.7 Scale factors and calibrations

Differences in detector response between data and Monte Carlo can be corrected for by the application of scale factors. Within the ATLAS collaboration, there are dedicated groups who study such differences and provide the analysis teams with scale factors to apply to their Monte Carlo (and sometimes data). Examples of such scale factors are the electron trigger, reconstruction, identification and isolation efficiencies [97]. By studying the efficiencies or energy scales in both data and MC, small differences are observed, from which can be derived scale factors to account for this small mis-modelling. These type of scale factors are applied as an event-wise weight to deteriorate the Monte Carlo in order to better model the data. The total weight of the event is equal to the product of all individual scale factor weights.

Furthermore, the pileup distribution of the Monte Carlo is corrected to more closely resemble that of the data. This is necessary as the pileup profile is not known exactly before the data is taken, and therefore any Monte Carlo that is generated before the entire dataset has been collected will likely have an imperfect estimate of the pileup profile. An additional event-level weight is applied to account for this difference. Finally, the number of generated events are normalised to the measured luminosity by calculating

$$w_{lumi} = \frac{L \times \sigma \times \varepsilon_{filter}}{N_{gen}}, \tag{5.16}$$

where L is the luminosity of the recorded dataset, σ is the production cross section of the process, ε_{filter} is the filter efficiency (ratio of events kept after removing events deemed not-of-interest to the total number of generated events) and N_{gen} is the number of generated events. The Monte Carlo samples are scaled to higher orders in QCD or EW using a k-factor, hence providing a more accurate description of the process without the need to generate the full statistics at this order. The $t\bar{t}$ background is generated at NLO in QCD, and has an additional reweighting to correct it to NNLO [162].

In addition to applying scale factors, corrections can be applied to variables themselves, examples of which are the electron and jet energy scale calibrations. Both of these calibrations are applied to data and Monte Carlo, with centrally produced calibrations provided by Refs. [87] and [163]. The energy values in data are corrected to those provided by the groups, while in MC the simulated resolution is smeared in order to more closely resemble that of data. These groups also provide the systematic uncertainties associated with these calibrations, as seen in Section 5.8.

5.8 Systematic uncertainties

Evaluation of sources of systematic uncertainty is an important component of any search for new physics beyond the Standard Model. There are many potential sources of systematic uncertainty, broadly falling into two categories: experimental and theoretical. The following sections will give an overview of the main sources of each and how they are evaluated.

5.8.1 Experimental Uncertainties

As discussed previously, experimental calibrations lead to sources of potential systematic uncertainty. When there is a calibration applied to a quantity, taking the example of the energy scale calibration, there is a central value corresponding to the value of the applied scale factor, which has associated with it its own uncertainty. By shifting the central value by its uncertainty and applying this as the calibration, propagating the result through the entire analysis chain and evaluating how it effects the final result, one can obtain an estimate of the systematic effect of this calibration by comparing to the nominal result. Table 5.8 summarises the main sources of experimental uncertainty, the number of associated nuisance parameters and their references.

Uncertainty	Nuisance Parameters	Reference	Legend
Electron reconstruction efficiency	1	[98]	EL_EFF_Reco_TOTAL_1NPCOR_PLUS_UNCOR__1up
Electron trigger efficiency	1	[89]	EL_EFF_Trigger_TOTAL_1NPCOR_PLUS_UNCOR__1up
Electron isolation efficiency	1	[98]	EL_EFF_Iso_TOTAL_1NPCOR_PLUS_UNCOR__1up
Electron identification efficiency	1	[98]	EL_EFF_ID_TOTAL_1NPCOR_PLUS_UNCOR__1up
Electron energy resolution	1	[98]	EG_RESOLUTION_ALL__1up
Electron energy scale	1	[98]	EG_SCALE_ALL__1up
Jet energy resolution	8	[109]	JET_JER_DataVsMC__1up JET_JER_EffectiveNP_1__1up JET_JER_EffectiveNP_2__1up JET_JER_EffectiveNP_3__1up JET_JER_EffectiveNP_4__1up JET_JER_EffectiveNP_5__1up JET_JER_EffectiveNP_6__1up JET_JER_EffectiveNP_7restTerm__1up
$E_{\mathrm{T}}^{\mathrm{miss}}$ resolution parallel	1	[112]	MET_SoftTrk_ResoPara
$E_{\mathrm{T}}^{\mathrm{miss}}$ resolution perpendicular	1	[112]	MET_SoftTrk_ResoPerp
$E_{\mathrm{T}}^{\mathrm{miss}}$ scale	1	[112]	MET_SoftTrk_ScaleUp
Pileup	1	[164]	PRW_DATASF__1up
Multijet background extrapolation	1	[3]	QCD_extrapolation
Top background extrapolation	1	[3]	TTST_extrapolation
Diboson background extrapolation	1	[3]	DB_extrapolation
Multijet background normalisation	1	[3]	-

Table 5.8: Sources of experimental systematic uncertainty considered in the electron channel analysis. The Legend column shows the names of these nuisance parameters as shown in Figure 5.11.

Any given uncertainty can be estimated by using many nuisance parameters, or all the contributions can be considered as fully uncorrelated and summed in quadrature, leading to a slight overestimate in the uncertainty. Other than the missing energy and jet energy resolution uncertainties, this analysis assumed all nuisance parameters associated with a given source of systematic uncertainty are fully correlated. This has the benefit of simplifying the statistical analysis, as well as ensuring that the estimate of the systematic uncertainty is slightly generous.

Not all sources of systematic uncertainty are estimated by shifting some nominal scale factor by its uncertainty however. For instance, the multijet background normalisation, as well as the multijet, top and diboson background extrapolation uncertainties are all estimated by the analysis team. As discussed previously, the mulitjet background normalisation uncertainty is estimated by varying the selection used in the determination of the fake efficiency, while the uncertainty associated to each of the background extrapolations is estimated by taking the envelope of all fits performed as the total systematic uncertainty.

Figure 5.11 shows all sources of experimental systematic uncertainty on the total background considered in the electron channel analysis. Not all of these sources of systematic uncertainty are considered in the final statistical analysis, as some sources have a negligible impact on the final uncertainty (some examples of which are jet energy resolution and scale uncertainties). The systematic uncertainties associated with the missing energy are dominant in the low-m_{T} region, while the background extrapolation uncertainties dominate the high-m_{T} region.

Only experimental systematic uncertainties are considered for the signal Monte Carlo in the statistical analysis, shown in Figure 5.12 for the 1 TeV SSM signal template. As this signal template is only one of many across the entire mass spectrum, the uncertainty estimate is only really important around the pole mass under consideration, and the plot is just shown as an illustrative example. In the limit setting procedure (Section 5.10.1), all of the signal templates have associated to them their respective errors.

As can be seen from Figure 5.11, by far the dominant systematic at high-m_{T} is the multijet background extrapolation, while at low-m_{T} the dominant contribution comes from the jet energy resolution (JER) uncertainties. The distributions in the figure have also been smoothed using the ROOT TH1::Smooth function, which is based on the "hsmoof" algorithm [165]. As the shape of the systematics influences the statistical analysis, this is an important step, as fluctuations due to low Monte Carlo statistics can lead to unphysical structures in the shapes of the systematics.

Some systematic uncertainties have an additional smoothing applied due to large fluctuations, particularly at high-m_{T}. This was achieved by rebinning the distribution before smoothing, in order to reduce large bin-by-bin fluctuations due to limited statistics. The electron identification efficiency systematic also has further smoothing applied, due to a sharp discontinuity at around $m_{\mathrm{T}} > 500\,\mathrm{GeV}$. This discontinuity is a result of the fact that the tag-and-probe method of estimating the efficiency runs out of statistics at high mass. To counteract this effect, a flat uncertainty of 5% was used in the region $m_{\mathrm{T}} > 500\,\mathrm{GeV}$ with a smooth straight line below $m_{\mathrm{T}} < 500\,\mathrm{GeV}$.

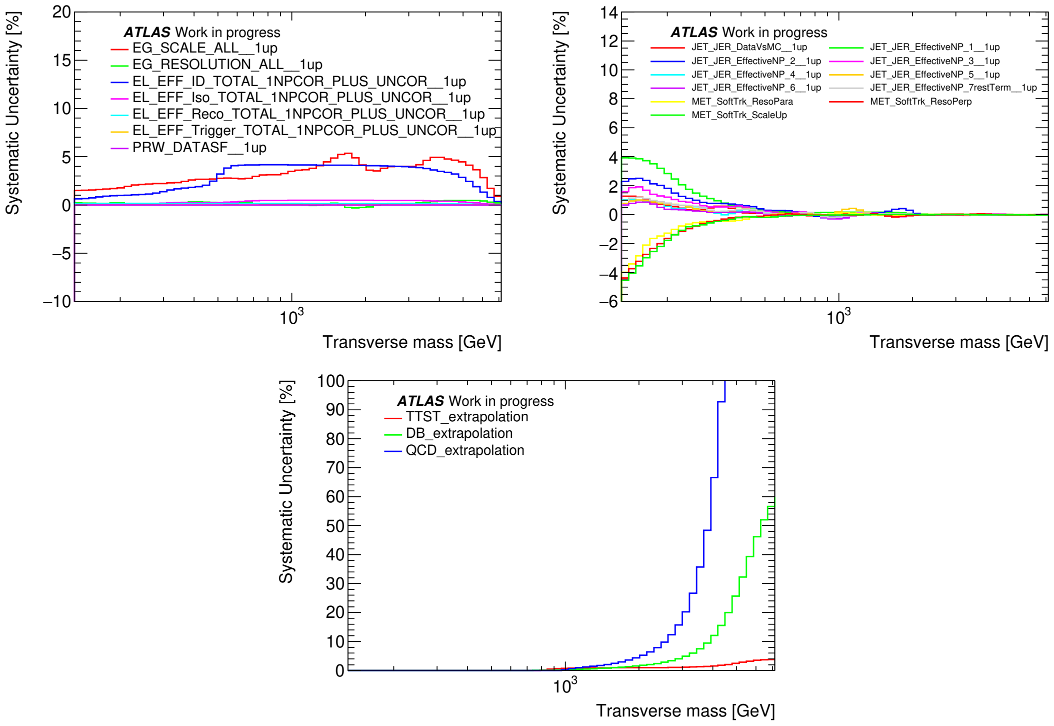

Figure 5.11: Relative experimental systematic uncertainties on the total background yield in the electron channel.

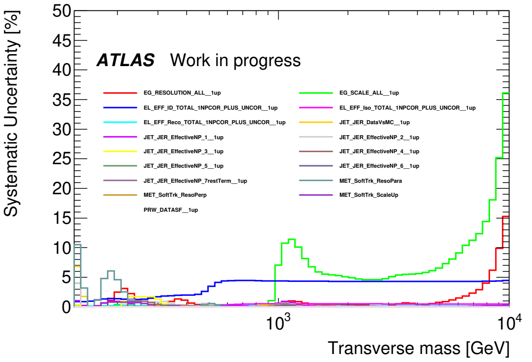

Figure 5.12: Relative experimental systematic uncertainties on the $m = 1\,\mathrm{TeV}$ SSM signal in the electron channel. The electron energy scale (green line) and resolution (red line) are the dominant uncertainties at high-m_{T}.

5.8.2 Theoretical uncertainties

The main sources of theoretical uncertainty in this search are the PDF uncertainties at high-m_{T}, which effect the cross section (event yield) of the background processes. In this analysis, the PDF uncertainties are only applied to the charged and neutral current Drell-Yan Monte Carlo background samples. No theoretical uncertainty is calculated for the signal Monte Carlo as this would be model dependent, especially in the case of EW corrections.

The primary evaluation of the PDF uncertainties comes from the eigenvectors of the nominal PDF choice. These are asymmetric systematic uncertainties associated with the nominal CT14 NNLO PDF fit, and are evaluated at 90% CL by varying the central value of each fit parameter by its uncertainty and repeating the fit. There are 28 such eigenvectors associated with the nominal PDF set used to generate the Drell-Yan background samples (CT14NNLO). To efficiently follow mass-dependent shape changes, these were bundled into 7 nuisance parameters (EV1-7), each of which propagated to a k-factor calculation which is then used to calculate the effect of the PDF systematic uncertainties on the event yields in the analysis.

The predicted cross sections obtained using the CT14NNLO PDF set are compared to predictions obtained using other PDF sets (MMHT2014 [166], CT14 [157], NNPDF3.0 [155], ABM12lhc [167], HERAPDF2.0 [168], JR14 [169]). Each of these predictions falls within the total uncertainty of the CT14NNLO PDF set, except for the NNPDF3.0 and HERAPDF2.0 predictions. An additional uncertainty is therefore applied to account for the fact that the predictions from NNPDF3.0 do not fall within the 90% CL uncertainty band of the CT14NNLO PDF set (REDCHOICE); the HERAPDF2.0 is not accommodated for since the HERA fits do not include data with high Bjorken x. This uncertainty becomes large at high transverse mass, approximately 30%, due to the difficulty of predicting PDFs at low Bjorken x. For NLO EW corrections, the difference between the additive and factorised k-factor approaches is also taken as an estimate of the systematic uncertainty. The full set of PDF uncertainties for the charged and neutral current Drell-Yan backgrounds can be found in Figure 5.13.

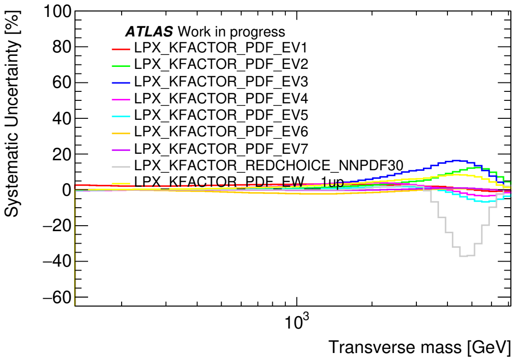

Figure 5.13: Relative theoretical systematic uncertainties on the total background yield in the electron channel.

A further source of uncertainty is the top background normalisation, which arises due to variations in the PDF and α_s values leading to a roughly 6% uncertainty on its normalisation. An additional systematic uncertainty is considered due to the mis-modelling in a top control region, defined by inverting the muon veto, thereby selecting events containing a signal like electron and a loose muon. By fitting the data/MC ratio with a smooth function, one can obtain a correction which in principle could be applied to the Monte

Carlo to more closely resemble data. Rather than changing the central value however, this function was simply used to define an additional systematic to the top background.

5.9 Kinematic distributions

Figure 5.14 shows a comparison of data and Monte Carlo after final signal selection for the main kinematic distributions studied in the analysis. Good agreement is observed across most of the phase space with some minor discrepancies observed at large pseudorapidities, as well as an excess of data/Monte Carlo in the low $E_{\mathrm{T}}^{\mathrm{miss}}/m_{\mathrm{T}}$ region, similar to what is seen in the multijet validation region.

The transverse mass distribution for each data taking period can be seen in Figure 5.15. No background extrapolation is applied to the top, multijet and diboson backgrounds in this figure. An excess of data is observed with respect to the expected Standard Model background in the low-m_{T} region, ranging from 10% at $130\,\mathrm{GeV}$ to approximately unity at around $200\,\mathrm{GeV}$. Figure 5.16 shows the transverse mass spectrum when taking into account the nuisance parameter pulls from a background only fit, and also applying the background extrapolation to the top, multijet and diboson backgrounds as discussed in Section 5.6. In the low-$E_{\mathrm{T}}^{\mathrm{miss}}/m_{\mathrm{T}}$ region, the jet energy resolution and $E_{\mathrm{T}}^{\mathrm{miss}}$ soft term nuisance parameters are significantly pulled, and taking into account these pulls brings the agreement between data/background closer to unity across the whole spectrum.

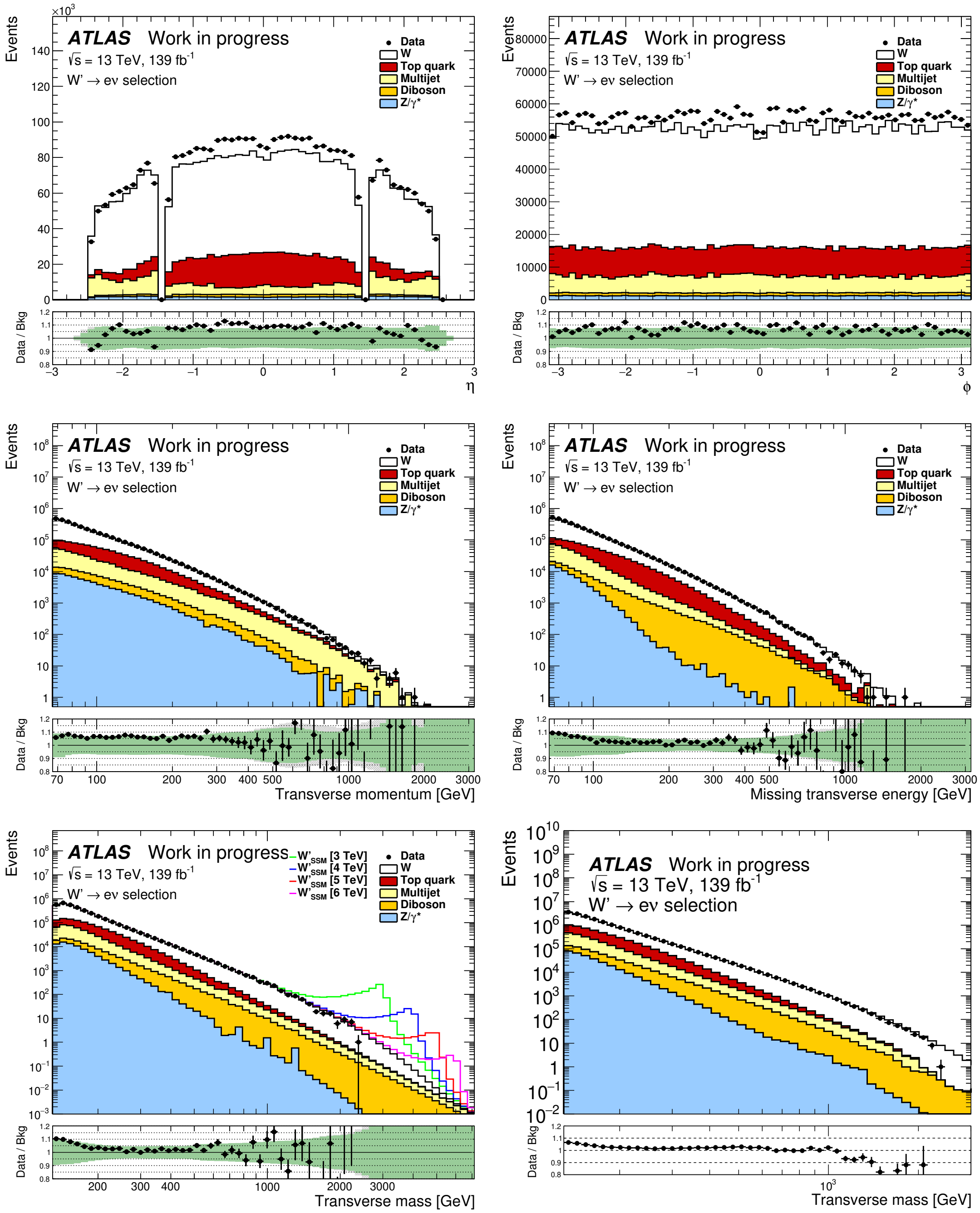

Figure 5.14: Electron channel kinematic distributions at final selection, shown with their full associated systematic uncertainties. Top: electron pseudorapidity (left), electron azimuthal angle (right). Middle: electron transverse momentum (left), missing energy (right). Bottom: transverse mass (left), cumulative transverse mass (right).

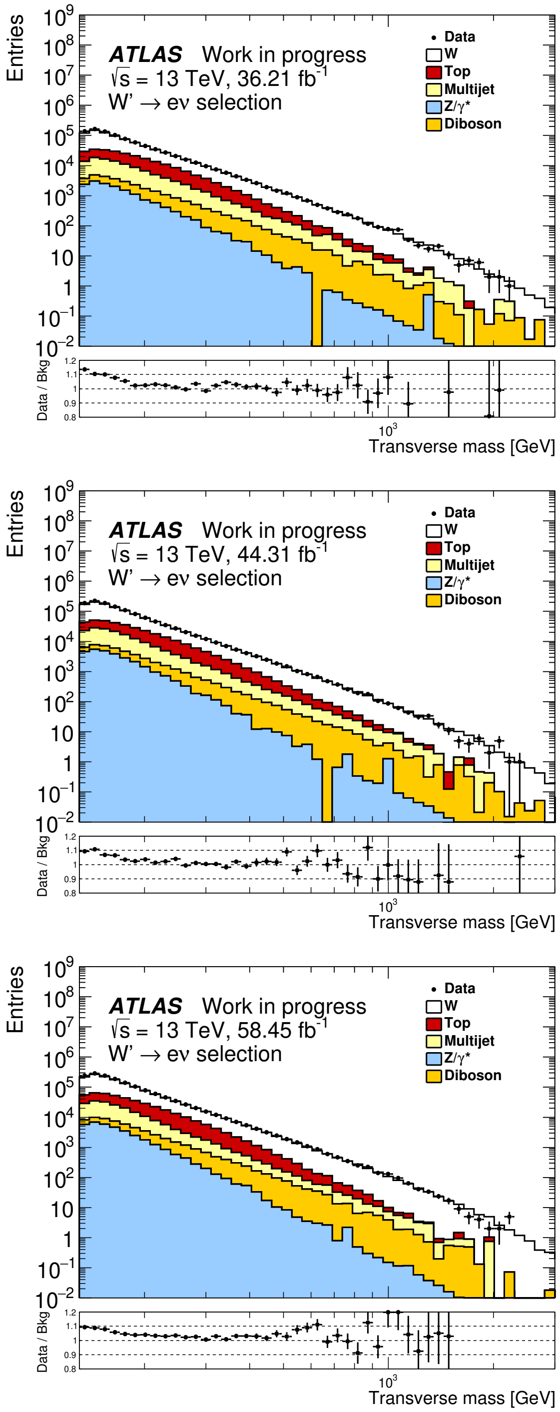

Figure 5.15: Transverse mass distribution in the electron channel after final selection for the 2015+2016 (top), 2017 (middle) and 2018 (bottom) datasets individually.

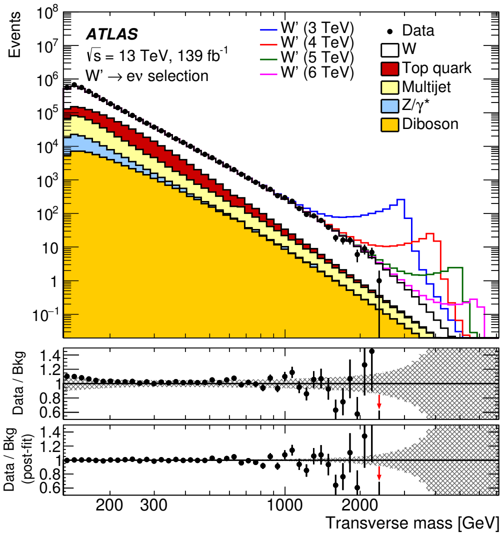

Figure 5.16: Transverse mass distribution in the electron channel including a post-fit ratio panel which takes into account the pulls on the nuisance parameters observed in the statistical analysis. Figure source: plot produced by M. K. Bugge using input data provided by the author [3].

5.10 Results

Table 5.9 shows the selected number of data and background events in different regions of transverse mass. All background event estimates are displayed with their associated statistical and systematic uncertainties, as well as being fully weighted to reconstruction level, and so can be compared directly to the data. Also displayed is the expected number of SSM W' events for different mass hypotheses in the range 2 - 6 TeV. As no excess is observed in data with respect to the total SM background, limits on the production cross section are set.

Process	m_{T} [GeV]					
	130-400	400-600	600-1000	1000-2000	2000-3000	3000-10000
W	2300000 ± 200000	25700 ± 1400	6000 ± 400	740 ± 60	18.0 ± 2.2	1.07 ± 0.21
Top	550000 ± 33000	5650 ± 280	580 ± 40	27 ± 8	0.28 ± 0.20	0.018 ± 0.016
Multi-jet	330000 ± 50000	2110 ± 320	400 ± 60	40 ± 12	1.1 ± 1.4	0.1 ± 0.4
Diboson	55500 ± 2700	1200 ± 60	247 ± 15	26 ± 5	0.7 ± 0.4	0.09 ± 0.11
$Z/\gamma*$	78000 ± 17000	190 ± 50	18 ± 7	1.5 ± 3.0	0.0113 ± 0.0018	0.00035 ± 0.00012
Total SM	3320000 ± 250000	34800 ± 1500	7200 ± 400	830 ± 80	20.2 ± 3.1	1.3 ± 0.5
Data	3538403	35568	7358	818	17	0
W' (2 TeV)	574 ± 22	720 ± 40	2190 ± 120	12200 ± 600	1130 ± 290	3.20 ± 0.25
W' (3 TeV)	68.4 ± 1.9	58.6 ± 2.6	127 ± 7	448 ± 22	860 ± 40	87 ± 23
W' (4 TeV)	19.6 ± 0.5	13.2 ± 0.5	22.1 ± 1.1	44.3 ± 2.2	49.2 ± 2.3	86 ± 4
W' (5 TeV)	7.85 ± 0.19	4.99 ± 0.18	7.26 ± 0.35	9.9 ± 0.5	5.82 ± 0.28	13.6 ± 0.7
W' (6 TeV)	3.76 ± 0.09	2.35 ± 0.08	3.28 ± 0.16	3.82 ± 0.18	1.41 ± 0.07	2.01 ± 0.10

Table 5.9: Number of selected background events for different transverse mass regions, where the uncertainties include both statistical uncertainty and all systematic uncertainties. All backgrounds are fully weighted, as such the total background level can be compared directly to the selected data in the electron channel. The systematic uncertainty includes all systematic uncertainties which are included in the statistical analysis.

5.10.1 Statistical interpretation

A statistical analysis was performed to determine whether or not there is any evidence of new physics. A p-value scan was performed to calculate the probability that the background fluctuates to produce an excess equal to or greater than what is observed. The expected number of counts in each bin can be parameterised as the sum of the signal ($s_i(\sigma, \theta)$) and background ($b_i(\theta)$) components,

$$\lambda_i = s_i(\sigma, \theta) + b_i(\theta). \tag{5.17}$$

The parameter of interest (σ) is the cross section times branching ratio of the W' signal model, and the nuisance parameters (θ) account for the effect of systematic uncertainties in the background estimate. The expected number of signal and background events are described by the log-normal probability density function

$$x_i = \overline{x_i} \cdot \exp\left(\sum_{j=1}^{n_{\text{sys}}} \text{sgn}[(\delta x_i)_j]\, \theta_j \sqrt{\ln\left[1 + \left(\frac{(\delta x_i)_j}{\overline{x_i}}\right)^2\right]}\right), \tag{5.18}$$

where x_i represents either $s_i(\sigma, \theta)$ or $b_i(\theta)$ with central value $\overline{x_i}$, and $(\delta x_i)_j$ is the shift in x_i due to nuisance parameter θ_j. The probability density function in Eq. 5.18 is only log-normal when the nuisance parameters are Gaussian distributed, a constraint which is enforced when calculating the likelihood function later on. The central value for signal events is calculated as the product of the integrated luminosity $\mathcal{L}_{\text{int}}$, the cross section times branching ratio, the acceptance times efficiency (A) and the fraction of selected events in bin i (ε_i),

$$\overline{s_i} = \mathcal{L}_{\text{int}} \cdot \sigma \cdot A \cdot \varepsilon_i. \tag{5.19}$$

The central value of the background (b_i) is taken directly from the total background estimate, as detailed in Section 5.4.2 and Section 5.5. The likelihood function can then be constructed by assuming that the number of events in each bin is Poisson distributed

$$L(\sigma, \theta) = \prod_{i=1}^{n_{\text{bins}}} \frac{\lambda_i(\sigma, \theta)^{N_i} e^{-\lambda_i(\sigma, \theta)}}{N_i!} \tag{5.20}$$

where N_i is the observed number of events in bin i. To ensure that the signal and background distributions are log-normal the nuisance parameters are constrained to be Gaussian distributed ($f(\theta_i)$)

$$L(\sigma, \theta) \Rightarrow L(\sigma, \theta) \prod_{i=1}^{n_{\text{sys}}} f(\theta_i). \tag{5.21}$$

Eq. 5.21 corresponds to the single-channel case, which can be extended to multiple channels by summing over all channels in the likelihood function. To simplify the notation, the following discussion will pertain to a single channel, but the procedure is identical for multiple channels, once the correlations between their nuisance parameters has been accounted for. Once the likelihood has been constructed, the test statistic used to determine the p_0-value can be defined. A profile likelihood test statistic (q_0) is used,

$$q_0 = \begin{cases} 0 & \text{for } \hat{\sigma} < 0, \\ \\ -2\ln\left[\frac{L(0,\hat{\theta}_0)}{L(\hat{\sigma},\hat{\theta})}\right] & \text{for } \hat{\sigma} \geqslant 0, \end{cases} \tag{5.22}$$

where $\hat{\sigma}$ and $\hat{\theta}$ are the values that maximise the likelihood function, and $\hat{\theta}_0$ are the nuisance parameter values which maximise the likelihood function under the background only hypothesis and the signal cross section set to zero. Large q_0 values are obtained when there is a large excess of data with respect to the background only hypothesis. The restriction below $\hat{\sigma} < 0$ is due to the fact that the cross section of the process cannot be negative. The p_0-value corresponding to the observed test statistic (q_0^{obs}) is measured by calculating the probability of observing a value equal to or greater than the observed value under the background only hypothesis

$$p_0 = P(q_0 \geqslant q_0^{\text{obs}} | \sigma = 0), \tag{5.23}$$

where P is a Poisson distribution. The p_0-value can then be converted to a significance (S) using the quantile of the Gaussian distribution (Φ^{-1})

$$S = \Phi^{-1}(1 - p_0) = \sqrt{2}\,\text{erf}^{-1}(1 - 2p_0). \tag{5.24}$$

Eq. 5.24 corresponds to the local significance, which describes the significance of an excess of data at a specific mass point. Since many mass points are probed, it is more useful to measure the global significance, which measures the probability observing an excess as significant as the one observed anywhere in the phase space of all mass points. The global significance (p_{global}) can be obtained by measuring the probability density function of all local significances ($f(S)$), and using the relationship

$$p_{\text{global}} = \int_S^{\infty} f(S)\, dS. \tag{5.25}$$

This is also known as the look elsewhere effect, and is necessary to properly determine the significance of any result due to the fact that many mass points are used and a p value of $1/n$ is expected to occur once (on average) for every n measurements. In the absence of any globally significant results upper limits are set on the W' signal cross section. This is done using the Bayesian technique implemented in

ROOT [170], where the cross section is assumed to be zero for $\sigma < 0$ and constant for $\sigma \geqslant 0$. Upper limits on the cross section are set at 95% confidence level (CL), meaning that the W' boson only has a 5% chance of existing below this limit, which is the standard level used in exotic physics searches. Observed limits are obtained from the data directly, while the expected limits are obtained by sampling a Poisson distribution of central value $\bar{b}_i$ under the background only hypothesis ($s_i(\sigma, \theta) = 0$). Frequentist limits were also calculated following the procedure outlined by Ellis Kay [171]. In the case of the SSM, 10% (20%) agreement was obtained between the Bayesian and frequentist observed (expected) limit, see Appendix B.4 for further details. A contributing factor to this level of agreement could also be the use of the asymptotic approximation in the frequentist analysis, whereby the test statistic is assumed to be Gaussian and Wilks' theorem is used to sample the distribution [172]. This reduces the computational load of the calculations, but is limited by the lack of statistics in the high mass region.

5.10.2 Sequential Standard Model limits

As was the case in previous rounds of the analysis, the primary interpretation of the results is in the context of the Sequential Standard Model. Continuing to provide updated limits in this context allows for a comparison with previously published results to see how the sensitivity increases with luminosity, and also allows for a comparison with the corresponding CMS result as the same model is used there. Signals are generated for many different pole masses, using the full signal line shape in the limit setting procedure and neglecting interference effects. The mass grid used in the analysis aims to provide good coverage across the entire spectrum, with mass points ranging from 150 GeV to 7 TeV, ensuring a high level of statistical precision.

Figure 5.17 shows the observed and expected upper limits on $\sigma(pp \rightarrow W' \rightarrow \ell\nu)$ at 95% CL in the electron, muon and combined channels. These results are then converted to a lower limit on the W' mass by finding the point at which the theoretical cross section intercepts with the observed and expected limit measurements, as summarised in Table 5.10. The limits obtained in the muon channel are weaker than those of the electron channel, due to the worse acceptance and momentum resolution at high mass (Figure 5.3). In the combined channel, an observed (expected) lower limit of 6 TeV (5.8 TeV) is set at 95% CL on the mass of W' bosons in the context of the SSM, dominated by the sensitivity of the electron channel at high-mass.

The agreement between the observed and expected limits in the electron channel is approximately 2σ, due to a deficit of signal-like events at high-m_{T}. This was studied by loosening the identification requirements from LHTight to LHLoose, and removing the isolation requirement completely. Doing so tests whether or not the deficit is a result of some inefficiency in the chosen working points. The ratio of the number of events selected using the nominal and loosened selection probes the efficiency of the ID

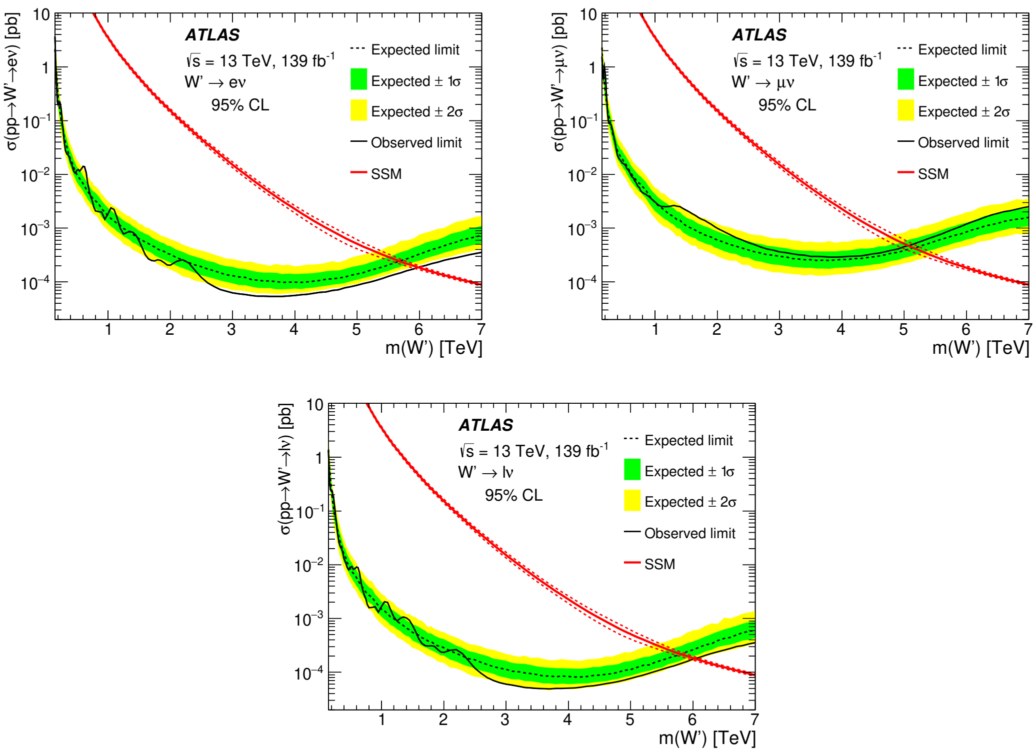

Figure 5.17: W' cross section limit results for the electron (top-left), the muon (top-right) and combined channels (bottom). Figure source: plot produced by M. K. Bugge using input data provided by the author [3].

	$m_{W'}$ lower limit [TeV]	
Decay	Expected	Observed
$W' \to e\nu$	5.7	6.0
$W' \to \mu\nu$	5.1	5.1
$W' \to \ell\nu$	5.8	6.0

Table 5.10: Expected and observed 95% CL lower limit on the W'_{SSM} mass in the electron and muon channels and their combination.

and isolation working points as a function of m_{T}, since an inefficiency would lead to a decreasing ratio towards high masses. No such gradient was observed, suggesting that the deficit of events is a feature of the data and not a result of acceptance effects.

In order to quantify the dependence of the limits on the parton luminosity tail, limits were placed on a restricted signal template by isolating the peak region only. The peak region is defined as $m_{\ell\nu} > 0.85 \times m(W')$, which was found to be optimal based on a study of the acceptance times efficiency for different pole mass cuts. These cuts were placed on the generator level invariant mass distributions, where the invariant mass of the electron neutrino system is well defined, and applied to both the signal shape and acceptance. The limits obtained with these truncated signal templates can be seen in Table 5.11. As expected, these limits are not as strong as those obtained using the full signal templates, as the width of the signal increases with increasing mass, thereby causing high-mass signals to have considerable low-mass tails. The observed (expected) limits are weaker by approximately 300 GeV (100 GeV) in the electron channel, and 50 GeV (50 GeV) in the muon channel, suggesting that even though the low-mass tail is considerable, it does not greatly effect the obtained mass limits. The difference is most noteworthy in the electron channel observed limit, where due to the deficit of events at high-m_{T}, the sensitivity to the parton luminosity tail is increased.

	$m_{W'}$ lower limit [TeV]	
Decay	Expected	Observed
$W' \to e\nu$	5.58	5.71
$W' \to \mu\nu$	5.05	5.04
$W' \to \ell\nu$	5.68	5.79

Table 5.11: Expected and observed 95% CL lower limit on the W'_{SSM} mass in the electron and muon channels and their combination. The numbers correspond to the limits calculated using signal templates with a generator level mass cut of $m_{\ell\nu} > 0.85 \times m(W')$.

5.10.3 Generic signal model interpretation

An interpretation with generic signal models of fixed Γ/m ranging from 1% to 15% is also presented. These signal models were produced by reweighting the same flat Monte Carlo as described in Section 5.4.1, however instead of calculating the relative width using an SSM calculation, fixed values of $\Gamma/m = 1\%, 2\%, 5\%, 10\%$ and 15% are used. Such signal samples are completely independent of the specifics of any given W' model, as the relative width is fixed for each individual mass point and does not come from a model prediction. These limits can therefore be interpreted in the context of any given model which predicts a W' signal with one of the widths presented, hence greatly increasing the theoretical scope of the analysis.

In order to reduce the dependence on the parton luminosity tail, which can be model dependent, these limits are set on the fiducial cross section defined by applying an invariant mass cut of $m_{l\nu} > 0.3 \times m_{W'}$ in the acceptance calculation. The full signal template is used over the entire mass range, but the acceptance is calculated relative to the fiducial phase space defined by the mass cut, meaning that the full signal template is normalised using the fiducial cross section. Figure 5.18 shows observed and expected limits on the fiducial cross section at 95% CL in the electron and muon channels, as well as their combination. The limits become relatively flat at high mass, as the total cross section has a larger component in the low-mass tail removed by the fiducial mass cut. These limits appear to be stronger than those obtained in Section 5.10.2, however it is important to consider that the corresponding fiducial theoretical prediction would also be lower at high-mass, so it is not necessarily the case that more stringent limits would be obtained.

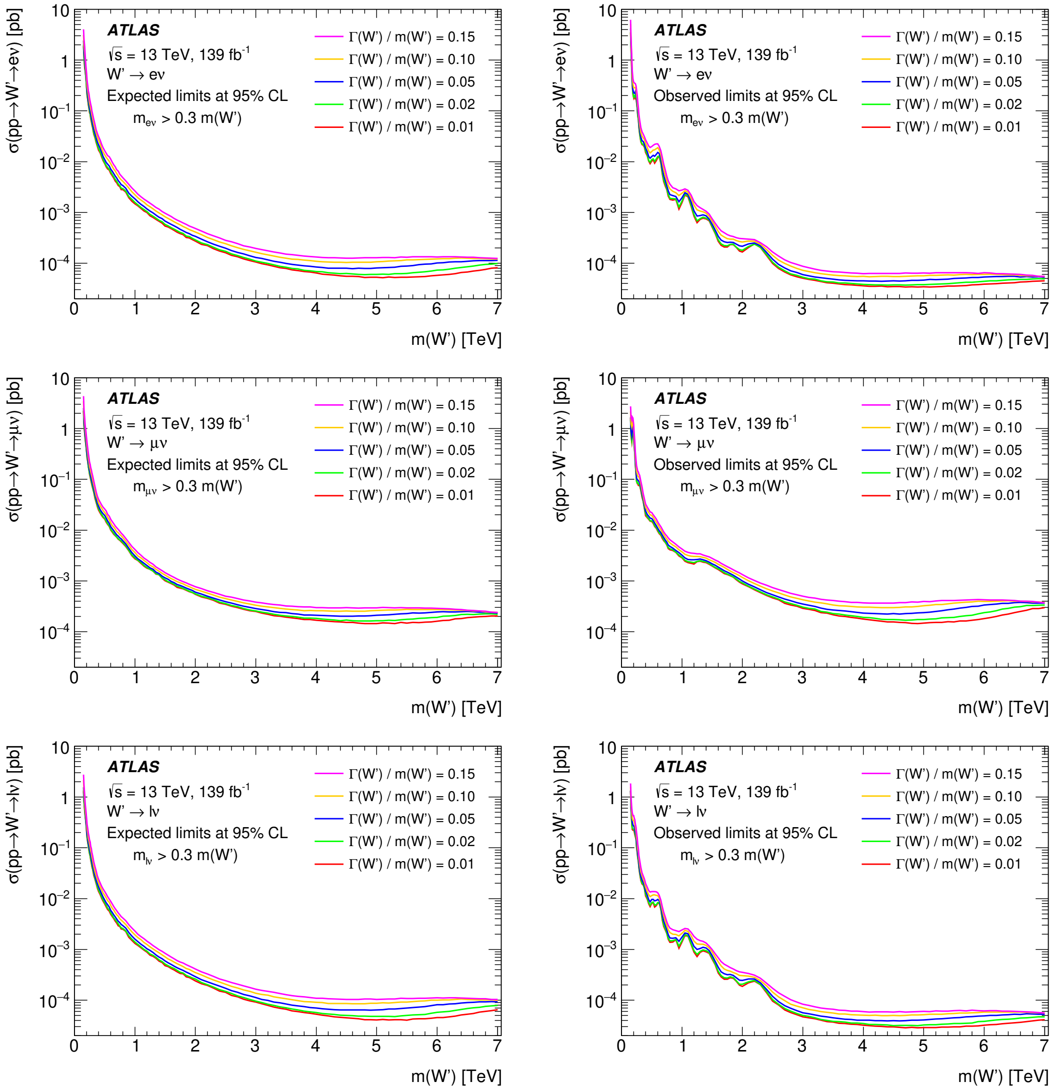

Figure 5.18: Expected (left) and observed (right) limits in the electron channel (top), muon channel (middle) and their combination (bottom). Figure source [3]. Plot produced by M. K. Bugge using input data provided by the author.

5.10.4 Model independent interpretation

Completely model independent limits are also set on the visible cross section, i.e. on the number of "signal like" events per unit of luminosity. These limits are set as a function of m_{T}^{min}, which is the threshold m_{T} above which the visible cross section is defined. This can be thought of as a variety of single-bin signal regions, where the signal region is defined by the lower limit on m_{T}. The obtained limits can then be interpreted in the context of any given model, by comparing the observed number of events in data to the expected background and model prediction; no assumption needs to be made about the kinematic properties of the W' boson in this interpretation. Figure 5.19 shows the observed and expected limits at 95% CL in the electron channel, with numerical results provided in Table 5.12. The observed visible cross section limit ranges from $4.6\,\mathrm{pb}$ at $m_{\mathrm{T}}^{min} = 130\,\mathrm{GeV}$ to 22 ab at high-m_{T}. Table 5.12 also provides limits on the number of expected signal events (N_{sig}) for $139\,\mathrm{fb}^{-1}$ of pp data; the visible cross section is a more universal quantity since it is independent of the total integrated luminosity of the data. The observed number of signal like data (N_{data}) and background (b) events are also shown.

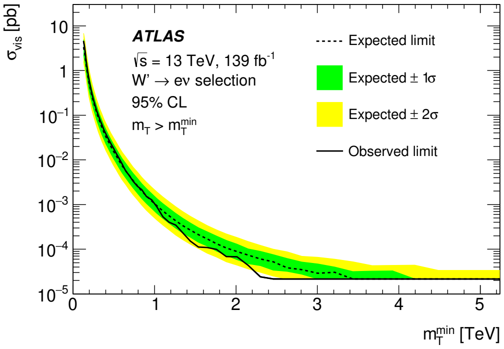

Figure 5.19: Model independent limit on the visible signal cross section σ_{vis} at final selection as function of the m_{T} threshold $m_{\mathrm{T}}^{\mathrm{min}}$ for the electron channel. Figure source [3]. Plot produced by M. K. Bugge using input data provided by the author.

$m_{\mathrm{T}}^{\mathrm{min}}$ [GeV]	N_{data}	b	Δb	Upper limit at 95% CL			
				$N_{\mathrm{sig}}^{\mathrm{obs}}$	$N_{\mathrm{sig}}^{\mathrm{exp}}$	$\sigma_{\mathrm{vis}}^{\mathrm{obs}}$ [pb]	$\sigma_{\mathrm{vis}}^{\mathrm{exp}}$ [pb]
130	3582164	3360000	250000	6.4×10^5	4.6×10^5	4.6	3.3
139	3018934	2850000	200000	5.1×10^5	3.8×10^5	3.7	2.7
149	2345269	2240000	150000	3.6×10^5	2.8×10^5	2.6	2.0
159	1784938	1720000	110000	2.5×10^5	2.0×10^5	1.8	1.4
170	1352988	1310000	80000	1.7×10^5	1.4×10^5	1.3	1.0
182	1028353	1000000	60000	1.2×10^5	1.1×10^5	0.90	0.76
194	784509	770000	40000	9.1×10^4	7.7×10^4	0.66	0.55
208	599989	588000	31000	6.7×10^4	5.8×10^4	0.48	0.42
222	459843	451000	23000	5.0×10^4	4.4×10^4	0.36	0.31
237	352825	347000	18000	3.8×10^4	3.4×10^4	0.27	0.24
254	270299	267000	14000	2.9×10^4	2.6×10^4	0.21	0.19
271	207728	204000	11000	2.3×10^4	2.0×10^4	0.16	0.15
290	159319	157000	8000	1.7×10^4	1.6×10^4	0.13	0.11
310	122150	120000	6000	1.4×10^4	1.2×10^4	0.10	0.088
331	93335	92000	5000	1.1×10^4	9.5×10^3	0.078	0.069
354	71416	70000	4000	8.6×10^3	7.4×10^3	0.062	0.053
379	54642	53500	3100	6.6×10^3	5.8×10^3	0.048	0.042
405	41745	40800	2400	5.3×10^3	4.5×10^3	0.038	0.033
433	31792	31100	1900	4.1×10^3	3.6×10^3	0.030	0.026
463	24257	23600	1500	3.3×10^3	2.8×10^3	0.023	0.020
495	18484	18000	1200	2.6×10^3	2.2×10^3	0.019	0.016
529	13937	13600	900	1.9×10^3	1.7×10^3	0.014	0.012
565	10548	10300	700	1.5×10^3	1.3×10^3	0.011	0.0096
604	7938	7800	500	1.1×10^3	1.0×10^3	0.0080	0.0074
646	5926	5900	400	7.8×10^2	8.0×10^2	0.0056	0.0057
691	4469	4470	330	6.2×10^2	6.2×10^2	0.0044	0.0044
739	3342	3360	250	4.6×10^2	4.8×10^2	0.0033	0.0034
790	2499	2510	190	3.6×10^2	3.7×10^2	0.0026	0.0026
844	1876	1850	140	3.0×10^2	2.8×10^2	0.0022	0.0020
902	1358	1370	110	2.1×10^2	2.2×10^2	0.0015	0.0016
965	1021	1010	80	1.8×10^2	1.7×10^2	0.0013	0.0012
1031	727	740	60	1.2×10^2	1.3×10^2	0.00088	0.00093
1103	495	540	50	74	1.0×10^2	0.00053	0.00072
1179	354	390	40	56	78	0.00040	0.00056
1260	260	278	27	48	60	0.00035	0.00043
1347	175	198	20	33	47	0.00024	0.00034
1441	113	140	15	21	37	0.00015	0.00027
1540	74	98	11	16	29	0.00011	0.00021
1647	55	68	8	15	24	0.00011	0.00017
1760	39	46	6	14	19	9.9×10^{-5}	0.00013
1882	23	31	5	9.6	15	6.9×10^{-5}	0.00011
2012	17	20.9	3.4	9.4	12	6.8×10^{-5}	8.9×10^{-5}
2151	8	13.7	2.5	6.0	10	4.3×10^{-5}	7.4×10^{-5}
2300	1	8.9	1.8	3.4	8.4	2.4×10^{-5}	6.1×10^{-5}
2458	0	5.7	1.4	3.0	7.3	2.2×10^{-5}	5.2×10^{-5}
2628	0	3.6	1.0	3.0	5.3	2.2×10^{-5}	3.8×10^{-5}
2810	0	2.2	0.8	3.0	4.9	2.2×10^{-5}	3.5×10^{-5}
3004	0	1.3	0.6	3.0	4.1	2.2×10^{-5}	2.9×10^{-5}
3212	0	0.8	0.5	3.0	4.2	2.2×10^{-5}	3.1×10^{-5}
3434	0	0.5	0.4	3.0	3.0	2.2×10^{-5}	2.2×10^{-5}
3671	0	0.28	0.28	3.0	3.0	2.2×10^{-5}	2.2×10^{-5}
3924	0	0.16	0.22	3.0	3.0	2.2×10^{-5}	2.2×10^{-5}
4196	0	0.09	0.17	3.0	3.0	2.2×10^{-5}	2.2×10^{-5}
4485	0	0.05	0.13	3.0	3.0	2.2×10^{-5}	2.2×10^{-5}
4795	0	0.03	0.10	3.0	3.0	2.2×10^{-5}	2.2×10^{-5}
5127	0	0.02	0.08	3.0	3.0	2.2×10^{-5}	2.2×10^{-5}

Table 5.12: Electron channel model independent limits on the expected number of signal events (N_{sig}) and corresponding visible cross section (σ_{vis}) at final selection for different m_{T} thresholds ($m_{\mathrm{T}}^{\mathrm{min}}$). The number of observed events in data is also presented (N_{data}), as well as the expected SM background (b) and its associated uncertainty (Δb). Table source [3].

5.10.5 Heavy resonance combination

Many different searches for new heavy gauge bosons are performed at ATLAS which can be combined to increase their sensitivity. The previous combination of heavy resonance results decaying to bosonic and leptonic final states was published by ATLAS using 36 fb^{-1} of pp data at $\sqrt{s} = 13$ TeV [173]. A full Run-2 analysis is currently ongoing using 139 fb^{-1} of data, and extending the channels to include hadronic final states, as well as final states containing τ leptons. This section will present some preliminary results of the $W' \to \ell\nu$ inputs to this combination.

The W' and Z' searches can be combined in the context of the HVT model, which predicts the existence of a new triplet state $\mathcal{W}$, where the charged W' states are degenerate in mass with the neutral Z' state [143, 144]. Signal templates were generated using the HVT model prediction (Section 5.2), with couplings of $g_q = 0.5540$, $g_\ell = 0.5540$ and $g_H = 0.5596$, where $g_{q,\ell,H}$ represent the coupling strength between the triplet field $\mathcal{W}$ and the quark, lepton, and Higgs fields. To reduce the effects of interference with SM processes, a generator level mass cut of $(m_\mathrm{T} - m_\mathrm{pole})/\sqrt{m_\mathrm{pole}} < \sqrt{8\,\mathrm{GeV}}$ is applied to the signal shape and the acceptance. This restricts both the line shape and the cross section to the fiducial phase space, which should cancel out in the normalisation to yield a limit on the total HVT cross section in the absence of interference.

Figure 5.20 shows the upper limits on the cross section at 95% CL in the electron and muon channels. The corresponding observed (expected) lower mass limits at 95% CL are 5.3 TeV (5.3 TeV) in the electron channel and 4.6 GeV (4.7 GeV) in the muon channel. These limits are slightly weaker than those obtained in the context of the SSM (Section 5.10.2), due to the loss of acceptance at high-m_T ($m_\mathrm{T} > 1\,\mathrm{TeV}$) due to the mass cut applied to the signal templates.

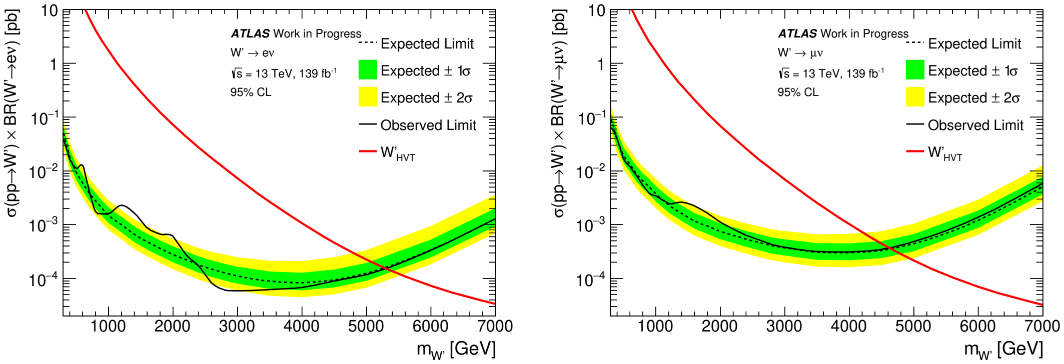

Figure 5.20: HVT signal templates with generator level $(m_\mathrm{T} - m_\mathrm{pole})/\sqrt{m_\mathrm{pole}} < \sqrt{8\,\mathrm{GeV}}$ cut. The sharp up-turn in the limit is a result of loss of acceptance at high-m_T due to the mass cut. Plots produced by the author, where the input $W' \to \mu\nu$ data was provided by M. K. Bugge.

In addition to the HVT signal interpretation, a generic signal model of fixed Γ/m was also investigated, using the same procedure as outlined in Section 5.10.3. The largest Γ/m value that is probed over the phase space covered by the analysis is approximately 5%, which is then used as a conservative estimate for all mass points. This interpretation uses the narrow width approximation (NWA), which assumes that the W' boson is always produced very near to its pole mass (and not off-shell) and that there is no interference between W' and SM W. In practice this is achieved by applying a generator-level mass cut of $m_{\ell\nu} > 0.3 \times m_{W'}$ to the signal shape only, but not applying any mass cut to the acceptance. This ensures that the cross section of the reduced template is equal to the full W' signal cross section, thus assuming that it is all concentrated in the "peak" region. The same procedure is followed in the $Z' \to \ell\ell$ channel [30], where $\Gamma/m = 2.5\%$.

Figure 5.21 shows the limits for these signal models overlaid with the HVT model prediction. As expected, these limits become flat at high mass due to a large part of the signal being concentrated in the low mass tail. These results are similar to those obtained in Section 5.10.3, although those limits were set on the fiducial cross section and these are set on the total cross section under the narrow width approximation. These signal templates will be propagated to the full combination analysis, where 2-dimensional limits will be set on the coupling between the triplet field and quarks, leptons and the Higgs boson.

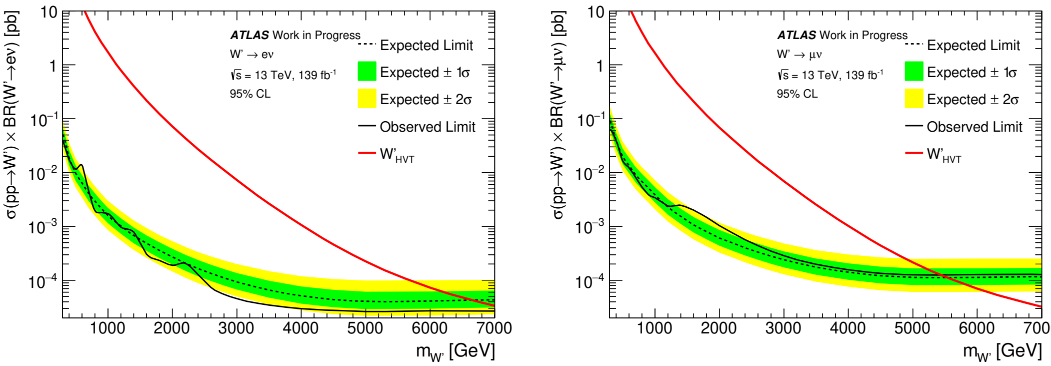

Figure 5.21: Generic templates with fixed $\Gamma/m = 5\%$ and a generator level mass cut of $m_{\ell\nu} > 0.3 \times m_{W'}$ applied to the signal shape only, i.e. under the narrow width approximation. Plots produced by the author, where the input $W' \to \mu\nu$ data was provided by M. K. Bugge.

5.11 Conclusion

A search for a new heavy resonance decaying into a lepton-neutrino pair has been presented in this chapter. The transverse mass of the lepton-neutrino system is used as the discriminating variable in this search, and no significant deviations are found between the data and the Standard Model background prediction. Upper limits are set on the $pp \to W' \to \ell\nu$ cross section at 95% CL. Different model interpretations are provided in the context of the Sequential Standard Model and Heavy Vector Triplet model, as well as generic limits that can be interpreted by a range of models. In the context of the SSM, a lower limit of 6 TeV is set on the mass of the W' boson by combining the statistics of the electron and muon channels. This result is dominated by the sensitivity of the electron channel in the high-mass region, where the muon channel suffers from poor resolution. Preliminary results are presented in the context of the HVT model using both a HVT model prediction, as well as signals with a conservative Γ/m of 5% under the narrow width approximation.

Fiducial cross section limits are set on resonances of fixed Γ/m ranging from 1% to 15%, facilitating the reinterpretation of the results over a range of potential model predictions. Completely model independent results are provided by measuring the visible cross section (number of selected signal events per unit of luminosity) in single-bin signal regions defined by a minimum transverse mass threshold. These range from 4.6 (15) pb at $m_{\mathrm{T}}^{min} = 130$ (110) GeV to 22 (22) ab at high-m_{T} in the electron (muon) channel. The results of this search have also been used to constrain scalar leptoquark models which could explain the mystery of the discrepancy between the observed and expected magnetic dipole moment of the muon [174]. In addition to this, these results have been used to constrain heavy quark effective field theory (HQEFT) models by investigating the semi-leptonic decays of $\bar{B} \to D^{(*)}\ell\nu$ [175].

Chapter 6

Final remarks

This thesis focuses on the Drell-Yan production of gauge bosons at the ATLAS detector using the full Run-2 dataset recorded in $\sqrt{s} = 13\,\text{TeV}$ pp collisions, both in the context of the Standard Model (Z) and beyond (W').

The first analysis presents a new method for monitoring the luminosity recorded by the ATLAS detector by measuring the production rate of the Z boson. This is done independently in the $Z \to e^+e^-$ and $Z \to \mu^+\mu^-$ channels, which rely on different sub-detectors and have independent data-driven and simulated corrections. These measurements are made over time periods of approximately 60 seconds, which provides good granularity with respect to the changing conditions inside the detector. Excellent agreement is observed between the two-channels, with a mean absolute ratio of 0.992 across the entire Run 2 dataset; suggesting that the data-driven corrections are effectively modelling the detector inefficiencies.

The $Z \to e^+e^-$ and $Z \to \mu^+\mu^-$ luminosity estimates can be combined to an average $Z \to \ell^+\ell^-$ luminosity, all three of which can be used to monitor the stability of the baseline ATLAS luminosity measurement. By normalising the $Z \to \ell^+\ell^-$ luminosity to the same integrated luminosity as the baseline ATLAS measurement, the time and pileup stability can be monitored by measuring the spread of their ratio around unity. This can be done for each individual data-taking period, or for the whole of Run 2. The time-dependent ratio has a spread around unity of about 0.8% (2015) to 0.4% (2018), while the pileup-dependent ratio has a spread of approximately 0.4% (2015) to 0.1% (2018). Across the whole Run-2 period the time-dependent ratio has a spread of 0.8%, almost twice as large as the corresponding 2016–2018 spreads (the vast majority of the data). This method could contribute to an improved characterisation of the systematic uncertainties affecting the baseline ATLAS luminosity, as this large spread over the entire Run-2 period suggests that there are significant inter-year calibration scale differences in the baseline ATLAS luminosity measurement. These results were published in an ATLAS Public Note [1], and were presented at the 2020 ICHEP conference [2]. Additional comparisons with the track-counting-based luminosity are also presented. The ratio of the Z-counting and track-counting luminosities has a spread of 0.3% over the full Run-2 data-taking period, further indicating the excellent stability of the Z-counting method.

The second analysis covers a search for a new heavy charged gauge boson (W') and the author's contribution to one of the first ATLAS analyses using the full Run 2 dataset. No significant excesses were observed with respect to the Standard Model, and limits are set in the context of the Sequential Standard Model. In the combined channel, a world leading observed (expected) lower limit of $6\,\mathrm{TeV}$ ($5.8\,\mathrm{TeV}$) is placed on the mass of the W' boson at 95% CL, which is dominated by the high-mass sensitivity of the electron channel analysis presented within. Generic limits are also provided for signal templates of fixed Γ/m, ranging from 1% to 15%, which can then be reinterpreted in the context of any signal model with signals covered by this range. To further increase the model independence of these limits, a fiducial cut of $m_{\ell\nu} > 0.3 \times m_{W'}$ is applied to the signal models to reduce the dependence on the low-mass parton luminosity tail. Completely model independent results are also provided in single-bin signal regions, by setting upper limits the number of signal events and on the visible cross section above a given transverse mass threshold. The visible cross section limits range from 4.6 pb to 22 ab over the transverse mass range covered by the analysis. These results were published in Phys. Rev. D [3]. Preliminary results are also presented in the context of the Heavy Vector Triplet model as part of the ongoing heavy resonance combination analysis, where many channels are combined to increase the sensitivity to new neutral or charged gauge bosons.

Appendices

Appendix A: Z-counting auxiliary information

Dataset	Muon triggers	Electron triggers

2015 high-μ	`HLT_mu20_iloose_L1MU15`
	`HLT_mu50`
		`HLT_e24_lhmedium_L1EM20VH`
		`HLT_e60_lhmedium`
		`HLT_e120_lhloose`

2016-8 high-μ	`HLT_mu26_ivarmedium`
	`HLT_mu50`
		`HLT_e26_lhtight_nod0_ivarloose`
		`HLT_e60_lhmedium_nod0`
		`HLT_e140_lhloose_nod0`

Table A.1: Triggers used to select events for different datasets.

A.1 Modelling of tag-and-probe efficiencies

Comparing the tag-and-probe efficiencies (Section 4.2.2) obtained in data and Monte Carlo shows how well the simulation models real events recorded by the detector. The same tag-and-probe procedure is performed in both cases, with the only difference being that no background estimation is performed in Monte Carlo; events are required to be truth-matched instead (as discussed in Section 4.2.3). Figures A.1 and A.2 compare the single-lepton trigger and reconstruction efficiencies in each data-taking period with their corresponding Monte Carlo samples. In this comparison, the efficiencies in data are calculated for a single luminosity block, and a weighted average taken across the entire data-taking period as a function of $\langle\mu\rangle$. Figure A.3 shows a similar comparison of the combined even-level efficiency in data and Monte Carlo.

The single-electron trigger efficiencies in Monte Carlo agree with those of data to within around 2% in all data-taking periods except for 2016, where the agreement is at the 5% level. Similarly the single-electron reconstruction efficiencies show agreement at the 1-3% level, with the worst agreement again seen in the 2016 data-taking period. As these single-electron efficiencies are combined into an event-level efficiency (Eq. 4.13), the effects are compounded due to the presence of two electrons. This can be seen clearly in Figure A.3, where the data is described by the Monte Carlo to within around 2% in 2015, 2017 and 2018, but the agreement is much worse in 2016 at around 8%.

The single-muon trigger efficiencies show slightly worse agreement than the electron channel, at approximately 5% in all years. However, the single-muon reconstruction efficiency is extremely well modelled, with agreement within approximately 1% in all years. While there is some small mis-modelling of the event-level efficiencies present in both channels, it does not necessarily negatively impact the final results in data. The important thing is that the simulation correctly models the relationship between born level and reconstructed electrons, assuming that the same then applies to recorded data.

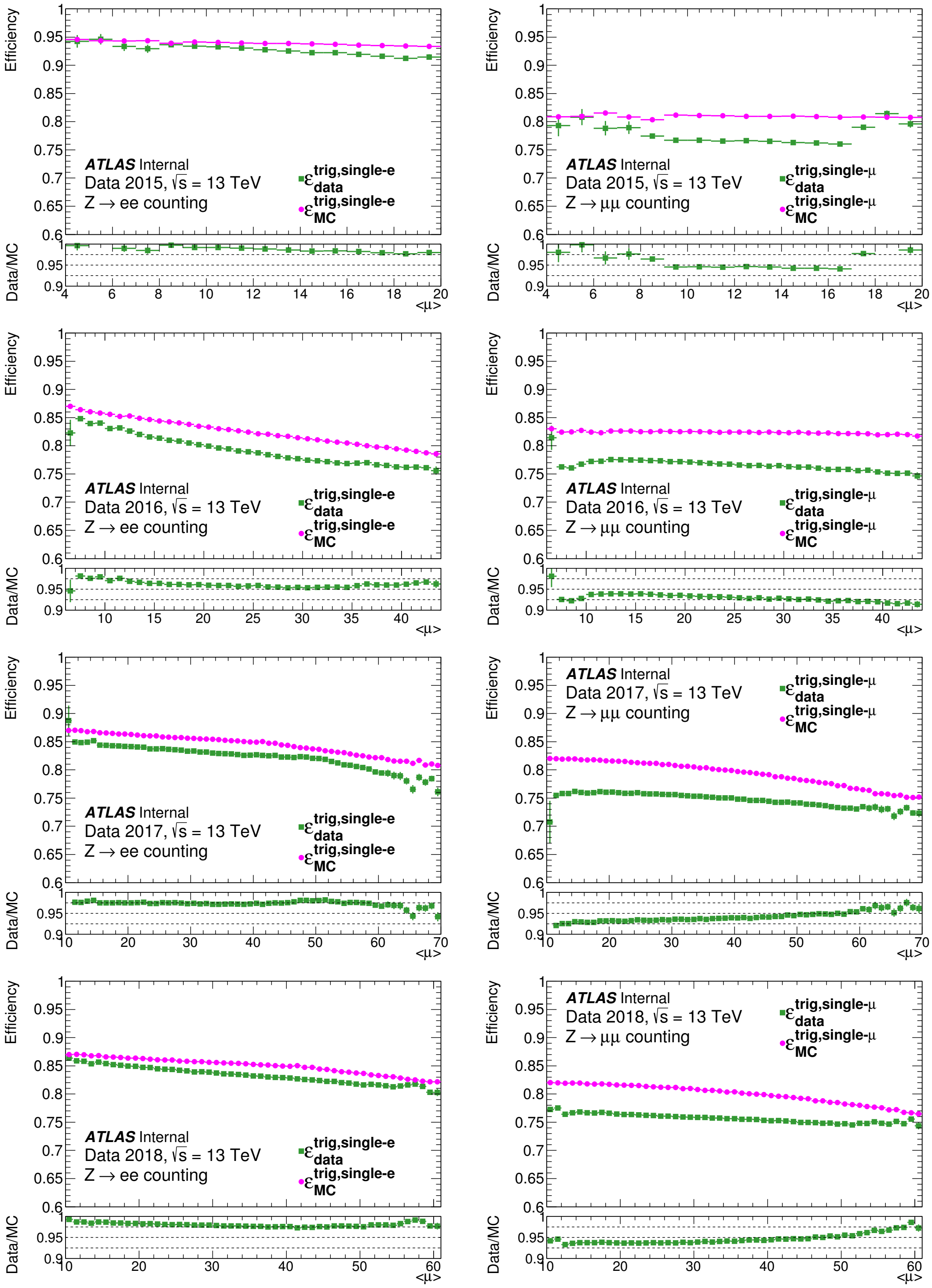

Figure A.1: Single-electron (left) and muon (right) trigger efficiency in data and Monte Carlo. The x-axis represents the average pileup parameter $\langle\mu\rangle$.

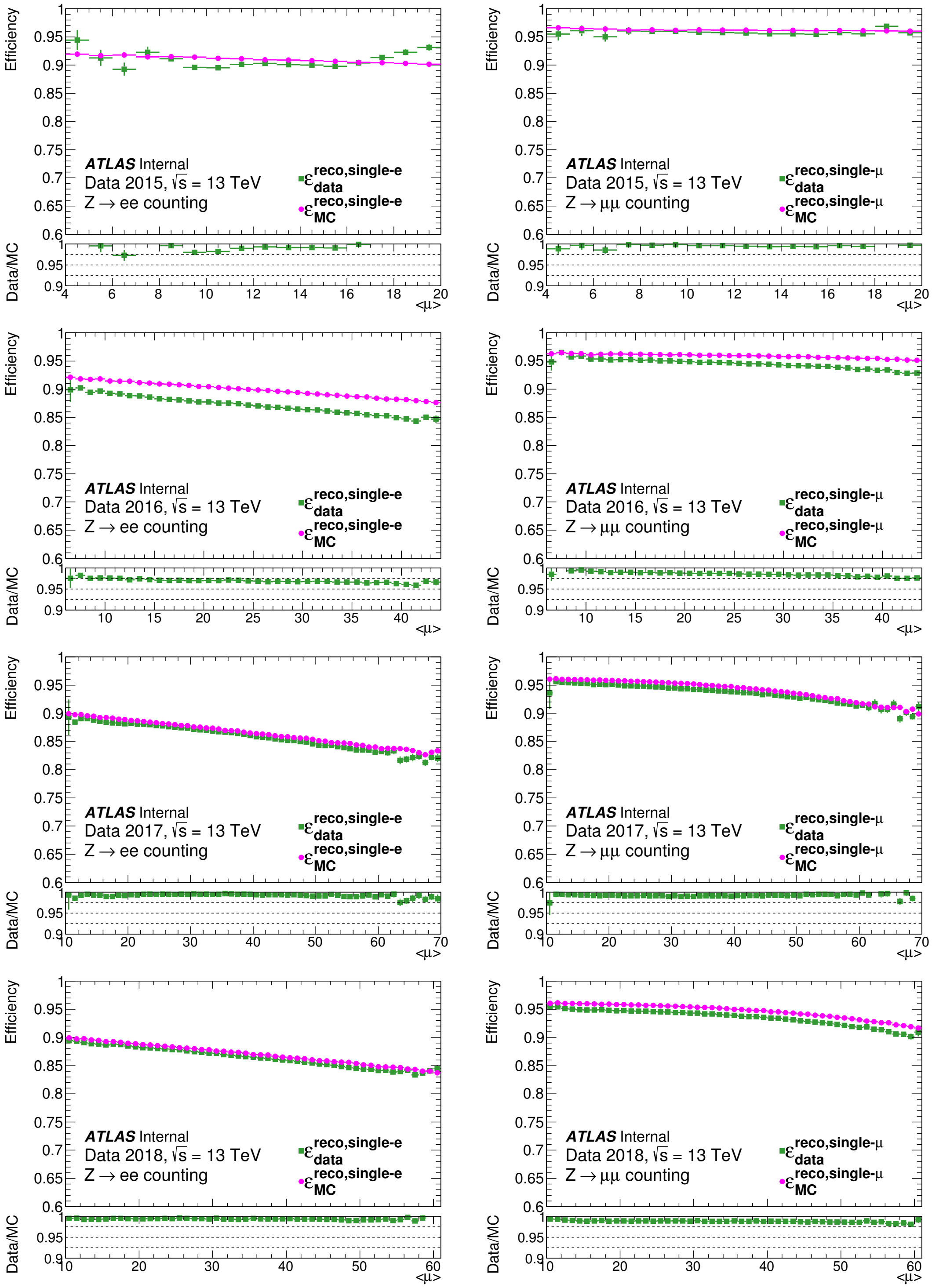

Figure A.2: Single-electron (left) and muon (right) reconstruction efficiency in data and Monte Carlo. The x-axis represents the average pileup parameter $\langle \mu \rangle$.

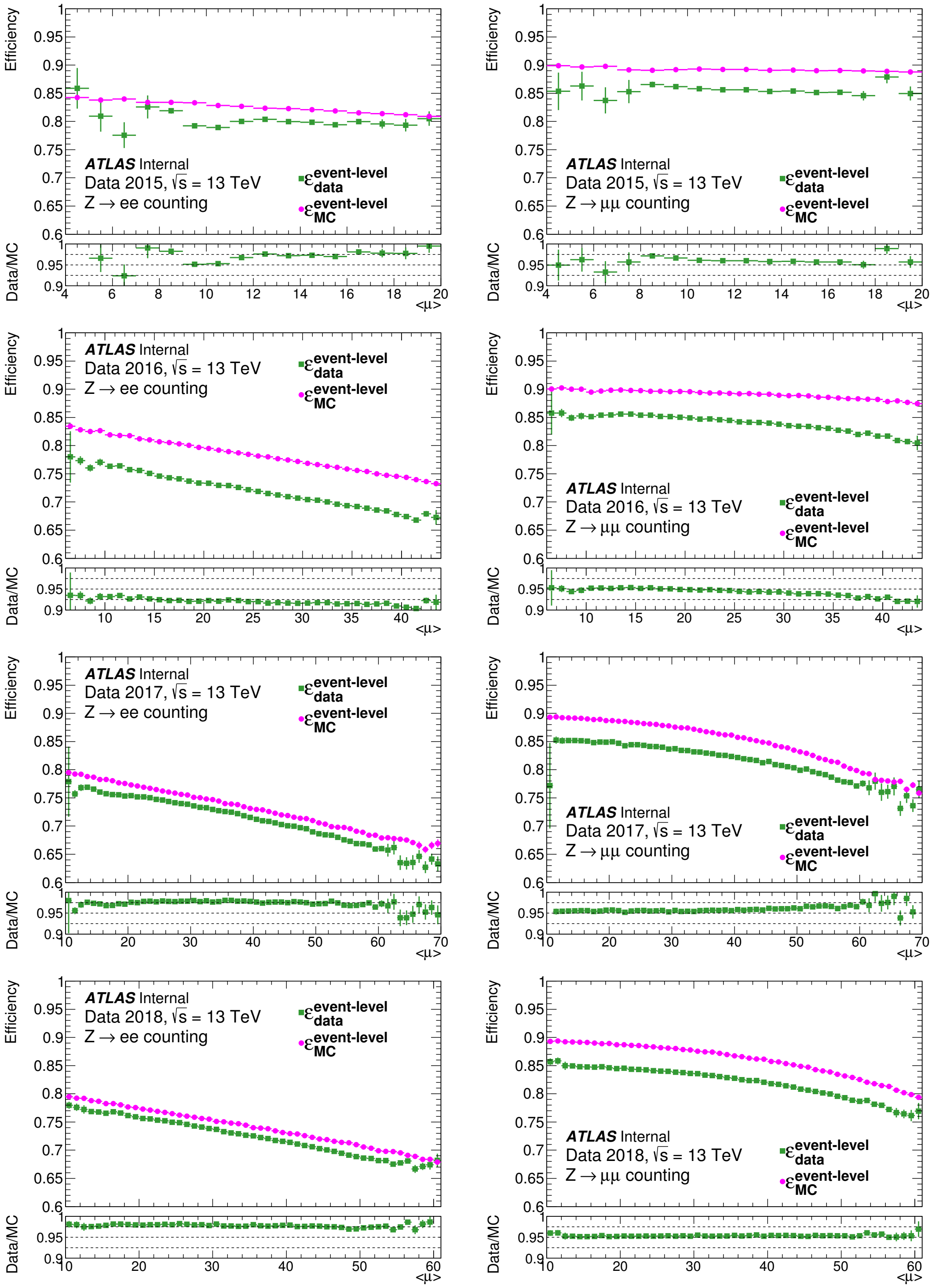

Figure A.3: Event-level (left) and muon (right) Z selection efficiency in data and Monte Carlo. The x-axis represents the average pileup parameter $\langle\mu\rangle$.

Appendix B: W' auxiliary information

B.1 Fake efficiency dilution

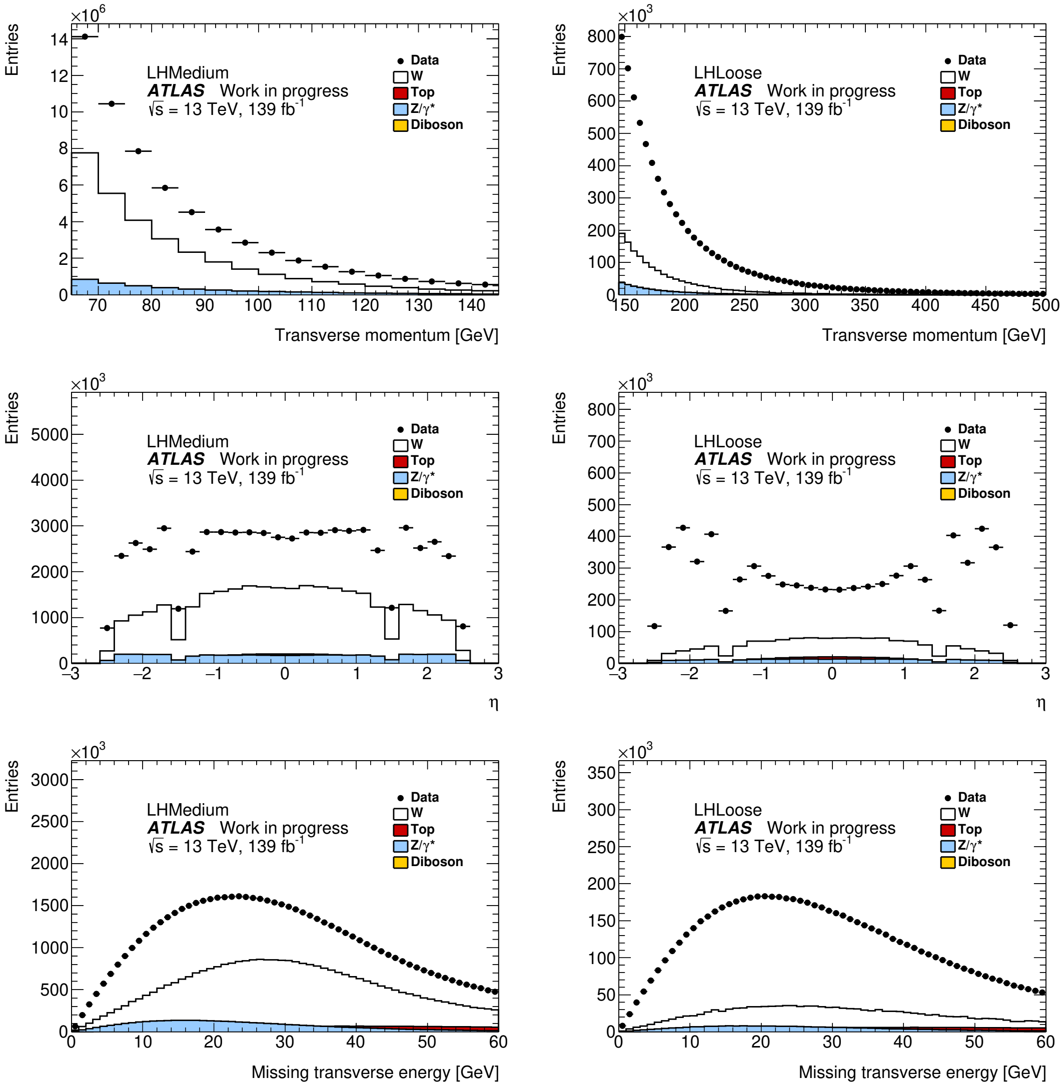

Figure B.1: Dilution in η, p_{T} and $E_{\mathrm{T}}^{\mathrm{miss}}$ for the two denominator categories.

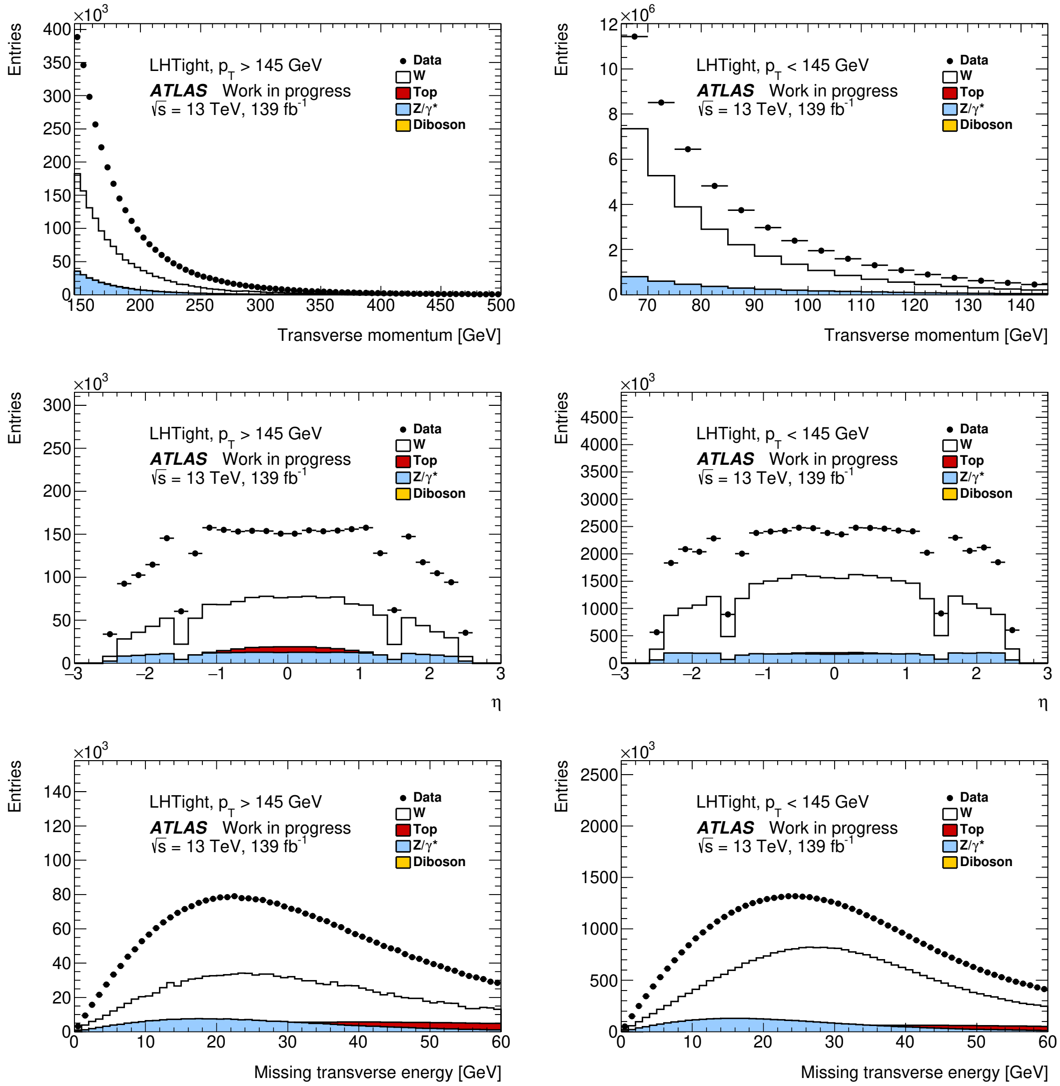

Figure B.2: Dilution in η, p_{T} and $E_{\mathrm{T}}^{\mathrm{miss}}$ for the two numerator categories.

B.2 High-m_{T} deficit

Throughout Run-2, a deficit of data with respect to the Standard Model background has been observed at high m_{T}. Presented is a study investigating the effect of loosening the identification and isolation requirements as a function of transverse mass, and the impact this has on the high-m_{T} deficit.

The nominal definition of the signal region requires electrons to pass LHTight identification and Gradient isolation, which was then loosened to LHLoose identification and no isolation requirement. Doing so allows one to test whether or not the deficit at high-m_{T} is a result of some inefficiency in the chosen working points. Figure B.3 shows the ratio of $(N_L + N_T)/N_T$ in Data (left), MC (right) and the ratio of Data/MC (bottom); where N_L is the number of events which pass LHLoose (exclusively), with no isolation requirement, and N_T is the number of events which pass the nominal signal selection (LHTight identification + Gradient isolation). Other than the differences in identification and isolation, all other selection cuts are identical.

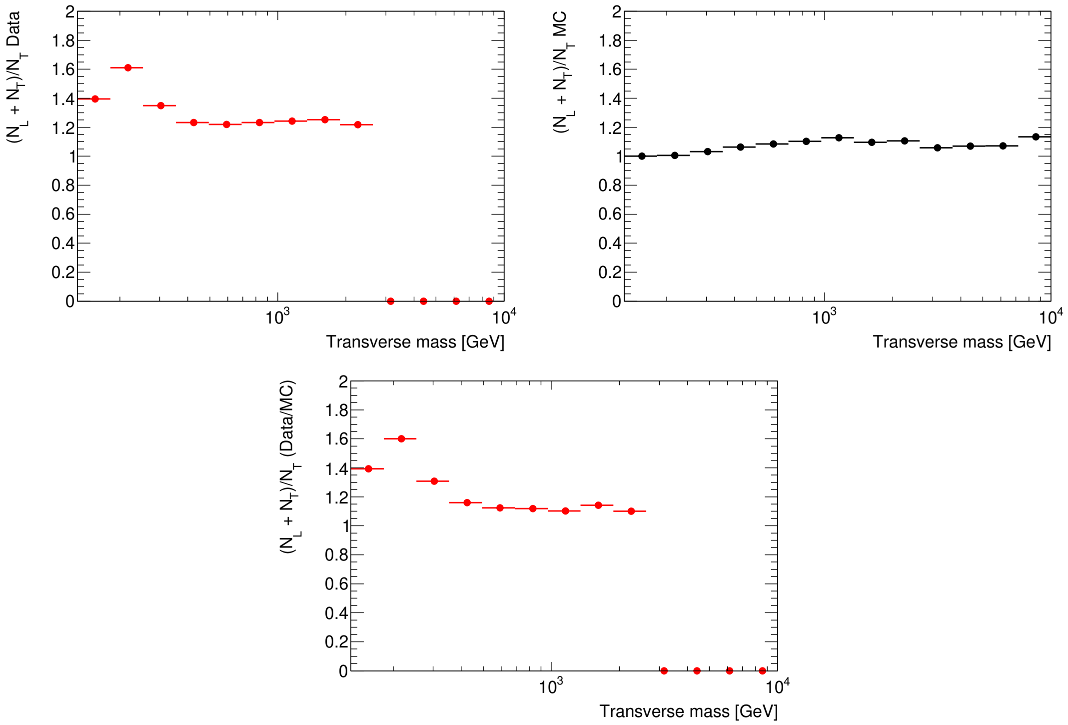

Figure B.3: Ratio of "loose" selection over "tight" selection.

If the high-m_{T} deficit was a result of some working point inefficiency, one would expect that the ratio would increase at higher transverse masses. As such an effect is not observed, it can be concluded that this is not in fact the case, while the actual cause of the deficit is still unknown. The excess in the ratio at low mass is likely a result of a higher multijet contribution in this region, which has low m_{T} in spite of having relatively high p_{T} ($p_{\mathrm{T}} > 145$ GeV cut applied to both numerator and denominator). This p_{T} cut is applied so that both regions are consistent, as the Loose region corresponds to the $p_{\mathrm{T}} > 145$ GeV region outlined in Section 5.5, while the nominal "Tight" definition only has a 65 GeV p_{T} cut applied.

B.3 Signal m_{T}-resolution

In order to help with reinterpretations, the electron/muon $p_{\mathrm{T}}/m_{\mathrm{T}}$ resolution was quantified. Focusing on the electron channel, the resolution was investigated by checking the migration of events in a small mass window around the 2, 4 and 6 TeV mass points. Here migration refers to the phenomena of electrons being reconstructed in a different bin of $p_{\mathrm{T}}/m_{\mathrm{T}}$ than they were generated in. The m_{T} resolution itself is made up of contributions from both the p_{T} and $E_{\mathrm{T}}^{\mathrm{miss}}$ resolutions, and by applying a similar procedure to these variables, the dominant contribution can be determing.

The resolution was determined by performing a Gaussian fit between -0.15 and 0.15, i.e. in the peak region only, with the standard deviation of this fit was then taken to be resolution. Example plots for the 2 TeV mass window can be seen in Figure B.4, while Table B.1 documents the p_{T}, $E_{\mathrm{T}}^{\mathrm{miss}}$ and m_{T} resolution for all mass points studied. These results show that the m_{T} resolution is in fact dominated by the $E_{\mathrm{T}}^{\mathrm{miss}}$ resolution component, as one would expect, and is of the order 1.0-1.3%.

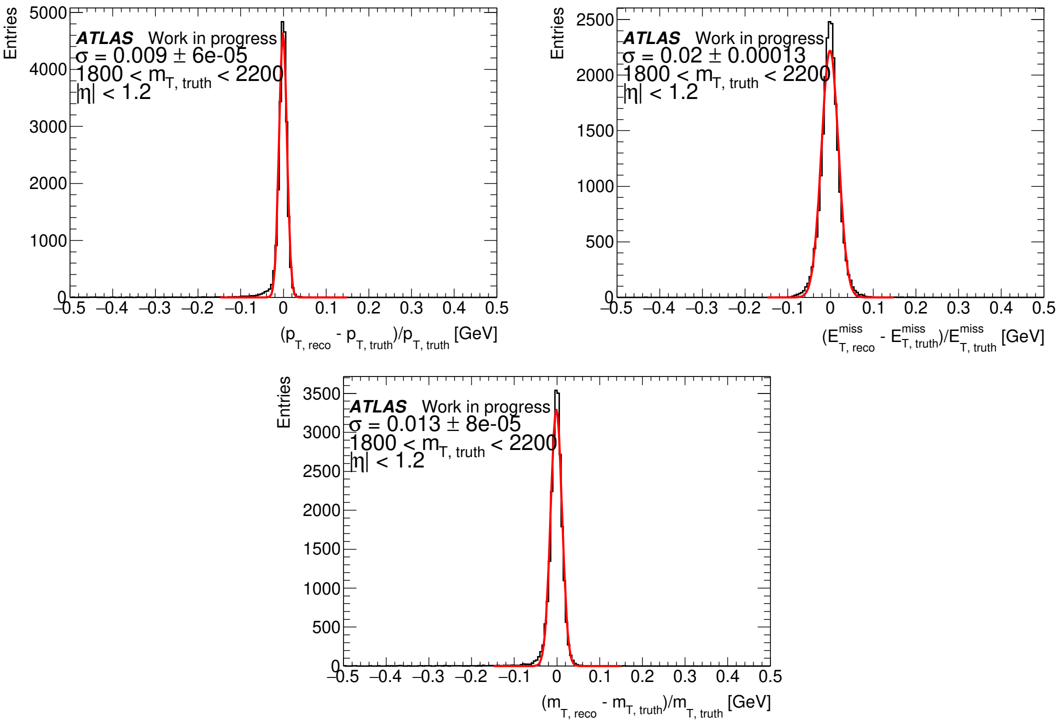

Figure B.4: Signal p_{T} (top), $E_{\mathrm{T}}^{\mathrm{miss}}$ (middle) and m_{T} (bottom) resolution of the 2 TeV W' signal in the electron channel.

Signal Mass [TeV]	p_{T}-resolution [%]	$E_{\mathrm{T}}^{\mathrm{miss}}$-resolution [%]	m_{T}-resolution [%]
2	0.9	2.0	1.3
4	0.9	1.3	1.0
6	0.9	1.2	1.0

Table B.1: Signal p_{T}, $E_{\mathrm{T}}^{\mathrm{miss}}$ and m_{T} resolution in a 400 GeV mass window around various mass hypotheses.

B.4 Frequentist limit setting

In addition to the Bayesian results presented in Section 5.10 a frequentist analysis was also performed. This interpretation follows the same procedure as outlined by Ellis Kay [171], using a profile likelihood test statistic similar to that used in the Bayesian analysis and the asymptotic approximation [176]. The asymptotic approximation refers to the assumption that the distribution of the test statistic is Gaussian, which in the limit of low statistics can start to break down. More accurate results can be obtained by performing pseudo-experiments, however these are much more computationally intensive and since the aim of this study is to cross check the limits obtained in the main analysis the asymptotic approximation is sufficient.

Figure B.5 shows the observed and expected limits obtained using the frequentist framework under the asymptotic approximation. The general shape and trend is similar to the limits shown in Figure 5.17, and Figure B.6 shows the ratio of the frequentist and Bayesian limits. The observed limits agree well at low mass with the agreement going to $\mathcal{O}(10\%)$ at high mass, and the same trend is seen in the expected limits, however the agreement at high mass is at the $\mathcal{O}(20\%)$ level. The discrepancy at high-mass is likely a result of the breakdown of the asymptotic approximation due to lack of statistics, however the general level of agreement is consistent with the results obtained in previous iterations of the analysis.

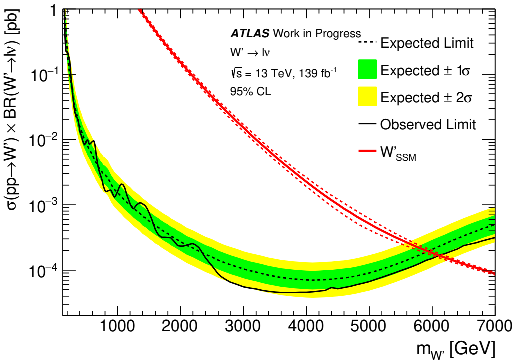

Figure B.5: Limits obtained in the frequentist analysis under the asymptotic approximation.

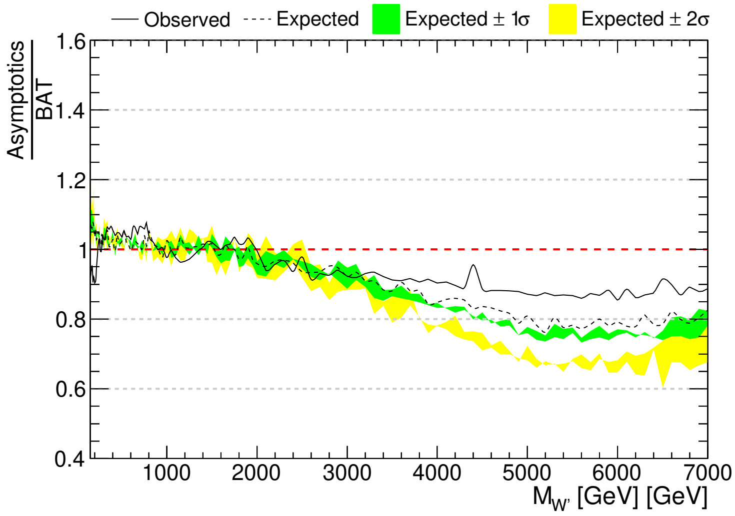

Figure B.6: Ratio of the observed, expected, 1σ and 2σ limit curves obtained using frequentist and Bayesian techniques.

Appendix C: Experimental test of Lorentz-invariance violation using $Z \to \ell^+\ell^-$ events

In addition to monitoring the luminosity delivered to the ATLAS detector, the framework outlined in Chapter 4 is also a powerful tool to test for time-dependent modulations in pp collisions as a result of interactions with Lorentz invariance violating fields. Since time-dependent detector inefficiencies are accurately accounted for over short time scales, this method is well suited to probing such modulations, as the Z production rate should be accurately corrected for changes in event selection efficiency.

C.1 Introduction

The independence of the physical parameters of a particle with respect to its direction of motion or velocity is a fundamental property of the Standard Model and is known as Lorentz invariance. All fields which obey Lorentz symmetry also obey CPT symmetry, which refers to the physical law that any particle is invariant under the simultaneous transformation of charge conjugation, parity inversion and time reversal [177]. Individually, each of these transformations do not form physical symmetries, and only the combination of all three transformations is a symmetry of the Standard Model (CP symmetry was found to be broken in 1964 by measuring the decay of neutral kaons [178]).

The Standard Model Extension (SME) is an effective field theory that extends the Standard Model to include General Relativity and operators that break Lorentz and CPT symmetry [35],

$$\mathcal{L}_{\text{SME}} = \mathcal{L}_{\text{SM}} + \mathcal{L}_{\text{GR}} + \mathcal{L}_{\text{Lorentz-violating}}. \tag{C.1}$$

The natural scale of this theory is the Planck mass (10^{19} GeV), which is well beyond the experimental reach of any existing collider experiment. However, small variations in the couplings of SM particles to a potential Lorentz-invariance violating field can be probed by measuring time-dependent modulations in experimental variables.

In the context of the SME, time-dependencies arise due to the rotation of the Earth on its axis, which transforms the couplings of the proposed Lorentz-invariance violating field. By convention, these couplings are defined in the Sun-centred reference frame, and the rotation of the Earth constitutes a transformation with period equal to one sidereal day. The Sun-centred frame has coordinates (T, X, Y, Z), where $T = 0$ is defined as the vernal equinox of the year 2000 (2000-03-20 07:35); X and Y are the basis vectors at a right ascension of 0° and 90° at time $T = 0$, and Z is the rotation axis of the earth [179]. This reference frame is illustrated in Figure C.1.

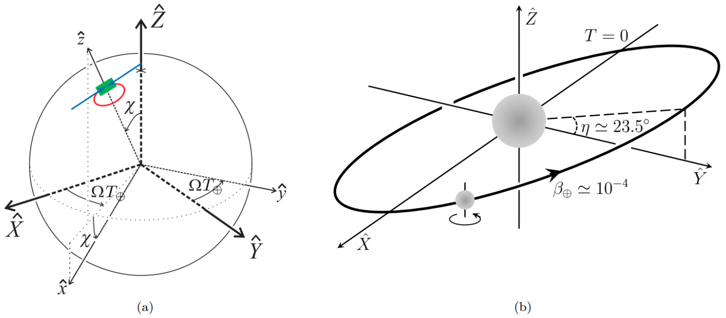

Figure C.1: Illustration of the Sun-centred coordinate system: (a) Earth (b) orbit of the Earth in the Sun-centred frame. Source: [180].

While this frame is the canonical choice in the literature, the results presented within are presented in the so called J2000 frame. This frame has a time origin of 2000-01-01 12:00, and should be consistent with the Sun-centred frame within a linear time translation. This difference in frame should be marginal and should not drastically impact the observation of sidereal time-dependent modulations. [1]

Sidereal time refers to the period of one rotation of the Earth around its axis and is measured by the amount of time between two successive meridian passages of a distant star. A sidereal day is equal to $23 : 56 : 04.1$ in solar time units, but can also be expressed as an angle of rotation, i.e. one sidereal day is equal to 2π radians. Measurements of the $t\bar{t}$ production cross section [181] and B_s^0 oscillation asymmetry [180] as a function of sidereal time have been performed by the D0 collaboration, however, no experimental evidence of Lorentz invariance has been observed.

C.2 Experimental methodology

In the SME, the cross section of $pp \to Z \to \ell^+\ell^-$ has a time dependence of the form

$$\sigma(t) \approx \sigma_{\text{ave}}(1 + f_{\text{SME}}(t)), \tag{C.2}$$

where t is the sidereal time, σ_{ave} is the time averaged cross section and f_{SME} is a function that encapsulates: the coupling between the SM particle and Lorentz-invariance violating field; the event kinematics in the lab frame; and a rotation matrix which transforms the kinematics from the lab frame to the Sun-centred frame.

---

[1] In the planned follow up analysis the Sun-centred frame will be used. These results are intended to be a proof-of-principle for the analysis.

As a result of Eq. C.2, in the presence of Lorentz invariance violating fields there are small periodic changes in the production cross section, which would therefore be visible in the number of reconstructed events. These modulations would have a period of one sidereal day, as the LHC proton beams rotate with the same frequency as the Earth's rotation relative to distant stars. The methodology outlined in Chapter 4 is well suited to such a measurement, as detector inefficiencies are modelled over short time periods in order to properly reflect the data-taking conditions at that time. The same event selection is applied as described in Section 4.2.1, and the same efficiency and Monte Carlo corrections applied to each 60 second interval of data. The corrected number of Z events and integrated luminosity is calculated for each 60 second interval, and then integrated in bins of sidereal phase (rotation angle divided by 2π). The fiducial cross section (σ) is then measured by

$$\sigma = \frac{N_Z}{\mathcal{L}_{\mathrm{ATLAS}}}, \tag{C.3}$$

where N_Z is the corrected number of selected Z events in each sidereal bin, and $\mathcal{L}_{ATLAS}$ is the corresponding baseline ATLAS integrated luminosity. In addition to calculating the fiducial cross section in each sidereal bin, the total fiducial cross section is calculated using the full Run-2 dataset. By calculating the fractional difference between each sidereal bin (i) and the full Run-2 dataset (total), sidereal-time dependent modulations in the ratio (R) can be probed

$$R_i = \frac{\sigma_i - \sigma_{\mathrm{total}}}{\sigma_{\mathrm{total}}}. \tag{C.4}$$

In the absence of any sidereal dependencies, this ratio should be consistent with zero. However, a sidereal variation would induce a sinusoidal variation in the ratio, where the phase and amplitude are proportional to the SME couplings and the event kinematics in the Sun-centred frame. Fits can be performed to extract limits on the SME couplings from the data [181]. In this analysis a simple test is performed to probe the compatibility of the data with the Standard Model by computing a χ^2 test statistic,

$$\chi^2 = \sum_{i=1} \frac{(R_i - \mu)^2}{\sigma_i^2}, \tag{C.5}$$

where σ_i is the uncertainty on R_i and $\mu = 0$ under the null hypothesis, i.e. there are no time-dependent modulations. The χ^2 probability density function is given by,

$$f(x,k) = \frac{1}{2^{k/2}\Gamma(k/2)}\, x^{k/2-1}\, exp(-x/2), \tag{C.6}$$

where x is the obtained χ^2 value and k the number of degrees of freedom. The probability of obtaining a value less than or equal to the observed value of x is given by,

$$F(x) = \int_{-\infty}^{x} f_k(x)dx. \tag{C.7}$$

From this a p-value can be calculated, which is the probability of observing results at least as extreme as the experimental measurement, under the assumption than the null hypothesis is true.

$$p = 1 - F(x) \tag{C.8}$$

The convention in particle physics is to reject the null hypothesis if the p-value is smaller than 3×10^{-7} (5σ). This simple methodology serves as a proof of concept for the analysis, which will be expanded upon considerably by a new analysis team in ATLAS in collaboration with external theorists[2].

C.3 Results

Figure C.2 shows the event-level $Z \to e^+e^-$ and $Z \to \mu^+\mu^-$ selection efficiencies binned as a function of pileup and sidereal phase. As expected, there is a strong dependence of the efficiency on pileup, however, there is no dependence on the sidereal phase.

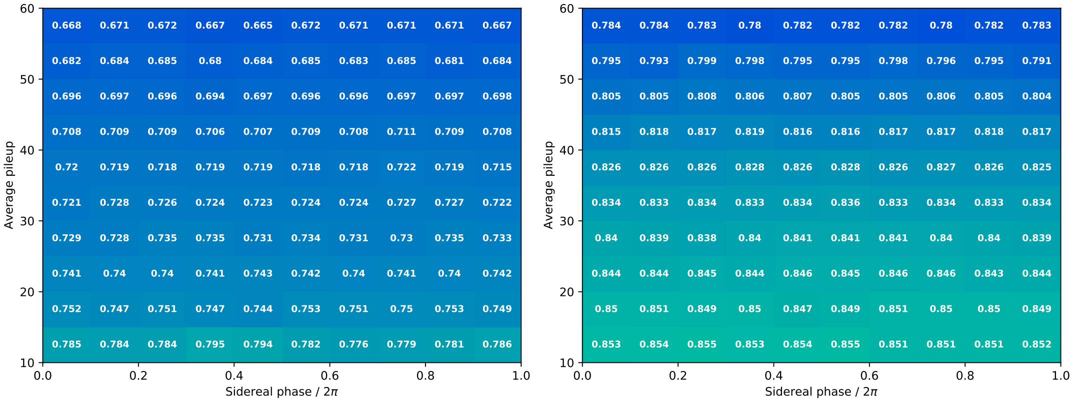

Figure C.2: Event-level $Z \to e^+e^-$ (left) and $Z \to \mu^+\mu^-$ (right) selection efficiency in bins of pileup and sidereal phase. The event-level efficiency is calculated using the same methodology outlined in Section 4.2.2.

Figure C.3 shows the modulation of the ratio R_i as a function of sidereal phase in the $Z \to e^+e^-$ and $Z \to \mu^+\mu^-$ channels. The χ^2 and p-values for these distributions are given in Table C.1, where the $Z \to e^+e^-$ channel has a p-value of 0.18 and the $Z \to \mu^+\mu^-$ channel a p-value of 0.08. Neither

---

[2] As discussed in the conclusion.

of these results suggest there are any significant deviations from the Standard Model, hence the null hypothesis cannot be rejected in this simple test; indicating there is no evidence for any Lorentz invariance violating effects. Visually, there does appear to be some periodic variation in the ratio, and perhaps tighter constraints could be achieved by performing a more sophisticated fit to the data and extracting SME coefficients, as will be done in the follow-up analysis.

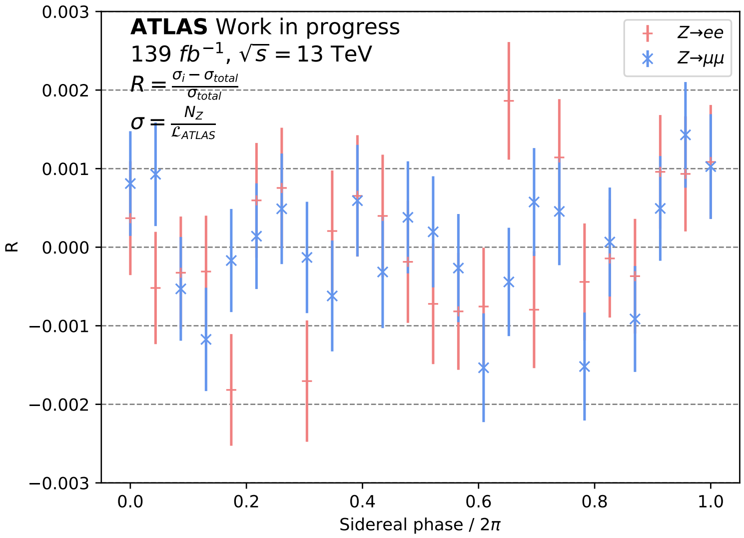

Figure C.3: Fractional difference in the fiducial cross section measured in each bin of sidereal phase with respect to the full Run-2 fiducial cross section.

	$Z \to e^+e^-$	$Z \to \mu^+\mu^-$
χ^2	30.26	32.94
$D.o.f$	23	23
$p - value$	0.14	0.08

Table C.1: χ^2 and p-value of the fiducial Z cross section sidereal modulation relative to the Standard Model.

C.4 Conclusion

This section has presented a reinterpretation of the Z-counting results in the context of probing sidereal-time dependent modulations in the fiducial $Z \to \ell^+\ell^-$ cross section. No evidence for Lorentz-invariance violating effects is observed in this simple test, however a more sophisticated analysis will be pursued by a new analysis team which has been setup within ATLAS in collaboration with theory experts in the field of Lorentz invariance violation. This team will perform a more detailed analysis of the data, looking for evidence of sidereal-time dependent effects by performing fits to the data, and in the absence of any signal set constraints on SME coefficients. Such an analysis has to date not been performed at ATLAS, and opens up an exciting new avenue to seek new physics with the LHC.

Bibliography

[1] ATLAS Collaboration, *Luminosity Determination using $Z \to \ell\ell$ events at $\sqrt{s} = 13$ TeV with the ATLAS detector*, Tech. Rep. ATL-DAPR-PUB-2021-001, CERN, Geneva, Feb, 2021. `https://cds.cern.ch/record/2752951`.

[2] M. W. O'Keefe, *Luminosity Determination using $Z \to \ell\ell$ events at $\sqrt{s} = 13$ TeV with the ATLAS detector*, PoS **ICHEP2020** (2021) 812.

[3] ATLAS Collaboration, *Search for a heavy charged boson in events with a charged lepton and missing transverse momentum from pp collisions at $\sqrt{s} = 13$ TeV with the ATLAS detector*, Phys. Rev. D **100** (2019) 052013, `arXiv:1906.05609 [hep-ex]`.

[4] M. W. O'Keefe, *Searches for W' and Z' in leptonic final states using 139 fb^{-1} of pp collision data collected at $\sqrt{s} = 13$ TeV with the ATLAS detector*, tech. rep., CERN, Geneva, Dec, 2020. `https://cds.cern.ch/record/2748137`. 07 January, 2021.

[5] A. Einstein, *The Foundation of the General Theory of Relativity*, Annalen Phys. **49** (1916) 769–822.

[6] S. L. Glashow, *The renormalizability of vector meson interactions*, Nucl. Phys. **10** (1959) 107–117.

[7] A. Salam, *Weak and Electromagnetic Interactions*, Conf. Proc. C **680519** (1968) 367–377.

[8] S. Weinberg, *A model of leptons*, Physical Review Letters **19** (1967) 1264–1266.

[9] M. Gell-Mann, *The Eightfold Way: a theory of strong interaction symmetry*, (1961), `https://www.osti.gov/biblio/4008239`.

[10] F. Englert and R. Brout, *Broken Symmetry and the Mass of Gauge Vector Mesons*, Phys. Rev. Lett. **13** (1964) 321–323, `https://link.aps.org/doi/10.1103/PhysRevLett.13.321`.

[11] P. W. Higgs, *Broken Symmetries and the Masses of Gauge Bosons*, Phys. Rev. Lett. **13** (1964) 508–509, `https://link.aps.org/doi/10.1103/PhysRevLett.13.508`.

[12] G. S. Guralnik, C. R. Hagen, and T. W. B. Kibble, *Global Conservation Laws and Massless Particles*, Phys. Rev. Lett. **13** (1964) 585–587, `https://link.aps.org/doi/10.1103/PhysRevLett.13.585`.

[13] K. Collaboration, *Improved Upper Limit on the Neutrino Mass from a Direct Kinematic Method by KATRIN*, Phys. Rev. Lett. **123** (2019) 221802, `https://link.aps.org/doi/10.1103/PhysRevLett.123.221802`.

[14] ATLAS Collaboration, *Test of the universality of τ and μ lepton couplings in W boson decays from $t\bar{t}$ events at* 13 *TeV with the ATLAS detector*, ATLAS-CONF-2020-014, 2020, `https://cds.cern.ch/record/2719520`.

[15] ATLAS Collaboration, *Measurement of the polarisation of single top quarks and antiquarks produced in the t-channel collected with the ATLAS detector at $\sqrt{s} = 13$ TeV and bounds on the tWb dipole operator*, tech. rep., CERN, Geneva, Jun, 2021. `https://cds.cern.ch/record/2773738`.

[16] ATLAS Collaboration, *Observation of $H \to b\bar{b}$ decays and VH production with the ATLAS detector*, ATLAS-CONF-2018-036, 2018, `https://cds.cern.ch/record/2630338`.

[17] ATLAS Collaboration, *Observation of photon-induced W^+W^- production in pp collisions at* $\sqrt{s} = 13$ *TeV using the ATLAS detector*, Phys. Lett. B **816** (2021) 136190, `arXiv:2010.04019 [hep-ex]`.

[18] ATLAS Collaboration, A. Collaboration, *Observation of a new particle in the search for the Standard Model Higgs boson with the ATLAS detector at the LHC*, Phys. Lett. **B716** (2012) 1–29, `arXiv:1207.7214 [hep-ex]`.

[19] CMS Collaboration, T. C. Collaboration, *Observation of a New Boson at a Mass of 125 GeV with the CMS Experiment at the LHC*, Phys. Lett. **B716** (2012) 30–61, `arXiv:1207.7235 [hep-ex]`.

[20] P. D. Group, *Review of Particle Physics*, Progress of Theoretical and Experimental Physics **2020** (2020), `https://doi.org/10.1093/ptep/ptaa104`, 083C01.

[21] M. $g-2$ Collaboration, *Measurement of the Positive Muon Anomalous Magnetic Moment to 0.46 ppm*, Phys. Rev. Lett. **126** (2021) 141801, `https://link.aps.org/doi/10.1103/PhysRevLett.126.141801`.

[22] ATLAS Collaboration Collaboration, A. Collaboration, *Search for squarks and gluinos in final states with one isolated lepton, jets, and missing transverse momentum at* $\sqrt{s} = 13$ *TeV with the ATLAS detector*, `https://cds.cern.ch/record/2748580`.

[23] ATLAS Collaboration Collaboration, A. Collaboration, *Search for squarks and gluinos in final states with jets and missing transverse momentum using 139 fb*$^{-1}$ *of* $\sqrt{s}$ *=13 TeV pp collision data with the ATLAS detector*, JHEP **2102** (2020) 143. 64 p, `https://cds.cern.ch/record/2742847`.

[24] ATLAS Collaboration, A. Collaboration, *Search for pairs of scalar leptoquarks decaying into quarks and electrons or muons in* $\sqrt{s}$ *= 13 TeV pp collisions with the ATLAS detector*, JHEP **10** (2020) 112, `arXiv:2006.05872 [hep-ex]`.

[25] ATLAS Collaboration Collaboration, A. Collaboration, *Search for pair production of scalar leptoquarks decaying into first- or second-generation leptons and top quarks in proton-proton collisions at* $\sqrt{s} = 13$ *TeV with the ATLAS detector*,.

[26] ATLAS Collaboration Collaboration, A. Collaboration, *Search for dark matter produced in association with a single top quark in* $\sqrt{s} = 13$ *TeV pp collisions with the ATLAS detector*, `https://cds.cern.ch/record/2744937`.

[27] ATLAS Collaboration Collaboration, A. Collaboration, *Search for dark matter in association with an energetic photon in pp collisions at* $\sqrt{s}$ *= 13 TeV with the ATLAS detector*, JHEP **2102** (2020) 226. 45 p, `https://cds.cern.ch/record/2744036`.

[28] ATLAS Collaboration Collaboration, A. Collaboration, *Search for resonances decaying into photon pairs in 139 fb*$^{-1}$ *of pp collisions at* $\sqrt{s}$ *= 13 TeV with the ATLAS detector*, `https://cds.cern.ch/record/2753130`.

[29] ATLAS Collaboration Collaboration, A. Collaboration, *Search for a heavy Higgs boson decaying into a* Z *boson and another heavy Higgs boson in the* $\ell\ell bb$ *and* $\ell\ell WW$ *final states in pp collisions at* $\sqrt{s} = 13$ *TeV with the ATLAS detector*, `https://cds.cern.ch/record/2744133`.

[30] ATLAS Collaboration, *Search for high-mass dilepton resonances using* 139 *fb*$^{-1}$ *of pp collision data collected at* $\sqrt{s} = 13$ *TeV with the ATLAS detector*, Phys. Lett. B **796** (2019) 68, `arXiv:1903.06248 [hep-ex]`.

[31] W. Buchmüller and D. Wyler, *Effective lagrangian analysis of new interactions and flavour conservation*, Nuclear Physics B **268** (1986) 621–653, `https://www.sciencedirect.com/science/article/pii/0550321386902622`.

[32] B. Grzadkowski, M. Iskrzynski, M. Misiak, and J. Rosiek, *Dimension-Six Terms in the Standard Model Lagrangian*, JHEP **10** (2010) 085, `arXiv:1008.4884 [hep-ph]`.

[33] B. Grzadkowski, M. Iskrzynski, M. Misiak, and J. Rosiek, *Dimension-Six Terms in the Standard Model Lagrangian*, JHEP **10** (2010) 085, `arXiv:1008.4884 [hep-ph]`.

[34] ATLAS Collaboration, *Higgs boson production cross-section measurements and their EFT interpretation in the* 4ℓ *decay channel at* $\sqrt{s}$ *=13 TeV with the ATLAS detector*, Eur. Phys. J. C **80** (2020) 957, `arXiv:2004.03447 [hep-ex]`, [Erratum: Eur.Phys.J.C 81, 29 (2021), Erratum: Eur.Phys.J.C 81, 398 (2021)].

[35] V. A. Kostelecký and S. Samuel, *Spontaneous breaking of Lorentz symmetry in string theory*, Phys. Rev. D **39** (1989) 683–685, `https://link.aps.org/doi/10.1103/PhysRevD.39.683`.

[36] S. D. Drell and T.-M. Yan, *Massive Lepton-Pair Production in Hadron-Hadron Collisions at High Energies*, Phys. Rev. Lett. **25** (1970) 316–320, `https://link.aps.org/doi/10.1103/PhysRevLett.25.316`.

[37] H1, ZEUS Collaboration, H. Abramowicz et al., *Combination of measurements of inclusive deep inelastic $e^{\pm}p$ scattering cross sections and QCD analysis of HERA data*, Eur. Phys. J. C **75** (2015) 580, `arXiv:1506.06042 [hep-ex]`.

[38] ATLAS Collaboration, *Precision measurement and interpretation of inclusive W^+, W^- and Z/γ^* production cross sections with the ATLAS detector*, Eur. Phys. J. C **77** (2017) 367, `arXiv:1612.03016 [hep-ex]`.

[39] R. P. Feynman, *Space-Time Approach to Quantum Electrodynamics*, Phys. Rev. **76** (1949) 769–789, `https://link.aps.org/doi/10.1103/PhysRev.76.769`.

[40] ATLAS Collaboration, *Double differential Z,W cross sections and their ratios in the electron channels*, tech. rep., CERN, Geneva, Oct, 2011. `https://cds.cern.ch/record/1387038`.

[41] M. Kobayashi and T. Maskawa, *CP-Violation in the Renormalizable Theory of Weak Interaction*, Progress of Theoretical Physics **49** (1973) 652–657, `https://academic.oup.com/ptp/article-pdf/49/2/652/5257692/49-2-652.pdf`, `https://doi.org/10.1143/PTP.49.652`.

[42] R. D. Ball et al., *Parton distributions with LHC data*, Nucl. Phys. B **867** (2013) 244, `arXiv:1207.1303 [hep-ph]`.

[43] T.-J. Hou et al., *New CTEQ global analysis of quantum chromodynamics with high-precision data from the LHC*, Phys. Rev. D **103** (2021) 014013, `arXiv:1912.10053 [hep-ph]`.

[44] L. A. Harland-Lang, A. D. Martin, P. Motylinski, and R. S. Thorne, *Parton distributions in the LHC era: MMHT 2014 PDFs*, Eur. Phys. J. C **75** (2015) 204, `arXiv:1412.3989 [hep-ph]`.

[45] M. Klein and R. Yoshida, *Collider Physics at HERA*, Prog. Part. Nucl. Phys. **61** (2008) 343–393, `arXiv:0805.3334 [hep-ex]`.

[46] J. D. Bjorken, *Asymptotic Sum Rules at Infinite Momentum*, Phys. Rev. **179** (1969) 1547–1553, `https://link.aps.org/doi/10.1103/PhysRev.179.1547`.

[47] V. N. Gribov and L. N. Lipatov, *Deep inelastic e p scattering in perturbation theory*, Sov. J. Nucl. Phys. **15** (1972) 438–450.

[48] L. N. Lipatov, *The parton model and perturbation theory*, Sov. J. Nucl. Phys **20** (1974) 181–198.

[49] Y. L. Dokshitzer, *Calculation of the Structure Functions for Deep Inelastic Scattering and e+ e- Annihilation by Perturbation Theory in Quantum Chromodynamics.*, Sov. Phys. JETP **46** (1977) 641–653.

[50] G. Altarelli and G. Parisi, *Asymptotic freedom in parton language*, Nuclear Physics B **126** (1977) 298–318, `https://www.sciencedirect.com/science/article/pii/0550321377903844`.

[51] I. Antoniadis, L. Baulieu, and C. Kounnas, *A proof of the factorization of mass singularities in the Bjorken limit*, Nuclear Physics B **168** (1980) 394–408, `https://www.sciencedirect.com/science/article/pii/0550321380901340`.

[52] G. 't Hooft, *Dimensional regularization and the renormalization group*, Nuclear Physics B **61** (1973) 455–468, `https://ui.adsabs.harvard.edu/abs/1973NuPhB..61..455T`.

[53] S. Weinberg, *New Approach to the Renormalization Group*, Phs. Rev. D. **8** (1973) 3497–3509, `https://ui.adsabs.harvard.edu/abs/1973PhRvD...8.3497W`.

[54] C. M. Carloni Calame, G. Montagna, O. Nicrosini, and A. Vicini, *Precision electroweak calculation of the charged current Drell-Yan process*, JHEP **12** (2006) 016, `arXiv:hep-ph/0609170`.

[55] C. M. Carloni Calame, G. Montagna, O. Nicrosini, and A. Vicini, *Precision electroweak calculation of the production of a high transverse-momentum lepton pair at hadron colliders*, JHEP **10** (2007) 109, `arXiv:0710.1722 [hep-ph]`.

[56] A. Sirlin, *Radiative corrections in the* $\mathrm{SU}(2)_L \times \mathrm{U}(1)$ *theory: A simple renormalization framework*, Phys. Rev. D **22** (1980) 971–981, `https://link.aps.org/doi/10.1103/PhysRevD.22.971`.

[57] A. Arbuzov, D. Bardin, S. Bondarenko, P. Christova, L. Kalinovskaya, U. Klein, V. Kolesnikov, L. Rumyantsev, R. Sadykov, and A. Sapronov, *Update of the MCSANC Monte Carlo integrator, v. 1.20*, JETP Lett. **103** (2016) 131, `arXiv:1509.03052 [hep-ph]`.

[58] C. M. Carloni Calame, G. Montagna, O. Nicrosini, and M. Treccani, *Higher order QED corrections to W boson mass determination at hadron colliders*, Phys. Rev. D **69** (2004) 037301, `arXiv:hep-ph/0303102`.

[59] ATLAS Collaboration, *Measurement of the W-boson mass in pp collisions at $\sqrt{s} = 7$ TeV with the ATLAS detector*, Eur. Phys. J. C **78** (2018) 110, `arXiv:1701.07240 [hep-ex]`.

[60] A. Denner, *Techniques for calculation of electroweak radiative corrections at the one loop level and results for W physics at LEP-200*, Fortsch. Phys. **41** (1993) 307–420, `arXiv:0709.1075 [hep-ph]`.

[61] P. Golonka and Z. Was, *PHOTOS Monte Carlo: a precision tool for QED corrections in Z and W decays*, Eur. Phys. J. C **45** (2006) 97, `arXiv:hep-ph/0506026`.

[62] A. D. Martin, R. G. Roberts, W. J. Stirling, and R. S. Thorne, *Parton distributions incorporating QED contributions*, Eur. Phys. J. C **39** (2005) 155–161, `arXiv:hep-ph/0411040`.

[63] e. a. A. Arbuzov, *Les houches physics at TeV colliders 2005, standard model and Higgs working group: Summary report*, Chapter 10 (2006), `arXiv:hep-ph/0604120`.

[64] S. Dittmaier and M. Huber, *Radiative corrections to the neutral-current Drell-Yan process in the Standard Model and its minimal supersymmetric extension*, JHEP **01** (2010) 060, `arXiv:0911.2329 [hep-ph]`.

[65] S. Catani, L. Cieri, G. Ferrera, D. de Florian, and M. Grazzini, *Vector boson production at hadron colliders: a fully exclusive QCD calculation at NNLO*, Phys. Rev. Lett. **103** (2009) 082001, `arXiv:0903.2120 [hep-ph]`.

[66] K. Melnikov and F. Petriello, *Electroweak gauge boson production at hadron colliders through $\mathcal{O}(\alpha_s^2)$*, Phys. Rev. D **74** (2006) 114017, `arXiv:hep-ph/0609070`.

[67] S. Höche, Y. Li, and S. Prestel, *Drell-Yan lepton pair production at NNLO QCD with parton showers*, Phys. Rev. D **91** (2015) 074015, `arXiv:1405.3607 [hep-ph]`.

[68] C. Duhr, F. Dulat, and B. Mistlberger, *Charged current Drell-Yan production at N^{3}LO*, JHEP **11** (2020) 143, `arXiv:2007.13313 [hep-ph]`.

[69] K. Melnikov and F. Petriello, *Electroweak gauge boson production at hadron colliders through $O(\alpha_s^2)$*, Phys. Rev. D **74** (2006) 114017, `arXiv:hep-ph/0609070 [hep-ph]`.

[70] R. Gavin, Y. Li, F. Petriello, and S. Quackenbush, *FEWZ 2.0: A code for hadronic Z production at next-to-next-to-leading order*, Comput. Phys. Commun. **182** (2011) 2388, `arXiv:1011.3540 [hep-ph]`.

[71] S. Catani and M. Grazzini, *An NNLO subtraction formalism in hadron collisions and its application to Higgs boson production at the LHC*, Phys. Rev. Lett. **98** (2007) 222002, `arXiv:hep-ph/0703012`.

[72] ATLAS Collaboration, *Measurement of the Transverse Momentum Distribution of W Bosons in pp Collisions at $\sqrt{s} = 7$ TeV with the ATLAS Detector*, Phys. Rev. D **85** (2012) 012005, `arXiv:1108.6308 [hep-ex]`.

[73] S. Catani et al., *QCD*, in *Workshop on Standard Model Physics (and more) at the LHC (First Plenary Meeting)*. 5, 2000. `arXiv:hep-ph/0005025`.

[74] S. Catani and M. Seymour, *A general algorithm for calculating jet cross sections in NLO QCD*, Nuclear Physics B **485** (1997) 291–419, `https://www.sciencedirect.com/science/article/pii/S0550321396005895`.

[75] U. Klein, *Les Houches 2013: Physics at TeV Colliders: Standard Model Working Group Report*, Chapter III.2 (2014) 80 – 91, `arXiv:1405.1067 [hep-ph]`.

[76] L. Evans and P. Bryant, *LHC Machine*, Journal of Instrumentation **3** (2008) S08001–S08001, `https://doi.org/10.1088/1748-0221/3/08/s08001`.

[77] ATLAS Collaboration, *The ATLAS Experiment at the CERN Large Hadron Collider*, JINST **3** (2008) S08003.

[78] The ALICE Collaboration, *The ALICE experiment at the CERN LHC*, Journal of Instrumentation **3** (2008) S08002–S08002, `https://doi.org/10.1088/1748-0221/3/08/s08002`.

[79] CMS Collaboration, *The CMS Experiment at the CERN LHC*, JINST **3** (2008) S08004.

[80] LHCb Collaboration, *The LHCb Detector at the LHC*, JINST **3** (2008) S08005.

[81] C. Lefèvre, *The CERN accelerator complex. Complexe des accélérateurs du CERN*, Dec, 2008.

[82] O. S. Brüning, P. Collier, P. Lebrun, S. Myers, R. Ostojic, J. Poole, and P. Proudlock, *LHC Design Report*. CERN Yellow Reports: Monographs. CERN, Geneva, 2004. `https://cds.cern.ch/record/782076`.

[83] ATLAS Collaboration, *ATLAS Experiment at the CERN Large Hadron Collider*, JINST **3** (2008) S08003.

[84] ATLAS Collaboration, *The ATLAS Simulation Infrastructure*, Eur. Phys. J. C **70** (2010) 823, `arXiv:1005.4568 [physics.ins-det]`.

[85] ATLAS Collaboration, *ATLAS Insertable B-Layer Technical Design Report*, 2010. `https://cds.cern.ch/record/1291633`.

[86] K. Potamianos, *The upgraded Pixel detector and the commissioning of the Inner Detector tracking of the ATLAS experiment for Run-2 at the Large Hadron Collider*, PoS **EPS-HEP2015** (2015) 261, `arXiv:1608.07850 [physics.ins-det]`.

[87] ATLAS Collaboration, *Electron and photon energy calibration with the ATLAS detector using 2015–2016 LHC proton–proton collision data*, JINST **14** (2019) P03017, `arXiv:1812.03848 [hep-ex]`.

[88] ATLAS Collaboration, *Performance of the ATLAS muon trigger in pp collisions at* $\sqrt{s} = 8$ *TeV*, Eur. Phys. J. C **75** (2015) 120, `arXiv:1408.3179 [hep-ex]`.

[89] ATLAS Collaboration, *Performance of electron and photon triggers in ATLAS during LHC Run 2*, Eur. Phys. J. C **80** (2020) 47, `arXiv:1909.00761 [hep-ex]`.

[90] ATLAS Collaboration, *Performance of the ATLAS trigger system in 2015*, Eur. Phys. J. C **77** (2017) 317, `arXiv:1611.09661 [hep-ex]`.

[91] R. A. et. al., *The ATLAS Level-1 Calorimeter Trigger*, Journal of Instrumentation **3** (2008) P03001–P03001, `https://doi.org/10.1088/1748-0221/3/03/p03001`.

[92] ATLAS Collaboration, *Expected Performance of the ATLAS Experiment - Detector, Trigger and Physics*, 2009.

[93] S. A. et. al., *The ATLAS central level-1 trigger logic and TTC system*, Journal of Instrumentation **3** (2008) P08002–P08002, `https://doi.org/10.1088/1748-0221/3/08/p08002`.

[94] G. Avoni et al, *The new LUCID-2 detector for luminosity measurement and monitoring in ATLAS*, Journal of Instrumentation **13** (2018) P07017–P07017, `https://doi.org/10.1088/1748-0221/13/07/p07017`.

[95] S. van der Meer, *Calibration of the effective beam height in the ISR*, `https://cds.cern.ch/record/296752`.

[96] ATLAS Collaboration, *Luminosity determination in pp collisions at* $\sqrt{s} = 13$ *TeV using the ATLAS detector at the LHC*, ATLAS-CONF-2019-021, 2019, `https://cds.cern.ch/record/2677054`.

[97] ATLAS Collaboration, *Electron reconstruction and identification in the ATLAS experiment using the 2015 and 2016 LHC proton–proton collision data at* $\sqrt{s} = 13$ *TeV*, Eur. Phys. J. C **79** (2019) 639, `arXiv:1902.04655 [hep-ex]`.

[98] ATLAS Collaboration, *Electron and photon performance measurements with the ATLAS detector using the 2015–2017 LHC proton–proton collision data*, JINST **14** (2019) P12006, `arXiv:1908.00005 [hep-ex]`.

[99] ATLAS Collaboration, *Measurement of the photon identification efficiencies with the ATLAS detector using LHC Run 2 data collected in 2015 and 2016*, Eur. Phys. J. C **79** (2019) 205, `arXiv:1810.05087 [hep-ex]`.

[100] ATLAS Collaboration, *Topological cell clustering in the ATLAS calorimeters and its performance in LHC Run 1*, Eur. Phys. J. C **77** (2017) 490, `arXiv:1603.02934 [hep-ex]`.

[101] A. Hoecker et al., *TMVA - Toolkit for Multivariate Data Analysis*, arXiv e-prints (2007) physics/0703039, `arXiv:physics/0703039 [physics.data-an]`.

[102] J. Illingworth and J. Kittler, *A survey of the hough transform*, Computer Vision, Graphics, and Image Processing **44** (1988) 87–116, `https://www.sciencedirect.com/science/article/pii/S0734189X88800331`.

[103] ATLAS Collaboration, *Muon reconstruction and identification efficiency in ATLAS using the full Run 2 pp collision data set at $\sqrt{s} = 13$ TeV*, Eur. Phys. J. C **81** (2021) 578, `arXiv:2012.00578 [hep-ex]`.

[104] ATLAS Collaboration, *Muon reconstruction performance of the ATLAS detector in proton–proton collision data at $\sqrt{s} = 13$ TeV*, Eur. Phys. J. C **76** (2016) 292, `arXiv:1603.05598 [hep-ex]`.

[105] M. Cacciari, G. P. Salam, and G. Soyez, *The anti-k_t jet clustering algorithm*, JHEP **04** (2008) 063, `arXiv:0802.1189 [hep-ph]`.

[106] ATLAS Collaboration, *Jet global sequential corrections with the ATLAS detector in proton–proton collisions at $\sqrt{s} = 8$ TeV*, ATLAS-CONF-2015-002, 2015, `https://cds.cern.ch/record/2001682`.

[107] ATLAS Collaboration, *Data-driven determination of the energy scale and resolution of jets reconstructed in the ATLAS calorimeters using dijet and multijet events at $\sqrt{s} = 8$ TeV*, ATLAS-CONF-2015-017, 2015, `https://cds.cern.ch/record/2008678`.

[108] ATLAS Collaboration, *Monte Carlo Calibration and Combination of In-situ Measurements of Jet Energy Scale, Jet Energy Resolution and Jet Mass in ATLAS*, ATLAS-CONF-2015-037, 2015, `https://cds.cern.ch/record/2044941`.

[109] ATLAS Collaboration, *Jet energy scale measurements and their systematic uncertainties in proton–proton collisions at $\sqrt{s} = 13$ TeV with the ATLAS detector*, Phys. Rev. D **96** (2017) 072002, `arXiv:1703.09665 [hep-ex]`.

[110] ALEPH Collaboration, D. Buskulic et al., *Performance of the ALEPH detector at LEP*, Nucl. Instrum. Meth. A **360** (1995) 481–506.

[111] ATLAS Collaboration, *Jet reconstruction and performance using particle flow with the ATLAS Detector*, Eur. Phys. J. C **77** (2017) 466, `arXiv:1703.10485 [hep-ex]`.

[112] ATLAS Collaboration, *Performance of missing transverse momentum reconstruction with the ATLAS detector using proton–proton collisions at $\sqrt{s} = 13$ TeV*, Eur. Phys. J. C **78** (2018) 903, `arXiv:1802.08168 [hep-ex]`.

[113] ATLAS Collaboration, *ATLAS data quality operations and performance for 2015–2018 data-taking*, JINST **15** (2020) P04003, `arXiv:1911.04632 [physics.ins-det]`.

[114] ATLAS Collaboration, *Luminosity Public Results Run 2*, 2021. `https://twiki.cern.ch/twiki/bin/view/AtlasPublic/LuminosityPublicResultsRun2`.

[115] Particle Data Group Collaboration, K. A. Olive et al., *Review of Particle Physics*, Chin. Phys. C **38** (2014) 090001.

[116] M. Dobbs and J. B. Hansen, *The HepMC C++ Monte Carlo Event Record for High Energy Physics*, tech. rep., CERN, Geneva, Jun, 2000. `https://cds.cern.ch/record/684090`. revised version number 1 submitted on 2001-02-27 09:54:32.

[117] P. Nason, *A new method for combining NLO QCD with shower Monte Carlo algorithms*, JHEP **11** (2004) 040, `arXiv:hep-ph/0409146`.

[118] S. Frixione, P. Nason, and C. Oleari, *Matching NLO QCD computations with parton shower simulations: the POWHEG method*, JHEP **11** (2007) 070, `arXiv:0709.2092 [hep-ph]`.

[119] T. Sjostrand, S. Mrenna, and P. Z. Skands, *A Brief Introduction to PYTHIA 8.1*, Comput. Phys. Commun. **178** (2008) 852–867, `arXiv:0710.3820 [hep-ph]`.

[120] T. Gleisberg, S. Höche, F. Krauss, M. Schönherr, S. Schumann, F. Siegert, and W. J., *Event generation with SHERPA 1.1*, JHEP **02** (2009) 007, `arXiv:0811.4622 [hep-ph]`.

[121] G. Corcella et al., *HERWIG 6: an event generator for hadron emission reactions with interfering gluons (including supersymmetric processes)*, JHEP **01** (2001) 010, `arXiv:hep-ph/0011363`.

[122] N. Davidson, T. Przedzinski, and Z. Was, *PHOTOS Interface in C++: Technical and Physics Documentation*, Comput. Phys. Commun. **199** (2016) 86–101, `arXiv:1011.0937 [hep-ph]`.

[123] S. Agostinelli et al., *GEANT4 – a simulation toolkit*, Nucl. Instr. Meth. A **506** (2003) 250.

[124] ATLAS Collaboration, *Measurement of the transverse momentum distribution of Drell–Yan lepton pairs in proton–proton collisions at* $\sqrt{s} = 13$ *TeV with the ATLAS detector*, `arXiv:1912.02844 [hep-ex]`.

[125] H. Lyons, *Private communication*, 2021.

[126] Y. Li and F. Petriello, *Combining QCD and electroweak corrections to dilepton production in the framework of the FEWZ simulation code*, Physical Review D **86** (2012), `http://dx.doi.org/10.1103/PhysRevD.86.094034`.

[127] T. Sjöstrand, S. Ask, J. R. Christiansen, R. Corke, N. Desai, P. Ilten, S. Mrenna, S. Prestel, C. O. Rasmussen, and P. Z. Skands, *An introduction to PYTHIA 8.2*, Comput. Phys. Commun. **191** (2015) 159–177, `arXiv:1410.3012 [hep-ph]`.

[128] ATLAS Collaboration, *Measurement of the* Z/γ^* *boson transverse momentum distribution in* pp *collisions at* $\sqrt{s} = 7$ *TeV with the ATLAS detector*, JHEP **09** (2014) 145, `arXiv:1406.3660 [hep-ex]`.

[129] ATLAS Collaboration, *The Pythia 8 A3 tune description of ATLAS minimum bias and inelastic measurements incorporating the Donnachie–Landshoff diffractive model*, ATL-PHYS-PUB-2016-017, 2016, `https://cds.cern.ch/record/2206965`.

[130] ATLAS Collaboration, *Luminosity determination in* pp *collisions at* $\sqrt{s} = 8$ *TeV using the ATLAS detector at the LHC*, Eur. Phys. J. C **76** (2016) 653, `arXiv:1608.03953 [hep-ex]`.

[131] S. van der Meer, *Calibration of the Effective Beam Height in the ISR*, 6, 1968. `https://cds.cern.ch/record/296752`. CERN-ISR-PO-68-31.

[132] M. O'Keefe, Z*-counting dashboard*, 2021. `https://zcounting-dash.web.cern.ch/`.

[133] ATLAS Collaboration, *Search for new particles in events with one lepton and missing transverse momentum in* pp *collisions at* $\sqrt{s} = 8$ *TeV with the ATLAS detector*, JHEP **09** (2014) 037, `arXiv:1407.7494 [hep-ex]`.

[134] ATLAS Collaboration, *Search for a new heavy gauge boson resonance decaying into a lepton and missing transverse momentum in* $36\,fb^{-1}$ *of* pp *collisions at* $\sqrt{s} = 13$ *TeV with the ATLAS experiment*, ATLAS-CONF-2017-016, 2017, `https://cds.cern.ch/record/2257952`.

[135] CMS Collaboration, *Search for physics beyond the standard model in final states with a lepton and missing transverse energy in proton-proton collisions at sqrt(s) = 8 TeV*, Phys. Rev. **D91** (2015) 092005, `arXiv:1408.2745 [hep-ex]`.

[136] CMS Collaboration, *Search for high-mass resonances in final states with a lepton and missing transverse momentum at* $\sqrt{s} = 13$ *TeV*, JHEP **06** (2018) 128, `arXiv:1803.11133 [hep-ex]`.

[137] R. N. Mohapatra and J. C. Pati, *Left-right gauge symmetry and an "isoconjugate" model of* CP *violation*, Phys. Rev. D **11** (1975) 566–571, `https://link.aps.org/doi/10.1103/PhysRevD.11.566`.

[138] G. Senjanovic and R. N. Mohapatra, *Exact left-right symmetry and spontaneous violation of parity*, Phys. Rev. D **12** (1975) 1502–1505, `https://link.aps.org/doi/10.1103/PhysRevD.12.1502`.

[139] N. Arkani-Hamed, A. G. Cohen, E. Katz, and A. E. Nelson, *The Littlest Higgs*, JHEP **07** (2002) 034, `arXiv:hep-ph/0206021 [hep-ph]`.

[140] Agashe, Kaustubh and Gopalakrishna, Shrihari and Han, Tao and Huang, Gui-Yu and Soni, Amarjit, *LHC signals for warped electroweak charged gauge bosons*, Phys. Rev. D **80** (2009) 075007, `https://link.aps.org/doi/10.1103/PhysRevD.80.075007`.

[141] Appelquist, Thomas and Cheng, Hsin-Chia and Dobrescu, Bogdan A., *Bounds on universal extra dimensions*, Phys. Rev. D **64** (2001) 035002, `https://link.aps.org/doi/10.1103/PhysRevD.64.035002`.

[142] G. Altarelli, B. Mele, and M. Ruiz-Altaba, *Searching for new heavy vector bosons in $p\bar{p}$ colliders*, Z. Phys. C **45** (1989) 109.

[143] J. de Blas, J. Lizana, and M. Perez-Victoria, *Combining searches of Z' and W' bosons*, JHEP **01** (2013) 166, `arXiv:1211.2229 [hep-ph]`.

[144] D. Pappadopulo, A. Thamm, R. Torre, and A. Wulzer, *Heavy Vector Triplets: Bridging Theory and Data*, JHEP **09** (2014) 060, `arXiv:1402.4431 [hep-ph]`.

[145] H. A. Bethe, *The Electromagnetic Shift of Energy Levels*, Phys. Rev. (1947) 339.

[146] J. Schwinger, *On Quantum-Electrodynamics and the Magnetic Moment of the Electron*, Phys. Rev. (1948) 416.

[147] R. Feynman, *Relativistic Cut-Off for Quantum Electrodynamics*, Phys. Rev. (1948) 1430.

[148] ATLAS Collaboration, *ATLAS Pythia 8 tunes to 7 TeV data*, ATL-PHYS-PUB-2014-021, 2014, `https://cds.cern.ch/record/1966419`.

[149] S. Alioli, P. Nason, C. Oleari, and E. Re, *NLO vector-boson production matched with shower in POWHEG*, JHEP **07** (2008) 060, `arXiv:0805.4802 [hep-ph]`.

[150] S. Alioli, P. Nason, C. Oleari, and E. Re, *A general framework for implementing NLO calculations in shower Monte Carlo programs: the POWHEG BOX*, JHEP **06** (2010) 043, `arXiv:1002.2581 [hep-ph]`.

[151] H.-L. Lai et al., *New parton distributions for collider physics*, Phys. Rev. D **82** (2010) 074024, `arXiv:1007.2241 [hep-ph]`.

[152] S. Frixione, P. Nason, and G. Ridolfi, *A Positive-weight next-to-leading-order Monte Carlo for heavy flavour hadroproduction*, JHEP **09** (2007) 126, `arXiv:0707.3088 [hep-ph]`.

[153] S. Alioli, P. Nason, C. Oleari, and E. Re, *NLO single-top production matched with shower in POWHEG: s- and t-channel contributions*, JHEP **09** (2009) 111, `arXiv:0907.4076 [hep-ph]`.

[154] E. Re, *Single-top Wt-channel production matched with parton showers using the POWHEG method*, Eur. Phys. J. C **71** (2011) 1547, `arXiv:1009.2450 [hep-ph]`.

[155] NNPDF Collaboration, R. D. Ball et al., *Parton distributions for the LHC Run II*, JHEP **04** (2015) 040, `arXiv:1410.8849 [hep-ph]`.

[156] C. Anastasiou, L. Dixon, K. Melnikov, and F. Petriello, *High-precision QCD at hadron colliders: Electroweak gauge boson rapidity distributions at next-to-next-to leading order*, Phys. Rev. D **69** (2004) 094008, `arXiv:hep-ph/0312266`.

[157] S. Dulat, T.-J. Hou, J. Gao, M. Guzzi, J. Huston, P. Nadolsky, J. Pumplin, C. Schmidt, D. Stump, and C. P. Yuan, *New parton distribution functions from a global analysis of quantum chromodynamics*, Phys. Rev. D **93** (2016) 033006, `arXiv:1506.07443 [hep-ph]`.

[158] M. K. Bugge et al., *Search for new particles in the charged lepton plus missing transverse energy final state using pp collisions at $\sqrt{s}$ = 13 TeV in the ATLAS detector*, `https://cds.cern.ch/record/2640567`.

[159] CDF Collaboration, *Search for new particles decaying into dijets in proton-antiproton collisions at* $\sqrt{s} = 1.96$ *TeV*, Phys. Rev. D **79** (2009) 112002, `arXiv:0812.4036 [hep-ex]`.

[160] ATLAS Collaboration, *Search for new phenomena in dijet events using 37 fb^{-1} of pp collision data collected at $\sqrt{s}$ =13 TeV with the ATLAS detector*, Phys. Rev. D **96** (2017) 052004, `arXiv:1703.09127 [hep-ex]`.

[161] CMS Collaboration, *Search for narrow and broad dijet resonances in proton-proton collisions at* $\sqrt{s} = 13$ *TeV and constraints on dark matter mediators and other new particles*, JHEP **08** (2018) 130, `arXiv:1806.00843 [hep-ex]`.

[162] A. Collaboration, *$t\bar{t}$ NNLO reweighter package*, 2019. `https://gitlab.cern.ch/lserkin/TTbarNNLOReweighter`.

[163] ATLAS Collaboration, *Determination of jet calibration and energy resolution in proton–proton collisions at* $\sqrt{s} = 8$ *TeV using the ATLAS detector*, `arXiv:1910.04482 [hep-ex]`.

[164] ATLAS Collaboration, *Identification and rejection of pile-up jets at high pseudorapidity with the ATLAS detector*, Eur. Phys. J. C **77** (2017) 580, `arXiv:1705.02211 [hep-ex]`.

[165] J. H. Friedman, *Data Analysis Techniques for High-Energy Particle Physics*, 1974 CERN School of Computing, Godoysund, Norway, 11-24 Aug 1974: Proceedings (1974) 271, `http://www-public.slac.stanford.edu/sciDoc/docMeta.aspx?slacPubNumber=slac-r-176.html`.

[166] L. A. Harland-Lang, A. D. Martin, P. Motylinski, and R. S. Thorne, *Parton distributions in the LHC era: MMHT 2014 PDFs*, Eur. Phys. J. C **75** (2015) 204, `arXiv:1412.3989 [hep-ph]`.

[167] S. Alekhin, J. Blümlein, and S. Moch, *The ABM parton distributions tuned to LHC data*, Phys. Rev. D **89** (2014) 054028, `arXiv:1310.3059 [hep-ph]`.

[168] H. Abramowicz, *Proton structure and the HERAPDF-2.0 parton densities*, 3rd International Conference on New Frontiers in Physics, Kolymbari, Crete (Greece), 28 Jul 2014 - 6 Aug 2014. Jul, 2014. `http://bib-pubdb1.desy.de/record/172047`.

[169] P. Jimenez-Delgado and E. Reya, *Delineating parton distributions and the strong coupling*, Phys. Rev. D **89** (2014) 074049, `arXiv:1403.1852 [hep-ph]`.

[170] A. Caldwell, D. Kollár, and K. Kröninger, *BAT – The Bayesian analysis toolkit*, Computer Physics Communications **180** (2009) 2197–2209, `http://dx.doi.org/10.1016/j.cpc.2009.06.026`.

[171] E. Kay, *Search for New Heavy Gauge Bosons in* $\sqrt{s} = 13$ *TeV pp Collisions with the ATLAS Detector*, `https://cds.cern.ch/record/2643855`, Presented 03 Jul 2018.

[172] G. Cowan, K. Cranmer, E. Gross, and O. Vitells, *Asymptotic formulae for likelihood-based tests of new physics*, Eur. Phys. J. C **71** (2011) 1554, `arXiv:1007.1727 [physics.data-an]`, [Erratum: Eur.Phys.J.C 73, 2501 (2013)].

[173] ATLAS Collaboration, *Combination of searches for heavy resonances decaying into bosonic and leptonic final states using* $36\,fb^{-1}$ *of proton–proton collision data at* $\sqrt{s} = 13$ *TeV with the ATLAS detector*, Phys. Rev. D **98** (2018) 052008, `arXiv:1808.02380 [hep-ex]`.

[174] I. Bigaran and R. R. Volkas, *Getting chirality right: Single scalar leptoquark solutions to the* $(g-2)_{e,\mu}$ *puzzle*, Phys. Rev. D **102** (2020) 075037, `arXiv:2002.12544 [hep-ph]`.

[175] S. Iguro and R. Watanabe, *Bayesian fit analysis to full distribution data of* $\overline{\mathrm{B}} \to \mathrm{D}^{(*)}\ell\overline{\nu} : |\mathrm{V_{cb}}|$ *determination and new physics constraints*, JHEP **08** (2020) 006, `arXiv:2004.10208 [hep-ph]`.

[176] G. Cowan, K. Cranmer, E. Gross, and O. Vitells, *Asymptotic formulae for likelihood-based tests of new physics*, Eur. Phys. J. C **71** (2011) 1554, `arXiv:1007.1727 [physics.data-an]`.

[177] G. Luders, *On the Equivalence of Invariance under Time Reversal and under Particle-Antiparticle Conjugation for Relativistic Field Theories*, Kong. Dan. Vid. Sel. Mat. Fys. Med. **28N5** (1954) 1–17.

[178] J. H. Christenson, J. W. Cronin, V. L. Fitch, and R. Turlay, *Evidence for the* 2π *Decay of the* K_2^0 *Meson*, Phys. Rev. Lett. **13** (1964) 138–140, `https://link.aps.org/doi/10.1103/PhysRevLett.13.138`.

[179] V. A. Kostelecký and C. D. Lane, *Constraints on Lorentz violation from clock-comparison experiments*, Phys. Rev. D **60** (1999) 116010, `https://link.aps.org/doi/10.1103/PhysRevD.60.116010`.

[180] D0 Collaboration Collaboration, D. collaboration, *Search for Violation of* CPT *and Lorentz Invariance in* B_s^0 *Meson Oscillations*, Phys. Rev. Lett. **115** (2015) 161601, `https://link.aps.org/doi/10.1103/PhysRevLett.115.161601`.

[181] D0 Collaboration, D. collaboiration, *Search for violation of Lorentz invariance in top quark pair production and decay*, Phys. Rev. Lett. **108** (2012) 261603, `arXiv:1203.6106 [hep-ex]`.